ASPECTS OF INTEGRITY ASSESSMENT OF 316LN AUSTENITIC STAINLESS STEEL WELD JOINT UNDER CREEP

By

DAVID VIJAYANAND V

(Enrollment No:- ENGG02201104008)

Indira Gandhi Centre for Atomic Research, Kalpakkam– 603 102

India

A thesis submitted to the

Board of Studies in Engineering Sciences

In partial fulfillment of requirements

for the Degree of

DOCTOR OF PHILOSOPHY

of

HOMI BHABHA NATIONAL INSTITUTE

August, 2016

Homi Bhabha National Institute

Recommendations of the Viva Voce Committee

As members of the Viva Voce Committee, we certify that we have read the dissertation prepared by Shri. David Vijayanand V. titled "Aspects of Integrity Assessment of 316LN Austenitic Stainless Steel Weld Joint under Creep" and recommend that it may be accepted as fulfilling the thesis requirement for the award of Degree of Doctor of Philosophy.

Chairman - Dr. K. Velusamy	Date: 17/2/2017
Guide / Convener - Dr. K. Laha	Date: 17.2.2017.
Examiner - Prof. B. P. Kashyap	Date: 17/02/2017
Member 1- Dr. B.P.C. Rao	Date: 17/2/2017
Member 2- Dr. G. Sasikala	Date: 17/2/2017

Final approval and acceptance of this thesis is contingent upon the candidate's submission of the final copies of the thesis to HBNI.

I hereby certify that I have read this thesis prepared under my/our direction and recommend that it may be accepted as fulfilling the thesis requirement.

Date: **17/02/2017**

Place: **Kalpakkam**

Guide

STATEMENT BY AUTHOR

This dissertation has been submitted in partial fulfillment of requirements for an advanced degree at Homi Bhabha National Institute (HBNI) and is deposited in the Library to be made available to borrowers under rules of the HBNI.

Brief quotations from this dissertation are allowable without special permission, provided that accurate acknowledgement of source is made. Requests for permission for extended quotation from or reproduction of this manuscript in whole or in part may be granted by the Competent Authority of HBNI when in his or her judgment the proposed use of the material is in the interests of scholarship. In all other instances, however, permission must be obtained from the author.

V. David

(David Vijayanand V)

DECLARATION

I, hereby declare that the investigation presented in the thesis has been carried out by me. The work is original and has not been submitted earlier as a whole or in part for a degree / diploma at this or any other Institution / University.

(David Vijayanand V)

LIST OF PUBLICATIONS ARISING FROM THE THESIS

Journals Papers

1. Microstructural evolution during creep of 316LN stainless steel multi-pass weld joints, **V.D. Vijayanand**, K. Laha, P. Parameswaran, V. Ganesan and M.D. Mathew, *Materials Science and Engineering A*, 607(2014)138-144.

2. Assessment of creep strain distribution across base metal of 316LN austenitic stainless steel weld joint by an EBSD based parameter, **V.D. Vijayanand**, V. Ganesan, J. Ganesh Kumar, P. Parameswaran, Naveena and K. Laha, *Metallurgical and Materials Transactions A*, 46(2015)5456-5466.

3. Influence of microstructural inhomogeneity on the creep rupture behaviour of 316LN weld joints, **V.D. Vijayanand**, M. Vasudevan and K. Laha *Transactions of the Indian Institute of Metals*, 69(2016)217-221.

4. Creep Deformation and Rupture Behaviour of Single and Dual-pass 316LN Stainless Steel Activated-TIG Weld Joints, **V.D. Vijayanand**, M. Vasudevan, V. Ganesan, K. Laha, and A. K. Bhaduri, *Metallurgical and Materials Transactions A*, 47(2016)2804-2814.

5. Studies on creep deformation and rupture behaviour of 316LN SS multi-pass weld joints fabricated with two different electrode sizes, **V.D. Vijayanand**, J Ganesh Kumar, P K. Parida, V.Ganesan and K. Laha. *Metallurgical and Materials Transactions A*, 48(2017)706-721.

Conference Proceedings

1. Creep property evaluation of high nitrogen 316LN weld joints**, V.D. Vijayanand**, V. Ganesan, K. Laha and M.D. Mathew, National conference on advances in materials and processing, PSG Tech., Coimbatore, India, May 4, 2013.

2. Strain mapping in creep tested weld joints by EBSD, **V.D. Vijayanand** and K. Laha, NMD-ATM 2015, Coimbatore, India, Nov. 12-16, 2015.

3. Influence of microstructural inhomogeneity on the creep rupture behaviour of 316LN weld joints, **V.D. Vijayanand**, M. Vasudevan and K. Laha, 7th Int. Conf. on Creep, Fatigue and Creep-Fatigue Interaction, IGCAR, Kalpakkam, India, Jan 19-22, 2016.

ACKNOWLEDGEMENTS

I express my deepest gratitude to Dr. K. Laha (Head, Mechanical Metallurgy Division), for mentoring, guiding and motivating me to accomplish this research work. His constant pursual for scientific excellence and perfection has helped me shape this thesis.

I thank Dr. S. Venugopal, (past Chairman, DC committee) for critically reviewing the progress of this study. I thank Dr. K. Velusamy (current Chairman, DC committee) and Dr. B.P.C. Rao (Member, DC committee) for giving their valuable suggestions during the DC committee meetings. This work would not have accomplished without the knowledge shared by Dr. G. Sasikala and Dr. M. D. Mathew through their dissertations. I sincerely acknowledge both of them.

I thank Dr. A. K. Bhaduri, (Director, Indira Gandhi Centre for Atomic Research) and Dr. M. Sai Baba (Director, Resources Management Group) for granting me permission for pursuing Ph.D in Homi Babha National Institute.

I thank Dr. Shaju K Albert (Head, Materials Technology Division), Dr. M. Vasudevan (Head, Advanced Welding Processes, Monitoring and Modeling Section) and Dr. S. Ravi for providing the welding resources. I acknowledge the technical support given by Shri. N. S Thampi and Shri V. Ganesan during the experimental work. I express my gratitude to Dr. Sunil Goyal and Shri J. Ganesh Kumar for their guidance while carrying out finite element analysis. I thank Shri S. Sakthy for helping me with the engineering drawings. The help rendered by Selvi S. Pannerselvi and Shri D. Manokaran are thankfully remembered.

The support given by Dr. P. Parameswaran (Head, XRD and Surface Engineering Section) and Dr. S Amirthapandian while carrying out TEM analysis is highly acknowledged. I thank Dr. Vani Shankar for establishing the EBSD facility in the Mechanical Metallurgy Division, which was widely used during the whole course of this study. I would like to extend my sincere gratitude to my friend and colleague Shri. J. Christopher for giving me mental rejuvenation at times when it was most needed. I would like to thank all my other colleagues in the Mechanical Metallurgy Division for their encouragement and motivation.

It is my great privilege to acknowledge Prof. S. Sundaresan, IIT Madras for introducing me to the fascinating field of welding metallurgy of stainless steels. I am delighted to record my acknowledgements to Prof. G. Phanikumar, IIT Madras for molding me as an experimentalist.

I am highly indebted to my parents and teachers for inculcating the interest in me for pursuing research as a career. Finally, I would like to acknowledge the sacrifices made by my wife Vilasini and daughter Jenita for energizing and sustaining me throughout the progress of this work.

CONTENTS

TITLE	Page No.
SYNOPSIS	i
LIST OF FIGURES	xiii
LIST OF TABLES	xxi
CHAPTER 1 - MOTIVATION AND SCOPE OF THE THESIS	
1.1 Introduction	1
1.2 Objectives of this study	2
1.3 Organisation of the thesis	4
CHAPTER 2 - LITERATURE SURVEY	
2.1 Creep deformation	5
2.2 Deformation mechanisms	7
2.3 Fracture	10
2.4 Creep cavitation	12
2.4.1 Cavity nucleation	14
2.4.2 Cavity growth	16
2.5 Relationship between deformation and fracture	18
2.6 Extrapolation methods for creep deformation and rupture	18
2.7 Austenitic stainless steels	20
2.8 Welding metallurgy of austenitic stainless steels	23

2.8.1 Solidification modes in stainless steel welds 24

2.8.2 Influence of delta ferrite in preventing hot cracking 27

2.9 Precipitation in austenitic stainless steels 28

2.9.1 Precipitation of carbides 29

2.9.2 Precipitation of intermetallics 30

2.9.3 Precipitation in the fusion zone 31

2.9.4 Influence of creep on precipitation kinetics 32

2.10 Evolution of various morphologies of delta ferrite 32

2.11 Creep properties of austenitic stainless steel fusion zone 35

2.11.1 Influence of welding process 37

2.11.2 Influence of electrode composition 37

2.11.3 Influence of specimen size and location 39

2.11.4 Influence of delta ferrite content 41

2.12 Material selection criteria for fast breeder reactors 41

2.13 Design of structural components for FBRs 45

2.14 Intention of the present work 46

CHAPTER 3 - EXPERIMENTAL DETAILS

3.1 Introduction 47

3.2 Material 47

3.3 Weld pad fabrication 48

3.4 Creep specimens 50

3.5 Uniaxial creep machine 50

3.6 Impression creep testing (ICT) machine 51

3.7 Automated ball indentation (ABI) machine 53

3.8 Microhardness tester 53

3.9 Optical metallography 54

3.10 Scanning electron microscope (SEM) 55

3.11 Transmission electron microscope (TEM) 55

3.12 Finite element analysis 56

CHAPTER 4 - MICROSTRUCTURAL INHOMOGENEITY AND ITS INFLUENCE ON CREEP PROPERTIES

4.1 Introduction 57

4.2 Microstructure of the as-deposited weld joint 57

4.2.1 Evolution of various morphologies of delta ferrite 60

4.2.2 Hardness variation across the joint 61

4.2.3 Dislocation substructure in the as-deposited fusion zone 63

4.2.4 Orientation gradients estimated by EBSD 64

4.3 Creep rupture properties 68

4.4 Creep rupture ductility 69

4.5 Microstructural evolution during creep 71

4.5.1 Evolution of creep damage during creep testing 72

4.5.2 Influence of morphological changes of delta ferrite 75

4.5.3 Influence of dislocation substructural variations 76

4.5.4 Dislocation substructural changes on creep exposure 77

4.6 Fractographic analysis 81

4.7 Conclusions and motivation for further work 84

CHAPTER 5 - ASSESSMENT OF THERMO-MECHANICAL EFFECT ON CREEP RUPTURE PROPERTIES

5.1 Introduction 85

5.2 A-TIG welding process 86

5.3 Fabrication of single and dual pass A-TIG joints 86

5.3.1 Initial microstructure 87

5.3.2 Hardness evaluation 91

5.3.3 Substructural characterization by TEM 93

5.4 Creep deformation and rupture properties 95

5.4.1 Analysis of the creep tested weld joints by TEM 97

5.4.2 Influence of fusion zone volume 99

5.5 Evaluation of localized creep properties by Impression Creep Testing 100

5.6 Effect of additional weld pass on creep cavitation 103

5.7 Rupture ductility and fractography 106

5.8 Conclusions 109

CHAPTER 6 - INFLUENCE OF SIMULTANEOUS VARIATION OF THE MICROSTRUCTURAL FEATURES

6.1 Introduction 111

6.2 Microstructure in as-welded condition 111

6.2.1 Hardness and KAM variation across weld pass interface 117

6.3 Rupture life and elongation 121

6.3.1 Variation in creep cavitation behavior with electrode diameter 124

6.4 Factors influencing the failure location 134

6.4.1 Evaluation of tensile properties of various weld joint constituents 135

6.4.2 Creep deformation properties of the weld joint constituents 136

6.4.3 Finite element (FE) simulation of stress state across the weld joints 139

6.5 Fractographic characteristics of failed weld joints 145

6.6 Conclusions 149

CHAPTER 7 - CREEP STRAIN ESTIMATION USING EBSD

7.1 Introduction 151

7.2 Strain measurement by EBSD- an overview 151

7.2.1 Quantification of orientation spread within the grain 153

7.2.2 Calculation of the parameter C_d 154

7.3 Evolution of strain gradients in weld joints 160

7.3.1 Estimation of local mechanical properties 160

7.3.2 FE analysis of stress distribution across the weld joint 164

7.4 Strain mapping using the EBSD parameter C_d 168

7.5 TEM analysis 171

7.6 Conclusion 173

CHAPTER 8 - SUMMARY AND RECOMMENDATIONS FOR FUTURE WORK

8.1 Summary 175

8.2 Suggestions for future work 179

REFERENCES 181

SYNOPSIS

Austenitic stainless steels (SS) are the prime structural materials for sodium cooled Fast Breeder Reactors (FBRs). The underlying reasons for preferring this material are its superior creep strength, better corrosion resistance and compatibility with liquid sodium. However, as large components of the breeder reactors made of this material are fabricated by welding, the assessment of creep strength of the weld joint is also essential in addition to that of the base metal. This is because of significant variation in creep strength across different constituents of weld joint viz., fusion zone, heat affected zone (HAZ) and base metal. Rupture life of the weld joint is usually inferior to that of the base metal and failure occurs in the fusion zone. Considering the reduction in creep strength of the weld joint, a weld strength reduction factor (WSRF) is incorporated to the base material data while designing the components of FBRs. The WSRF are often over-conservative as they take into account the significant scatter in the data obtained from testing weld metal and weld joints. The source of scatter is the variations caused by a number of factors associated with the welding processes. These variations result in formation of a complex microstructure comprising of many types of inhomogeneities. Systematic studies are required to understand the evolution of various inhomogeneities and their influence on the creep rupture behaviour of the joints. This can help interpret the reason behind the scatter in properties of weld joints.

This study presents the various types of inhomogeneities present in 316 LN stainless steel weld joints. The influence of these inhomogeneities on creep behaviour of the joints has been assessed. The study has helped in developing a clear understanding of creep damage evolution during elevated temperature exposure under stress. The understanding could satisfactorily explain the variations in rupture life brought about by changes in welding process and parameters. A number of characterization tools have been used in this study, which could illustrate the various inhomogeneities associated with microstructure and micro-strain.

The microstructure of the fusion zone in shielded metal arc (SMA) welded joints are tailored in such a way that 3-5 vol.% of delta ferrite is retained along with the austenite phase to prevent hot cracking during welding. Hot cracking has been reported to occur in stainless steel fusion zone, due to the presence of some deleterious elements in this region which aid the formation of low-melting eutectics. It was understood that the main source of these deleterious elements is the electrode. The intentionally added delta ferrite in the solidified fusion zone usually exists as continuous stringers comprising a ‘vermicular’ structure. But, upon deposition of subsequent weld beads, the vermicular morphology transforms in to a globular structure. This is because of the shape instability resulting from a higher surface to volume ratio in the vermicular morphology. This transformation to globular morphology pertains to a narrow region in the previously deposited weld bead just adjacent to the weld pass interface, where the influence of the weld thermal cycle is relatively more pronounced.

Apart from the morphological variations in delta ferrite, the same region adjoining the weld pass interface in the previous bead is also subjected to thermo-mechanical processing (TMP) due to the thermal cycling arising due to subsequent weld metal deposition. The TMP results in significant variations in dislocation substructure across the weld pass interface. The region pertaining to the previous weld pass contains denser dislocation tangles even within the delta ferrite, suggesting that this narrow region adjoining the weld pass interface has hardened to a greater extent. The misorientation evaluation along both sides of the weld pass interface by electron back-scatter diffraction (EBSD) and hardness support the presence of the TMP zone conclusively. It can be stated that globular ferrite region not only exhibits a change in delta ferrite morphology but is also hardened due to the TMP by the deposition of successive weld beads. Therefore, two types of inhomogeneities i.e. morphological changes in delta ferrite and sub-structural changes evolve in the fusion zone of weld joints fabricated by multiple passes. It is necessary to understand the deformation and damage behaviour of the fusion region during creep of austenitic weld metal, before assessing the implication of the two inhomogeneities on the rupture life of the joint.

It has been shown by many researchers that elevated temperature exposure results in the precipitation of intermetallic brittle phases like sigma, chi and Laves from the delta ferrite. It has also been reported that during creep, the precipitation of these phases is further accelerated due to generation of dislocations which provide additional diffusion paths for Cr and Mo which aid these transformations. Under the influence of external stress, cavities nucleate along the austenite/intermetallic interface due to the strength mismatch between the transformed phases and austenite matrix. It has been documented that the propagation of the cavities occurs under the influence of the external stress and failure occurs subsequently after significant loss in load bearing cross sectional area. The influence of microstructural inhomogeneities on the nucleation and propagation of cavities has not been addressed adequately so far.

As the vermicular morphology is more continuous, the diffusion of Cr and Mo is more feasible in this morphology when compared to the globular morphology. Hence, the transformation to intermetallic phases is likely to occur earlier in this region. The presence of TMP globular ferrite region on the previous pass generates a stress gradient across the weld pass interface during creep. The preferential plastic deformation of the softer vermicular region results in cavity nucleation caused by stress concentration at the matrix/intermetallics interface. The propagation of cavities is enhanced in the vermicular delta ferrite region due to its continuous morphology. On the other hand, creep cavities could not propagate easily into the globular ferrite region as it was strengthened to comparatively higher extent due to the TMP effect. Thus it can be stated that in the fusion zone of 316 LN SS, both the inhomogeneities have a synergistic role in influencing both cavity nucleation and propagation which ultimately dictates the rupture life of the joints.

In order to clearly understand the influence of TMP developed due to the deposition of the subsequent weld passes, the influence of delta ferrite is needed to be minimised. 316 LN SS joints fabricated by Activated-Tungsten Inert Gas (A-TIG) welding offer the precise perspective in this regard. Since A-TIG is an autogenous welding process, where external filler wires are not used, which prevents deleterious elements present in the electrode from entering into the weld pool. Therefore, the A-TIG weld joints are completely resistant to hot cracking and there is no requirement of delta ferrite in the microstructure. Comparison between single and dual pass A-TIG weld joint of the same section thickness would clearly demonstrate the influence of TMP. The dual-pass weld joint was fabricated by incorporating two passes of comparatively lower heat input than what was used for fabricating the single pass weld joints. It was ensured that in the dual pass weld joint, there was a small overlap between the two passes.

Since the width of various regions in the A-TIG weld joints was higher than that of the SMA weld joints, impression creep technique could be used to evaluate the localised creep properties. Impression creep is a miniature specimen technique which can be used to assess localised creep properties. In this technique, a compressive load is applied to specimen of comparatively smaller size by using an indenter of 1 mm diameter. The penetration of the indenter against the elapsed time is monitored; this helps in generating the impression creep curve. The steady state penetration rate of the indenter obtained from the impression creep curve of the unaffected base metal was comparable to the steady state creep rate obtained from the uniaxial creep testing. For, the dual pass weld joints, the penetration rate in the fusion zone of the first pass especially around the overlap region was significantly lower than the penetration rate obtained in the second pass. This clearly demonstrated that the deposition of the subsequent pass strengthened the previous pass significantly. The complex deformation characteristics in the dual pass weld joints would drastically influence its rupture life under uniaxial testing conditions.

It was found that the rupture life of the dual pass A-TIG weld joint was significantly higher than that of the single pass weld joint. Though there were evidences of creep cavitation in both the joints, the creep damage mechanism was quite different. In case of the single pass weld joints, the propagation of creep cavities in the fusion zone proceeded without any hindrance. This is contrast to the dual pass weld joints, where cavitation was more prevalent in the second pass when compared to the first pass. The strength mismatch across the weld pass interface resulted in initiation of cavities in the second pass region which was less resistant to creep deformation. These cavities did not propagate in the first pass and were arrested at the weld pass interface. Thus the presence of an additional interface and strengthened first pass improved the rupture life of the dual pass weld joints. The fractographic examination of the dual pass weld joints showed inter-dendritic facets in the second pass region and dimples relating to ductile failure in the first pass region. This suggests that the propagation of creep cavities occurred along the inter-dendritic facets of the second pass and ultimate failure in these joints occurred in a ductile manner in the first pass after significant loss in cross sectional area with relatively high ductility.

It was clearly demonstrated that the formation of a ‘thermo-mechanically processed’ first pass generated a microstructural inhomogeneity in the fusion zone of the dual-pass weld joint, which delayed the propagation of cavities and improved the rupture life. It would be rational to study how much more the strength of the weld joint can be enhanced by increasing the number of weld passes by generating more such ‘beneficial’ microstructural inhomogeneities. Towards this perspective, SMA weld joints were fabricated with two electrodes of varying diameters viz. 2.5 and 4 mm. For the same section thickness, the number of weld passes required to complete the weld joints was considerably higher when using the 2.5 mm electrode when compared to the weld joint which was fabricated using 4 mm electrode diameter.

As the fusion zone contained 3.5- 5 vol.% of delta ferrite, the morphological changes of this phase were evident in both the SMA weld joints. Since the volume of weld metal deposited in subsequent passes was higher in case of the joint made with 4 mm electrode, the extent of the globular delta ferrite and the extent of TMP region in the previous passes were higher in this joint. The formation of the TMP region in the previous pass adjoining the weld pass interface could be successfully mapped by EBSD technique by estimating the localised variation in orientation. The calculated variations in local misorientation and hardness obtained across the weld pass interface confirmed that for the weld joint made with larger electrode the formation of TMP region was more pronounced when compared to the joint made with smaller electrode.

It was found that the rupture life of the weld joints fabricated with larger electrode diameter was considerably higher than the weld joint made with smaller electrode size. The variations in microstructural inhomogeneity in the two weld joints influenced the rupture life significantly. The cavities nucleated in the vermicular region adjacent to the weld pass interface in both the weld joints. However, the propagation of creep cavities across the weld pass interface was restricted to a greater extent in case of the weld joint made with the larger electrode diameter, due to the presence of a comparatively stronger TMP globular delta ferrite region. Another attribute which influenced the propagation of creep cavities is the spatial distance between the cavity nucleating regions. In case of the weld joint made with smaller electrode diameter, the cavity nucleating vermicular regions adjoining the weld pass interface were present in closer proximity. This was favourable for interlinking the cavitated regions, thereby resulting in shorter rupture lives when compared to the joints made with larger electrode diameter.

There was one noticeable observation pertaining to the failure location of the weld joint made with larger electrode size at certain stress levels. In case of austenitic SS weld joints, the fusion zone is the weakest region where creep cavitation is more pronounced; therefore failure usually occurs in the fusion zone. But for the weld joints made with 4 mm electrode diameter, the failure occurred at the fusion zone/HAZ interface at certain stress levels. Whereas, for the weld joint made with 2.5 mm electrode diameter, the failure occurred within the fusion zone at similar stress levels. The deformation properties of the individual regions of the weld joints are needed to be evaluated to understand the variations in failure locations in both the joints. In addition to the localised creep properties which had been obtained from impression creep testing (ICT), the tensile properties of the individual regions of the weld joint were also obtained using automated ball indentation testing (ABI) system which is yet another miniature specimen technique. Using ABI testing technique, tensile properties were obtained on various regions of the weld joint using 0.76 mm spherical silicon carbide indenter. The obtained load-displacement plot was converted into true plastic stress and true plastic strain plots by established conversion factors.

The tensile results obtained from ABI tests showed that the yield stress (YS) of the fusion zone was highest followed by the HAZ and base metal. The YS was highest in case of the fusion zone due to the presence of the hard as-cast structure, which contains higher dislocation tangles produced by the stress generated during contraction of the weld pool. The HAZ has higher YS when compared to the base metal as it is subjected to multiple thermal cycles which results in work hardening of this region. The trend in variation of YS among the three regions was similar in both the weld joints. However, the values of YS in all the three regions were higher in case of the weld joint fabricated with smaller electrode diameter when compared to the similar corresponding regions in the weld joint which was fabricated by larger electrode diameter. This is because this joint fabricated with smaller diameter is subjected to comparatively higher degrees of work hardening due to deposition of more number of weld beads.

The steady state creep rates obtained from the ICT showed that the fusion zone had the lowest penetration rate, followed by HAZ and the base metal. This trend was evident in both the weld joints. However, for the weld joint made with smaller electrode diameter, the HAZ and the fusion zone exhibited almost equal rates of penetration. The base metal of this weld joint had significantly higher penetration rate when compared to both the fusion zone and HAZ. In case of the weld joint fabricated with larger electrode diameter, the penetration rates of the base metal and HAZ were almost equal. But, penetration rate of the fusion zone was considerably lower than that of the base metal and HAZ for this weld joint. The impression creep tests were carried out at varying stress levels at 923 K to obtain the values of coefficient A and exponent, n in the Norton equation ($\dot{\varepsilon}_s = A \sigma^n$) which relates the steady state creep rate $\dot{\varepsilon}_s$ and stress σ. Geometries corresponding to the two weld joints were generated using ABAQUS Finite element analysis (FEA) simulation software and the localized creep and tensile properties obtained from miniature specimen testing were incorporated in the respective regions. FEA simulation was carried out on both the geometries under the external stress of 175 MPa and duration of 750 hours. The steady state von-Mises stress and the principal stress contours showed that the stress gradients across the HAZ/ fusion zone interface was steeper than the stress gradients in the HAZ/ base metal interface for the weld joint fabricated with larger electrode diameter. This could be the possible reason for failure to occur at this interface. In case of the weld joint fabricated with smaller electrode diameter, the gradients were steeper in the HAZ/base metal interface. However, the damage caused by cavitation in the fusion zone was more dominant which prevented the failure from occurring in the HAZ/ base metal interface for the weld joint fabricated with smaller electrode. For the weld joint made with smaller electrode diameter, the damage caused by creep cavitation was more prominent and therefore failure of this joint occurred in the fusion zone. The tri-axiality factor derived from FEA simulation, which denotes the propensity for creep cavitation, was significantly higher for the joint made with larger electrode diameter.

Though formation of cavities was more prevalent in case of the weld joint made with larger electrode, the cavity nucleating sites were not as interlinked as in case of the joint made with smaller electrode diameter as mentioned earlier.

Since the mechanical properties of the fusion zone, HAZ and base metal vary substantially, it generates a complex stress distribution across these three regions on creep exposure, which result in gradients in strain. It is difficult to use conventional methods for estimating the localized strain gradients across the sample gauge. In this work an effort has been made to estimate the variation of strain across different regions in the weld joint by an EBSD based technique. This method has a potential to be used for remnant life assessment for service exposed components.

EBSD can estimate the orientation of the individually scanned points on the sample with respect to the sample orientation. In the solution annealed condition, the orientations within a grain does not vary significantly. However, with the application of plastic strain the orientation of each of the scan points within a grain begins to vary. In other words an 'orientation gradient' starts to evolve within a grain. This orientation gradient increases with increase in plastic strain. Therefore, quantifying the orientation spread can give a measure of the plastic strain induced in the material. In this work the orientation gradient was quantified using a crystal deformation parameter C_d. A linear relationship could be derived relating the parameter C_d and known amount of plastic strain. This relationship could be used as master curve for estimating the strain in situations where conventional measurements are not possible.

This method was used for estimating the strain gradients at three locations in the base metal region of the weld joint. FEA simulations were first carried out on representative weld joint geometry incorporating mechanical properties obtained from

ABI and ICT tests to validate the results obtained from C_d parameter. It was found that the variation of von-Mises stress and the equivalent strain obtained from FEA under the influence of external stress could be successfully correlated with the variation in the strain values obtained from the C_d parameter.

In this thesis work, the different types of inhomogeneous present in 316 LN SS weld joint have been studied. Within the fusion zone, the inhomogeneities resulted due to morphological changes and formation of the TMP region near the weld pass interface which influenced the nucleation and propagation of the creep cavities and hence the creep rupture life. Depending on the welding process, the spread of these inhomogeneities could be altered by adjustments in welding parameters. This has enhanced the rupture life of the weld joints. This study also demonstrated the use of a new EBSD based parameter for estimating the strain distribution across the base metal region of the weld joint

LIST OF FIGURES

Figure No.	Title	Page No.
	CHAPTER 2	
Figure 2.1	Typical creep curve.	6
Figure 2.2	A schematic deformation mechanism map.	7
Figure 2.3	Grain boundary sliding in Al-1.92 Mg alloy.	10
Figure 2.4	A schematic fracture mechanism map applicable for fcc materials.	10
Figure 2.5	Broad classes of failure.	11
Figure 2.6	Influence of nitrogen on fracture mode of 316 LN SS at 923 K/140 MPa (a) ductile failure characterized by dimples for the steel containing 0.07 wt. % nitrogen (rupture life 3177 hours) and (b) brittle transgranular failure for the steel containing 0.22 wt. % nitrogen (rupture life 15974 hours) showing grain facets.	13
Figure 2.7	(a) Wedge crack in Al-20Zn alloy and (b) round cavities in Ag.	14
Figure 2.8	Larson-Miller plot of 316 SS.	19
Figure 2.9	Erection of the main vessel of PFBR constructed by 316 L(N) stainless steel. The whole structure was fabricated by fusion welding process.	24
Figure 2.10	Various solidification modes of austenitic steel fusion zone.	24
Figure 2.11	Pseudo-binary diagram of Fe-Cr-Ni system sectioned at 70 wt.% Fe.	25
Figure 2.12	WRC-92 diagram. The delta ferrite content in the fusion zone can be obtained from this diagram. The possible solidification modes can also be predicted from this diagram. The delta ferrite content is given in terms of the ferrite number (FN). The FN and volume % ferrite are equivalent for values upto 28.	27
Figure 2.13	TTP diagram of 316 SS base metal and 19-12-3 SS weld metal (fusion zone).	32

Figure 2.14	Various morphologies of delta ferrite (a) vermicular, (b) lacy, (c) acicular and (d) Globular.	34
Figure 2.15	Creep cavitation along the sigma/austenite interface.	36
Figure 2.16	Scatter in 0.2% proof stress for 316 SS weld metal (fusion zone).	36
Figure 2.17	Comparison of 10000 hour rupture strength of 316 SS weld metal (fusion zone) and wrought metal.	36
Figure 2.18	(a) Schematic showing the locations from where the specimens were extracted (b) Plot of creep rupture strength of the corresponding specimens.	40
Figure 2.19	Schematic of the PFBR assembly components. (PS-primary sodium, ARDM- absorber rod drive mechanism, CS A48P2- carbon steel with composition Fe-0.22C-0.8Mn-0.4Si-0.035P-0.012S-0.2Cr-0.3Ni-0.1Mo wt.%).	43

CHAPTER 3

Figure 3.1	Schematic of weld pad showing the locations from where the specimens were extracted.	49
Figure 3.2	Schematic of (a) SMAW and (b) A-TIG weld joint specimen.	50
Figure 3.3	An ATS® creep machine used in the study.	51
Figure 3.4	Impression creep machine integrated to the vacuum system.	52
Figure 3.5	Automated Ball Indentation testing machine.	53
Figure 3.6	Austenitic stainless steel fusion zone etched using 60% HNO_3 and 40% H_2O solution for (a) 10 s and (b) 30 s at a current density of 0.75 mA/mm^2.	54

CHAPTER 4

Figure 4.1	Macrostructure of the as-weld joint showing X-X′ and Y-Y′ sections where hardness values were taken, the dashed line shows the region from which the creep specimen was extracted.	58
Figure 4.2	Schematic showing the location of the two morphologies of delta ferrite and the representative regions where EDS analysis and TEM specimens were extracted.	59

Figure 4.3	Microstructure of as-welded fusion zone showing delta-ferrite with (a) vermicular and (b) globular morphologies.	60
Figure 4.4	Variation of hardness along X-X′ and Y-Y′ sections.	62
Figure 4.5	Variation of hardness along a weld pass interface.	62
Figure 4.6	TEM micrograph of the as-weld material showing (a) vermicular interconnected delta-ferrite (δ) and (b) globular delta-ferrite with higher density of dislocations.	64
Figure 4.7	(a) EBSD map showing the regions where the orientation line scans were obtained and (b) orientation profiles taken on either side of the weld pass interface along these lines.	65
Figure 4.8	Variation of rupture life with applied stress.	68
Figure 4.9	Variation of rupture elongation with rupture life.	69
Figure 4.10	Variation of residual delta-ferrite with rupture life.	70
Figure 4.11	Variation of percentage area reduction with rupture life.	71
Figure 4.12	Intergranular cracking occurring preferentially in the vermicular region for the weld joint tested at 175 MPa.	72
Figure 4.13	Variation of Cr and Mo content in transformed regions with rupture life.	74
Figure 4.14	(a) Dislocation pile up, (b) slip bands in vermicular region and (c) subgrain formation in globular region after creep testing at 175 MPa.	77
Figure 4.15	TEM micrographs of weld joint tested at 120 MPa (rupture life 7820 hours) (a) vermicular region consisting subgrains and precipitate A with Fe-Cr-Mo and B with Fe-Mo enrichment (b) globular region showing the possible onset of formation of subgrains.	78
Figure 4.16	EDS spectra of (a) precipitate A and (b) precipitate B.	79
Figure 4.17	(a) Fractograph of weld joint tested at 175 MPa, (b) region *I* showing interdendritic failure and (c) region *D* showing ductile failure.	82
Figure 4.18	(a) Fractograph of weld joint tested at 120 MPa, (b) region *B* showing cracks in brittle transformed intermetallics and (c) region *D* showing ductile failure.	83

CHAPTER 5

Figure 5.1	Macrostructure of (a) single-pass weld joint (b) dual-pass weld joint. The region from where the creep specimens were extracted are shown. The region of the dual-pass weld joint showing the overlap between the passes (c).	88
Figure 5.2	Optical micrographs showing delta ferrite distribution in (a) columnar region and (b) equiaxed region of single-pass weld joint (c) columnar region and (d) equiaxed region of dual-pass weld joint. The arrows indicate delta ferrite phase.	90
Figure 5.3	Microstructure in HAZ region of the single-pass weld joint showing significant grain coarsening.	91
Figure 5.4	Hardness profile of (a) single-pass (b) dual-pass and (c) along weld centre line of both the joints.	92
Figure 5.5	TEM micrographs taken from various regions of fusion zone in as welded condition (a) columnar region of single-pass (b) equiaxed region of single-pass weld joint (c) columnar region of second pass and (d) columnar region of first pass of the dual-pass weld joint.	94
Figure 5.6	Comparison of rupture life variation with applied stress for the single and dual-pass weld joint along with the base metal.	95
Figure 5.7	Micrographs showing the failure location in (a) single-pass and (b) dual-pass weld joints tested at 923 K at a stress level of 175 MPa.	96
Figure 5.8	Creep curves of the base metal, single-pass and dual-pass weld joints tested at 923 K and applied stress of 140 MPa. The interrupted tests on which TEM examinations were performed are indicated.	97
Figure 5.9	TEM micrographs of (a) base material tested up to failure (rupture life 9279 hours) (b) columnar region of single-pass weld joint interrupted at 2500 hours and (c) in the columnar region of dual-pass weld joint interrupted at 5500 hours. All these specimens were creep tested at 923 K and 140 MPa.	98
Figure 5.10	Impression creep curves of (a) single-pass weld joint and (b) dual-pass weld joint, the steady state creep rates are mentioned within brackets.	101

Figure 5.11 (a) SEM image showing nucleation of cavities (indicated by arrows) along second phase particles (b) energy-dispersive X-ray spectroscopic (EDS) analysis on the second phase particle revealed that these were rich in Cr, Fe and Mo. 103

Figure 5.12 The arrest of creep cracks at the weld pass interface in the fusion zone of the dual-pass weld joint tested at 923 K and applied stress of 175 MPa. 104

Figure 5.13 Macrostructure of dual-pass weld joint tested at 923 K and applied stress of 140 MPa. The possible location where the cavitation could have initiated is indicated. 105

Figure 5.14 Plot of (a) percentage elongation and (b) percentage area reduction with rupture life. 107

Figure 5.15 Fractographs of (a) single-pass weld joint (c) dual-pass weld joint tested at 140 MPa; figures (b) and (d) show the respective magnified images. 108

CHAPTER 6

Figure 6.1 Macrostructure of the weld joints fabricated with (a) 2.5 mm and (b) 4 mm electrode diameter showing the weld passes. Lines are inscribed to demarcate weld pass interface. The dashed line shows the region from where the creep specimens were extracted. 113

Figure 6.2 Microstructure near the weld pass interface of weld joints fabricated with (a) 2.5 mm and (b) 4 mm electrode diameter, and delta ferrite having (c) globular morphology and (d) vermicular morphology (micrographs from weld joint made with 2.5 mm electrode size). 114

Figure 6.3 Hardness variations across the transverse direction of the weld joints. 115

Figure 6.4 TEM microstructure taken from vermicular delta ferrite region of fusion zone for weld joints fabricated with (a) 2.5 mm and (b) 4 mm diameter in as-welded condition. 116

Figure 6.5 Hardness variations across the weld pass interface in weld joint fabricated with (a) 2.5 mm and (b) 4 mm electrode diameter. 118

Figure 6.6 IQ maps of weld joints fabricated with (a) 2.5 mm, (c) 4 mm electrode diameter and the corresponding KAM maps (b) and (d). 120

Figure 6.7	Rupture life variations of the weld joints as compared to the base material.	122
Figure 6.8	Comparison of (a) rupture ductility and (b) reduction in area with life for the weld joints and the base metal.	123
Figure 6.9	Macrostructure of weld joints tested at (a) 200 MPa (2.5 mm electrode diameter, (b) 200 MPa (4 mm electrode diameter), (c) 175 MPa (2.5 mm), (d) 175 MPa (4 mm), (e) 140 MPa (2.5 mm) and (f) 140 MPa (4 mm).	127
Figure 6.10	Micrograph showing the cavity nucleation sites in weld joints fabricated with (a) 2.5 mm and (b) 4 mm electrode diameter creep tested at 175 MPa.	128
Figure 6.11	Phase map and the corresponding band contrast map showing creep cavitation across the intermetallic/matrix interface in fusion zone of weld joint tested at 140 MPa.	130
Figure 6.12	Schematic depicting the nucleation and propagation of creep cavities in both the weld joints.	133
Figure 6.13	Tensile properties estimated by ABI technique across various zones of the weld joints.	135
Figure 6.14	Impression creep curves showing the penetration with time for various regions in the weld joints made with (a) 2.5 mm and (b) 4 mm electrode diameter.	137
Figure 6.15	Stress dependence of steady state strain rate of the base metal, heat affected zone and fusion zone of both the weld joints.	138
Figure 6.16	One fourth of the weld joint geometry meshed using quadrilateral elements showing the boundary conditions and the surface where load was applied.	141
Figure 6.17	Stress contours on the deformed geometries modelled with an applied stress of 175 MPa for 750 hours. The region where significant deformation occurred in 4 mm electrode diameter weld joint is indicated.	141
Figure 6.18	Variation of von-Mises stress for weld joint made with (a) 2.5 mm electrode diameter and (b) 4 mm electrode diameter along the set of nodes indicated in Figure 6.16 with different durations of creep exposure.	142
Figure 6.19	Variation of (a) tri-axiality factor (b) normalised von-Mises stress and (c) normalised principal stress across the set of nodes indicated in Figure 6.16.	143

Figure 6.20	Fractograph of the weld joint specimen fabricated with 2.5 mm electrode diameter creep tested at (a) 175 MPa and (b) 140 MPa. A and B refers to the leading and trailing ends respectively.	147
Figure 6.21	Fractograph of the weld joint specimen fabricated with 4 mm electrode diameter creep tested at (a) 175 MPa and (b) 140 MPa. A and B refers to the leading and trailing ends respectively.	148

CHAPTER 7

Figure 7.1	IPF map of (a) solution annealed and (c) with a cold work of 0.15 and their corresponding misorientation profiles (b) and (d).	157
Figure 7.2	Calibration graph relating crystal deformation parameter C_d and plastic strain ε_p at 300 and 923 K.	158
Figure 7.3	Schematic showing the locations from where the EBSD analysis was performed in the weld joint specimen.	159
Figure 7.4	(a) One-half of the meshed weld joint specimen partitioned into different regions based on the variation of microstructure and geometry (b) Schematic of the 4-node linear tetrahedron element (C3D4) used for meshing the specimen geometry.	161
Figure 7.5	Plot of time to onset of tertiary in base metal, the rupture life of weld joint and the duration of simulation. The duration of simulation for both the stress levels was shorter than the time to onset of tertiary in the base metal and was equivalent to the duration of the secondary state regime of the weld joint specimen.	162
Figure 7.6	Variation of yield stress and ultimate tensile strength of the fusion zone, HAZ and base metal at 923 K.	163
Figure 7.7	Contours of von-Mises stress for weld joints creep tested at (a) 175 MPa and (b) 225 MPa after running the simulation up to the duration of the secondary creep regime in the weld joint specimen.	165
Figure 7.8	von-Mises stress distribution along the axis of the creep specimen tested at (a) 175 MPa and (b) 225 MPa.	166
Figure 7.9	Equivalent strain distribution along the axis of the creep specimen tested (a) 175 MPa and (b) 200 MPa.	167

Figure 7.10 Variation of orientation spread within typical grains located in each of the three regions indicated in Figure 7.3. Variation of strain values at various regions in the base metal of the weld joint calculated using the EBSD parameter C_d is also given in the figure. 169

Figure 7.11 Phase map showing $Cr_{23}C_6$ carbides precipitated along austenitic grain boundaries in the near HAZ region of the specimen tested at 225 MPa. 170

Figure 7.12 TEM micrographs of the near HAZ region (region 1) (a) in as-welded condition, (b) creep tested at 175 MPa and (c) 225 MPa. 172

LIST OF TABLES

Table No.	Title	Page No.
	CHAPTER 2	
Table 2.1	Variation in lattice distortion and strengthening due to addition of C and N.	22
Table 2.2	The four possible solidification types in austenitic stainless steel fusion zone and the associated microstructures.	26
Table 2.3	Some properties of the prominent precipitates which can form in austenitic stainless steels during elevated temperature aging.	29
Table 2.4	Comparison between the alloy composition of ASTM, RCC-MR codes with the FBR specification for 304L(N) and 316L(N) SS (in wt.%).	44
Table 2.5	Weld Strength reduction factor for 316L(N) SS recommended by RCC-MR.	46
	CHAPTER 3	
Table 3.1	Chemical composition range of 316LN SS base metal and 316(N) electrodes in wt.%.	48
	CHAPTER 4	
Table 4.1	Welding Parameters.	58
Table 4.2	Contribution of the two types of microstructural inhomogenities on the cavitation behaviour of weld joints.	76
	CHAPTER 5	
Table 5.1	Welding Parameters.	87
	CHAPTER 6	
Table 6.1	Welding Parameters.	113
Table 6.2	Values of the Norton’s power law constants A and n used in the ABAQUS simulation.	139

CHAPTER 7

Table 7.1	Values of the Norton's power law constants A and n used in the ABAQUS simulation.	164

CHAPTER 1

MOTIVATION AND SCOPE OF THE THESIS

Chapter 1

Motivation and Scope of the Thesis

1.1 Introduction

Fast breeder reactors (FBRs) hold an indispensable role in fulfilling the energy requirement of India. It aims in effectively utilizing the vast fertile thorium reserves available in the country by converting into fissile material on adopting the three-stage Nuclear Energy Program. The prototype fast breeder reactor (PFBR), which is being constructed to demonstrate the use of this technology on a commercial scale, is designed for 40 years. In order to improve the economic competitiveness, the commercial fast breeder reactors (CFBRs) are being designed for a life of 60 years by incorporating several changes in design of certain components. Improving the mechanical properties of the structural materials is also pivotal for enhancing the design life of the components.

Towards this end, research is being continuously nurtured at Indira Gandhi Centre for Atomic Research (IGCAR), Kalpakkam, India to evolve new materials and improve the existing materials which would enhance the design life of FBRs. Around the world, austenitic stainless steels (SS) and Grade 91 ferritic steel have been used in fabrication of the main structural components and the steam circuit components for FBRs, respectively. The unanimous choice of austenitic stainless steels for the main structural materials in FBRs is due to their superior mechanical properties, corrosion resistance, ease of fabrication and availability. The operating temperature scrutinises the use of either 316LN or 304LN SS for various structural components of PFBR paying due consideration to weldability. Impetus is now being given to improve the properties of candidate materials for CFBRs by suitable adjustments in chemical composition as well as processing techniques. This would enhance the performance and life of the components which will be more economically viable.

In the last couple of decades, significant progress has been made towards the development of high nitrogen stainless steel. It has been proven that increasing the nitrogen content in these steels can result in better mechanical properties especially at high temperatures. The innovations in modern steel making technology have pushed the upper limits of nitrogen content which can be added in austenitic stainless steel. In IGCAR, a study was initiated to evaluate the mechanical properties of stainless steel containing four different nitrogen contents, viz., 0.07, 0.11, 0.14 and 0.22 wt.%. Through meticulous investigations it was concluded that 0.14 wt. % nitrogen possessed the best combination of creep and fatigue properties. Worldwide experience has also shown that nitrogen content in the range of 0.12-0.14 wt.% resulted in optimum mechanical properties. Hence, it was established that 316LN SS with enhanced nitrogen content could be considered as a candidate material for CFBRs. This work pertains to investigations carried on 316LN SS having 0.14 wt.% nitrogen.

1.2 Objectives of this study

The design of components of FBRs is based on the ASME and the RCCMR design codes. Both these codes consider the time dependent deformation for components operating at higher temperatures. Thus the generation of abundant creep data of the materials used in the fabrication of these components is vital for establishing these design codes. Fusion welding is an indispensable joining process which is used in the fabrication of especially large components of the FBRs. The design of welded components is generally carried out on incorporating Weld Strength Reduction Factors (WSRF) on the base metal data available in the design codes. The ASME

Boiler and Pressure Vessel code defines the WSRF as ratio of the uniaxial weld metal (fusion zone) creep rupture strength to the uniaxial base metal creep rupture strength. But in most of the engineering materials the creep rupture strength of the weld joint consisting of fusion zone, heat affected zone (HAZ) and the base metal is quite different from that of the base metal and the fusion zone. In RCC-MR, the French code for design of the nuclear components, this problem has been circumvented by refining its definition of WSRF as the ratio of the strength of the weld joint to the strength of the base metal. The creep rupture strength of the weld joint up to the envisaged design lives is extrapolated by standard parametric methods based on laboratory experimental data which are carried out for relatively shorter durations. The existing WSRF do not consider several aspects of weld joints such as variations in welding processes, volume fraction of fusion zone, weld joint geometry etc. These variations are very likely to influence the creep properties of weld joints. Variations in microstructural features brought about by the change in parameters of the same welding technique can also adversely influence the rupture life of the joint which in turn can alter the calculated WSRFs.

The reduction in the creep rupture strength of austenitic stainless steel weld joint at elevated temperatures is due to instability caused by creep cavitation in the fusion zone. The associated damage caused by cavitation reduces the ductility of the fusion zone resulting in lower rupture lives when compared to the base metal. The microstructural modifications which occur in the weld region due to deposition of the subsequent weld pass can adversely influence the creep cavitation behaviour. The evolution of such microstructural inhomogeneities is dependent on the associated welding processes and its parameters. Consecutively the microstructure of the fusion zone can be tailored in such a way to harness the beneficial influences of the modifications associated with subsequent weld bead deposition. These modifications can in turn enhance the rupture life of 316LN SS weld joints.

This thesis examines more precisely the influence of two microstructural modifications in the fusion zone on the creep rupture properties of 316 LN SS weld joints.

1.3 Organization of the thesis

The organization of the chapters in this thesis is as follows. Chapter I is the present one describing the motivation and scope of the thesis. Chapter II presents the available literature on microstructure of the stainless steel and the weld joint. The creep properties and the associated cavitation phenomenon in the fusion zone of austenitic stainless steel are also discussed in this chapter. Chapter III gives the complete description of the experimental facility and the characterization tools used in this study. Chapter IV examines the creep properties of multi-pass shielded metal arc (SMA) welded 316LN SS joint and highlights the microstructural features that can affect the creep strength of the joint. Chapter V clearly reports the influence of the thermo-mechanical effect caused by subsequent deposition of the weld beads by analyzing the variation in rupture properties of single and dual pass activated tungsten inert gas (A-TIG) weld joints. Chapter VI describes how the thermo-mechanical effect and the morphological changes in delta ferrite can be utilized beneficially by varying the number weld passes vis-à-vis changing diameter of electrodes in SMA weld joints. An attempt made to measure the gradient in strain which evolves during creep testing of 316LN SS weld joints using an Electron Backscatter Diffraction Parameter is reported in Chapter VII. Concluding remarks and the scope for future work has been presented in Chapter VIII.

CHAPTER 2

LITERATURE SURVEY

Chapter 2

Literature Survey

Literature detailing the aspects of creep deformation, rupture, austenitic stainless steel and the performance of its weld joints under creep condition are vast. However, in this section the salient features which are more relevant to the current work are revisited. Aspects regarding creep deformation, evolution of cavitation and their relevance to austenitic stainless steel weld joint performance under creep are discussed in detail. The knowledge about mechanical behavior of stainless steel weld joint from the literature lays a strong foundation and offers new possibilities for weld joint strength improvement through microstructural modification.

2.1 Creep deformation

Components for load bearing applications at high temperatures are designed to withstand deformation and damage during service. Creep is a type of deformation process which is time dependent and occurs when the material is subjected to elevated temperatures under load [1]. Therefore, for materials which will be used for fabricating components exposed to elevated temperatures under load, evaluation of its creep properties is essential. In order to systematically study the creep deformation of materials, tests are conducted based on certain standards at constant temperatures and stress on representative specimens. The elongation so obtained due to the applied load is plotted with elapsed time to construct what is called a creep curve. Figure 2.1 depicts a typical creep curve showing its three distinct stages after an instantaneous deformation. The first stage is the primary creep regime where the work hardening dominates over the recovery process [2]. As a consequence, the creep rate (the rate of elongation) in this region decreases with increase in time. In the second stage of creep deformation the recovery and the work hardening balance each other, which results in a steady state creep deformation. During the final third stage, the creep rate increases rapidly denoting a clear domination of recovery.

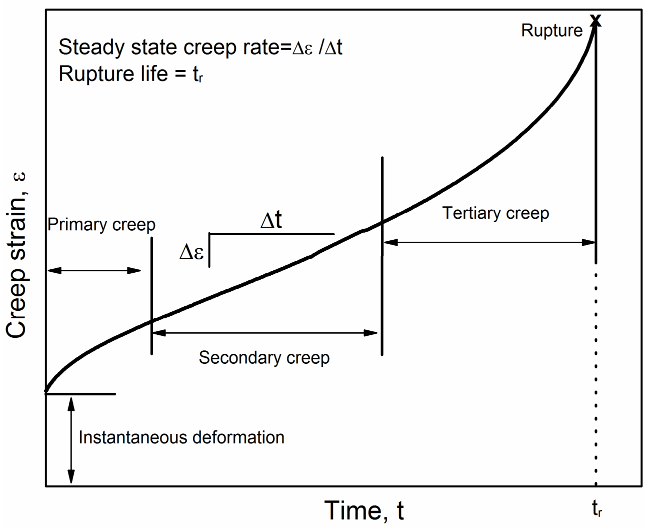

Figure 2.1 Typical creep curve.

The onset of the third stage is due to either a) mechanical instability b) microstructural instability possibly caused by coarsening of precipitates and subgrain structure or c) formation of cavities [3]. The fundamental engineering properties which can be obtained from a creep test are the rupture life and the steady state creep rate. Tests over wide ranges of stress and temperature help to construct the deformation mechanism maps [4]. These maps give an insight to the operating deformation mechanism at the given stress and temperature. Knowledge about the operating mechanism can help to improve the deformation resistance by engineering a suitable microstructure of the material.

2.2 Deformation mechanisms

A schematic of a deformation mechanism map is shown in Figure 2.2. The abscissa and ordinate of the graph are normalised with the absolute melting point and the shear modulus respectively to enable comparison with the deformation mechanisms of different materials/alloy systems. A contour of a typical constant strain rate is superimposed on this map. At very high stress levels, the deformation is by dislocation glide (shown as plasticity regime in the figure) and the role of thermally activated deformation processes is insignificant. Since the stress levels considered in this regime are considerably higher than the yield stress, this deformation is not categorized as creep.

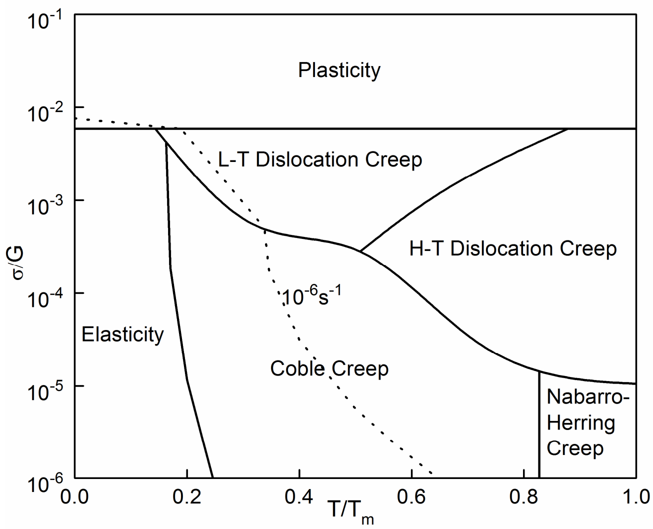

Figure 2.2 A schematic deformation mechanism map.

Two types of mechanisms are responsible for deformation in the creep regime viz., dislocation creep and diffusion creep. In the dislocation creep regime, the movement of dislocations is aided by vacancy diffusion. When dislocations get arrested at obstacles, the vacancy diffusion can aid the glide of dislocations by surmounting the obstacles by climb process. Therefore, in addition to the applied stress, diffusion also influences the deformation process. Mukherjee et al. [5] proposed an equation which shows the combined effect of stress (σ) and diffusion on the steady state creep rate $\dot{\varepsilon}_s$ as

$$\dot{\varepsilon}_s = \frac{AD_v\mu b}{kT}\left(\frac{\sigma}{\mu}\right)^n \tag{2.1}$$

where A and n are material constants, D_v is the diffusion coefficient, μ is the shear modulus, b is the Burgers vector of dislocation, k is the Boltzmann's constant and T is the absolute temperature. Depending on the type of diffusion, the dislocation creep can be further classified as low temperature (L-T) dislocation creep and (H-T) dislocation creep. L-T dislocation creep occurs at comparatively lower temperatures when diffusion through dislocation cores dominates. Whereas, H-T dislocation creep occurs due to lattice diffusion which is more pronounced at high temperatures.

The equation [1] can be further simplified by ignoring the influence of temperature as

$$\dot{\varepsilon}_s = B\,\sigma^n \tag{2.2}$$

Since the stress and steady state creep rate can be related by a power law equation, this regime is also termed as 'power law creep'. At very high stress levels, the strain rate depends exponentially on the applied stress and this is called the 'power law breakdown' regime [3]. Most of the laboratory tests are usually conducted in the dislocation creep regime.

Diffusion creep occurs at relatively lower applied stresses and relatively higher temperatures. The deformation here is primarily caused by diffusion aided movement of atoms under the influence of external stress. Strain is produced as a result of stress directed diffusion of atoms and vacancies. Depending on the path of diffusion, the mechanisms are classified as Nabarro-Herring [6, 7] or Coble creep [8]. At lower temperature regime, diffusion is more favourable along grain boundaries and dislocation core. As a consequence, the steady state creep rate $\dot{\varepsilon}_s$ in this regime is dependent on the grain boundary diffusion coefficient, D_{gb} and third power of grain size (d), this regime is called Coble creep $(\dot{\varepsilon}_s \propto \sigma D_{gb} d^3)$. Nabarro-Herring creep occurs at higher temperature regimes when lattice diffusion is more favourable, when compared to grain boundary diffusion. The creep rate in this case is dependent on the lattice diffusion coefficient, D_l and the second power of grain size $(\dot{\varepsilon}_s \propto \sigma D_l d^2)$. The stress exponent is 1 for diffusion creep as the dominance of stress for deformation is lower when compared to dislocation creep.

There is yet another deformation mechanism which is operative at low stress regimes, where the creep rate and applied stress are linearly dependent i.e when stress exponent is 1, but occurs due to dislocation movement. This is called Harper-Dorn creep and in this regime the deformation rate is independent of grain size and has been reported in aluminium [9], lead and tin [10]. This type of mechanism is operative in materials having large grain sizes and in alloy systems where the dislocation density does not increase with the applied stress.

The aforementioned mechanisms pertain to the influence of stress and temperature on dislocation movement by slip and stress directed movement of atoms. In addition to deformation by slip, polycrystalline materials can also deform by grain boundary sliding (GBS) and this occurs principally during creep. GBS usually refers to sliding of grains with respect to each other and this is usually significant at elevated test temperatures and lower strain rates. The GBS occurs due to the net shear force acting along the grain boundaries (Figure 2.3). The strain contribution by GBS can vary between 0.8-93 % [12]. The important consequence of GBS is its role in nucleating cavities which lead to fracture.

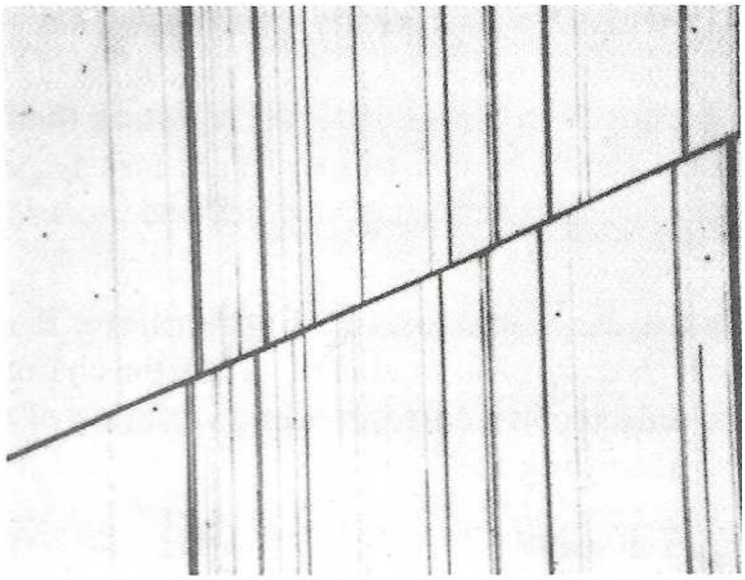

Figure 2.3 Grain boundary sliding in Al-1.92 Mg alloy [11].

2.3 Fracture

As in the case of deformation, depending on the applied stress and temperature, the failure mechanisms also vary. Figure 2.4 gives the schematic of a fracture mechanism map applicable for fcc materials.

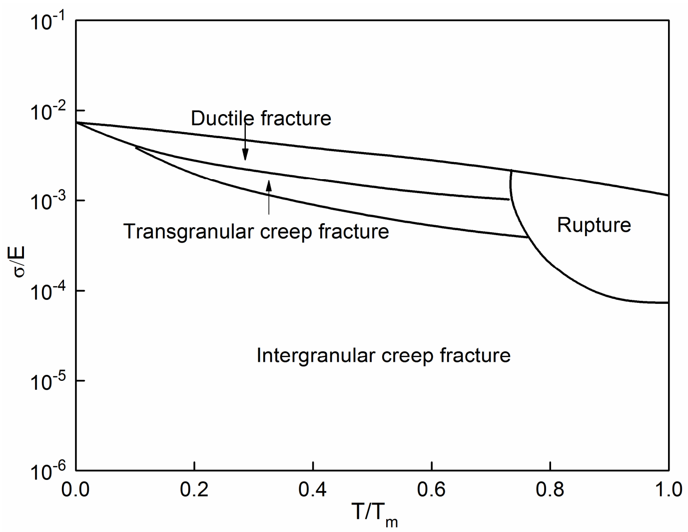

Figure 2.4 A schematic fracture mechanism map applicable for fcc materials.

The abscissa (temperature) and ordinate (stress) of the graph are normalised with the absolute melting point and the Young's modulus, respectively. A number of failure mechanisms operating in their respective regimes are shown in the figure. Figure 2.5 gives the broad classes of failure. Cleavage fracture occurs due to propagation of cracks along crystallographic planes. Such failures usually occur at lower temperatures. This type of failure is prominent in BCC systems, where the number of slip systems is highly temperature dependent [13]. In the following section the failures occurring during creep are more closely examined.

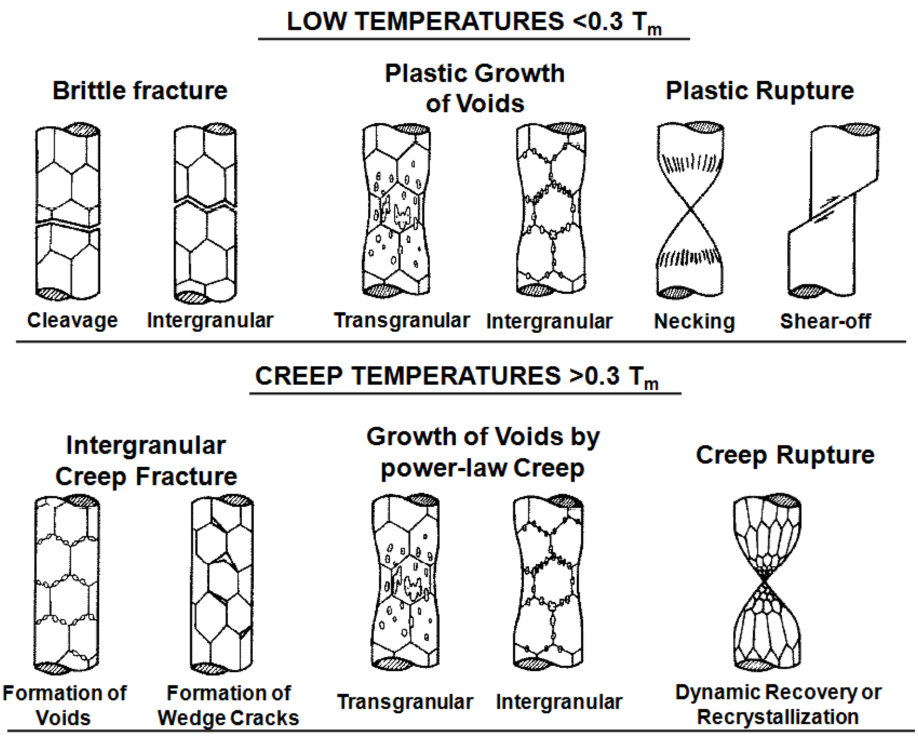

Figure 2.5 Broad classes of failure [13].

The onset of tertiary stage during creep deformation denotes the initiation of failure. In the creep curve this is demarcated by increase in the creep rate and departure from steady state creep regime. The formation of cavities and its propagation is one of the causes for failure during creep. Though the nucleation of cavities can occur much earlier during creep, its propagation in the form of cracks occurs more rapidly after the onset of tertiary creep. The majority of creep failures are classified as intergranular or transgranular depending on the propagation paths of the cracks. As a thumb rule, below the equicohesive temperature (ECT), the propagation of the cracks occurs within the grains and is referred as transgranular cracking. Above ECT, the propagation occurs along the grain boundaries and is termed as intergranular cracking. However, with reduction in strain rate, the ECT can be pushed to lower temperatures. When no fracture mechanisms are dominant, necking will precede upto zero gauge diameter and result in rupture. Rupture can also occur as a result of dynamic recrystallization. The role of nucleation and propagation of cavities are paramount in determining the creep failure mechanisms.

2.4 Creep cavitation

Nucleation of cavities can occur within the grains and at grain boundaries leading transgranular or intergranular failure, respectively. The creep cavitation which leads to transgranular failure is similar to the one occurring during low temperature ductile failure.

The low temperature ductile failure proceeds in the following sequence. Considerable localised strain accumulation occurs especially at the second phase particles and matrix interface, which results in the nucleation of cavities. This locally deformed region generates a tri-axial state of stress. The hydrostatic stress which develops after necking results in the formation of cavities. In pure materials devoid of any secondary phases, nucleation can occur at grain boundary triple points. With progressive straining these cavities get interlinked leading to crack propagation; this is termed as micro-void coalescence [13].

Transgranular creep cavitation differs from the low temperature ductile failure in two aspects. Firstly, since local relaxation of stress occurs during creep, the nucleation of cavities is postponed to higher stain levels. Secondly, during creep as the strain rates are comparatively lower, the flow is stabilized which results in delay in cavity growth. The fracture morphology in case of transgranular failure is characterised by dimples (Figure 2.6(a)).

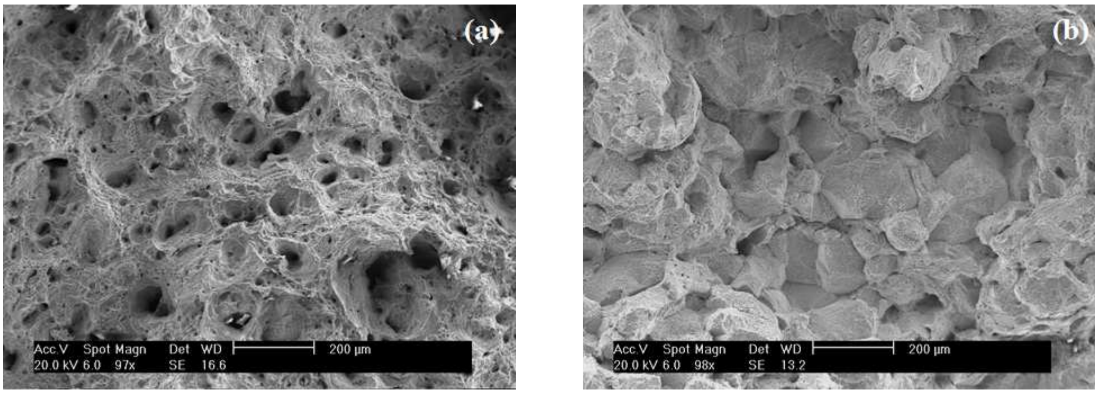

Figure 2.6 Influence of nitrogen on fracture mode of 316 LN SS at 923 K/140 MPa (a) ductile failure characterized by dimples for the steel containing 0.07 wt.% nitrogen (rupture life 3177 hours) and (b) brittle transgranular failure for the steel containing 0.22 wt.% nitrogen (rupture life 15974 hours) showing grain facets [14].

Intergranular fracture is the most frequently encountered failure in material subjected to damage caused by creep cavitation and its growth. The decrease in strain rate can further enhance the intergranular cavitation regime. As mentioned earlier, above ECT intergranular cavitation occurs due to the weakening of grain boundaries. Intergranular cavitation can also occur below the ECT due to excess strengthening of the matrix most commonly by secondary phases. Alternatively during prolonged elevated temperature exposure, the matrix itself can be hardened due to formation of embrittling phases, leading to intergranular cavitation. Since the matrix deformation is limited in this case, the ductility values are always lower after failure when compared to transgranular failures. The fractographs of specimens failed due to intergranular cracking consists of grain facets (Figure 2.6(b)).

Formation of cavities is paramount for intergranular cracking to occur during creep. Depending on the shape of the cavities, they are classified as wedge shaped or round shaped. The wedge shaped cavities usually occur at the grain boundary triple points (Figure 2.7(a)), whereas the round shaped occur in grain boundaries at the vicinity of the second phase particles (Figure 2.7(b)). The applied stress and temperature have a significant role in dictating the nucleation and growth of cavities. The various mechanisms of cavity nucleation and growth are dealt with in the next few sections.

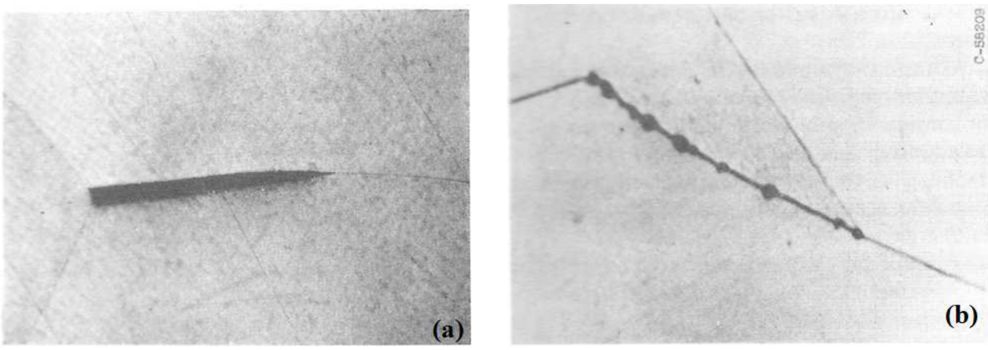

Figure 2.7 (a) Wedge crack in Al-20Zn alloy [15] and (b) round cavities in Ag [16].

2.4.1 Cavity nucleation

There are two widely accepted mechanisms governing cavity nucleation viz., vacancy condensation and athermal decohesion.

The vacancy condensation mechanism postulates that vacancies generated when tensile stress acts on grain boundaries or particles on grain boundaries, condense into voids [17,18]. There is usually an incubation time for the nucleation of vacancies and their growth is stable after they attain a threshold size. It was theoretically calculated that the stress required for the agglomeration of vacancies into cavities is around

E/100 [19], which is significantly higher than the applied stress levels. Hence, localised stress concentrations should develop for nucleation of cavities. Besides, the vacancy super-saturation needed for vacancy condensation is not likely to be available during creep. Though the vacancy condensation mechanism is more prominent during irradiation creep, its potential for nucleating voids during thermal creep is negligible. Thus the prevalence of vacancy condensation mechanism in engineering materials is highly speculative.

Athermal decohesion is the most likely mechanisms operative in engineering materials. According to this mechanism, nucleation of cavities occurs due to decohesion of atomic bonds caused by local stress concentration. There are two possible sources for localised stress concentrations (a) arrest of GBS at grain boundary triple points and (b) arrest of GBS by secondary particles at grain boundaries or grain boundary ledges. It has been already discussed that GBS is a possible deformation mechanism during creep. The stress concentration caused due to hindrance of GBS can result in developments of fold [20] or result in grain boundary migration to enable stress redistribution [1]. When these two mechanisms of stress relaxation fail due to the excessive strengthening in the matrix, stress is likely to build up near such grain boundaries. The athermal decohesion could be the possible mechanism responsible for nucleation of creep cavities in austenitic steels. The stress concentration in this steel can be developed as a result of arrest of grain boundary sliding by carbides and intermetallics [21] which evolve due to prolonged creep exposure. Another phenomenon giving rise to stress concentration at the grain boundary is the dislocation pile up interaction with hard particles at grain boundaries [22,23]. Though such an interaction can occur at grain interiors, cavity growth will be rather slow, as lattice diffusion is comparatively slower than the grain boundary diffusion. The presence of surface active elements like sulphur also enhance decohesion of atomic bonds.

The nucleation of creep cavities is believed to occur instantaneously during the initial loading as the strain accumulation and strain rate in this stage is comparatively significant. The growth of cavities progresses throughout the primary and secondary creep regime, and only during the tertiary regime it can be visualised by conventional characterization tools.

2.4.2 Cavity growth

The damage caused by cavitation becomes significant only when the nucleated cavities grow and get interlinked. A number of cavity growth mechanisms have been proposed and a few of which are described below.

(a) *Pure diffusion growth* - At low stress regimes when power law creep is not significant, the growth of cavities occurs due to difference in chemical potential between the grain boundaries and void surface. The application of external stress lowers the chemical potential at the grain boundaries causing atoms and ions to diffuse from void surfaces to the matrix. There are two types of diffusion controlled growth mechanisms a) unconstrained and b) constrained.

Unconstrained cavity growth - This mechanism occurs usually in bi-crystals. As mentioned earlier, the growth of cavities is caused by diffusion of vacancies into the cavities and removal of matter followed by plating it out at grain boundaries. When a number of cavity sites are present, the diffusion field of neighbouring sites overlap, and matter is uniformly deposited on the grain boundaries. The unconstrained cavity growth occurs when there is a wider distribution of cavity nucleation sites. This happens when the cavity spacing exceeds the diffusion distance. Hull and Rimmer

[24] proposed that the cavities formed by this mechanism maintain an equilibrium shape as the diffusion of vacancies on grain boundaries is slower than on the cavity surface.

Constrained cavity growth - This is the most widely occurring phenomenon in engineering materials which suggested that the cavity growth is not homogenous [25]. Cavities tend to nucleate more readily at transverse sections with respect to the loading axis. Hence, their growth is constrained when they encounter a non transverse grain boundary. Another reason for constrained growth is the exhaustion of vacancies from sources like grain boundaries [26]. The growth of the cavities in this case is dependent on the balance between diffusion of vacancies and the creep flow of the surrounding matrix.

(b) *Power law assisted* - It has been shown that plastic deformation can interact with the diffusion process and assist cavity growth [27]. The cavities grow by unloading the voids in the adjacent region by diffusion. The adjacent void depleted regions around the cavities do not overlap and consecutively the ligament between the voids has to deform by power law creep for further growth of the cavities.

(c) *Grain boundary sliding assisted* - In addition to deformation, GBS which results in nucleation of cavities can also assist in its growth [28,29]. In this case there is no significant changeover in mechanisms during nucleation and growth. The growth of cavities due to GBS will be significant at grain boundaries oriented at about 45° to the loading axis, as this is the orientation where the shear stress is maximum [30]. Cavitation can also occur at boundaries oriented at 90° to the loading axis indicating that the driving force in this case is diffusion [31].

2.5 Relationship between deformation and fracture

The preceding deformation during creep has an distinctive influence on the failure which is described by a semi empirical equation proposed by Monkmann and Grant [32].

$$\dot{\varepsilon}_s^m t_r = \text{Constant} \tag{2.3}$$

where $\dot{\varepsilon}_s$ is the steady state creep rate, t_r is the rupture life, m is a constant which is usually equal to 1. Modifications were made to this equation by incorporating the rupture ductility, ε_r [33] as

$$\frac{\dot{\varepsilon}_s^m t_r}{\varepsilon_r} = \text{Constant} = \frac{1}{\lambda} \tag{2.4}$$

where λ is the damage tolerance parameter, which gives an insight about the possible damage which has occurred leading to onset of tertiary creep [34].

When λ = 2-5, it suggests that failure occurred due to mechanical instability (necking) and cavitation.

$\lambda > 5$ suggests that failure occurred due to microstructural instability like precipitate and substructure coarsening, etc.

In general materials exhibiting large λ are preferred as it indicates that the material can accommodate significant strain before the onset of damage.

2.6 Extrapolation methods for creep deformation and rupture

Creep tests performed at laboratories are usually accelerated tests conducted at higher stresses and/or temperatures than what is experienced by the components made of the materials being tested. This is because it is impractical to carry out tests as long as the design life, which in case of nuclear components can span up to 40 years. Therefore, reliable extrapolation techniques are adopted which utilize short term data in the deformation regimes usually encountered by the components in service. Extrapolation may also be considered in environments where the components are subjected to varying stress and temperature. In some other cases the stress state which the component experiences may be multi-axial. The uniaxial creep data obtained during testing at constant stress and temperature must cater to all the above conditions.

The Larson-Miller parametric method [35] is the most popular method used for extrapolating to longer times. In this method a parameter which is a function of time and temperature is calculated as $P = f(t_r,T) = T(\log t_r + C)$.

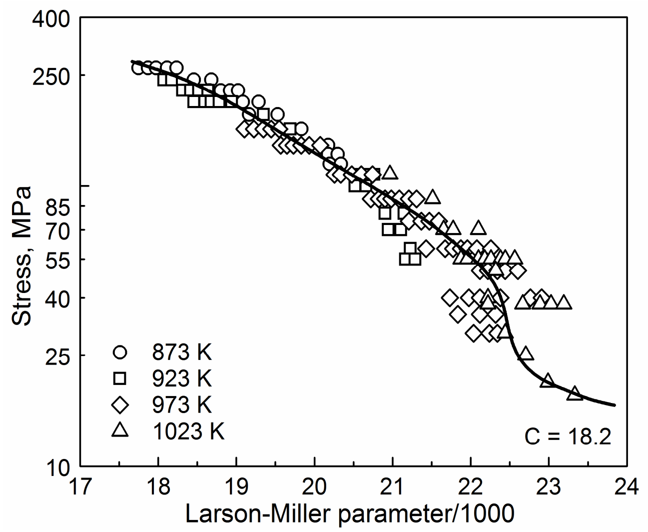

Figure 2.8 Larson-Miller plot of 316 SS [36].

A master curve is plotted with various values of stress σ and P (the Larson Miller parameter -LMP). The value of C in the equation is optimised to get minimum spread in the data (Figure 2.8). A polynomial fit is then made with the stress and LMP which can be extended up to longer rupture lives.

In cases where extrapolation is needed in dynamic loading conditions or environments where fluctuations in temperature can occur, the Robinson’s life fraction rule can be adopted [37].

If the rupture life of the material at a stress level of σ_i is t_{ri}, then

$$\sum_{0}^{i} \frac{t_i}{t_{ri}} = C \qquad (2.5)$$

where t_i is the time spent at the same stress σ_i, C is a constant which is unity if only one deformation mechanism dominates across the various stress levels. But in practice, many mechanisms operate simultaneously thereby reducing the value of C less than 1.

For extrapolation under multi-axial conditions, the conventional design practice is to obtain rupture life values for the calculated von-Mises stress or the maximum principal stress [38].

2.7 Austenitic stainless steels

Stainless steels are one of the most versatile materials developed in the last century. They are being widely used in power, chemical, petrochemical, off shore industries. Their unique combination of mechanical strength and corrosion resistance makes their utilization indispensable. These steels contain a minimum of 10.5 wt. % chromium which renders it corrosion resistant. Based on their microstructure, these steels are broadly classified into five types- austenitic, ferritic, martensitic, duplex and precipitation hardenable steels [39]. Out of these five, the usage of austenitic steels account for 65-70%. Its applicability spans from their use in cryogenics to fabrication of elevated temperatures components.

Austenitic stainless steel as the name implies have retained austenite phase at room temperature. This is possible with additions of austenite stabilizing elements like nickel, manganese, carbon and nitrogen to counter the effect of ferrite stabilizing elements (chromium, molybdenum). The austenite phase renders the steel more deformable, which makes fabrication of complex components more feasible.

Furthermore, there are no major weldability issues with using this steel. The 304 grade stainless steel containing 18 % Cr- 8 % Ni was one of the first stainless steel to be developed. It was proven that addition of molybdenum to this grade further improves the creep strength and corrosion resistance which led to the development of 316 grade steel. The nickel content in this steel was enhanced to counteract the ferrite stabilizing tendency caused by increase in molybdenum.

Sensitization is a major issue in austenitic stainless steels which limits the usage of the components made up of this material in the temperature range of 823-1023 K for prolonged time periods [40]. Sensitization is a result of preferential precipitation of chromium carbide ($Cr_{23}C_6$) along the grain boundaries. It is a thermally activated process which requires diffusion of both Cr and C to the grain boundaries. The formation of $Cr_{23}C_6$ reduces the chromium content at regions adjacent to the grain boundaries [41]. As a result, these chromium depleted regions are prone to corrosion attack, which results in intergranular cracking thereby lowering the load bearing capacity of the components made of this steel. Sensitization can be prevented by re-solutionising the microstructure, this dissolves the precipitated $Cr_{23}C_6$. But this again prevents the material to be used in the temperature range of 823-1023 K. This led to the development of what was termed as the ‘stabilized’ 321 and 347 grades of stainless steel containing Ti and Nb respectively [42]. These elements form stable intra-granular mono carbides which prevent the precipitation of $Cr_{23}C_6$ [43]. But the inherent shortcoming of these steels is that their welds developed cracking during welding or exposure to elevated temperature. In addition to this, the excessive strengthening of the matrix over that of grain boundary due to the precipitation of mono carbides results in more creep cavitation in these alloys resulting in low ductility failure during creep.

The only alternative solution to produce weldable steel, which would not sensitize after prolonged elevated temperature exposure, is to reduce the carbon content. Consecutively 304L and 316L stainless steels were developed with carbon content less than 0.03 wt.%.

The reduction of carbon content, however, decreases the mechanical properties of the steel. In order to offset the strength reduction, nitrogen is added [44]. Stainless steels with nitrogen content in the range of 0.07- 0.1 wt. % are designated as 'LN' grades.

Table 2.1 Variation in lattice distortion and strengthening due to addition of C and N [45].

Solute element	$\Delta a/a_0$ per 1 at.% $\times 10^3$ a_0-Lattice Parameter	ΔYield stress per 1 at.% (MPa)	Δ Ultimate tensile strength per 1 at.% (MPa)
Nitrogen	2.34	124.0	213.1
Carbon	1.67	76.6	116.2

Addition of nitrogen has several advantages over carbon. Austenite has higher solubility for nitrogen when compared to carbon resulting in more solid solution strengthening [46]. Though the size of nitrogen (65 pm) is smaller than that of carbon (70 pm), the distortion caused by nitrogen addition is more significant (Table 2.1) [47]. This is because of the variations in inter-atomic electron exchange mechanisms between the interstitial nitrogen and carbon atoms with iron. The distortions impede the mobility of dislocations thereby increasing the strength. Nitrogen also decreases the stacking fault energy, thereby preventing cross slip which helps to delay recovery of dislocation during mechanical loading. It has been shown that nitrogen improves both the yield stress and ultimate tensile strength up to 1.5 times when compared to carbon [45]. Nitrogen also helps in slowing down the precipitation kinetics of the deleterious intermetallic compounds which are formed during prolonged elevated temperature exposure [48].

2.8 Welding metallurgy of austenitic stainless steels

Welding is the most viable process for fabricating large components of reactors (Figure 2.9). The weldability of austenitic stainless steels is better when compared to other types of stainless steels. The only weldability issue in stainless steel is the occurrence of solidification or hot cracking. These cracks are found in various regions of the weld and with different orientations. They include centerline crack, transverse cracks, microcracks in fusion zone and microcracks in the heat affected zone (HAZ) [49]. Amongst these, hot cracking in the fusion zone is most widely reported. Hot cracking primarily occurs due to formation of eutectics (P, S, B with Si, Ni and Ti). These are low melting phases which crack during solidification of the weld pool, due to the restraint caused by shrinkage stresses [49,50]. Hot cracking can also occur due to grain boundary embitterment caused by the segregation of P, S and Si. Regions of fusion zone subjected to multi-pass, are also prone to hot cracking due to the dissolution of low melting eutectics. Austenitic stainless steels with no ferrite content are most prone to hot cracking. This is because of the limited solubility of P, S and B in austenite when compared to ferrite. Thus, retaining ferrite in the final microstructure can help reduce the susceptibility to hot cracking during welding [51]. Higher amount of delta ferrite content (>30 vol. %) again increases the susceptibility to hot cracking [51]. A brief discussion on the various solidification modes which an austenitic stainless steel weld is presented in the next subsection before understanding the implication of delta ferrite retention in the microstructure.

Figure 2.9 Erection of the main vessel of PFBR constructed by 316 L(N) stainless steel. The whole structure was fabricated by fusion welding process.

2.8.1 Solidification modes in stainless steel welds

The solidification mode in austenitic steel weld joints depends on the amount of ferrite or austenite stabilizing elements. Their quantification is possible by calculating the Cr and Ni equivalent. Hammer and Svennson [52] have developed the following formula of estimating the equivalents : $Cr_{eq} = Cr + 1.37\ Mo + 1.5\ Si + 2\ Nb + 3Ti$ and $Ni_{eq} = Ni + 0.31Mn + 22C + 14.2\ N + Cu$, where the elemental composition is given in wt.%.

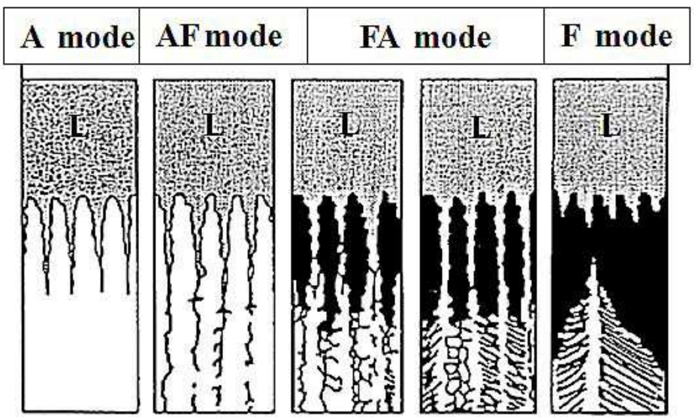

Figure 2.10 Various solidification modes of austenitic steel fusion zone [53].

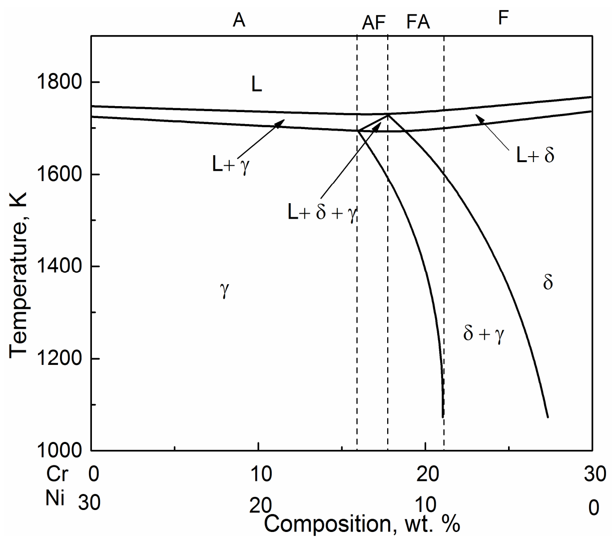

Figure 2.11 Pseudo-binary diagram of Fe-Cr-Ni system sectioned at 70 wt.% Fe [54].

Depending on the relative contents of the Cr and Ni equivalent the primary solidification mode can vary from austenitic to ferrite. The various mode of solidification is depicted in Figure 2.10 [53]. It was shown that in cases where the Cr_{eq}/ Ni_{eq} were higher than 1.5, the solidification changes from primary austenitic mode to primary ferritic mode [55]. The change in solidification mode can be more precisely understood by considering the pseudo-binary section of Fe- Cr- Ni ternary at 70% Fe (Figure 2.11). All the possible two phase field regions which bound the eutectic triangle consisting of L + δ + γ (Liquid + delta ferrite + austenite) are shown in the figure. The four solidification sequences are enumerated in Table 2.2. Compositional adjustments are made in such a way that the solidifying weld pool enters the AF or FA phase field and pass through the eutectic triangle before solidification. FA mode of solidification is more preferred than the AF mode because the formation of primary ferrite results in irregular boundaries between the austenite and ferrite. This forms a more tortuous path for crack propagation, making the fusion zone more resistant to failure caused by hot cracking [54,56].

Table 2.2 The four possible solidification types in austenitic stainless steel fusion zone and the associated microstructures.

Solidification mode	Reaction	Microstructure
A	$L \rightarrow L+\gamma \rightarrow \gamma$	Fully austenitic, well defined solidification structure
AF	$L \rightarrow L+\gamma \rightarrow L+\gamma+(\gamma+\delta)_{eut} \rightarrow \gamma+\delta_{eut}$	Ferrrite at cell and dendrite boundaries
FA	$L \rightarrow L+\delta \rightarrow L+\delta+(\delta+\gamma)_{per/eut} \rightarrow \delta+\gamma$	Skeletal and/or lathy ferrite resulting from ferrite to austenite transformation
F	$L \rightarrow L+\delta \rightarrow \delta \rightarrow \delta+\gamma$	Acicular ferrite or ferrite matrix with grain boundary austenite and Widmanstätten side plates

Although the phase diagram predicts complete transformation of delta ferrite to austenite, during welding the rapid cooling rates make the microstructure depart from equilibrium conditions. As a result higher amount of delta ferrite is retained at room temperature. Therefore, a better way of predicting the final phase distribution in the fusion zone is to take into consideration the non-equilibrium transformation. The WRC-92 diagram was developed based on this perspective [57] (Figure 2.12). This diagram is an improvement over the Schaeffler [58] and Delong [59] diagrams as phase predictions in WRC-92 diagram are based on thermodynamic stability and take into consideration the effects of nitrogen and manganese. The estimated microstructure requires the calculation of Ni and Cr equivalents which are slightly different from what was calculated for predicting the solidification mode as the non-equilibrium cooling effects are considered in this case.

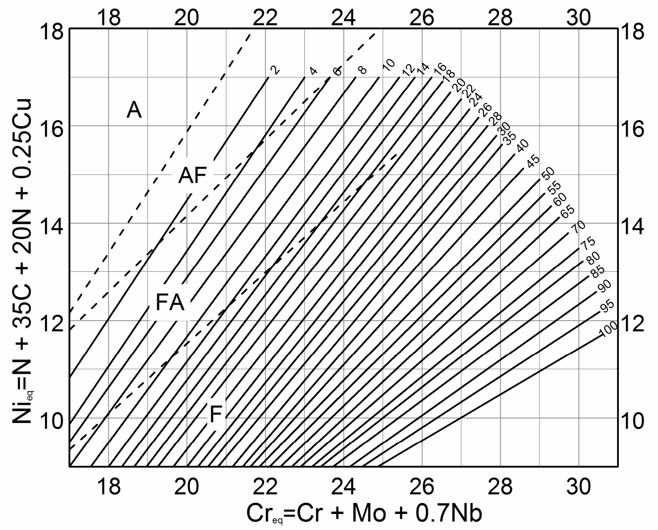

Figure 2.12 WRC-92 diagram [57]. The delta ferrite content in the fusion zone can be obtained from this diagram. The possible solidification modes can also be predicted from this diagram. The delta ferrite content is given in terms of the ferrite number (FN). The FN and volume % ferrite are equivalent for values upto 28 [60].

2.8.2 Influence of delta ferrite in preventing hot cracking

The major beneficial effects of delta ferrite in the austenitic fusion zone are [56] enumerated below

1. Delta ferrite has comparatively higher solubility of impurities which attribute to hot cracking
2. The thermal contraction of delta ferrite is lower than that of austenite as a result the tendency of cracking during solidification of the fusion zone is reduced.
3. The ferrite/austenite boundaries are not easily wetted by liquid films as ferrite/ferrite or austenite/austenite boundaries. Hence the tendency for cracking along these boundaries is reduced.
4. The ductility of delta ferrite is higher than that of austenite at higher temperatures, this causes the relaxation of thermally generated stresses

Though addition of delta ferrite is beneficial, an upper limit is specified. This is because delta ferrite is more prone to transformation into intermetallic phases during elevated temperature exposure. This is detrimental to the mechanical strength of the joints. Hence the amount of delta ferrite prescribed in the fusion zone is 3-9 vol.% [61].

In nitrogen bearing stainless steels, it was shown that the tendency to hot cracking is enhanced as nitrogen is an austenite stabilizer. However, it was shown that the strength of the fusion zone can be increased with nitrogen content [62]. Nitrogen also reduces the tendency for formation of brittle intermetallic compounds during elevated temperature exposure. Careful alloying adjustments are usually carried out so as to harness the benefits of nitrogen keeping into account its austenite stabilizing tendency in the stainless steel fusion zone [48].

2.9 Precipitation in austenitic stainless steels

The intention of subjecting the stainless steels to solution annealing temperature in the range of 1323-1423 K is to dissolve any remnant carbides or intermetallics. As a result in the mill annealed condition, the austenitic stainless steels are more or less precipitate-free. However, during prolonged elevated temperature exposure, precipitation of carbide and intermetallics occur [63,64]. Formation of secondary phases significantly influences the mechanical properties of the steel. Carbides and intermetallics are the two main phases which precipitate from the austenite matrix, their evolution and influence on mechanical properties are discussed in the subsequent sections. Some physical properties of the prominent phases in stainless steel are given in Table 2.3.

Table 2.3 Some properties of the prominent precipitates which can form in austenitic stainless steels during elevated temperature aging.

Phases	Crystal structure	Lattice parameter (nm)	Possible chemical composition
$M_{23}C_6$ [66]	fcc	a = 1.0569	$(Cr_{16}Fe_5Mo_2)C_6$
M_6C [66]	fcc	a = 1.095	Fe_3Mo_3C
MX [63]	fcc	a ≈ 0.4	TiC, TiN, NbC, NbN
Cr_2N [63]	hcp	a = 0.478, c = 0.444	Cr_2N
sigma (σ) [66]	tetragonal	a = 0.8828, c = 0.4597	44 wt.%Fe-29.2 Cr-8.3 Mo
chi (χ) [66]	bcc	a = 0.8878	$(FeNi)_{36}Cr_{18}Mo_4$
Laves η [66]	hexagonal	a = 0.473, c = 0.772	Fe_2Mo

2.9.1 Precipitation of carbides

Carbides of the type $M_{23}C_6$ are most prominent in stainless steel, though M_6C and MX have also been reported [63]. The M component in $M_{23}C_6$ consists predominantly of Cr atom which can be partially substituted by Mo and Fe. The precipitation of $M_{23}C_6$ usually occurs at the grain boundaries which lead to intergranular corrosion when subjected to certain temperature range as discussed earlier. Precipitation of $M_{23}C_6$ is more rapid as its evolution grossly depends on the diffusion of the smaller carbon atoms. Addition of nitrogen delays the precipitation of $M_{23}C_6$ because nitrogen forms clusters with Cr which later on can precipitate as Cr_2N if nitrogen content is high [65]. Weiss and Sticker [66] have reported that M_6C can precipitate from $M_{23}C_6$ after prolonged elevated temperature exposure. The formation of monocarbides (MX) usually occurs in stabilized steels which have additions of Ti and Nb [40]. These usually are intragranular in nature precipitating along dislocations [63]. The formation of MX precipitates improves the mechanical properties, but its ductility is reduced. The addition of nitrogen promotes the precipitation of mono carbo-nitrides.

2.9.2 Precipitation of intermetallics

The major intermetallics which precipitate during thermal aging of stainless steel are sigma (σ), chi (χ) and Laves (η) phase. When compared to the carbides, the precipitation of these intermetallics is more sluggish as it requires diffusion of heavier substitutional elements. Hence, their precipitation occurs at higher temperatures and after longer durations. They either get precipitated from the matrix or get transformed from carbides [63]. The precipitation of chi and Laves phases can occur simultaneously with carbides, as carbon is appreciably soluble in these phases. But precipitation of sigma usually proceeds after the formation of $M_{23}C_6$, as the solubility of C in sigma is limited. The sequence of precipitation of intermetallics and carbides has been clearly described by Weiss and Sticker [66]. They showed that formation of $M_{23}C_6$ results in lowering the carbon content in the matrix, whereas the formation of chi and Laves phase reduces the chromium and molybdenum content. But the solubility of carbon in austenite increases with decrease in Cr and Mo. As a result the $M_{23}C_6$ gets dissolved in the matrix after prolonged elevated temperature exposure, which initiates the formation of sigma and chi phases.

The formation and dissolution of $M_{23}C_6$ does not influence the precipitation of Laves phase, due to the replenishment of Cr and Mo in the matrix. The precipitation of intermetallic phases is usually detrimental in austenitic steels because it brings down the ductility and reduces the creep rupture life. The influence of nitrogen on the precipitation of intermetallics has been reviewed by Their et al. [48]. He showed that the precipitation of sigma and chi phases is delayed due to nitrogen additions, whereas it shifts the precipitation of Laves phase to higher temperatures.

2.9.3 Precipitation in the fusion zone

The presence of delta ferrite in the austenitic steel weld metal (fusion zone) accelerates the formation of carbides and intermetallics during elevated temperature exposure (Figure 2.13) [67]. This is because of two reasons: (a) The solubility of Cr and Mo is higher in delta ferrite when compared to austenite due to the ferrite stabilizing tendency of these elements and (b) The delta ferrite has a more open bcc crystal structure which makes diffusion faster. In addition to the above reasons the presence of additional delta/gamma and gamma/gamma interfaces accelerates the precipitation kinetics [68]. The possible sequence of transformation of delta ferrite under elevated temperature exposure has been reviewed by Thomas [69]. Since C is an interstitial element its diffusion is relatively faster in the austenite matrix. This results in the formation of $M_{23}C_6$ precipitates at the delta/gamma interface even after shorter exposure durations. This moves the delta/gamma interface further into the delta ferrite, and also enriches it with Cr and Mo when compared to austenite. Prolonged exposure to higher temperature causes diffusion of these bulkier substitutional elements. At a certain point of time, the composition in delta ferrite is favorable for the precipitation of sigma phase. Subsequently the sigma phase tends to further grow in size at the expense of $M_{23}C_6$. It should be noteworthy to mention that though delta ferrite has significantly higher concentrations of Cr and Mo when compared to austenite, they continuously diffuse uphill during aging. This is because the chemical potential of these elements are higher in austenite when compared to delta ferrite.

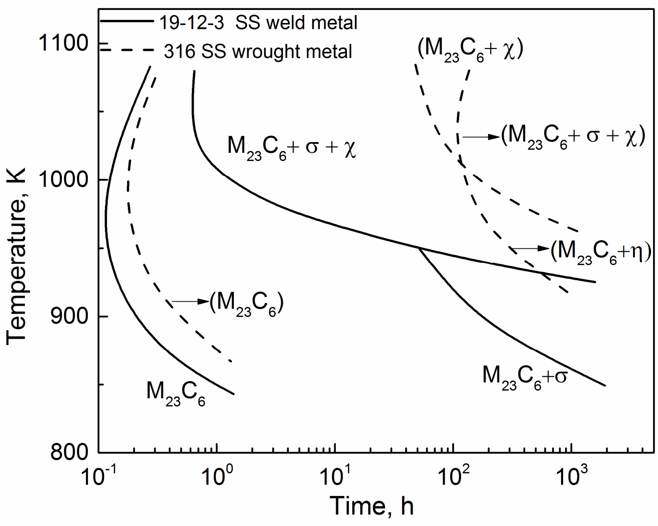

Figure 2.13 TTP diagram of 316 SS base metal and 19-12-3 SS weld metal (fusion zone) [67].

2.9.4 Influence of creep on precipitation kinetics

Mathew et al. [70] have shown that the transformation of delta ferrite into intermetallics occurred readily in the gauge portion of the all weld creep tested specimens, when compared to the shoulder portion. He reported that the generation of dislocations in the gauge portion results in more diffusion paths along its core, thereby enhancing transformation rates. Similar findings have been reported by Senior [71].

2.10 Evolution of various morphologies of delta ferrite

The ferrite content in austenitic stainless steel fusion zone gives us first hand information about the hot cracking susceptibility. However its distribution and morphology can still influence the precipitation kinetics of intermetallics which has not been clearly understood yet. Hence, knowledge of various morphologies of ferrite is essential to get a clearer insight about the elevated temperature performance of the fusion zone. The variations in delta ferrite morphology during solidification of the austenitic steel fusion zone arises due to the localised changes in composition and cooling rate adjacent to the solidification front [56]. The amount and distribution of these morphologies in the fusion zone is not uniform and hence the interpretation of microstructural evolution during subsequent aging becomes even more complex. Depending on its directionality and shape, delta ferrite in the as solidified fusion zone has been classified as vermicular, lacy and acicular [72] (Figure 2.14).

Vermicular morphology consists of continuous skeleton network aligned along the primary dendritic growth direction (Figure 2.14(a)). The orientation of the primary dendrites is along the heat flow direction. Delta ferrite is usually found in the cores of the primary and the secondary dendritic arms. Vermicular morphology occurs due to the incomplete transformation of delta into austenite. Delta ferrite having thinner interlaced structure oriented along the growth direction constitutes lacy morphology (Figure 2.14(b)). This morphology occurs in regions with higher ferrite content and is a product of rapid incomplete transformation of primary delta ferrite to Widmanstätten austenite. The delta ferrite exhibiting a needle shape, aligned randomly without directionality is termed as acicular (Figure 2.14(c)). As the ferrite content ahead of the solidification front increases, the morphology changes from vermicular to lacy and then to acicular.

The similarity between these three morphologies is that they are almost continuous in shape having higher surface area to volume ratio. On exposure to higher temperatures, the continuous cylindrical form of delta ferrite tends to transform to rows of small globules having less surface area to volume ratio (Figure 2.14(d)). This transformation occurs in all the aforementioned three morphologies and this constitutes the formation of globular delta ferrite.

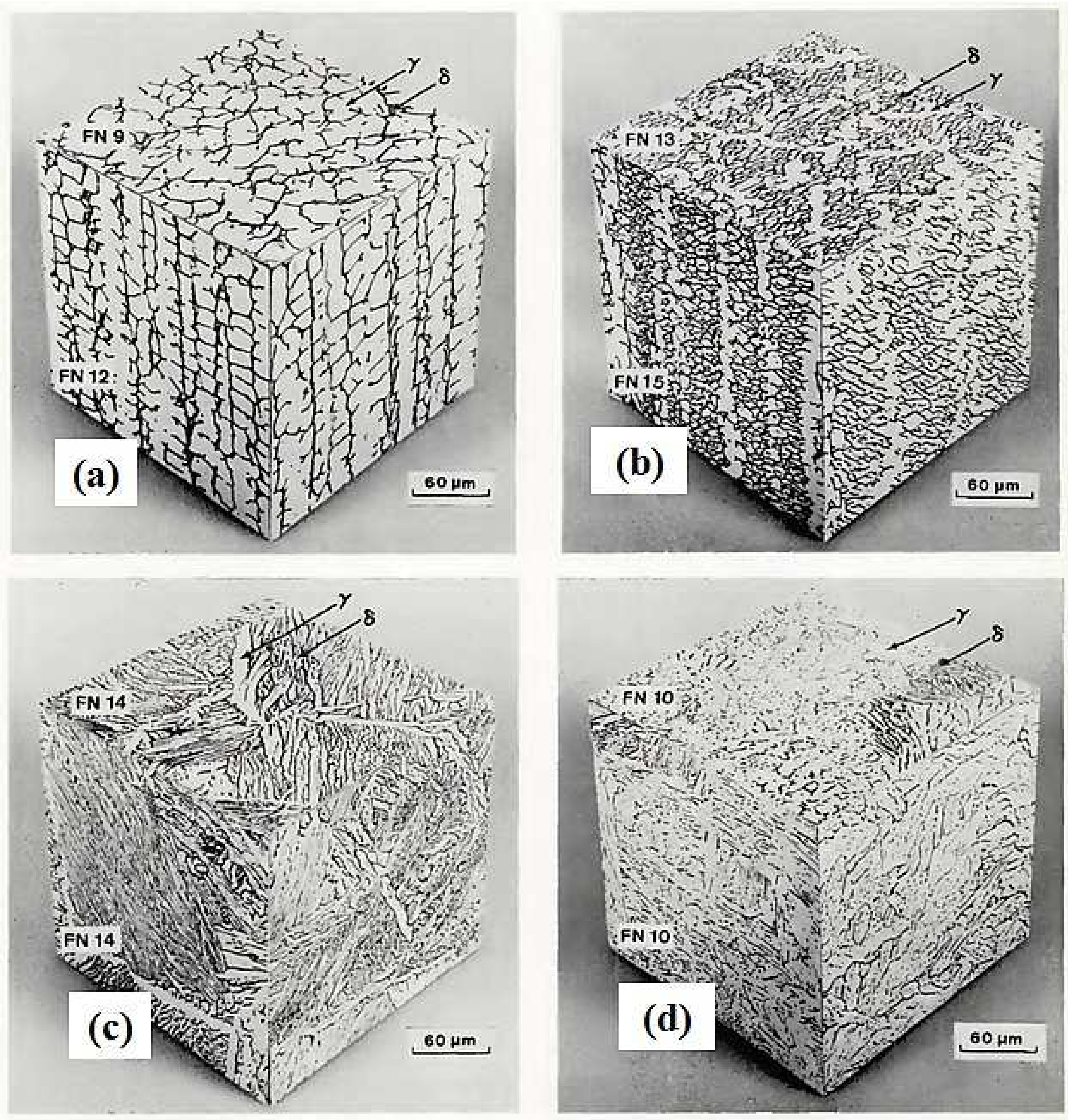

Figure 2.14 Various morphologies of delta ferrite (a) vermicular, (b) lacy, (c) acicular and (d) globular [72].

A continuous shape has higher gradients in chemical potential which tends to equilibrate upon higher temperature exposure leading to the shape change. In multi-pass welding, transition to globular morphology is likely to occur in the previous weld pass. The extent to which the changes in morphology occur will invariably depend on the heat input of the welding process. As the formation of globular ferrite is accompanied by partial transformation to austenite, there is a small reduction in delta ferrite content [72].

2.11 Creep properties of austenitic stainless steel fusion zone

The rupture properties of the austenitic steel weld metal (fusion zone) are usually lower to that of the base metal because propensity for creep cavitation is more in the fusion zone. The sequence by which creep cavitation progresses is discussed below.

1. Creep cavitation in the fusion zone usually occurs at the vicinity of prior ferrite transformation products like σ, χ and η intermetallic precipitates (Figure 2.15).
2. Under the influence of external stress the cavity proceeds along the intermetallic/ austenite interface. This propagation is dictated by the morphology of delta ferrite.
3. The propagation of cracks is usually obstructed at interfaces. Their propagation is dependent on the stress level and the ability of the cavitated cracks to get interconnected.

When compared to the wrought austenitic steels, the fusion zone exhibits significant scatter in tensile and creep properties [73,74] (Figures 2.16 and 2.17). The reasons for scatter in properties can be linked to the changes in creep cavitation phenomenon caused by the following reasons changes in welding process, variations in electrode composition location where specimen is extracted and variations in delta ferrite morphology.

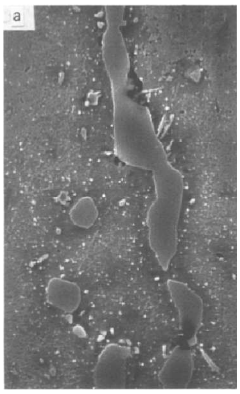

Figure 2.15 Creep cavitation along the sigma/austenite interface [71].

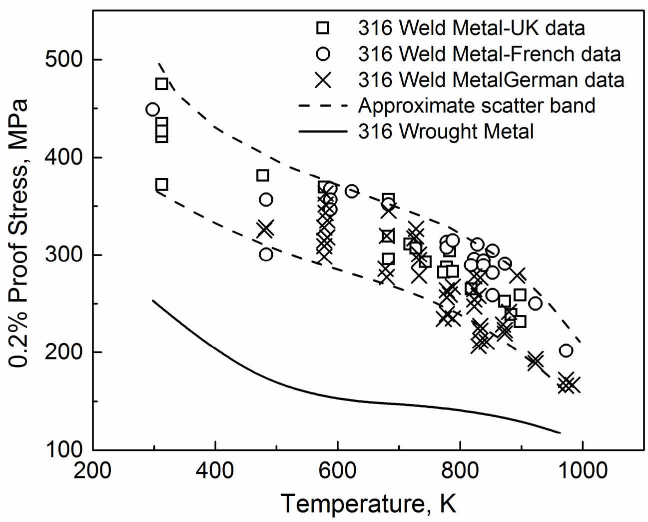

Figure 2.16 Scatter in 0.2% proof stress for 316 SS weld metal (fusion zone) [73].

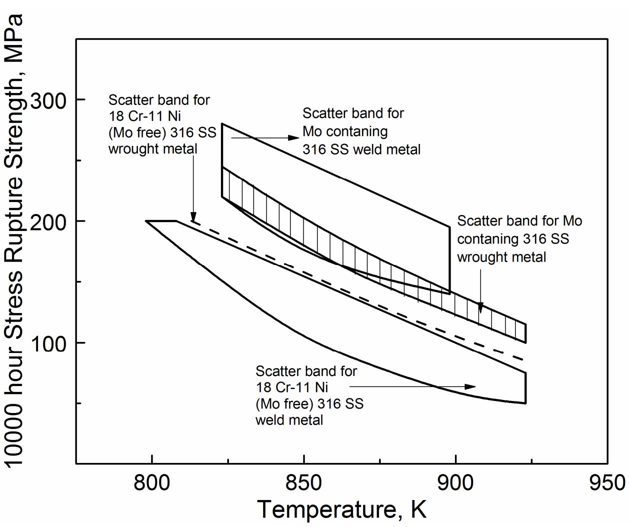

Figure 2.17 Comparison of 10000 hour rupture strength of 316 SS weld metal (fusion zone) and wrought metal [74].

2.11.1 Influence of welding process

Variations in welding process can result in changes in weld heat input, which can alter the volume of fusion zone and induce changes in delta ferrite morphology.

In addition to these modifications, the variations in thermal cycle in the adjoining base metal can cause restraint of varying degrees. One of the earliest studies by van der Scaaf [75] showed that the weld joints made by GTAW (gas tungsten arc welding) were stronger than those made with SA (submerged arc), MMA (manual metal arc) and EBW (electron beam welding). A recent study has shown that the creep properties of the transverse joints fabricated by A-TIG (activated tungsten inert gas) process are superior to those fabricated by TIG (tungsten inert gas) process [76]. Joining by A-TIG process was accomplished by a single pass, whereas the TIG process was carried out by depositing multiple weld passes. The increase in strength of these joints were attributed to 1) lower delta ferrite content 2) lower strength gradient within the fusion zone and 3) alignment of delta ferrite and the solidified grains along the loading direction. Through this study it was concluded that the variations in microstructure can be reduced if the number of weld passes are less. However, Gowrishankar et al. [77] showed that the tensile properties improved with the increase in the number of passes. The influence of the number of passes on the weld joints mechanical properties has not been thoroughly understood.

2.11.2 Influence of electrode composition

One of the earliest works by Senior [71] showed that the creep rupture life of the fusion zone improves with increase in carbon content. They argued that increased carbon content caused significant precipitation of $M_{23}C_6$. Even distribution of $M_{23}C_6$ delays the precipitation of the more deleterious sigma phase, which results in failure associated with low ductility. The effect of carbon in enhancing the rupture life was more pronounced in case of fully austenitic fusion zone [78]. Addition of nitrogen has been proven more beneficial than carbon because it slows down the precipitation of $M_{23}C_6$ and intermetallic phases. Unlike carbon which can be removed from matrix due to the precipitation of $M_{23}C_6$, nitrogen is usually found in solution when its level is less than 0.15 wt. % [44]. However, adding higher nitrogen to the fusion zone can result in porosity. Ogawa [79] had suggested that by increasing the amount of Ti, Zr, Nb, V, Cr, Mo and Mn the amount of nitrogen in the fusion zone can be enhanced. They showed that increase in nitrogen content improved the creep strength of the fusion zone significantly.

Use of electrodes or filler wires having Controlled Residual Elements (CRE) like boron, phosphorus and titanium in electrodes has also showed increase in the creep rupture life. Cole et. al. [80] have shown that the addition of 0.007 wt. % B, 0.42 wt. % P and 0.06 wt% Ti produced the best results. Addition of Ti increases the amount of delta ferrite in the microstructure as it is a strong ferrite stabilizer. It was also shown by Klueh and Edmonds [81] and Vitek and David [82] that since titanium retards the formation of $M_{23}C_6$, sigma precipitation occurs more readily in the CRE fusion zone. However, the striking difference between the CRE and the non-CRE grade fusion zones is the morphology of sigma phase. In case of the fusion zone made with CRE grade, the sigma phase is more dispersed and is not as interconnected as in the non-CRE grades. The interconnected sigma phases are more deleterious because they offer little resistance to crack propagation causing low ductility failures. Boron is thought to enter into $M_{23}C_6$ precipitates, lowering their mismatch between the austenite matrix. This slows down the coarsening rate of the precipitates [83]. Phosphorus also has a similar effect as that of boron. Phosphorus forms precipitation of the form $M_{23}(PC)_6$ [84], which is finer and it alters the morphology of the carbides and hence lowers down its coarsening rate.

2.11.3 Influence of specimen size and location

The fusion zone exhibits higher dislocation density than the base metal, due to the constraint generated on the solidifying weld by the adjoining base metal. But the substructure is not uniform throughout the fusion zone region and can vary significantly especially in multi-pass weld joint. Foulds and Moteff [85] have shown that depending on the location in the fusion zone the dislocation substructures vary considerably. Consequently, the mechanical properties of the weld joints are likely to vary depending on the locations from where they where extracted. Horton and Lai [86] have showed that the transverse specimens extracted near the root regions exhibited higher rupture life when compared to those extracted near the crown region. They suggested that the dissolution of delta ferrite due to subsequent thermal cycling is more significant in the root pass, which should possibly reduce the susceptibility of the fusion zone to creep cavitation in this region.

Similar results were reported in a more recent study on 316FR SS all weld specimens [87]. It was shown in this study that the creep strength improved progressively as the sampling location changed from near surface to the root pass (Figure 2.18). A systematic study by King et al. [88] by extracting specimens from different locations of the 308 stainless steel weld joint also showed a similar trend. The investigators recorded higher dislocation density in the root passes in the as-welded condition and also reported formation of cell structures in this region. Formation of fine $M_{23}C_6$ precipitates was also observed in the root pass due to the repeated thermal cycling. King et al. [88] have also reported that the transverse joints are the stronger than the longitudinal all weld joints. They suggested that the properties of the fusion zone are anisotropic and the specimens taken along the longitudinal section show the least strength.

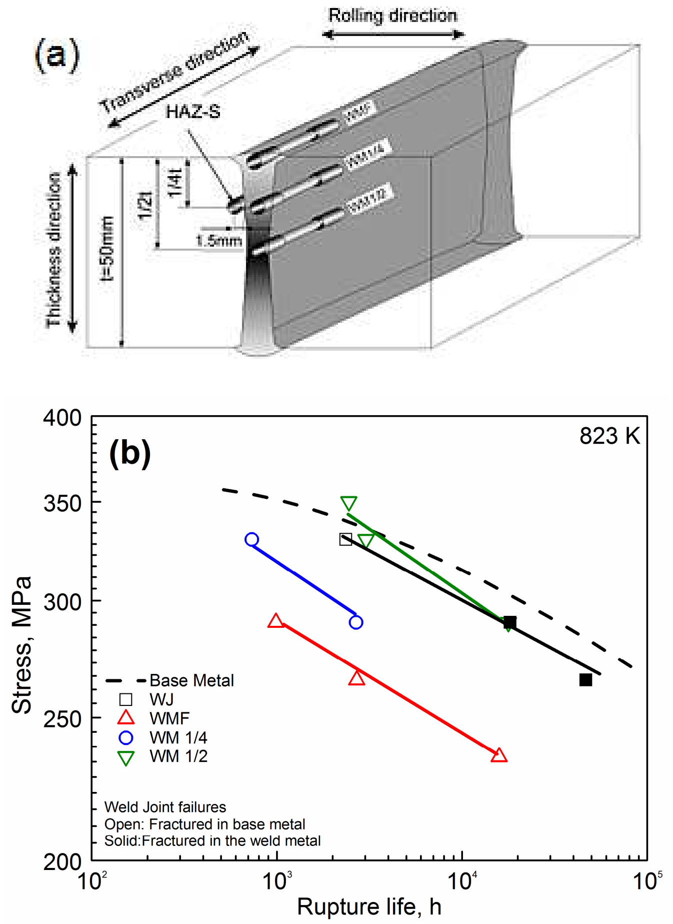

Figure 2.18 (a) Schematic showing the locations from where the specimens were extracted (b) Plot of creep rupture strength of the corresponding specimens [87].

Manjoine [89] has shown that the presence of the fusion zone creates a multi-axial state of stress during loading. He found that the complexity of the stress distribution generated due to the presence of the fusion zone is similar to that arising due to the presence of a mechanical notch. It is he who coined the termed "metallurgical notch" for describing the generation of stress gradients occurring due to the variation in properties of different regions in the weld joint. He has also discussed the fact that the weld joint design can also have implications on the multi-axial stress distribution thereby influencing the creep rupture properties.

In light of the above discussion, it is clear that the gradient in the mechanical properties can be minimised if the specimen extracted from the weld joints is large enough to average out the localised variations. More specifically it should be noted that the specimen diameter should incorporate more number of weld passes to get a representative strength value of the joints [46].

2.11.4 Influence of delta ferrite content

It was shown by Berggren et al. [61] that increase in delta ferrite content decreases the creep rupture life. The obvious reason is that higher content of delta ferrite can result in a microstructure more susceptible to creep cavitation. Thomas [90] has shown that delta ferrite content of 5 vol.% is optimum for preventing hot cracking and creep cavitation. With the increase in FN, delta ferrite becomes more continuous, offering little resistance to creep crack propagation, thus lowering the rupture life of the fusion zone.

2.12 Material selection criteria for fast breeder reactors

The material which is used for fabrication of main structural components of FBRs viz., reactor vessel, intermediate heat exchangers (IHX) and piping, demand stringent property requirements [91]. This is because these structures will be in operation for about 40 years in the temperature range of 673 – 873 K. Though the structural materials are not directly exposed to the high neutron flux as the core components; they may still be subjected to a cumulative dosage up to 5 dpa (displacements per atom). Compatibility with liquid sodium is also a prime requirement. Though all the structural components do not operate at temperature regimes where creep deformation is significant, the whole structure of the reactor is made of austenitic stainless steel. This mono-metallic design is to prevent diffusion of interstitials from one material to another through the coolant. Based on the international experience and the availability of design data, austenitic stainless steels of the grade 304L(N) and 316L(N) are the chosen material for fabricating most of the structural components (Figure 2.19). At temperatures above 770 K, the more creep resistant 316L(N) stainless steel is preferred. 304L(N) SS with higher thickness is used for fabricating components which are subjected to lower temperatures. Nitrogen in the nuclear grade 316L(N) SS is denoted by parenthesis when compared to the commercial 316LN SS to emphasize that its content is controlled within a narrow specified range.

Apart from this, there are few other variations between commercial and the nuclear grades

1. Narrower compositional range of almost all alloying elements.
2. Tighter specifications to control the amount of sulphur, phosphorus and silicon
3. Lower inclusion content to improve ductility
4. Intermediate grain size to facilitate in-service ultrasonic inspection

These variations in nuclear grade stainless steels are intended to avoid scatter in mechanical properties. The out of core structural components of the fast breeder reactors are fabricated based on the design criteria laid down by RCC-MR [92] and ASME codes [93].

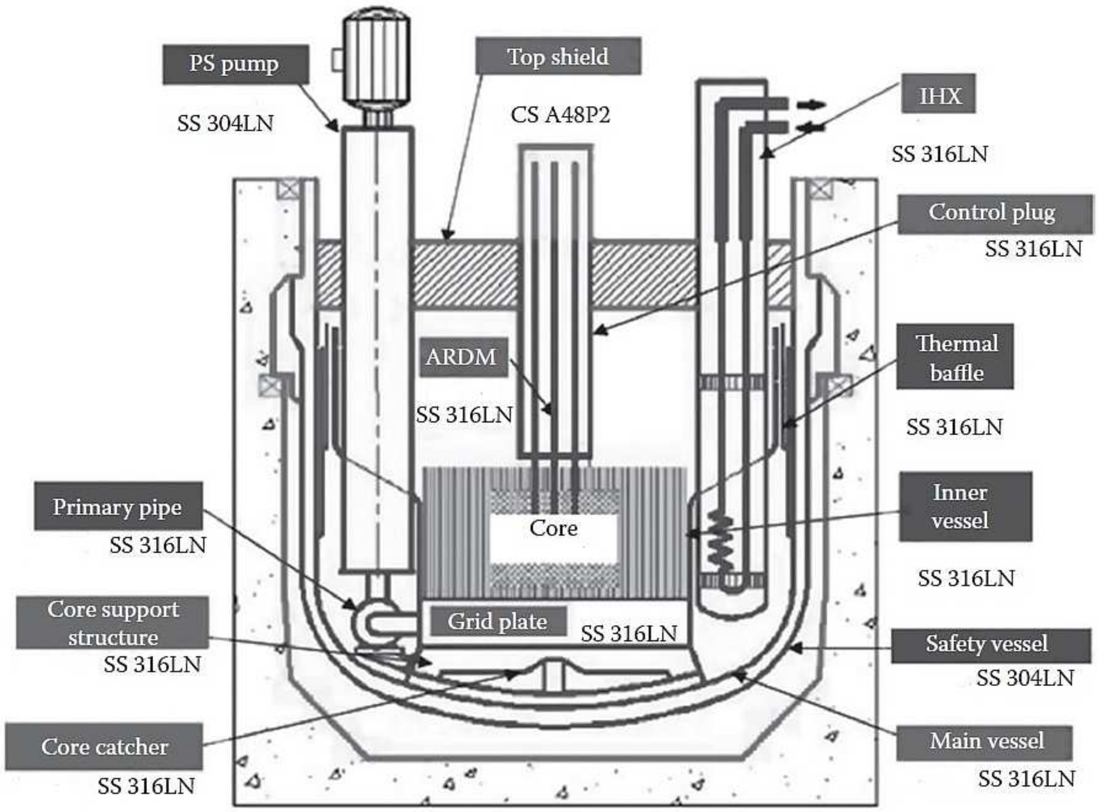

Figure 2.19 Schematic of the PFBR assembly components [91]. (PS- primary sodium, ARDM- absorber rod drive mechanism, CS A48P2- carbon steel with composition Fe-0.22C-0.8Mn-0.4Si-0.035P-0.012S-0.2Cr-0.3Ni-0.1Mo wt.%).

Considering the susceptibility of 316 and 304 grade stainless steel to intergranular corrosion, the contents of chromium, molybdenum, nickel and carbon have been altered in these codes. Carbon and nitrogen contents have been specified with a upper limit so that the properties of the L(N) grades match with the plain 304 and 316 grades for which the design data is available. A maximum limit for titanium, niobium copper and boron is specified to prevent hot cracking tendency during welding. A closer control of especially sulphide inclusions have been specified as its presence results in poor weldability.

Table 2.4 Comparison between the alloy composition of ASTM, RCC-MR codes with the FBR specification for 304L(N) and 316L(N) SS (in wt.%).

	304L(N)		316L(N)		
Element	**ASTM**	**FBR**	**ASTM**	**FBR**	**RCC-MR**
C	0.03	0.024-0.03	0.03	0.024-0.03	0.03
Cr	18-20	18.5-20	16-18	17-18	17-18
Ni	8-12	8-10	10-14	12-12.5	12-12.5
Mo	NS	0.5	2-3	2.3-2.7	2.3-2.7
N	0.1-0.16	0.06-0.08	0.1-0.16	0.06-0.08	0.06-0.08
Mn	2.0	1.6-2.0	2.0	1.6-2.0	1.6-2.0
Si	1.0	0.5	1.0	0.5	0.5
P	0.045	0.03	0.045	0.03	0.035
S	0.03	0.01	0.03	0.01	0.025
Ti	NS	0.05	NS	0.05	NS
Nb	NS	0.05	NS	0.05	NS
Cu	NS	1	NS	1.0	1.0
Co	NS	0.25	NS	0.25	0.25
B	NS	0.002	NS	0.002	0.002

The difference between the ASTM, RCC-MR specified composition and the FBR composition is given in the Table 2.4. Likewise the composition of the electrodes for fabricating structural components has also been altered to meet the special requirements of the FBRs. 316(N) electrode is used for fabricating components made of both 316L(N) and 304L(N) stainless steels, to avoid the possible mix-up of electrodes during welding. The composition of the fusion zone is altered to bring the amount of delta ferrite in the range of 3-7 vol.%. The specified upper limit range is more conservative to prevent precipitation of brittle intermetallics at higher temperatures in welded components which are envisaged to be in service for around 60 years. Nitrogen addition in the FBR grades is specified to harness its strengthening effect.

2.13 Design of structural components for FBRs

The ASME Boiler and Pressure Vessel Code, is usually followed for establishing the stress limit for components which are subjected to creep. It defines the allowable stress for a designated design life as the minimum of the following three stresses

1. minimum stress required to cause 1 % total strain (including elastic, plastic and creep)
2. 80% of the minimum stress to cause onset of tertiary
3. 67% of the minimum stress required to cause rupture

Each of the above mentioned stresses represent the materials resistance to creep deformation, creep damage and rupture respectively. Therefore all the three important parameters determining the creep strength are accounted for while arriving at the designated allowable stress. The allowable stress is usually multiplied by various factors which take into considerations the variations in design and loading environments. One such factor which considers the modification in strength level due to the presence of weld joint is the Weld Strength Reduction factor (WSRF).

The ASME defines the WSRF as the creep ratio of the uniaxial creep strength of the weld metal (fusion zone) to the uniaxial creep strength of the base metal. But often the strength of the weld joint is quite different to that of the corresponding base metal and fusion zone. This is a result of a complex stress distribution across the weld joint due to the presence of microstructurally varying regions. The RCC-MR code gives a more practical calculation of the WSRF; it considers the ratio of the uniaxial creep strength of the weld joint to that of the base metal. The WSRF is time and temperature dependent and typical values of WSRF are given in Table 2.5. The calculated WSRF are more conservative as it takes into account the scatter in rupture life values of the joints.

Table 2.5 Weld Strength reduction factor for 316L(N) SS recommended by RCC-MR [92].

Time (h)	873 K	923 K
1	0.99	0.92
10	0.99	0.92
30	0.99	0.92
100	0.94	0.85
300	0.86	0.78
1000	0.78	0.76
3000	0.76	0.73
10000	0.74	0.70
30000	0.72	0.66
100000	0.70	0.63
300000	0.66	0.58

2.14 Intention of the present work

The microstructural inhomogeneity is the prime reason for scatter in the mechanical properties of weld joints resulting in the underestimation of the WSRF. The underlying damage mechanism in the fusion zone which results in strength reduction is the nucleation and growth of cavities. In this work, an effort has been made to understand more clearly how damage proceeds in the complex fusion zone microstructure. The systematic study of inherent microstructural inhomogeneity in the fusion zone offered a fresh perspective towards understanding its influence on creep cavitation. This knowledge resulted in adopting a damage tolerance methodology by tailoring the microstructure to mitigate the adverse effects of creep cavitation thereby enhancing the rupture life of the weld joints.

CHAPTER 3

EXPERIMENTAL DETAILS

Chapter 3

Experimental details

3.1 Introduction

This chapter gives details of the material and the methodologies used for the fabrication of the weld joint. Subsequently information regarding creep testing is presented. This thesis describes the extensive investigation carried out on creep ruptured weld joints employing different characterization techniques, each of which have been described briefly in this chapter.

3.2 Material

The material used is 316LN austenitic stainless steel (SS) containing 0.14 wt.% nitrogen (Heat No. H8334) and was procured from MIDHANI, Hyderabad, India. The steel was produced through double melting process. Air induction melting was used as the primary melting process where the raw materials are charged to get the desired composition. Nitrogen addition was carried out by charging nitrided ferrochrome. To lower the inclusion content, secondary melting was carried out by Electro-Slag Remelting (ESR) process. The ingots were hot forged into slabs, the final plates of 22 mm thickness was obtained after hot rolling the forged slabs. The rolled plates were then mill annealed at a temperature of 1375 ± 10 K for one hour for dissolving any remnant secondary phases. The chemical composition of the steel and the electrodes are given in Table 3.1. It can be noticed that the electrodes supplied by M/s. Mailam India Limited, Puducherry, India had higher nitrogen content when compared to those supplied by M/s. D&H Secheron, Indore, India. Both SMAW technique (employing electrodes of different electrode diameters 2.5, 3.15 and 4 mm) and Activated - TIG (with single and dual pass) have been used to fabricate weld pads.

Table 3.1 Chemical composition ranges of 316LN SS base metal and 316(N) electrode in wt.%.

Material	C	Ni	Cr	Mo	Mn	Si	S	P	N
316 LN SS base metal	0.025	12.15	17.57	2.53	1.74	0.2	0.004	0.017	0.14
316 (N) SS Electrode 3.15 mm diameter Supplier: M/s. D&H Secheron, Indore	0.052	11.5	18.6	2.2	1.74	0.64	0.007	0.022	0.1
316 (N) SS Electrode 2.5 mm diameter Supplier: M/s. Mailam India Limited, Puducherry	0.05	11.1	18.5	1.9	1.4	0.46	0.006	0.025	0.12
316 (N) SS Electrode 4 mm diameter Supplier: M/s. Mailam India Limited, Puducherry	0.051	11.2	18.45	1.94	1.37	0.48	0.005	0.024	0.13

3.3 Weld pad fabrication

Both SMAW and A-TIG welding processes were used for fabrication of the weld pads in this study. The SMAW electrode was coated with a basic flux. This flux generates vapours and a slag layer which protects the molten weld pool from atmospheric contamination. TIG welding uses a non-consumable tungsten electrode with or without using a filler metal. The molten weld pool in this process is protected by shielding with inert gases like argon. The A-TIG welding process is an advancement of the conventional TIG process. In this process, flux containing surface active elements is applied on the surface of the edges to be welded [94,95]. The flux improves the penetration of the arc due to the reversed Marongoni convection in the molten weld pool and as a consequence, the weld joint of thicker sections can be fabricated by less number of passes.

Plates of dimensions 250 × 250 × 22 mm^3 were used for the preparation of the SMAW weld pads. The groove angle was 10° and the root gap was 16 mm Figure 3.1. An increased root gap was used to maximize the fusion metal region in the specimen, as the study focussed on the creep cavitation behaviour in this region. In case of the A-TIG weld pads, plates of the dimension 250 × 250 × 10 mm^3 were used. No edge preparation was required for these joints. The fabricated weld pads were inspected using radiographic testing to detect possible weld defects for their soundness. Both the plates were fabricated in fully restraint condition to prevent distortion during welding. The sensitivity of the radiographic testing was 2 %. The ferrite content in the fusion zone was measured using Fischer Feritscope® FMP 30, which quantifies the ferrite by calculating the magnetic permeability. Since the ferrite number (FN) measured is quite low (upto 5 FN), it can be directly related to the ferrite volume % [60].

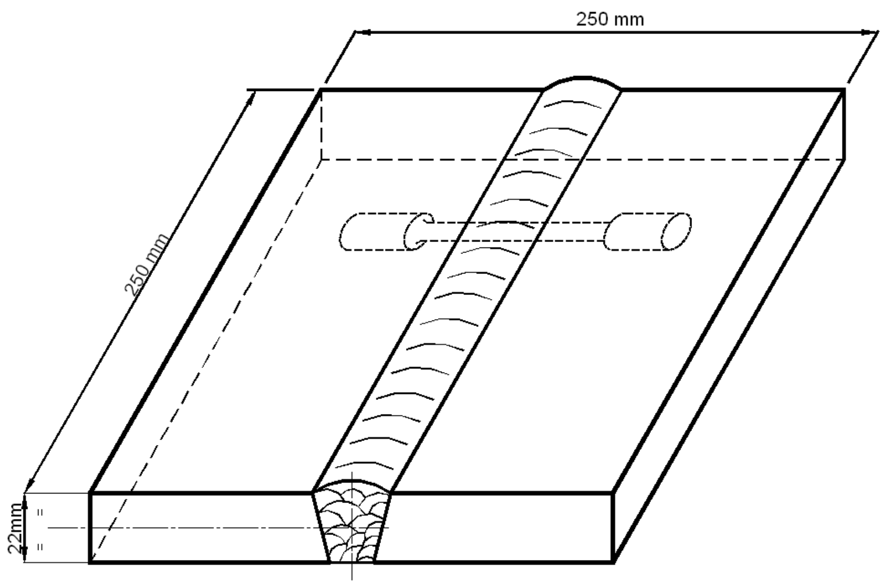

Figure 3.1 Schematic of weld pad showing the locations from where the specimens were extracted.

3.4 Creep specimens

Transverse weld joint creep specimens comprising base metal, HAZ and fusion zone in the central region were extracted from the fabricated weld pads. A schematic describing the location where the specimens were extracted is given in Figure 3.2. Specimens with M16 thread (Gauge diameter 10 mm) were extracted from the SMAW weld pads (Figure 3.2 (a)). Since the plate thickness of the A-TIG weld pads was lower, specimens with M8 thread (Gauge diameter 5 mm) were machined from it (Figure 3.2 (b)) .

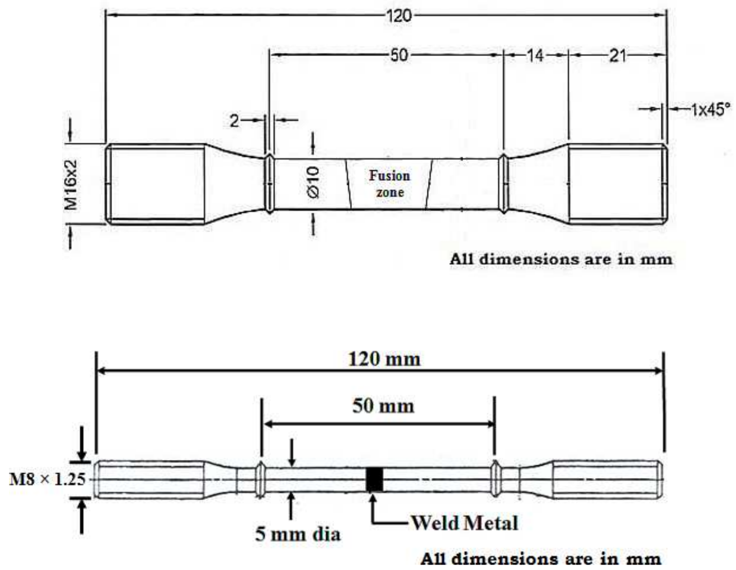

Figure 3.2 Schematic of (a) SMAW and (b) A-TIG weld joint specimen.

3.5 Uniaxial creep machine

The creep testing was performed according to the ASTM standard E 139 [96]. Single lever ATS® creep testing machines having a lever ratio of 1 : 10 were used in the investigation (Figure 3.3). The machines were equipped with a 3-zone split furnace with independent power control units. All the creep tests were performed at a test temperature of 923 K. Temperature was measured using K-Type thermocouple and throughout the creep tests the variation was maintained within the range of ± 2K. Elongation measurements on the specimen were done using LVDT attached to the extensometer which was fastened to the specimen. The resolution of the LVDT was 0.001 mm. Though the creep curve of the composite weld joint is of no significance due to the non-homogenous deformation across the different regions, elongation measurements were useful for interrupting the creep tests before the onset of tertiary. Such interrupted tests were useful for studying the dislocation sub-structural evolution of weld joints.

Figure 3.3 An ATS® creep machine used in the study.

3.6 Impression Creep Testing (ICT) Machine

To evaluate the creep properties of the various regions in the weld joint, the impression creep testing system was used (Figure 3.4). In this testing, a constant compressive load was applied against a small volume of specimen using a tungsten carbide (WC) indenter. The indenter used in this study was a flat ended cylinder with a diameter of 1 mm. The typical dimensions of the specimen was 25 × 10 × 10 mm^3 and consisted of all the three regions (fusion zone, heat affected zone and the base metal). The penetration of the indenter into the specimen was monitored against the elapsed time. The testing was done in vacuum of around 10^{-6} mbars, to prevent the oxidation of the indenter and the specimen surface. The displacement of the indenter was monitored using an LVDT attached to the load train, which had a resolution of 0.001 mm. The loading was performed using a lever arm system with a ratio of 1:10. Continuous cooling was provided in the vacuum chamber using chilled water to prevent any possible damage in the O-ring which was used for vacuum sealing. Data was recorded in a PC based on-line acquisition system. All the tests were carried out at 923 K with punching stress levels ranging from 591-760 MPa. A scaling factor of 0.33 was used to convert the punching stress to the uniaxial stress [98].

Figure 3.4 Impression creep machine integrated to the vacuum system.

3.7 Automated Ball Indentation (ABI) Machine

A Stress-Strain Microprobe® (SSM) (Figure 3.5) which was based on the principle of automated ball indentation technique (ABI) was used to obtain the tensile properties of the various regions of the weld joint. A spherical silicon carbide indenter with 0.76 mm diameter was used in the analysis. The system consists of a stress-strain microprobe (SSM) which was fully automated and had a closed loop for feedback mechanism consisting of load cell, LVDT and computer. The testing was carried out at 923 K on specimen which had dimensions of $25 \times 10 \times 10$ mm^3. The indentation loads and the penetration depths were converted in to the uniaxial stress-strain plots by semi-empirical relationships [99].

Figure 3.5 Automated Ball Indentation testing machine.

3.8 Microhardness tester

Walter UHL-VMHT® Vickers microhardness tester employing a load of 100 and 200 gf for 15 seconds was used to obtain the hardness profiles across the various regions in the weld joint. The specimens were polished up to 1 µm surface finish and etched before acquiring the hardness values. The equipment was calibrated using standard blocks of known hardness before testing. The microhardness was performed in accordance with ASTM standards E384 [100]. The hardness profiles were taken in the as-welded condition.

3.9 Optical metallography

Specimens for metallographic examination were extracted from relevant regions and polished upto a surface finish of 1 µm. SiC grit papers were used upto 6 µm finish, beyond which diamond suspension was used. The specimens were cleaned using ultrasonic cleaner both before and after etching to remove possible dust and residue adhering to the specimen surface. The specimens were electrolytically etched at a current density of 0.75 mA/mm^2 for 15 seconds [97]. The electrolytic solution composed of 60% HNO_3 and 40% demineralised water. The duration of etching was a critical parameter which affected the microstructural features in the specimen. Figures 3.6 (a) and (b) show the microstructure obtained after electrolytically etching at two different time periods. It can be seen that in the case where the duration is shorter, only austenitic grain boundaries were visible. Etching for longer durations revealed even the orientation of delta ferrite. Optical microscopic analysis was carried out using Carl Zeiss Axio Observer® equipped with a camera and a PC interface.

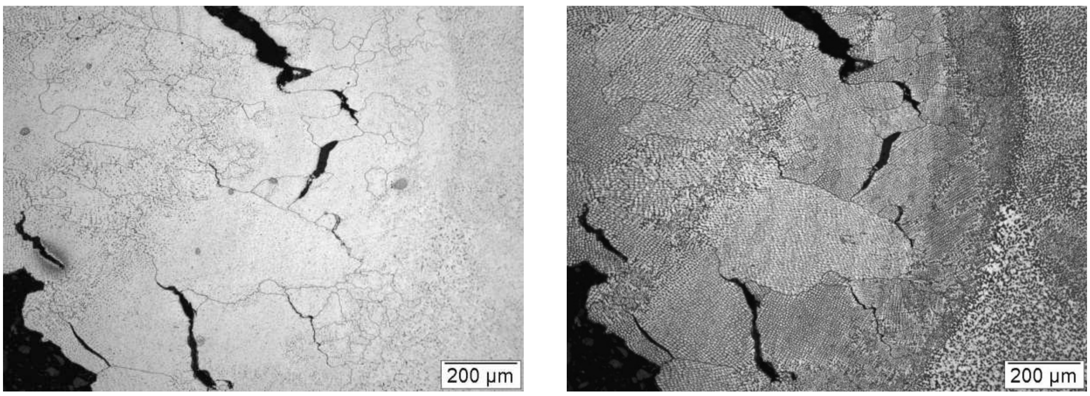

Figure 3.6 Austenitic stainless steel fusion zone etched using 60 % HNO_3 and 40 % H_2O solution for (a) 10 s and (b) 30 s at a current density of 0.75 mA/mm^2.

3.10 Scanning electron microscope (SEM)

Analysis using SEM was carried out on optically polished specimen and the failed specimen for fractographic analysis. The SE mode was used during the fractographic analysis, whereas both the BSE and SE mode were used for analyzing optically polished specimens in the etched condition. The estimation of elemental distribution adjacent to weld pass interface was carried out using energy dispersive x-ray spectrum (EDS) analyzer attached to the SEM. The SEM characterization was done using Carl Zeiss Supra 55® FEG-SEM.

Orientation Imaging Microscopic (OIM) analysis was carried out on EBSD data obtained using the same FEG-SEM. Specimens for EBSD investigation were subjected to controlled polishing using colloidal silica (0.03 μm) to relieve the stress which would have been induced during polishing. For the EBSD analysis the electron gun was subjected to an accelerating voltage of 20 kV. The specimen was placed in a 70° pre-tilted holder at a working distance of around 16 mm. The distance between the specimen and phosphor screen was 178 mm and an indexing algorithm based on eight detected bands was utilized. Aztec® software was used for data collection and HKL-Channel 5® software was used for post processing of the data. EBSD analysis was carried out to obtain the localised strain distribution in the material by correlating misorientation with strain. In this thesis, the Kernel Average Misorientation (KAM) mapping was done using the HKL-Channel 5® software. In addition to this an attempt has been made to estimate strain by a newly developed empirical correlation.

3.11 Transmission electron microscope (TEM)

Specimens for TEM analysis were extracted from the representative locations in weld joint using slow speed saw cutting. They were subsequently thinned down to a thickness of about 100 µm by mechanical polishing. Discs of 3 mm diameter were punched from these specimens and were further thinned down using Struers Tenupol® dual jet polishing machine to obtain an electron transparent region. The electrolyte used was 10 % perchloric acid and 90 % methonal. The temperature of the bath was around 233 K and the voltage used was 20 V. The current varied between 50-80 mA during the thinning process. TEM analysis was carried out using Phillips CM200 TEM with an accelerating voltage of 200 kV.

3.12 Finite element analysis

Finite element analysis of stress and strain distributions across the weld joint on creep exposure was carried out using ABAQUS® version 6.11 finite element solver [101]. Only a portion of the weld joint specimen was simulated in the model after incorporating appropriate boundary conditions. The partitioning of each region of the simulated geometry was based on microstructure and hardness measurements. The tensile properties of the individual regions in the weld joints were obtained by ABI technique and the creep properties were obtained using ICT technique. The Hollomon equation ($\sigma_t = K\,\varepsilon_p^{n_1}$, where σ_t is the true plastic strain, ε_p is the true plastic strain, K is the strength coefficient and n_1 the stress exponent) was used to simulate the elasto-plastic behaviour, the Norton's creep equation ($\dot{\varepsilon}_s = A\sigma^{n_2}$, where $\dot{\varepsilon}_s$ is the steady state secondary creep rate, σ is the stress, A and n_2 are temperature dependent material constants) was used for visco-plastic analysis. A biased mesh sizing was used at regions near the interface.

CHAPTER 4

MICROSTRUCTURAL INHOMOGENEITY AND ITS INFLUENCE ON CREEP PROPERTIES

Chapter 4

Microstructural Inhomogeneity and its Influence on Creep Properties

4.1 Introduction

In this chapter, the microstructural inhomogeneity across the multipass weld joint of 316LN stainless steel and its consequence on the creep deformation and rupture behaviour of the joint have been investigated, analysed and discussed. The basis behind evolution of different morphologies of delta ferrite across the weld pass interface in the as-deposited fusion zone is presented. The variation in dislocation substructure in the fusion zone containing the different morphologies has been elucidated with transmission electron microscopic analysis. EBSD analysis using misorientation profile and microhardness investigation across the weld pass interface were used to support the findings of TEM analysis. The influence of microstrctural inhomogeneity on creep cavitation in the weld joint has been critically examined. The theory of creep cavity evolution in the fusion zone contaning delta ferrite has been revisited to explain the localised damage in the creep tested specimen. TEM characterization has been carried out on creep tested specimens to explain the variations in dislocation evolution and precipitation behaviour across the weld pass interface on creep exposure. SEM examination of the failed weld joints was carried out to study how the microstructural inhomogeneity influenced the fractography. The conclusions drawn from this investigation set the direction for further studies.

4.2 Microstructure of the as-deposited weld joint

Multi-pass SMAW fusion joining process was employed for preparing the weld pads. The parameters used during the fabrication of the weld pad are given in Table 4.1

Macrostructure of the weld joint in as-received condition is shown in Figure 4.1, indicating the regions from where the creep specimen was extracted. The sections along which hardness values were obtained are also shown in the figure. The weld joint broadly consisted of as-deposited fusion zone, heat affected zones (HAZ) in base metal on both sides of deposited fusion zone and the base metal unaffected by the thermal cycles resulting from the multi-pass welding process. The grain size of the heat affected zone was marginally larger than that of the base metal.

Table.4.1 Welding Parameters.

Electrode Size (mm)	3.15
Current (A)	150
Voltage (V)	25
Travel speed (mm/min)	180

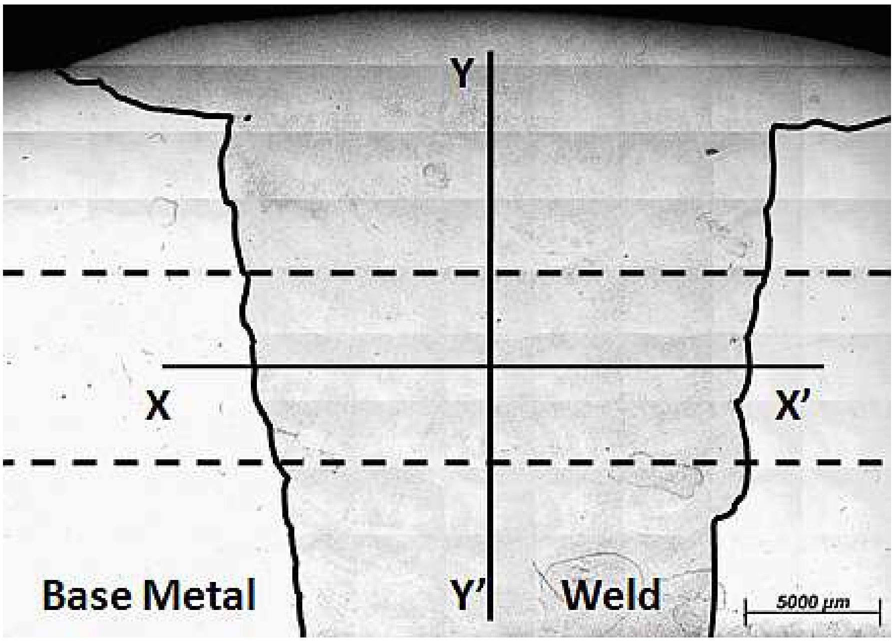

Figure 4.1 Macrostructure of the as-weld joint showing X-X′ and Y-Y′ sections where hardness values were taken, the dashed line shows the region from which the creep specimen was extracted.

Microstructure across the fusion zone was inhomogeneous as it consisted of two different morphologies of delta-ferrite namely vermicular and globular. The morphology transformation from vermicular to globular occurred in the previous pass adjoining to the weld pass interface. Figure 4.2 shows the regions corresponding to the different morphologies of delta ferrite across the weld pass interface. The figure also shows the locations where the EDS and TEM analysis was performed. The vermicular delta ferrite region, as the name indicates, consisted of interconnected delta-ferrite packets present in the inter-dendritic and grain boundary regions of austenite (Figure 4.3(a)). This morphology was found in regions which had not been affected by weld thermal cycles caused by subsequent weld bead deposition. This morphology constituted a major volume of the deposited fusion zone. Ferrite of globular morphology was present in region near to the weld pass interface over which the subsequent weld pass was laid; in other words it can be said that this region is the 'heat affected zone' in the fusion zone (Figure 4.3(b)).

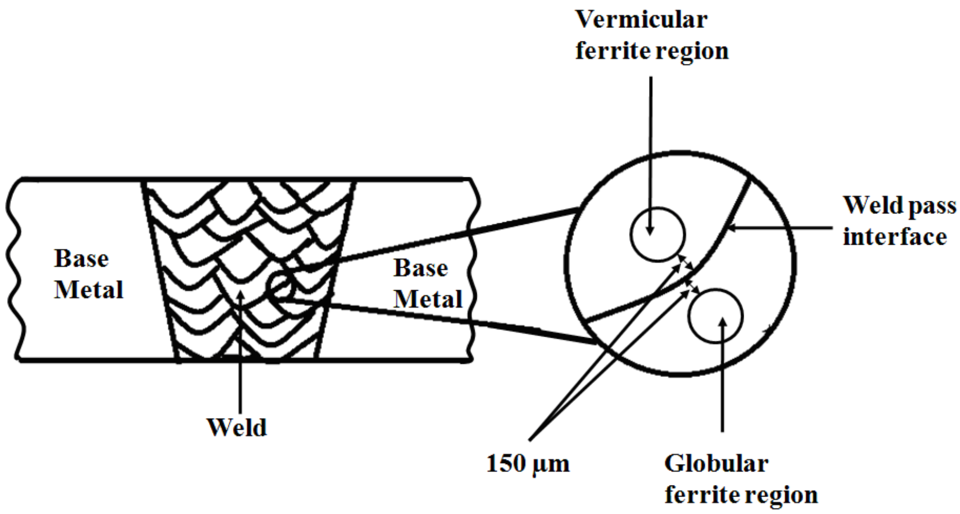

Figure 4.2 Schematic showing the location of the two morphologies of delta ferrite and the representative regions where EDS analysis and TEM specimens were extracted.

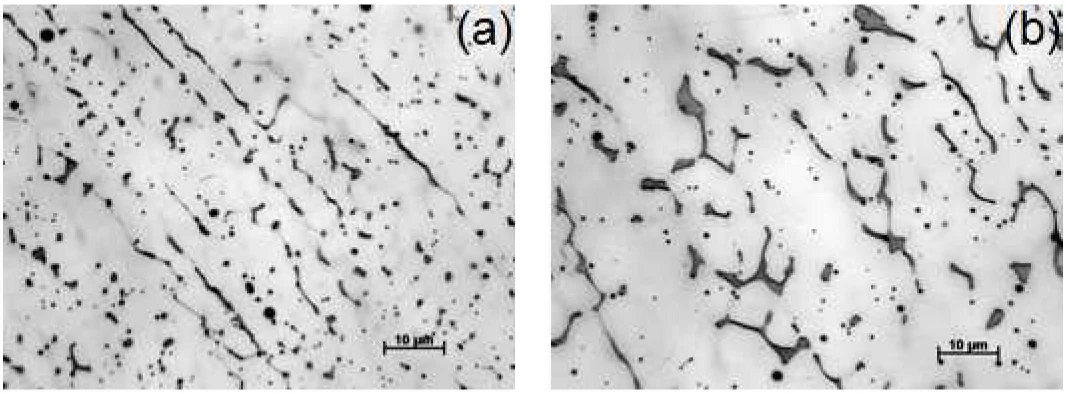

Figure 4.3 Microstructure of as-welded fusion zone showing delta-ferrite with (a) vermicular and (b) globular morphologies.

4.2.1 Evolution of various morphologies of delta ferrite

The solidification in the fusion zone proceeds in a way that some residual delta ferrite is retained to prevent hot cracking [51,102]. Even during solidification, the variation in morphologies of delta ferrite have been reported and this is attributed to localised changes in composition and cooling rate adjacent to the solidification front. The formation of various morphologies in the austenitic fusion zone has been discussed in detail in Chapter 2 [72]. The four morphologies which were observed in austenitic steel fusion zone are-vermicular, acicular, lathy and globular. In this study, the prominent morphology of the unmodified delta ferrite in the fusion zone was vermicular, although traces of lacy morphology could also be seen. The vermicular morphology constitutes a continuous skeleton of delta ferrite aligned along the primary growth direction. The lacy morphology also constitutes delta ferrite oriented towards the growth direction but it contains comparatively thinner structures. The similarity between these two morphologies apart from being oriented along the primary growth direction is that they are continuous having higher surface area to volume ratio. Since the creep cavitation associated with both vermicular and lacy structures were found to be similar, separate discussion on damage in delta ferrite region containing lacy morphology has not been presented in this work. Delta ferrite with acicular morphology was not observed in this study as the Cr/Ni equivalent of around 2 is required for its formation [72]. In the present study, the calculated Cr/Ni equivalent was 1.6, which was lower than what was required for acicular morphology to evolve.

Due to the exposure to subsequent thermal cycles a narrow region of the previous weld passes are subjected to changes in morphological change from vermicular to globular. Measurements using feritscope showed a reduction of FN from 5 to 3; this is possible due to dissolution of delta ferrite into austenite [72] during subsequent weld pass deposition. But the values obtained by the feritscope should be taken with caution as the probe diameter was comparable to the width of the region which had globular ferrite.

4.2.2 Hardness variation across the joint

The variations of hardness across base metal-heat affected zone to fusion zone-heat affected zone-base metal (X–X′ section in Figure 4.1) and across crown to root (Y–Y′ section in Figure 4.1) are shown in Figure 4.4. The fusion zone in general exhibited higher hardness than the base metal. This is due to the higher dislocation density resulting from the stresses developed during contraction of the liquid weld metal pool. The dislocation substructure evolved in the fusion zone is often comparable to that obtained after heavy cold working [103]. The heat affected zone in the base metal also exhibited higher hardness than the base metal; this is attributed to increased dislocation density produced by weld thermal cycles [104]. The hardness values increase from crown to root (in the Y–Y′ section) of the joint because the fusion zone in the root region experiences comparatively higher number of weld thermal cycles.

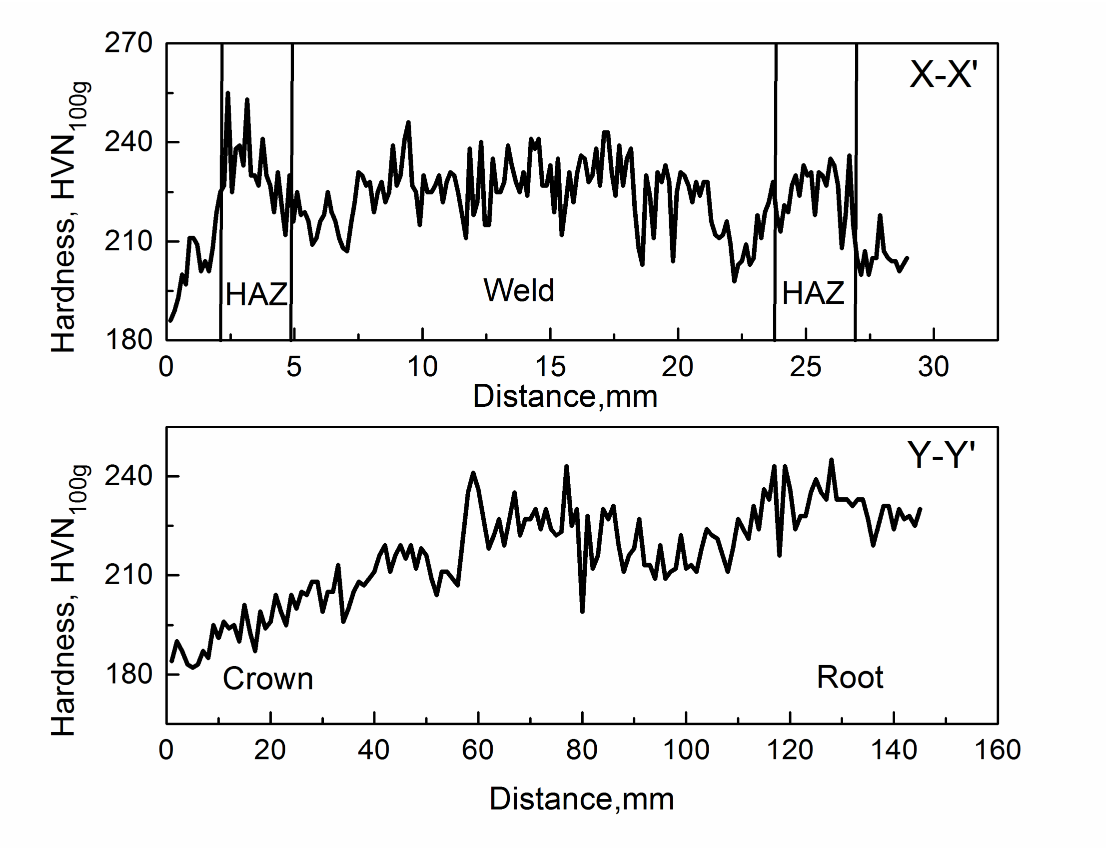

Figure 4.4 Variation of hardness along X-X′ and Y-Y′ sections.

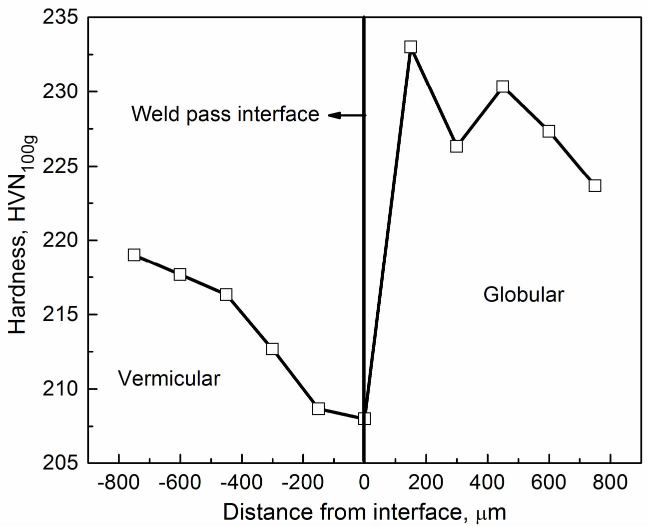

Figure 4.5 Variation of hardness along a weld pass interface.

The appreciable scatter in hardness is observed due to the inhomogeneity in microstructure caused by multi-pass welding. To study the origin of the scatter in fusion zone hardness more precisely, the hardness variation between successive weld passes was investigated (Figure 4.5). The globular delta-ferrite region, exhibited higher hardness than that of the vermicular ferrite region. Reduction in ferrite content in the globular morphology would decrease the hardness as it is a stronger phase than austenite at ambient temperature [105]. But the increase in hardness in the globular ferrite region suggests that there could be changes in dislocation substructure brought about by the 'thermo-mechanical effect' induced by the thermal cycle generated by subsequent fusion zone deposition. Thermo-mechanical treatment usually refers to the microstructural effect induced by an external control of load, strain, strain rate and temperature. But during a multi-pass welding, the variations in all these factors are controlled by weld thermal cycle, intrinsically. It is this thermal cycle which generates an internal constraint and consequently modifies the microstructure and property. In this thesis the 'intrinsic thermo-mechanical effect' is simply referred as 'thermo-mechanical effect'.

4.2.3 Dislocation substructure in the as-deposited fusion zone

TEM micrographs of the vermicular and globular ferrite regions of the fusion zone are shown in Figures 4.6(a) and (b), respectively. The interconnected delta-ferrite could also be seen in this TEM micrograph along with comparatively less dislocations in both delta-ferrite and austenite, wheras the globular region exhibited a forest dislocation structure even within delta-ferrite. Keown and Thomas [68] had indicated that in the fusion zone of stainless steels, the dislocation density in austenite is considerably higher than in delta ferrite. This is due to the difference in the thermal coefficient of expansion between the two phases. The austenite/ferrite boundary in particular had significantly higher dislocation density when compared to the bulk. The gradient in the stresses which developed due to the contraction of delta ferrite and austenite during solidification is highest at the interface, which resulted in higher dislocation density. In case of the region containing globular ferrite, tangled dislocation structures could be found even within the delta ferrite. This dislocation sub-structure within the delta ferrite is likely to have evolved while laying the subsequent weld passes and would not have evolved during solidification. The dislocation forest structure (Figure 4.6(b)) results in strengthening of this region [106].

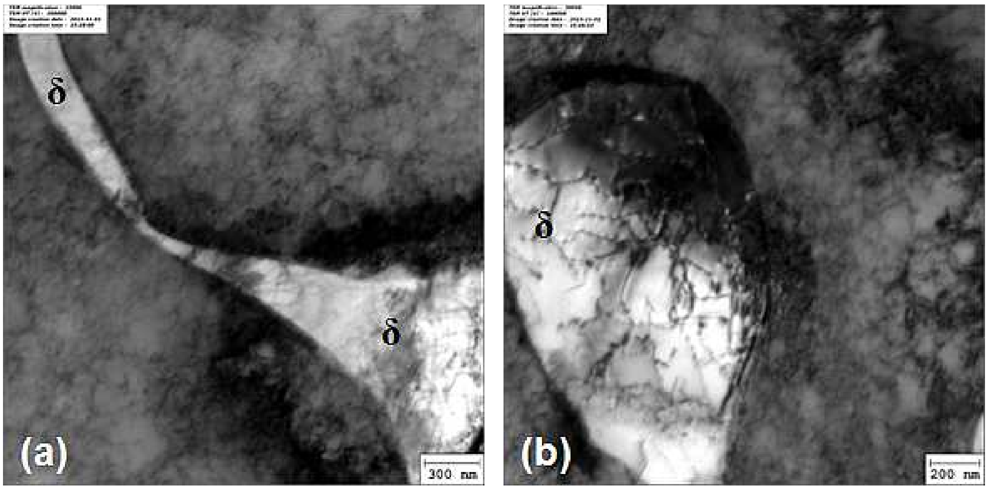

Figure 4.6 TEM micrograph of the as-weld material showing (a) vermicular interconnected delta-ferrite (δ) and (b) globular delta-ferrite with higher density of dislocations.

4.2.4 Orientation gradients estimated by EBSD

EBSD maps give the orientation relationship between the individually scanned pixels and the specimen orientation. These orientation relationships can give an estimate of the strain induced in the material. A more detailed discussion regarding usage of EBSD technique for strain measurements is presented in Chapter 7. However, a brief discussion is presented in this section.

In the solution annealed condition or in an unstrained material, the orientation gradients within a grain are negligible, therefore all the pixels scanned within a grain show similar orientation relationship with respect to the specimen co-ordinates.

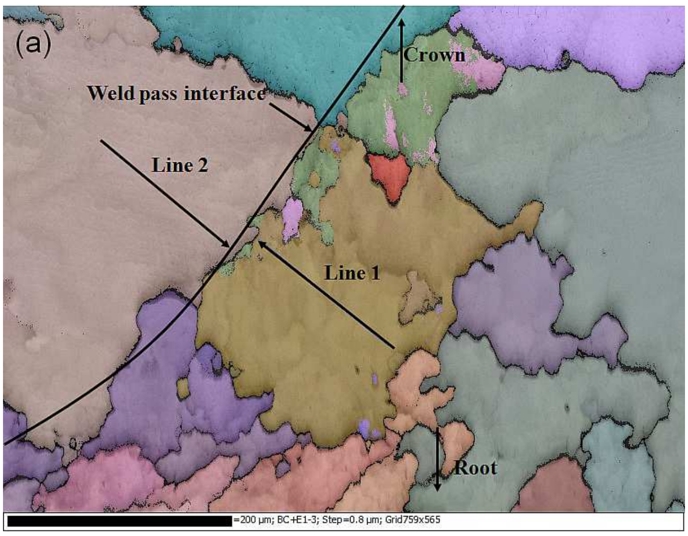

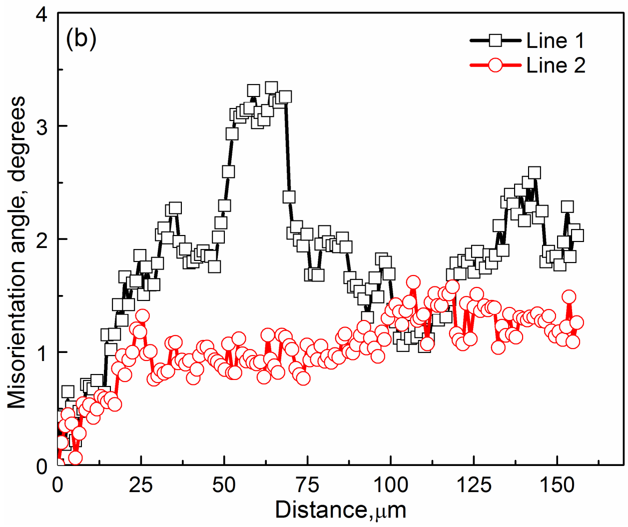

Figure 4.7 (a) EBSD map showing the regions where the orientation line scans were obtained and (b) orientation profiles taken on either side of the weld pass interface along these lines.

When strain is induced in the material, the orientation gradient within the grain also increases. Therefore, the estimation of the misorientation of the pixels, with respect to a reference pixel within the same grain, can help to quantify the strain induced in the grain. The misorientation profile obtained from the EBSD is popular method for estimating the strain gradients [107] in engineering materials.

EBSD map indicating the profile vectors along which the orientation values were obtained is shown in Figure 4.7(a). The profile vectors were around 150 microns in length and proceeded from the grain interior to the weld pass interface boundary. Both the misorientation profiles were plotted with respect to the orientation of the initial pixel (Figure 4.7(b)). It was observed that for the grain in the previous pass the orientation gradients were significantly high when compared to the gradients in the grain of the subsequent pass. The results are in line with the observations made from TEM and hardness studies. The laying of subsequent passes generates thermal cycles which result in localised expansion and contraction in a narrow region of the previously solidified fusion zone. The material in the bulk (far from the weld pass interface) resists the localised expansion and contraction thereby inducing strain in regions along the weld passes. This induced 'thermo-mechanical' effect results in strengthening this narrow region near the weld pass interface.

Microstructural characterization carried out on fusion zone of the as-welded specimens generated the following observations. There are two types of microstructural inhomogeneity which occur in the fusion zone, both of which arises due to the laying of subsequent pass over the previously deposited fusion zone. One is the change in delta ferrite morphology and other is the modification in the dislocation substructure. These changes in microstructure occur within a narrow region on the previously deposited weld pass adjacent to the weld pass interface. Though these changes occur in the same region, the driving force for both these microstructural modifications is different. The morphological change occurs due to shape instability of delta ferrite whereas the substructural evolution occurs due to plastic strain to redistribute the localised stress gradients. Therefore, the extent to which both these modifications can occur in the previous pass would also vary. The extent to which both these variations can occur would be different from the root to the crown regions. Since the root region experiences considerably more thermal cycles, the microstructural inhomogeneity across the weld pass interface may not be significant as repeated thermal cycling annealed out differences in microstructure. On the other hand, the crown region is subjected to comparatively fewer number of thermal cycles, thus the inhomogeneity across the weld pass interface was more prominent in this region. The specimens on which the creep tests were carried out were extracted from the central region of the transverse section, which would delineate the possibility of any extreme variations in microstructural gradient across the weld pass interface.

It was not possible to clearly demarcate separately the modification caused by morphological and substructural changes through the existing characterization tools. However, through hardness values it was determined that the distance up to which the microstructure hardened was around 750 μm from the weld pass interface in the mid transverse region of the weld joint. There was significant scatter in the width of the modified globular region. In this study, it has been assumed that the extent to which both these microstructural modifications occurred in the previous weld pass overlapped each other. Hereafter, globular region is referred to as regions containing globular delta ferrite and the hardened microstructure due to the 'thermo-mechanical effect'. The vermicular region refers to region containing vermicular delta ferrite morphology and comparatively softer microstructure with lower dislocation density.

4.3 Creep rupture properties

A comparison between creep rupture lives of the base metal and cross weld joints tested at 923 K at various stress levels is shown in Figure 4.8. The rupture life of both the base metal and weld joint increased steadily with decrease in applied stress. At higher applied stresses, the life of the joints and the base metal are comparable. However, the rupture life of weld joints is substantially lower than that of the base metal, at relatively lower applied stresses. The difference in creep rupture life between the base metal and weld joint increased with decrease in applied stress and for longer test durations. Failure of all the weld joints occurred in the fusion zone region indicating that this region was the weakest link. The microstructural instability of delta ferrite contained in weld region at elevated temperatures is the prime reason for the reduction in creep rupture life of weld joint when compared to that of the base metal. Since the transformation of delta ferrite to brittle intermetallics is time dependent, the difference in rupture life of the base metal and weld joints increased with longer creep exposure.

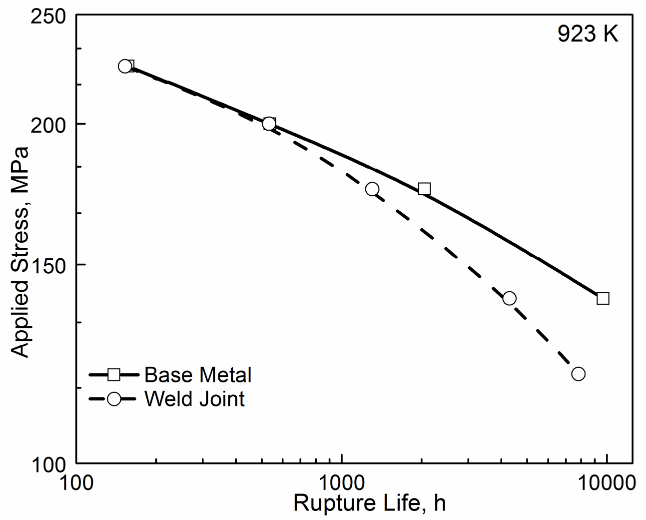

Figure 4.8 Variation of rupture life with applied stress.

4.4 Creep rupture ductility

The variations of creep rupture ductility with creep rupture life of both the base metal and the weld joint are shown in Figure 4.9. For the weld joints tested at stress levels of 200 and 225 MPa, the ductility values were lower than that of the base metal though the rupture lives were almost equal. This is because failure in the base metal occurred by excessive necking resulting in higher values of percentage elongation. Whereas, in the weld joint elongation values were lower as failure occurred due to the complex stress state generated by the 'metallurgical notch' resulting from creep strength inhomogeneity across the joint. Creep ductility decreased with creep exposure for the weld joints whereas it increased for the base metal. The gradual reduction in creep rupture ductility in the weld joint can be attributed to the time dependent creep cavitation phenomenon [67]. Therefore, the ductility values of the weld joint can be directly linked to the amount of delta-ferrite transformed (Figure 4.10) and the associated damage caused by cavitation, details of which will be discussed in the subsequent sections. The transformation of delta ferrite was almost complete for the weld joint with longest rupture life, which showed the least ductility.

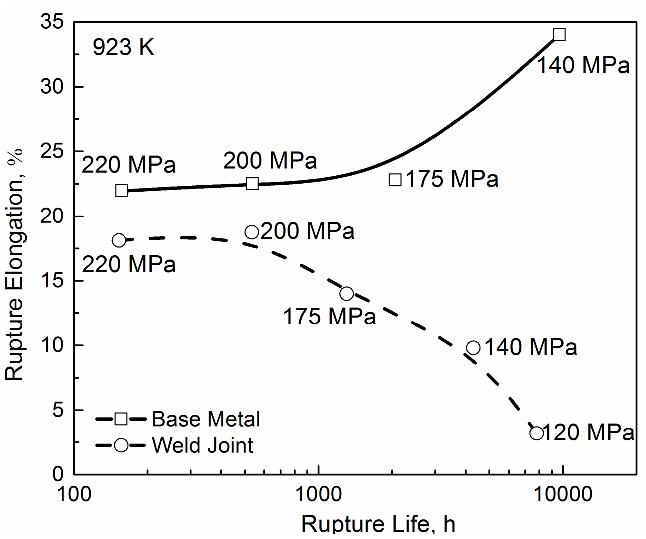

Figure 4.9 Variation of rupture elongation with rupture life.

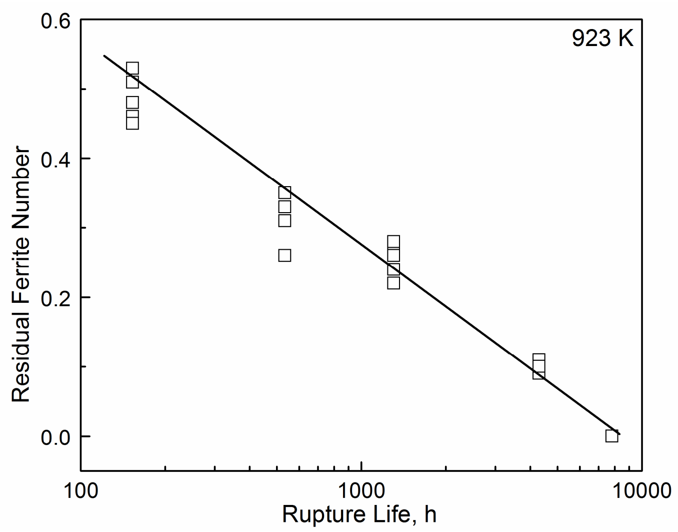

Figure 4.10 Variation of residual delta-ferrite with rupture life.

The percentage reduction in area plotted against rupture life is shown in Figure 4.11. The percentage area reduction measured at the failure vicinity is a better measure of ductility in weld joints as it quantifies the localised deformation characteristics. The elongation measurements take into consideration the deformation characteristics of the base metal region of the weld joint also. Since necking was less significant in the weld joint, the values of percentage area reduction was lower than that of the base metal under the same testing condidtions. The presence of ‘as-cast hardened microstructure’ containing higher dislocation density in the fusion zone region resists necking and consequently its values are significantly lower. As observed in case of percentage elongation values, the percentage reduction in area for the weld joints reduced even further with rupture life due to the low ductility failure associated with creep cavitation which is discussed in detail in the following section. The trend in the plot of percentage area reduction is similar to that of the elongation plot. The difference however, lies in the values obtained at higher stress levels. Since the area reduction was calculated from the location very near the failure tip, these values was considerably lower than the elongation values.

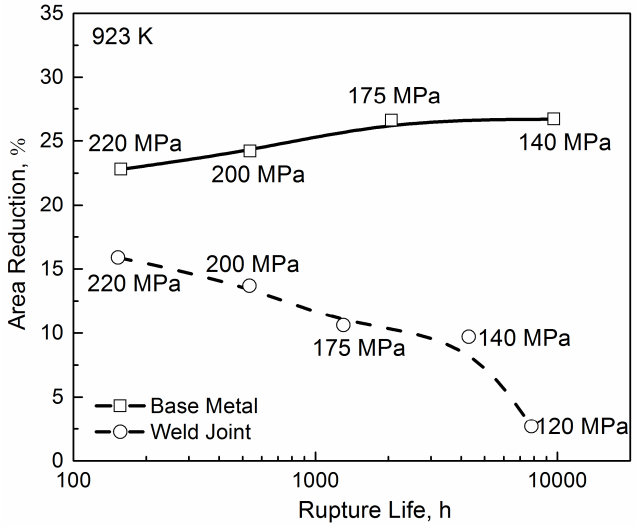

Figure 4.11 Variation of percentage area reduction with rupture life.

The three main causes of failure after the onset of tertiary creep have already been reviewed in Chapter 2; they are 1) mechanical instability caused by necking, b) microstructural instability resulting due to the phenomena like second phase particle coarsening and c) formation of linkage of cavities. While in the base metal failure grossly occurs by excessive necking, for the weld joint the formation of cavities in the fusion zone is the primary cause for failure.

4.5 Microstructural evolution during creep

Microstructure of the weld joint tested at 175 MPa showed intragranular cracking in the vermicular regions adjoining the weld pass interface (Figure 4.12) whereas regions with globular morphology did not exhibit any cracking. The micrograph clearly indicates that vermicular region is more susceptible to creep cavitation. For the weld joint tested at 225 MPa, damage caused by creep cavitation in the fusion zone was not significant. This is because exposure to elevated temperatures is for shorter durations in this weld joint, which circumvents the domination of 'time dependent' creep cavitation process. The reason causing preferential creep cavitation for the weld joints subjected to relatively lower stress levels is explained in the following section.

4.5.1 Evolution of creep damage during creep testing

The creep damage evolves in the fusion zone in two distinct stages. First is the transformation of delta ferrite in to brittle intermetallic phases and secondly the nucleation and propagation of creep cavities formed along the intermetallic/matrix interface.

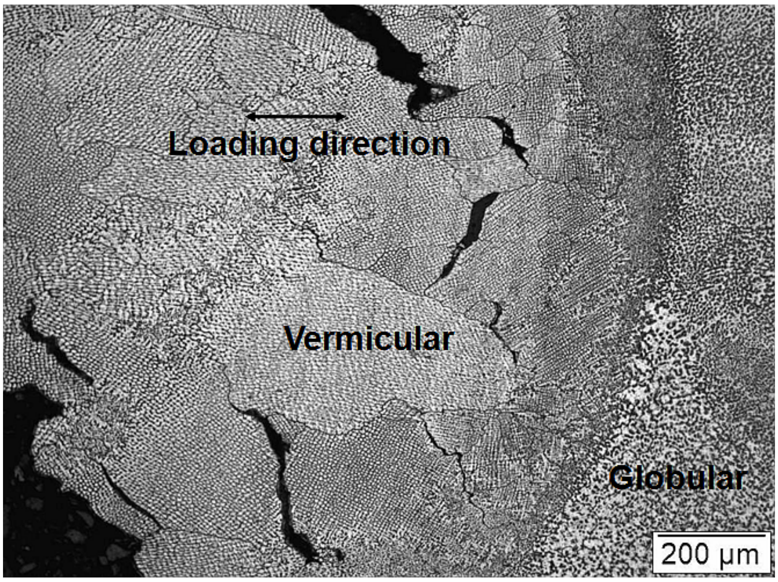

Figure 4.12 Intergranular cracking occurring preferentially in the vermicular region for the weld joint tested at 175 MPa.

Stage 1 : Elevated temperature transformation of delta-ferrite has been widely studied in austenitic stainless steel welds [69] and has been presented in Chapter 2. However, a brief summary is given in this section for systematic understanding with relevance to the current investigation. The transformation commences with the formation of continuous beads of $M_{23}C_6$ at the austenite/delta-ferrite interface. On prolonged exposure, the formation of carbides results in reduction of ferrite stabilizing elements in the austenite region especially adjoining the austenite/delta-ferrite interface; this causes the delta ferrite to shrink in size. On further exposure, ferrite stabilizing elements like Cr and Mo diffuse into delta ferrite. The diffusion of these elements is also aided by dissolution of Cr rich $M_{23}C_6$ precipitates which are abundantly available adjacent to the austenite/delta-ferrite interface. At a certain stage, the amount of ferrite forming elements in the delta ferrite is sufficient for the precipitation of intermetallic phases such as σ, χ and η. Further exposure leads to coarsening of these precipitated intermetallic phases. During creep exposure, precipitation of these phases is enhanced than in thermal aging due to the stress induced diffusion of the elements [70,71].

In light of the above discussion it is clear that the essential factor for the precipitation of intermetallic phases is the diffusion of Cr and Mo [108]. A continuous network of delta-ferrite results in higher delta-ferrite/austenite interface boundaries which results in easier diffusion of these elements. As a consequence, the continuous morphology act as better nucleation sites for intermetallics. In the present investigation, the globular morphology consisted of isolated delta-ferrite which lowers interface boundaries. Thus the transformation of delta-ferrite into carbides and intermetallics is delayed in regions where delta ferrite exhibited globular morphology. Figure 4.13 shows the variations of contents of Cr and Mo in the transformed intermetallic phases with increase in creep exposure, estimated by EDS attached with SEM, in both the globular and vermicular region of the fusion zone. It can be clearly seen that the enrichment of Cr and Mo in the intermetallics phases was higher in the vermicular regions when compared to the globular regions. Hence, it can be ascertained that the transformation of delta-ferrite into carbides and intermetallics could readily occur in the vermicular region than that in globular region. Dissolution of delta ferrite into austenite is also possible during subsequent weld pass deposition and this can reduce the delta ferrite content in the globular ferrite region as mentioned earlier. Since, the variation in delta ferrite content in the vermicular (~5 FN) and globular ferrite (~3 FN) regions was quite low the influence of variations in initial delta ferrite content on creep cavitation is negligible for the weld joints under current investigation.

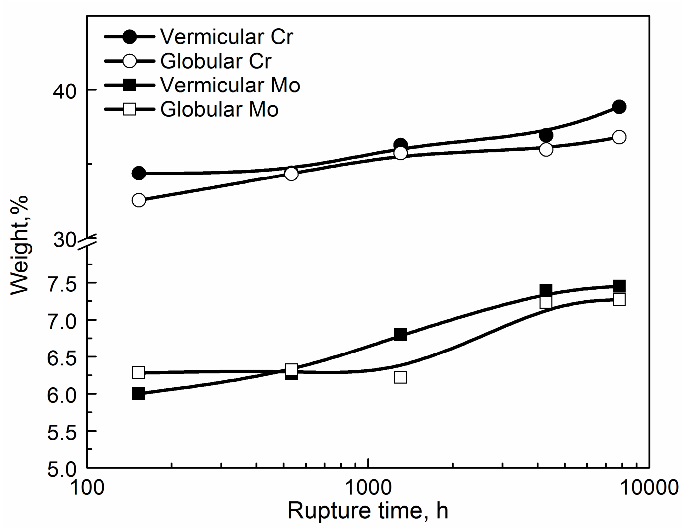

Figure 4.13 Variation of Cr and Mo content in transformed regions with rupture life.

Stage 2: Damage during creep of stainless steel welds as a result of the transformed intermetallics has been reviewed by many researchers. A sequence for damage evolution which has been given by Senior [71] is elaborated in more detail below with the knowledge about the underlying creep cavitation phenomenon [21].

1. Nucleation of cavities- There can be two possible mechanisms for cavity nucleation in austenitic steel weld metals.

(a) *The strength mismatch between the austenite and prior ferrite transformation products*- while the austenite undergoes plastic deformation, the harder precipitates deform elastically under the influence of an external stress. After a critical strain accumulation, cavitation occurs at the interface [109] of the austenite and transformed intermetallics on rupturing the bond.

(b) *Obstruction of grain boundary sliding by the precipitated intermetallics*- since the facet length of the austenitic grains is higher due to the larger grain size in the fusion zone, significant sliding can occur. This sliding when obstructed by transformed intermetallics can cause stress concentration resulting in creep cavitation.

2. Propagation of cavities-If the morphology of the delta ferrite is more continuous, the crack propagation is enhanced. In situations where the morphology is discontinuous, the crack is arrested at the austenite matrix. Greater stress gradients are required for further propagation of the cracks. For the weld joint under the current investigation the orientation of the majority of the cracks to the loading axis was around 45-60° (Figure 4.12) indicating that the applied stress is the main driving mechanisms for failure [30]. The influence of the two types of microstructural inhomogeneities on the creep damage sequence is presented below.

4.5.2 Influence of morphological changes of delta ferrite

Since vermicular morphology is continuous, transformation of delta ferrite into intermetallics is more favourable in this region, when compared to the region containing globular morphology. As a consequence, during creep exposure the vermicular morphology serves as preferred nucleation site for cavities. It has been already shown by Thomas [90] that a more continous delta ferrite morphology results in significant creep cavitation during creep exposure.

Propagation of cavities is also dependent on the morphology of the prior ferrite transformed phases. Vitek and David [82], in their investigation on 308 stainless steel welds have shown that even though the precipitation of sigma phase is enhanced due to titanium addition, its distribution was more isolated and homogenous. This was in contrast to the more continuous sigma ferrite morphology which evolved in the fusion metal containing less titanium. It was shown by them that the continuous morphology was more detrimental and resulted in lower creep rupture life. Thus the propagation of cavities would occur more readily in the vermicular region. Cavity growth occurs as a consequence of deformation caused by diffusion or plastic flow.

4.5.3 Influence of dislocation substructural variations

The hardened region in the previous pass sets up a strength gradient across the weld pass interface, which during creep results in steep stress gradients. The resultant gradients across the interface causes stress redistribution in the comparatively softer vermicular region. Hence it can be concluded that changes in dislocation substructure provides the driving force for nucleation of cavities. The hardened region also resists the propagation of creep cavities thereby delaying failure. The realtive contribution of the two microstructural inhomogeneities to creep damage is summarised in Table 4.2.

Table 4.2. Contribution of the two types of microstructural inhomogenities on the cavitation behaviour of weld joints.

Various stages during creep cavitation	**Microstructural inhomogeneity caused by morphological changes**	**Microstructural inhomogeneity caused by dislocation sub-structural changes**
Preferential precipitation of intermetallics in one side of the weld pass interface	**Contributing factor** Due to the more continuous morphology precipitation of intermetallics occur readily in the vermicular morphology	**Not a contributing factor**
Nucleation of cavities under the influence of external stress	**Contributing factor** Since the precipitation of intermetallics occurs faster in vermicular region, creep cavities are likely to get nucleated in this region.	**Contributing factor** The preferential plastic deformation of the softer vermicular region results in cavity nucleation caused by stress concentration at the matrix/intermetallics interface
Propagation of creep cavities	**Contributing factor** A vermicular morphology of delta ferrite results in a continuous morphology of transformed intermetallics making cavity propagation easier	**Not a contributing factor**
Arrest of creep cavities	**Not a contributing factor**	**Contributing factor** The strengthened region in the previous pass is more resistant to crack propagation hence these cavities are arrested at the interface.

Both these microstructural modifications complement each other and are responsible for the resultant preferential creep damage in one side of the weld pass interface. It can be inferred from the Table 4.2 that each of the stages associated with the nucleation and growth of cavities is primarily dependent on the applied stress. With the decrease in the applied stress, the failure caused by the creep cavitation is postponed to longer durations.

4.5.4 Dislocation substructural changes on creep exposure

The evolution of dislocation substructure in the fusion zone has been studied in detail for one short term test (applied stress 175 MPa, rupture life 1300 hours) and one long term test (applied stress 120 MPa, rupture life 7820 hours).

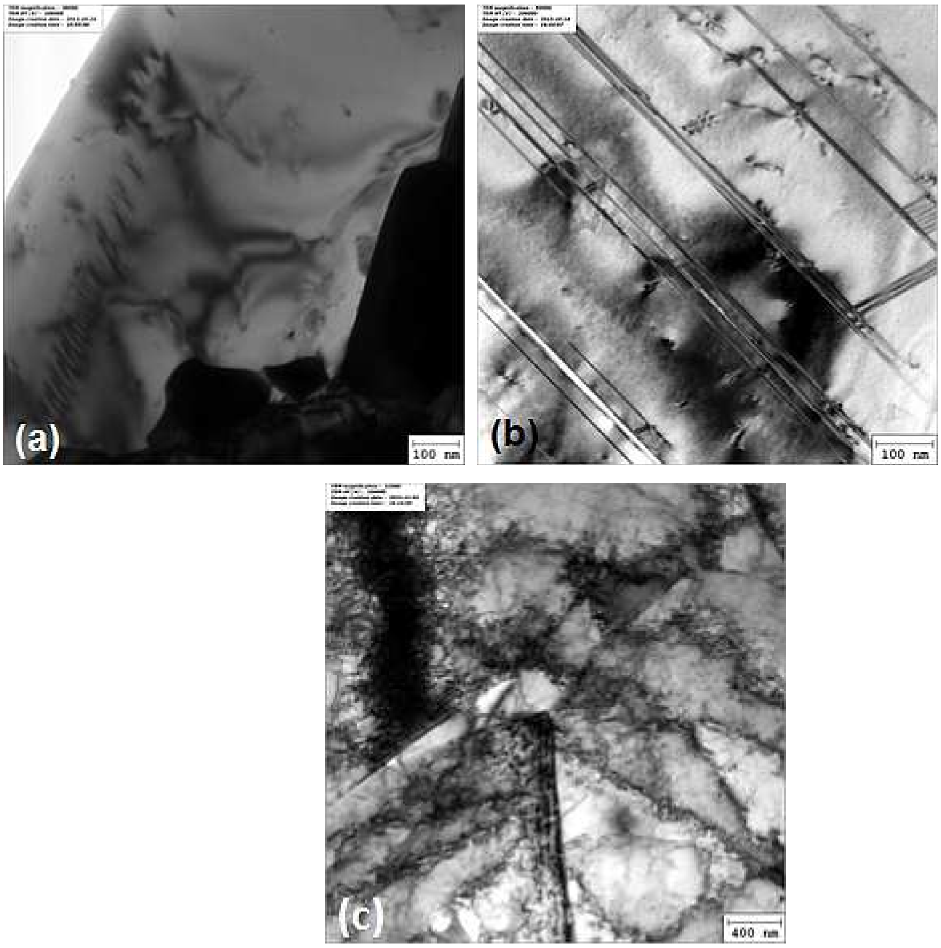

Figure 4.14 (a) Dislocation pile up, (b) slip bands in vermicular region and (c) subgrain formation in globular region after creep testing at 175 MPa.

The weld joint tested at 175 MPa showed dislocation pile ups and slip bands in the vermicular region (Figures 4.14(a&b)). However in the globular region, the onset of subgrain formation could be seen (Figure 4.14(c)). Figure 4.15 (a) shows the dislocation substructure in the vermicular region of the weld joint tested at 120 MPa.

The cell structure which is a characteristic feature occurring due to the onset of recovery is clearly visible along with coarsened intermetallics. EDS spectra on these intermetallics revealed that they were Fe-Cr-Mo and Mo-Fe rich suggesting that they could be σ and η respectively (Figure 4.16). The TEM micrograph taken in the globular region also showed intermetallics and subgrains (Figure 4.15 (b)). However, the dislocation distribution inside the subgrains was higher in this region when compared to those in the vermicular region.

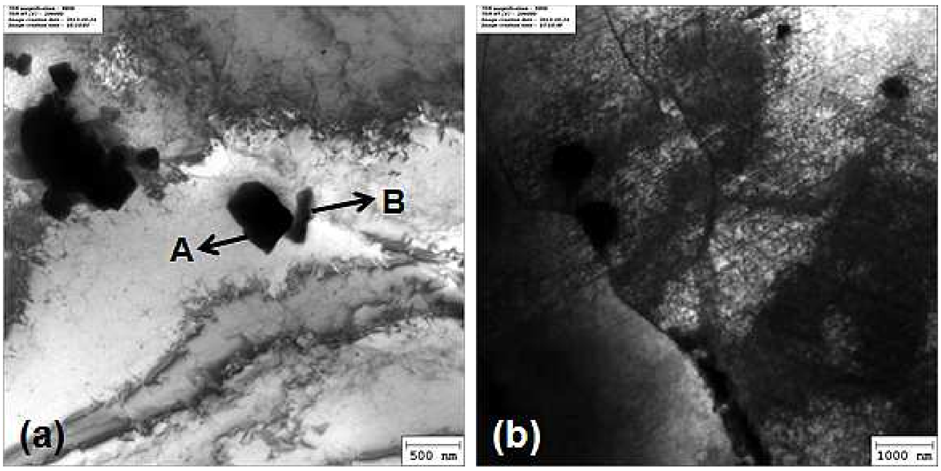

Figure 4.15 TEM micrographs of weld joint tested at 120 MPa (rupture life 7820 hours) (a) vermicular region consisting subgrains and precipitate A with Fe-Cr-Mo and B with Fe-Mo enrichment (b) globular region showing the possible onset of formation of subgrains.

The evolution of dislocation substructure during creep of austenitic steel welds is well documented [110, 85]. At high stress levels, for a microstructure containing relatively lower dislocation density similar to what was observed in the vermicular region in the current investigation- planar slip is the principal deformation mechanism and the matrix resistance to plastic deformation is quite low. In a cold worked structure with higher dislocation density such as the one observed in the globular region, subgrains form which is the signature of recovery during creep deformation. Keown [68] has shown that the kinetics of subgrain formation in fusion zones containing delta ferrite is faster when compared to the fully austenitic stainless steel welds. This is because when solidification occurs in the fusion zone, partitioning of ferrite and austenite stabilizing elements occur in the austenite and ferrite phase. This leaves more nickel in the austenite phase. Nickel increases the stacking fault energy and this causes cross slips to occur readily resulting in the formation of subgrains [68].

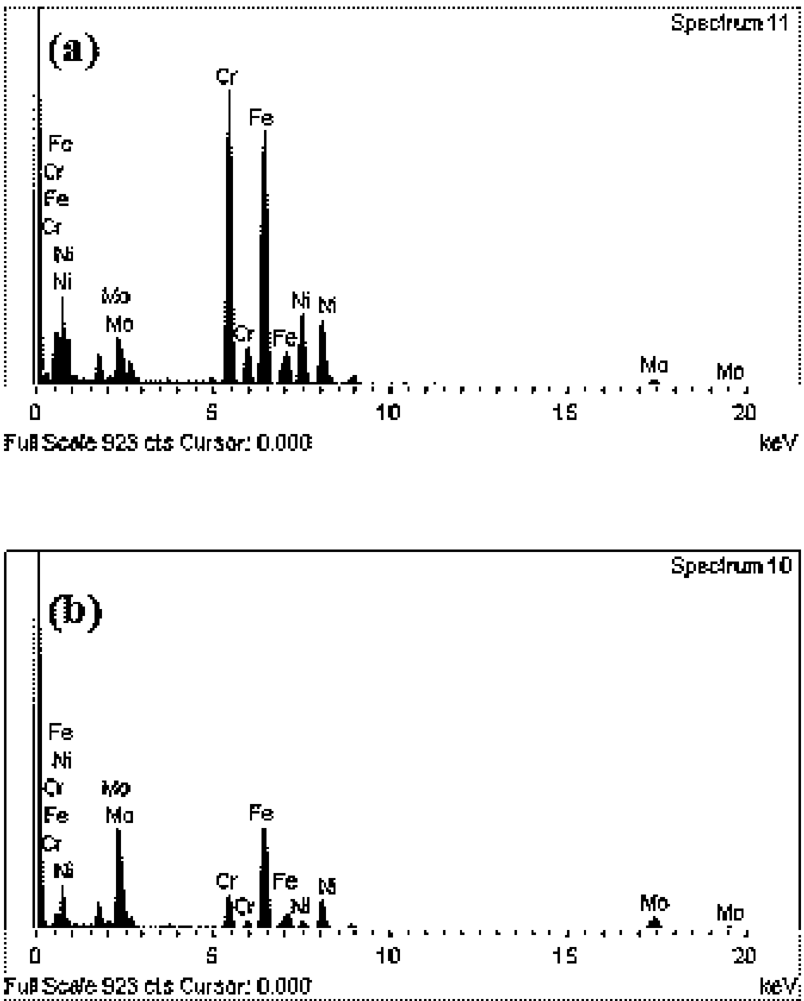

Figure 4.16 EDS spectra of (a) precipitate A and (b) precipitate B.

Although prolonged creep exposures (creep exposure at lower stress levels) produced subgrains in the in both vermicular and globular regions, there were some remnant dislocations within the subgrains of globular regions. This suggests that the formation of subgrains is not complete in this region. The intermetallics in this region do not influence the substructural changes as they are considerably coarse [110]. In the vermicular regions the initial dislocations density was less when compared to a more tangled dislocation structure in the globular region. The applied stress in this case was not high enough for recovery mechanisms such as dislocation climb to operate; hence formation of sub-grains was delayed in the globular region. From the above discussions it is clear that the only significant influence of dislocation substructural change on creep damage is the generation of dislocation pile up and slips bands which could have possibly enhanced the nucleation of cavities at higher stress levels in the vermicular region [22, 23]. After the onset of cavitation, there would be no significant influence of substructural changes in dislocations such as recovery on creep damage. Though there were signatures of recovery, they could not proceed further to form stable subgrains. This is because recovery is caused by diffusion enabled dislocation climb which is a time dependent process. After onset of cavitation in the fusion zone, damage proceeds rapidly, limiting the operations of other deformation assisted mechanisms.

It should be noted that significant segregation can occur in the fusion zone duing the solidification process. The seggregations can also influence the caviation behaviour. However, the observed cavities were confined to the near weld pass interface region suggesting that the influence of morhological changes and evolution of the thermo-mechnically treated zone are the most dominating factors influening the caviation phenomenon.

4.6 Fractographic analysis

Fractographic analysis of failed specimens can enhance understanding of the damage mechanisms during creep testing. Figures 4.17 and 4.18 show the fractographs of weld joints tested at 175 and 120 MPa, respectively. Since both the joints failed in the fusion zone the dendritic facets were visible in both the fractographs. It could be seen from these figures that both the fractographs contained features relating to both brittle and ductile failures. However, the extent to which these features were observed varied with applied stress and rupture life. The presence of ductile features denotes the region where the final failure had occurred, this is a result of a possible ‘overload’ caused by reduction in cross sectional area due to formation and interlinked cavities. The fracture surface of the weld joint tested at 120 MPa contained comparatively more regions exhibiting interdendritic mode of failure (Figure 4.18). On the contrary, the extent of ductile region was more in the weld joint tested at 175 MPa.

As discussed earlier the failure in weld joints is caused predominantly by the nucleation and propagation of cavities. At a stress level of 175 MPa, the creep cracks originated at the interface between the transformed intermetallics and austenite. But these cavities were arrested at the weld pass interface due to the resistance of the hardened globular region. The cracks which propagated in the vermicular region were intergranular in nature. After significant number of cracks had nucleated and propagated in the vermicular region, there is a reduction in the load bearing cross sectional area. This resulted in final ductile failure of the globular ferrite regions. In case of the weld joint tested at 175 MPa, the extent of ductile features was higher when compared to the joint tested at 120 MPa as the applied stress was high enough to cause failure before there was significant reduction in load bearing cross sectional area caused by intergranular cracking.

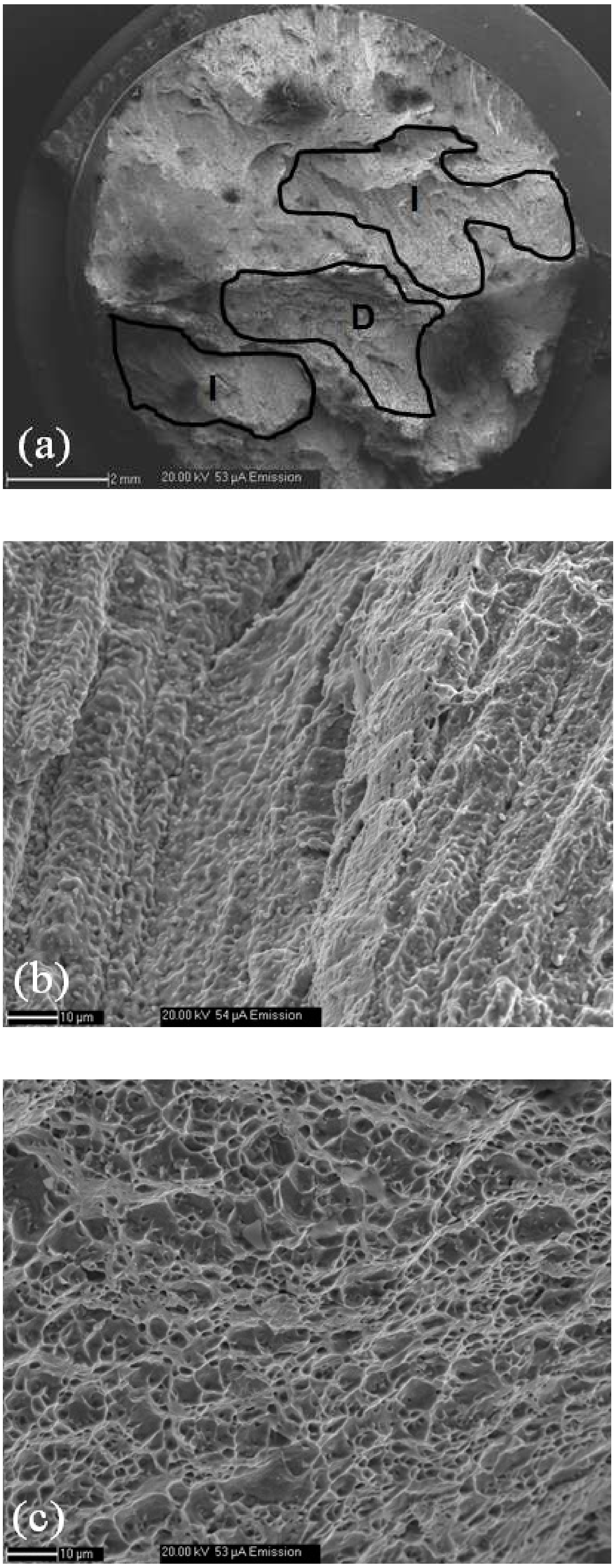

Figure 4.17 (a) Fractograph of weld joint tested at 175 MPa, (b) region *I* showing interdendritic failure and (c) region *D* showing ductile failure.

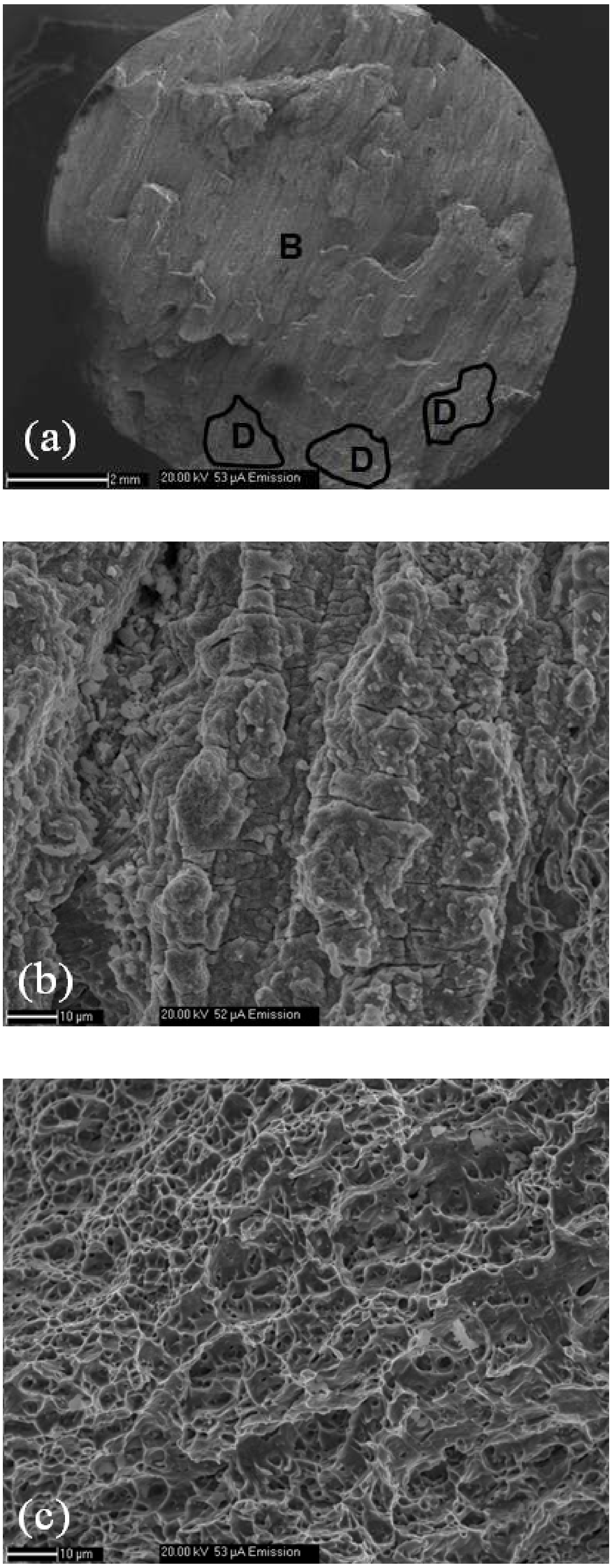

Figure 4.18 (a) Fractograph of weld joint tested at 120 MPa, (b) region *B* showing cracks in brittle transformed intermetallics and (c) region *D* showing ductile failure.

Therefore, failure in the sample tested at 175 MPa occurred even without significant intergranular propagation of the cracks. At the stress level of 120 MPa, the time was sufficient for transformation to occur in both the vermicular and globular regions, hence the extent of ductile features in this weld joint was lower.

4.7 Conclusions and motivation for further work

Multi-pass welding generates two types of microstructural inhomogeneities: one is brought about by change in delta ferrite morphology and the other by change is dislocation substructure. Both these changes are the result of the thermal cycle generated during deposition of a new pass. These microstructural changes play a synergistic role in dictating the creep cavitation and propagation. The globular ferrite region was more resistant to creep cavitation and had a major influence in arresting the propagation of cracks.

From the detailed analysis in this chapter, the following conclusion can be made. The microstructure of the weld joint can be enhanced by a) creating regions in the fusion metal which are more resistant to creep damage and b) delaying the propagation of damage induced by creep cavitation. The next two chapters demonstrate the use of these two methodologies to enhance the creep life of the joints.

CHAPTER 5

ASSESSMENT OF

THERMO-MECHANICAL EFFECT

ON CREEP RUPTURE PROPERTIES

Chapter 5

Assessment of Thermo-mechanical Effect on Creep Rupture Properties

5.1 Introduction

In the previous chapter it has been demonstrated how the two types of microstructural features viz. morphological changes in delta ferrite and 'thermo-mechanical effect', which evolved due to multi-pass welding, influences the creep rupture properties of the weld joint. It will be interesting to assess the influence of 'thermo-mechanical effect' alone, by minimising the effects of morphological change in the fusion zone. With this perspective, the creep deformation and rupture behaviour of single-pass and dual-pass 316LN SS weld joints fabricated by activated tungsten inert gas welding (A-TIG) process has been assessed in this chapter. The A-TIG welding is an autogenous process, where the ferrite content in the fusion zone is minimum as it is dictated by the ferrite potential of the 316LN base metal only. The A-TIG is a welding process where high weld penetration can be achieved and weld joints of thicker cross sections could be fabricated in a single pass. The fusion zone in this case is devoid of any further microstructural modifications as no subsequent weld passes are laid. Creep rupture properties of the weld joints made with an additional pass was studied to clearly understand how the subsequent thermal cycle induced microstructural gradient across the fusion zone. The effect of creep cavitation as a result of the microstructural modification in the fusion zone of the dual-pass weld joint is discussed in detail. Since the width of the individual regions in the high heat input A-TIG weld joint were considerably higher when compared to those observed in the SMA weld joint (Chapter 4), miniature specimen technique could be used to characterize the creep behaviour of each of these regions. The localised deformation behaviour which was obtained from miniature specimen technique has been augmented well with the microstructural findings and has helped to demarcate the variations in cavitation behaviour of the single and dual-pass A-TIG weld joints.

5.2 A-TIG welding process

For fabricating thicker sections, several weld passes are required to complete the weld joint. Depending upon the welding process, intricate edge preparation techniques is also essential. Deposition of weld metal by subsequent passes in a multi-pass weld joint introduces more inhomogeneity in the fusion zone microstructure, which can influence the performance of the weld joints at higher temperatures during service. Furthermore, reducing the number of passes increases the productivity and decreases the cost for joint preparation. With this perspective a number of high energy density welding processes like electron beam, laser beam and A-TIG have been developed. Amongst these, A-TIG welding holds a definitive edge in the sense that it can be very easily augmented to the existing conventional systems and does not require stringent edge preparation. Other details of A-TIG joint fabrication are presented in Chapter 3. This process has been successively demonstrated for welding of 316LN SS [111]. Weld joints produced by this process have showed lower distortions and enhanced creep rupture life. The presence of lower amount of delta ferrite, which is unstable at higher temperatures, in the A-TIG weld joint has been considered as the main reason for enhanced creep strength of the A-TIG joint over the conventional TIG joints [76].

5.3 Fabrication of single and dual-pass A-TIG joints

Single-pass joint was prepared by joining plates of 10 mm thickness with one pass. For analyzing the creep behavior due to the deposition of the second pass, a weld pad was fabricated with a dual-pass technique. Reduction of the heat input decreased the arc penetration, hence an additional pass was required to complete the weld joint of plates with similar thickness (10 mm). The second pass in the dual-pass joint was laid by inverting the plate consequent to the deposition of the first pass. The second pass in the dual-pass joint was deposited in such a way that there was an overlap, which was not extensive between the first and the second passes. The welding parameters used for fabrication of both the weld joints are given in Table 5.1.

Table 5.1 Welding Parameters

Process	Single-Pass	Dual-Pass
Current (A)	300	200
Voltage (V)	15.5	13.5
Travel speed (mm/min)	60	80
Heat input (kJ/mm)	4.65	2.03(each pass)
Interpass temperature		423 K (150 °C)

5.3.1 Initial microstructure

The initial microstructure of the fusion zone of the single-pass weld joint consisted of columnar grain region adjacent to the base metal and equiaxed grain in the central part of the fusion zone (Figure 5.1(a)). In the creep specimen extracted from the single-pass weld joint, the columnar grains were parallel to the loading direction. The columnar to equiaxed transition during fusion zone solidification is reported to be promoted by high welding speed and higher alloying contents [112]. The presence of the central equiaxed grain improves ductility of the joint and prevents centerline hot cracking during welding.

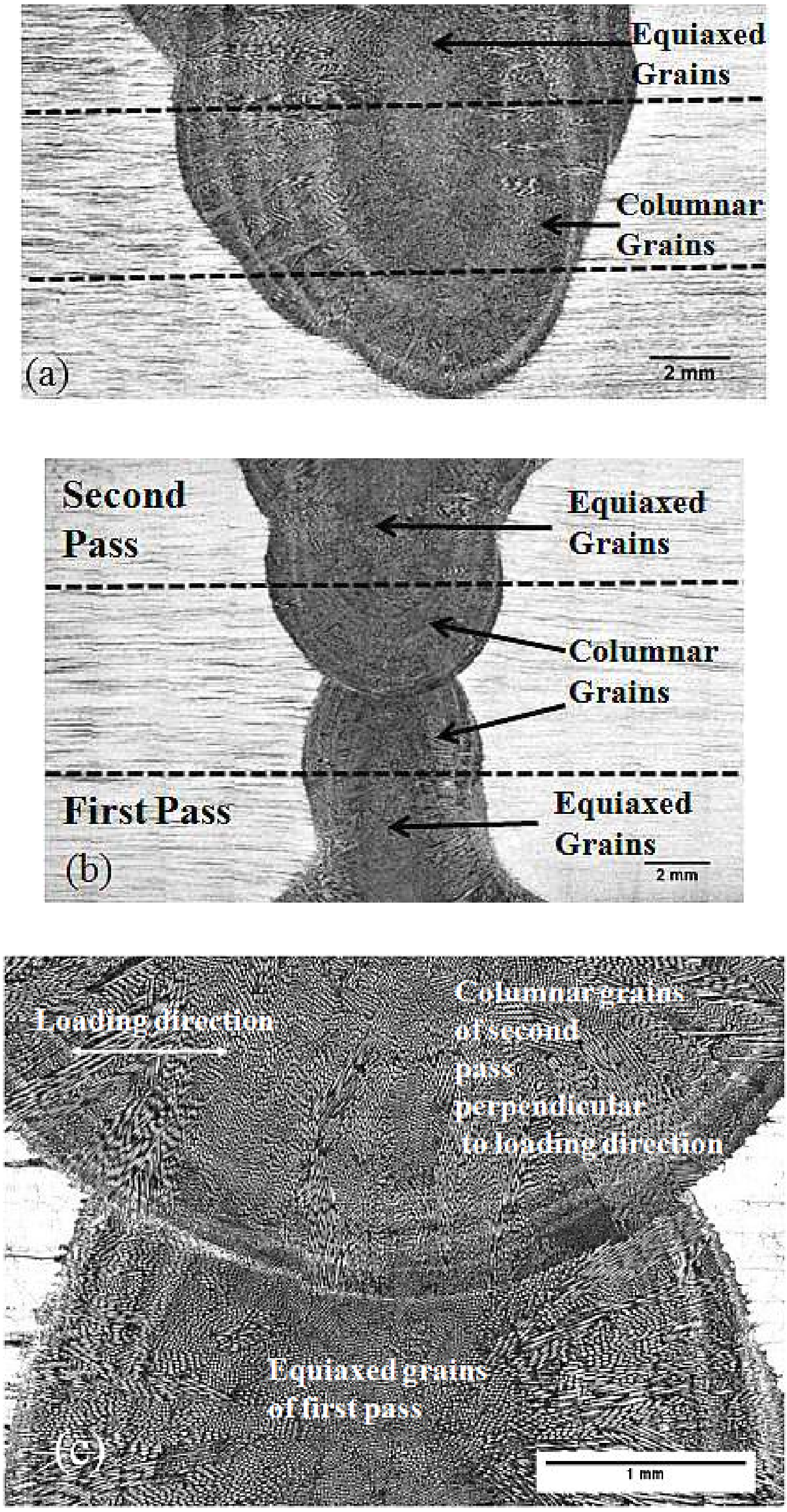

Figure 5.1 Macrostructure of (a) single-pass weld joint (b) dual-pass weld joint. The region from where the creep specimens were extracted are shown. The region of the dual-pass weld joint showing the overlap between the passes (c).

The fusion zone of dual-pass weld joint also consisted of columnar and equiaxed regions but the width of these regions was much lower than those of the single-pass joint (Figure 5.1(b)). A small overlap in the fusion zone of the two weld passes was ensured to induce significant microstructural modification in the first pass. Columnar grains in the central region of the fusion zone of the second pass nucleated from the equiaxed grains of the first pass. As a consequence, in the dual-pass weld joint specimen these columnar grains were almost perpendicular to the loading direction (Figure 5.1(c)). The size of the cells in the equiaxed region of the dual-pass weld joint was smaller than that of the size of the cells in the single-pass zone as these joints were fabricated with comparatively higher welding speed and lower heat input [113]. The lower heat input and higher travel speed in the A-TIG weld results in negligible delta ferrite content in the fusion zone. The delta ferrite content in the dual-pass weld joint was around 0.04 FN as against around 0.24 FN in single-pass weld joint. Despite of lower delta ferrite content, A-TIG weld joints are not prone to hot cracking. This is because the A-TIG process is an autogenous process requiring no additional filler material. Hence, there is no possibility of inducing elements like P, S and Si into the weld pool, which promote hot cracking during welding. Another possible cause for enhanced hot cracking resistance is the lower residual stress in the ATIG joints when compared to conventional welding processes. The reduction of restraint in these weld joints is a result of higher width to depth ratio [114].

Figures 5.2(a,b,c and d) show the distribution of delta ferrite in various regions of the fusion zone of both the weld joints. The delta ferrite could be seen on the grain boundaries of the columnar and equiaxed grain for both the weld joints. It could also be noticed that the amount of delta ferrite in the equiaxed region was higher than in the columnar zone. This is because the equiaxed region is the final region to solidify and excessive segregation of ferrite stabilizing elements occurs in this region promoting the formation of delta ferrite [54]. The delta ferrite content was much lower in this study than what was observed in the multi-pass joint discussed in chapter 4. This helped to delineate the influence of morphological changes in delta ferrite on the creep rupture behavior of the joint.

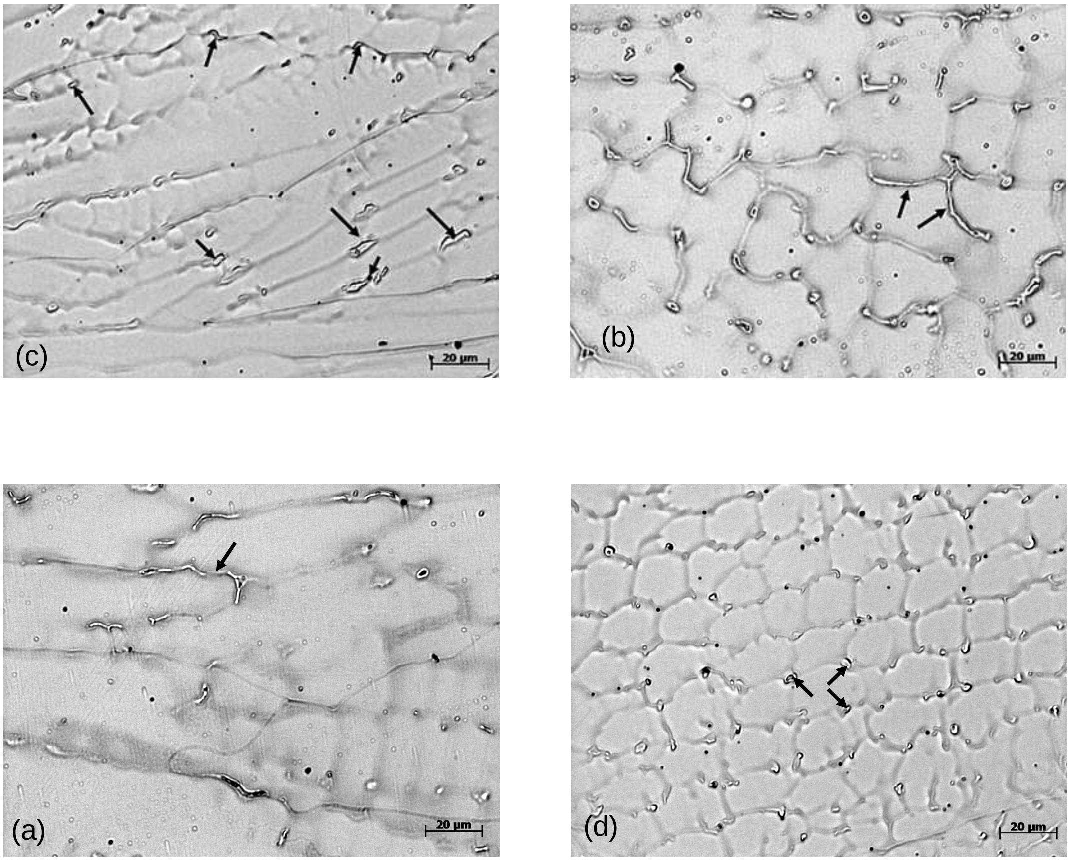

Figure 5.2 Optical micrographs showing delta ferrite distribution in (a) columnar region and (b) equiaxed region of single-pass weld joint (c) columnar region and (d) equiaxed region of dual-pass weld joint. The arrows indicate delta ferrite phase.

Due to the increased heat input, there was significant coarsening of the grains in the HAZ region of A-TIG joint when compared to that of the SMA weld joints [115]. The average size of the grains in the HAZ region in the both the A-TIG weld joint was around 200 µm (base metal grain size-85 µm) (Figure 5.3). But the width of the coarse grained HAZ region of the single-pass weld joint was higher than that of the dual-pass weld joint. The width of the HAZ region can be linked to the volume of fusion zone. The volume fraction of the fusion zone with respect to the base metal within the gauge length of the creep specimen was around 18% and 10% for the single-pass and dual-pass joints respectively. In order to get a complete penetration of the arc in the single-pass weld joint a higher heat input was used, this resulted in excessive dissolution of the base metal when compared to the dual-pass weld joint resulting in a higher volume fraction of fusion zone and a wider HAZ.

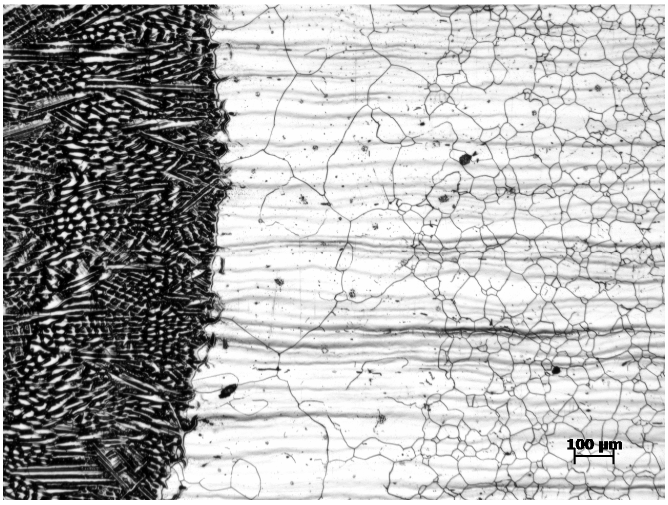

Figure 5.3 Microstructure in HAZ region of the single-pass weld joint showing significant grain coarsening.

5.3.2 Hardness evaluation

Hardness profiles of single–pass and dual-pass weld joints are shown in Figures (5.4(a) and (b)) respectively. The equiaxed region of the fusion zone possessed lower hardness in the single-pass weld joint followed by the HAZ region. Higher hardness in the columnar zone was due to the directional solidification (Figures 5.1 and 5.2). The equiaxed region has random orientation of grains, which enables easier plastic deformation which resulted in lower hardness. It has been reported that the presence of a softer equiaxed zone enhances the ductility of the weld joints [116,117].

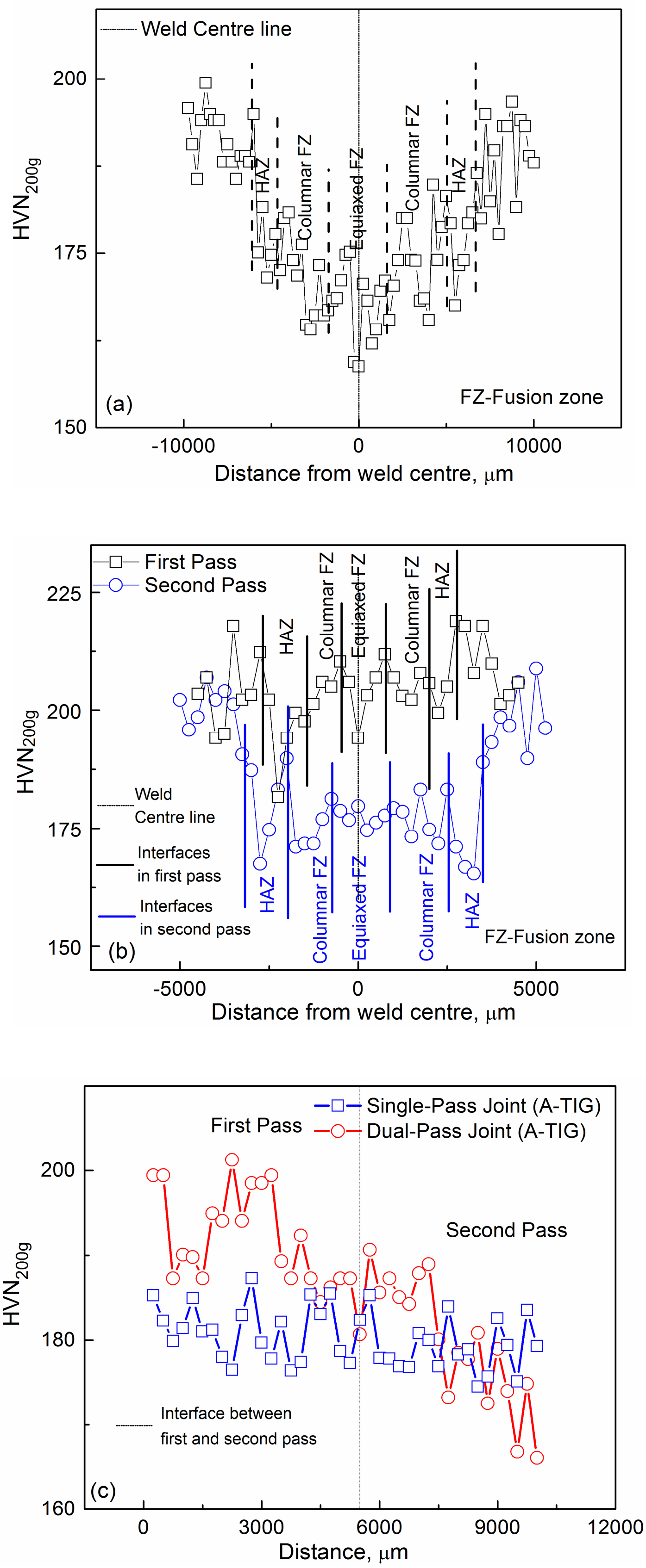

Figure 5.4 Hardness profile of (a) single-pass b) dual-pass and c) along weld centre line of both the joints.

The lower hardness in the HAZ was due to the pronounced grain coarsening which was observed in this region. This is in contrast to the hardness profile of SMAW 316LN SS weld joints (Figure 4.4), where the HAZ possessed higher hardness. Due to excessive thermal cycling induced by subsequent passes, the HAZ in SMA joint hardened significantly. Both the single-pass and dual-pass weld joints showed almost a similar trend in hardness variation in all the regions of the weld joint. However, the hardness values in the first pass of the dual-pass weld joint was considerably higher than the values obtained in the second-pass region (Figure 5.4(b)), which could be more clearly seen in the hardness profile taken across the transverse direction along the weld centre line (Figure 5.4(c)). There was no significant variation in hardness across the transverse direction along the weld centre line of the single-pass weld joint.

It has been shown that A-TIG weld joints have lower residual stress in the as-welded condition [114] when compared to conventional TIG joints. Therefore, the effect of residual stress during high temperature creep exposure was neglected considering quick relaxation of this stress on creep exposure.

5.3.3 Substructural characterization by TEM

TEM micrographs of the single-pass and the dual-pass weld joints taken from the specimens extracted from the different regions from the fusion zone are shown in Figures 5.5 (a, b, c and d). There were dislocation pile ups (Figure 5.5(a)) in the columnar region of the single-pass weld joint, suggesting the strain in this region was considerably small [118] when compared to that in dual-pass joint as discussed below. The source of this micro strain is the shrinkage stresses which the fusion zone is subjected to during solidification. The TEM micrograph taken in the equiaxed region showed isolated dislocations (Figure 5.5(b)). The TEM microstructure taken in the columnar region of the first pass of the dual-pass joint showed substructure consisting of dislocation tangles (Figure 5.5 (d)) which was more extensive than what was observed in the second pass (Figure 5.5(c)). This suggested that the dislocation interaction was more significant in the first pass when compared to the second pass.

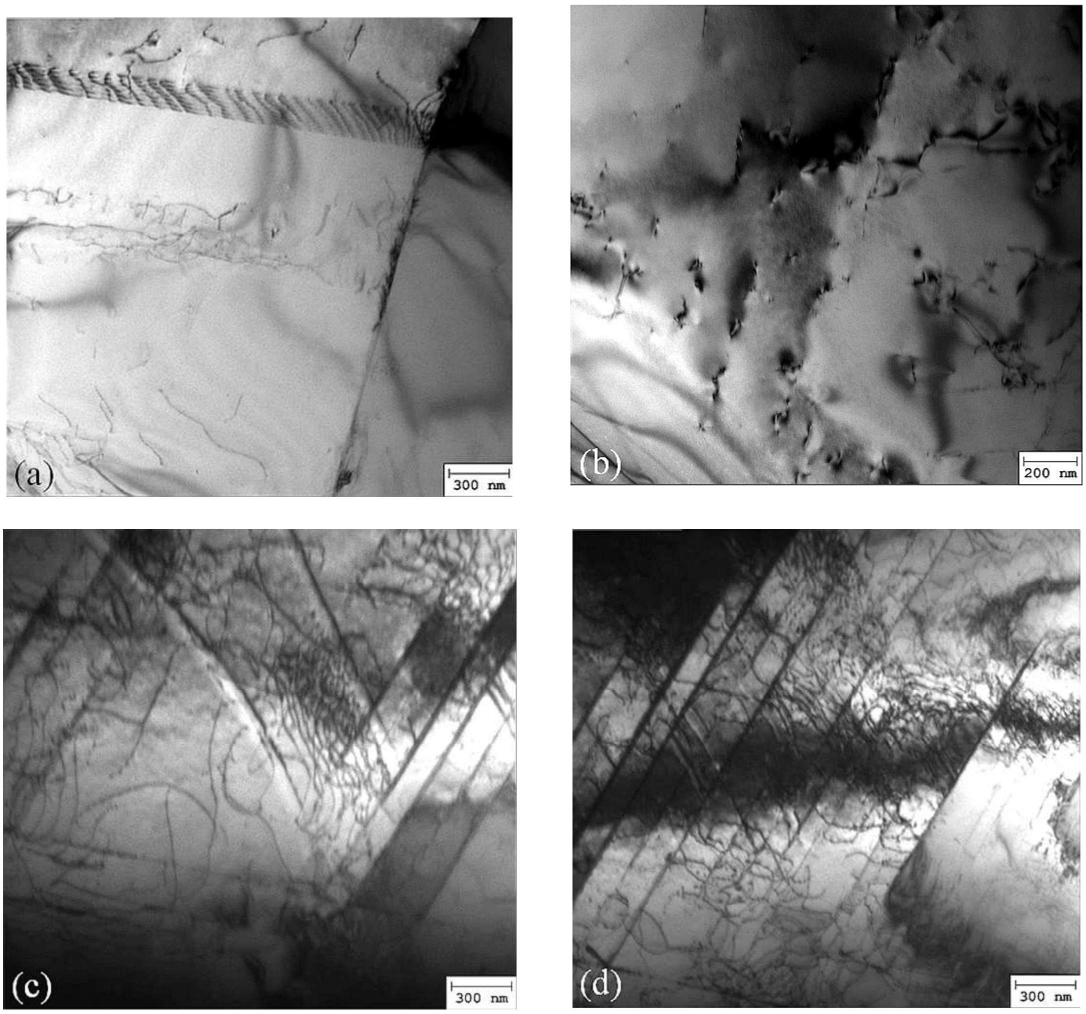

Figure 5.5 TEM micrographs taken from various regions of fusion zone in as welded condition (a) columnar region of single-pass (b) equiaxed region of single-pass weld joint (c) columnar region of second pass and (d) columnar region of first pass of the dual-pass weld joint.

From the microstructural study and hardness profile taken across the transverse direction, the following conclusions can be made with reference to the deposition of the additional weld pass in the fusion zone. Since the delta ferrite content is significantly lower in the A-TIG joint, the associated morphological changes are negligible. The only significant microstructural modification in the fusion region of the first pass of the dual-pass weld joint is the change in dislocation substructure which strengthens this region. The deposition of the second pass and the associated thermal cycling induces a 'thermo-mechanical treatment' which is responsible for strengthening the first pass.

5.4 Creep deformation and rupture properties

Uniaxial creep tests were carried out at 923 K and at stresses of 140, 175, 200 and 225 MPa. The variations in rupture life of the base metal, single-pass and dual-pass A-TIG weld joints with applied stress are shown in Figure 5.6. The rupture life of both the weld joints and base metal decreased steadily with decrease in applied stress level. The rupture lives of both the weld joints were inferior to that of the base metal at all the investigated stress levels. But the life of the dual-pass weld joint was considerably higher than that of the single-pass weld joint. In fact, the lives of the dual-pass joints were almost equivalent to that of the base metal at higher stress levels.

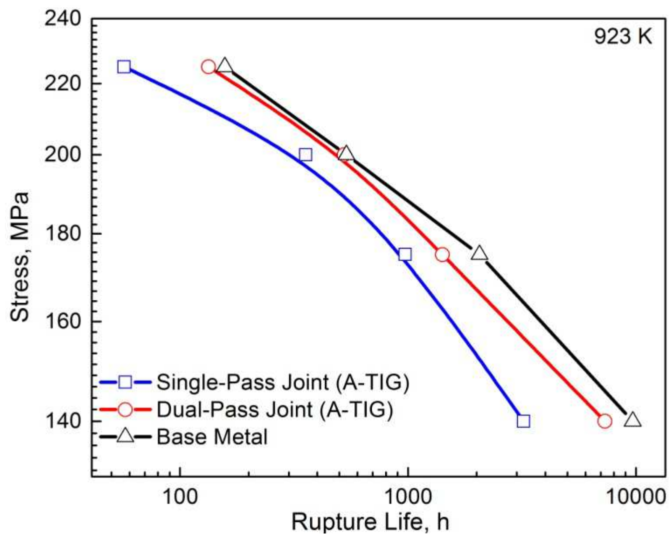

Figure 5.6 Comparison of rupture life variation with applied stress for the single and dual-pass weld joint along with the base metal.

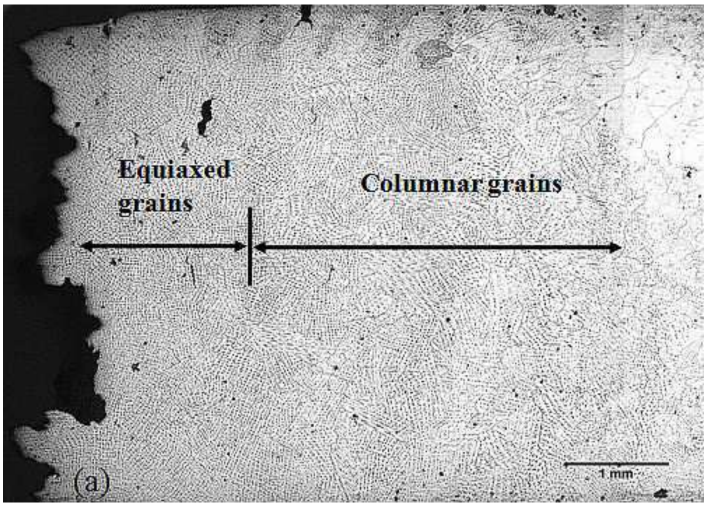

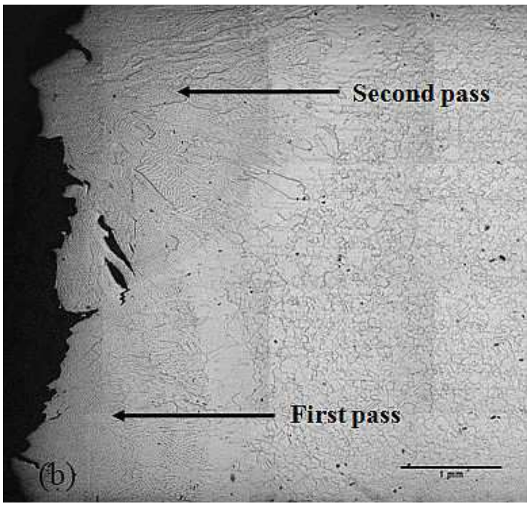

Figure 5.7 Micrographs showing the failure location in (a) single-pass and (b) dual-pass weld joints tested at 923 K at a stress level of 175 MPa.

The failure of both the weld joints occurred in the fusion zone as shown in Figures 5.7 (a and b). The typical creep curves of the base metal, single–pass and dual-pass weld joints tested at 140 MPa are shown in Figure 5.8. The apparent steady state creep rate in both the weld joints were comparable but were substantially lower than that of the base metal. This could be attributed to the presence of the as-cast dendritic microstructure in the fusion zone, which is more resistant to plastic deformation. It has been shown by Monkman and Grant that the rupture life of materials subjected to creep is dependent on the minimum creep rate and varies inversely with respect to one another [32]. But in case of composite materials such as weld joints this relationship is not valid. This suggests that the deformation mechanism linked to the steady state creep rate is not the prime contributing factor in determining the rupture life of the weld joints.

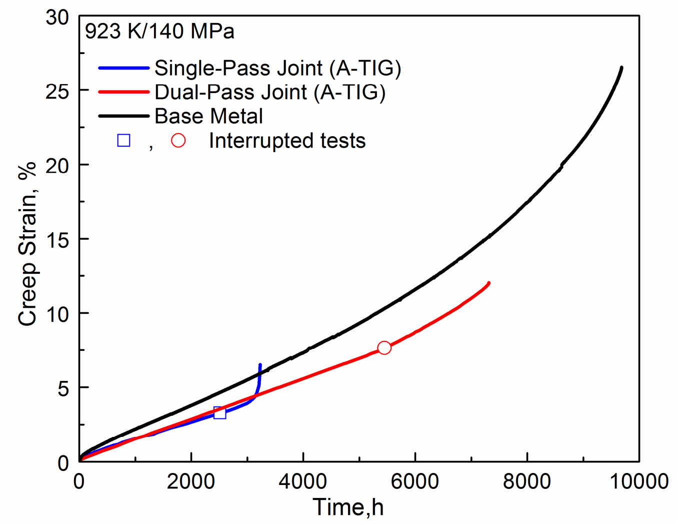

Figure 5.8 Creep curves of the base metal, single-pass and dual-pass weld joints tested at 923 K and applied stress of 140 MPa. The interrupted tests on which TEM examinations were performed are indicated.

5.4.1 Analysis of the creep tested weld joints by TEM

The TEM analysis was carried out on specimens creep tested at 140 MPa interrupted just before the onset of tertiary. For the dual-pass joints, the creep specimens were extracted from the second pass as the volume fraction of the first pass in the creep specimen was not adequate to prepare TEM specimens by dual jet thinning technique. The evolution of dislocation substructure during creep of 316 LN base material has been discussed prior to understanding the substructural evolution in the fusion zone of the weld joints.

As plastic deformation proceeds during creep, the excessive dislocations rearrange themselves to a low angle configuration which is usually in the form of subgrains as shown in the micrograph of the parent base metal, creep tested at 923 K at a stress level of 140 MPa (Figure 5.9 (a)). The formation of sub-grains, which is a signature of the dominating recovery process, has been well documented for grade 316 stainless steel base metals [110].

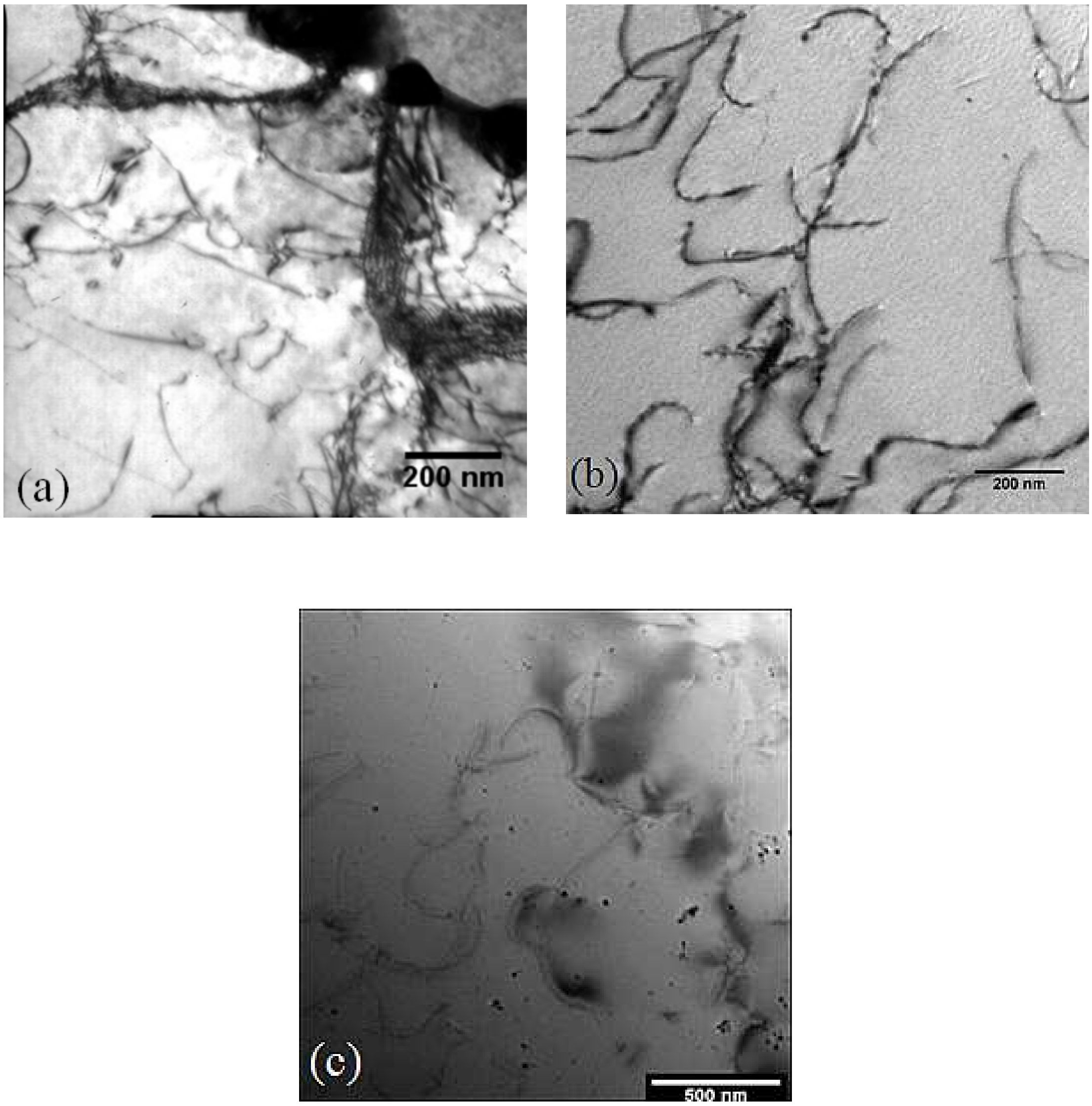

Figure 5.9 TEM micrographs of (a) base material tested up to failure (rupture life 9279 hours) (b) columnar region of single-pass weld joint interrupted at 2500 hours and (c) in the columnar region of dual-pass weld joint interrupted at 5500 hours. Both these specimens were creep tested at 923 K and 140 MPa.

It has been reported in this work that the dislocation substructure evolution depends on the interactions with solute/precipitates and other dislocations. For the weld joint specimens under similar testing conditions, dislocations in the fusion zone of the single-pass showed extensive bowing (Figure 5.9(b)), whereas the dislocations in the dual-pass weld joints had a wavy structure (Figure 5.9(c)). These images are the typical micrographs taken over several regions in the TEM specimen. Though there was significant change from the initial dislocation which consisted of pileups and dislocation tangles (Figure 5.5), there was no evidence for the formation of sub-grains in both these welds joints. As in case of the weld joints fabricated by SMAW (Figures 4.16 and 4.17), for the A-TIG weld joints the damage induced by creep cavitation is more dominant than the microstructural instability induced by recovery processes like sub-grain formation.

5.4.2 Influence of fusion zone volume

Before assessing the cause for failure in the weld joints it is essential to understand the influence of fusion zone volume on the deformation characteristics. Although there is no literature quoting the significance of fusion zone volume on the mechanical properties of the weld joint specimens, it is quite apparent that the change in volume of the fusion zone will have definitive role in the deformation process. With the increase in fusion zone volume, the extent of columnar and equiaxed regions also increases, resulting in wider regions having similar microstructure. Within these regions, the variations in deformation behaviour are likely to be insignificant. In contrast to the single-pass weld joint, for a dual-pass weld joint the volume of all the constituents is significantly lower. The heterogeneity in microstructure is further enhanced with the deposition of additional pass. The deformation mechanism which is dependent on the microstructure is bound to vary more significantly across different regions of the weld joint. Hence, the volume of the constituent regions can significantly influence the deformation behaviour and consecutively affect the rupture life. The single and dual-pass joints, exhibited similar creep rate upto the onset of tertiary creep (Figure 5.8). This suggests that the variation in fusion zone volume did not have considerable effect on the deformation behavior. However, increase in fusion zone volume increased the region which is more susceptible to creep cavitation, which during high temperature creep exposure reduced the rupture life of the single-pass weld joint by initiating the tertiary stage earlier.

5.5 Evaluation of localized creep properties by Impression Creep Testing

In order to clearly understand the rupture behaviour of the weld joints, the creep properties of the individual regions of the weld joint has to be assessed. Impression creep testing (ICT) is one such miniature testing technique which has been successively used in estimating the creep deformation properties of narrow regions in the 316LN SMA weld joint [119]. Though the duration of the test is short it can give valid details on the time dependent deformation behavior of the material. The penetration rate using this testing technique gives the understanding of the creep deformation behaviour of the material/region tested upon. ICT on different constituents of both the weld joints have been carried out at 923 K and at a punching stress of 680 MPa. This stress is equivalent to a uniaxial stress of 225 MPa taking into consideration the conversion factor 0.33 which has been used in previous investigations [98] . Since the width of the equiaxed region in the dual-pass weld joint was comparable to the indenter diameter (1 mm), the regions adjoining the equiaxed region can also contribute to the deformation process. Care has been taken such that major portion of the punched region was under the intended zone.

The impression creep curves of the different constituents of the fusion zone, base metal and the HAZ region of the single-pass joint and the dual-pass joints are shown in Figures 5.10 (a) and (b), respectively. For the single-pass weld joint, the penetration depth was highest in the equiaxed region followed by the HAZ region for the same test durations. However, the steady state deformation rate of the HAZ was comparable to that of the base metal. It can also be noted that the penetration rate of the columnar region was lowest when compared to all the other regions; this could be because of its hard directionally solidified microstructure.

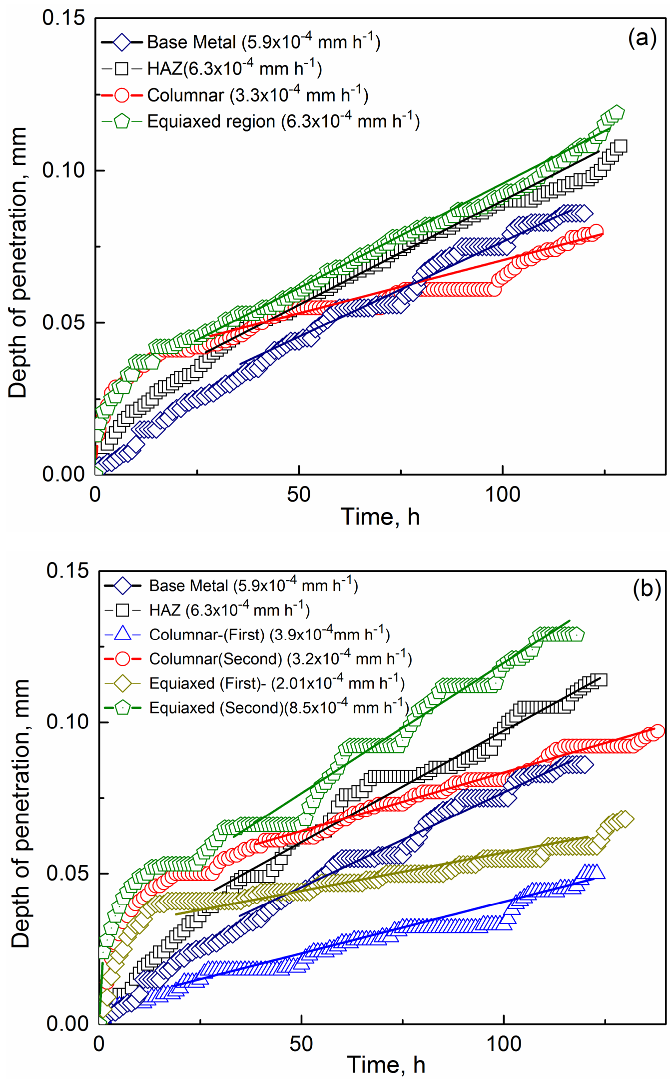

Figure 5.10 Impression creep curves of (a) single-pass weld joint and (b) dual-pass weld joint, the steady state creep rates are mentioned within brackets.

In case of the dual-pass weld joint, the trends in the penetration rate of the various regions in the first and the second pass were similar to that of the corresponding regions in the single-pass joints. However, in case of the dual-pass joints there was a well defined primary creep regime for the columnar region of the second pass when compared to the columnar region in the first pass. The negligible primary creep in the first pass could be possibly due to the hardening induced by the subsequent thermal cycle during second weld pass. There was significant variation in depth of penetration for the first and second pass for the same test duration. This variation can generate a constraint at the interface between the zones during the initial stages of creep deformation, when strain accumulation is significant. In the equiaxed region, there was a prominent primary stage and this region exhibited comparatively higher penetration rate than the adjoining columnar region in both the passes which is substantiated by the lower hardness values (Figure 5.4 (a and b)).

Through the findings of the impression creep testing, it is concluded that the creep deformation behavior of microstructurally distinct regions in the weld joint viz, base metal, HAZ, columnar fusion zone and equiaxed fusion zone vary appreciably. Variations in mechanical properties in the distinct regions of the weld joint create constraint during creep deformation. This constitutes the 'metallurgical notch'.

In case of the dual-pass weld joint, where the extent of the fusion zone was lower, such variations occurred within a smaller volume. The presence of an additional pass created regions with higher gradient in mechanical properties. Hence, it can be stated that the 'notch' in case of dual-pass weld joint had more acuity when compared to single-pass joint. The presence of this 'notch' with higher acuity resulted in longer rupture life of the dual-pass weld joint due to enhanced 'notch strengthening' (Figure

5.6). Though with decrease in the applied stress level, the constraints caused by the changes in mechanical properties across the various regions of the weld joint become less significant, they still play a major role in nucleation of creep cavities.

5.6 Effect of additional weld pass on creep cavitation

Despite the fact that delta ferrite content in both the single and dual A-TIG weld joints are significantly lower when compared to the SMAW joints, they still act as potential nucleating sites for creep cavitation. Figure 5.11 shows the cavities nucleating at the intermetallic/matrix interface in the equiaxed region of the single-pass weld joint tested at 175 MPa.

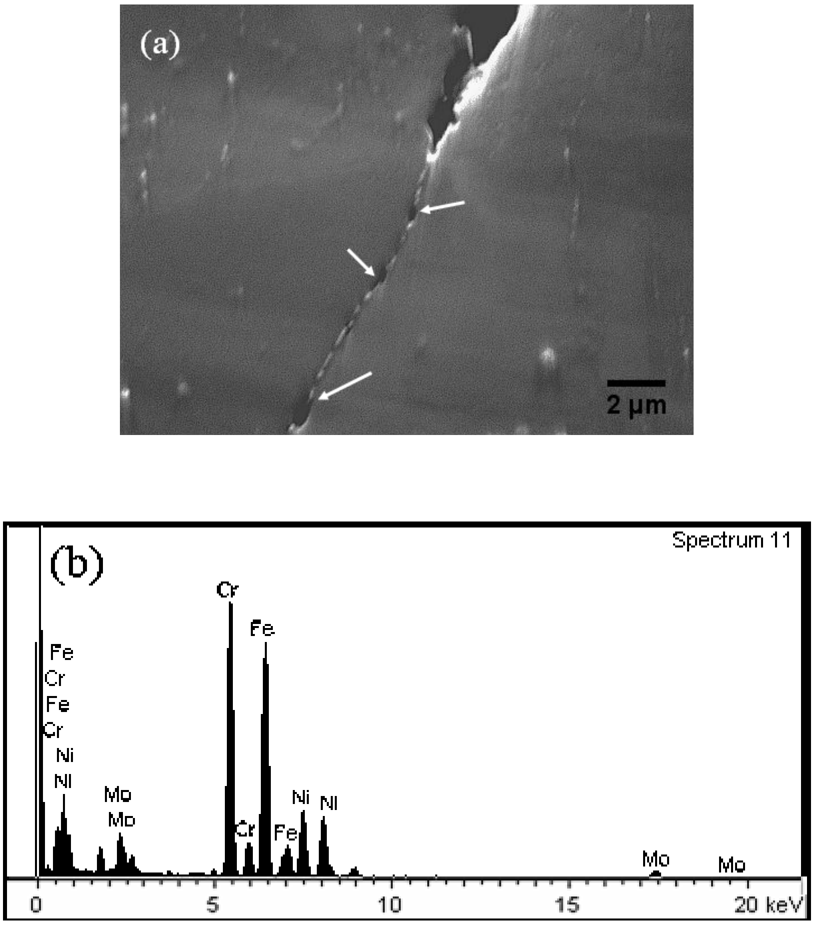

Figure 5.11 (a) SEM image showing nucleation of cavities (indicated by arrows) along second phase particles (b) energy-dispersive X-ray spectroscopic (EDS) analysis on the second phase particle revealed that these were rich in Cr, Fe and Mo.

The orientation of the delta ferrite with respect to the loading axis is also a critical factor determining creep failure. In the columnar regions of the single-pass weld joint, delta ferrite was found along the direction parallel to the loading direction as a consequence the initiation of cavitation in this region was not significant (Figure 5.7(a)). Cavities in this case initiated preferentially at the interfaces of the equiaxed grains (Figure 5.7(a)) which were aligned perpendicular to the loading direction. In case of dual-pass weld joints, the creep cavities nucleated in the columnar region of the second pass, but its propagation was intercepted at the weld pass interface (Figure 5.12). A more detailed explanation needs to be presented for explaining the cavitation behavior in the dual-pass joints.

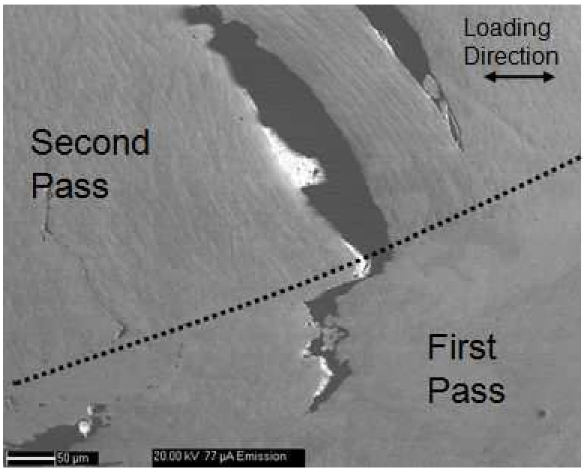

Figure 5.12 The arrest of creep cracks at the weld pass interface in the fusion zone of the dual-pass weld joint tested at 923 K and applied stress of 175 MPa.

In the previous chapter it was shown how the microstructural inhomogenity caused by substructural and morphological changes, influence the creep cavitation behavior of the multi-pass SMA weld joints. Both these changes are generated due to the deposition of the subsequent weld pass. The precipitation of intermetallics which is the primary requirement for cavitation to commence occurs readily in morphology which is relatively more continuous. The strength mismatch between the two regions is yet another attribute for cavity nucleation and propagation. In case of the fusion zone in A-TIG weld joints, the delta ferrite content is considerably low, consecutively the associated morphological changes which evolve during subsequent weld pass deposition is negligible. Therefore in these joints, strength gradients across the various regions of the weld joints play a more pivotal role in dictating the rupture life.

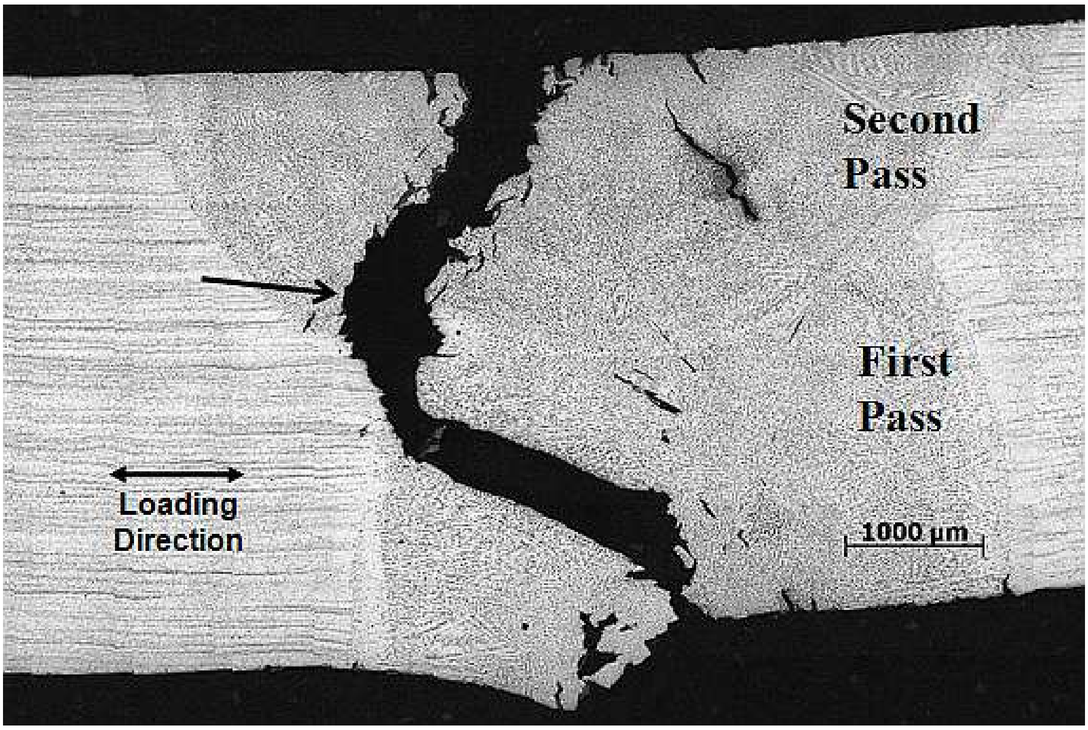

Figure 5.13 Macrostructure of dual-pass weld joint tested at 923 K and applied stress of 140 MPa. The possible location where the cavitation could have initiated is indicated.

Figure 5.13, shows the optical micrograph of the dual-pass weld joint which was creep ruptured at 140 MPa. The sequence by which damage occurred in this joint due to creep cavitation is more complicated when compared to the single-pass weld joint. As the morphological variation in the first and second pass of the dual-pass joint is not significant, transformation kinetics in both these regions would be alike. However, the propensity of cavity nucleation would be more in the second pass. This is due to the constraint created as a result of the gradient in strength across the weld pass interface.

The boundaries of columnar grains in the second pass containing the transformed intermetallics/$M_{23}C_6$ precipitate would be the likely initiation site for creep cavities. The propagation of the creep cavities were more pronounced along columnar grain boundaries which were oriented at angles close to 45° with respect to the applied stress as indicated in Figure 5.13. It is at this orientation where the shear stress is maximum [30]. As in case of the multi-pass weld joint, the propagation of the cracks did not proceed into the first pass which was 'thermo-mechanically treated' and was obstructed at the weld pass interface (Figure 5.13). Only after significant propagation of the cavities into the second pass, did failure occur in the weld joints due to the reduction in the load bearing cross sectional area. In case of SMA weld joints, the presence of relatively continuous morphologies of prior ferrite transformed precipitates would have easily enabled crack propagation (Figure 4.13). This is the prime reason why the rupture lives of the SMA weld joints are inferior to those made with A-TIG.

5.7 Rupture ductility and fractography

Elongation of the weld joint and base material plotted against rupture life is shown in Figure 5.14(a). As observed in case of SMAW joints (Figure 4.12), the presence of the fusion zone reduces the values of elongation of both the A-TIG joints drastically when compared to that of the base metal. The elongation values of the dual-pass weld joint is marginally higher than that of the base metal, which could be attributed to the lower volume fraction of the fusion zone in these joints. As mentioned in Chapter 4, the percentage area reduction taken near the fracture tip for a specimen whose failure location is in the fusion zone, would give a more relevant measure of rupture ductility for weld joints. From the area reduction plot (Figure 5.14(b)) it was clear that the ductility values of both the weld joints were lower than that of the base metal and this is due to the presence of the as cast dendritic microstructure in the fusion zone [120]. There was no significant change in ductility of the weld joint specimen with respect to rupture life. At higher applied stress levels, it was the constraint created by the 'metallurgical notch' which limited the ductility of the weld joints. At lower stress levels, pronounced creep cavitation in the fusion zone caused reduction in ductility.

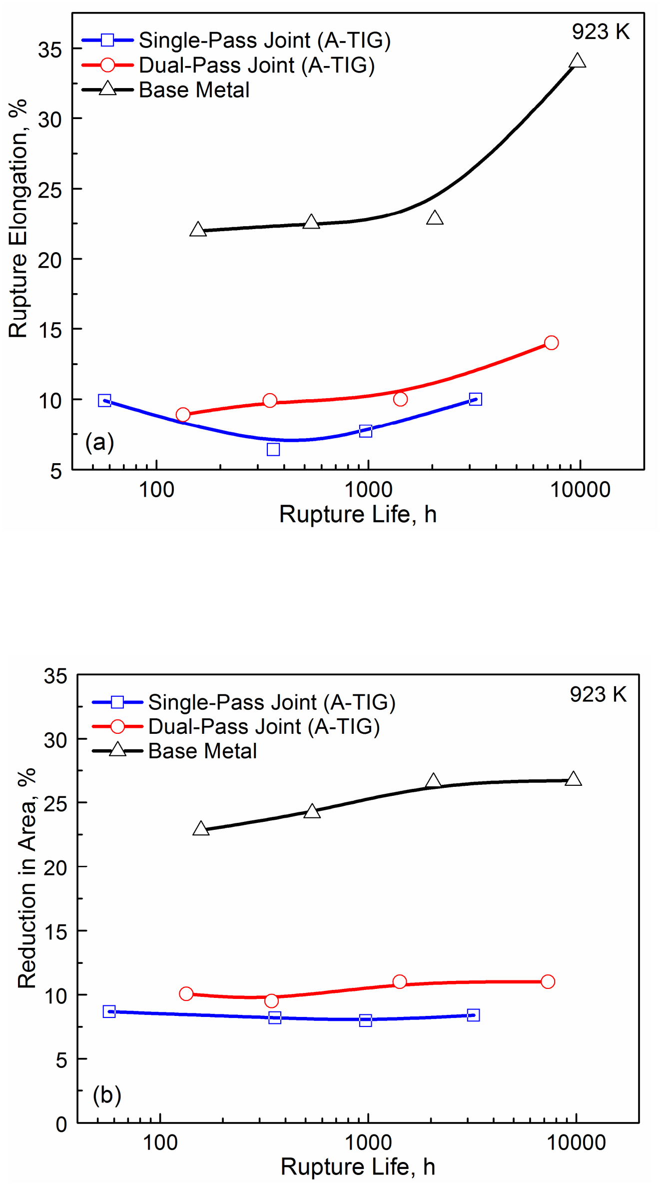

Figure 5.14 Plot of (a) percentage elongation and (b) percentage area reduction with rupture life.

Fractographic analysis was carried out to further understand the nature of failure and correlate it with the rupture ductility values. The fractographs of the single-pass and dual-pass weld joints tested at 140 MPa are shown in Figures 5.15(a, b, c and d). It could be clearly seen that for the single-pass weld joint, the fractured surface consists of facets of equiaxed dendritic grains indicating a clear intergranular failure.

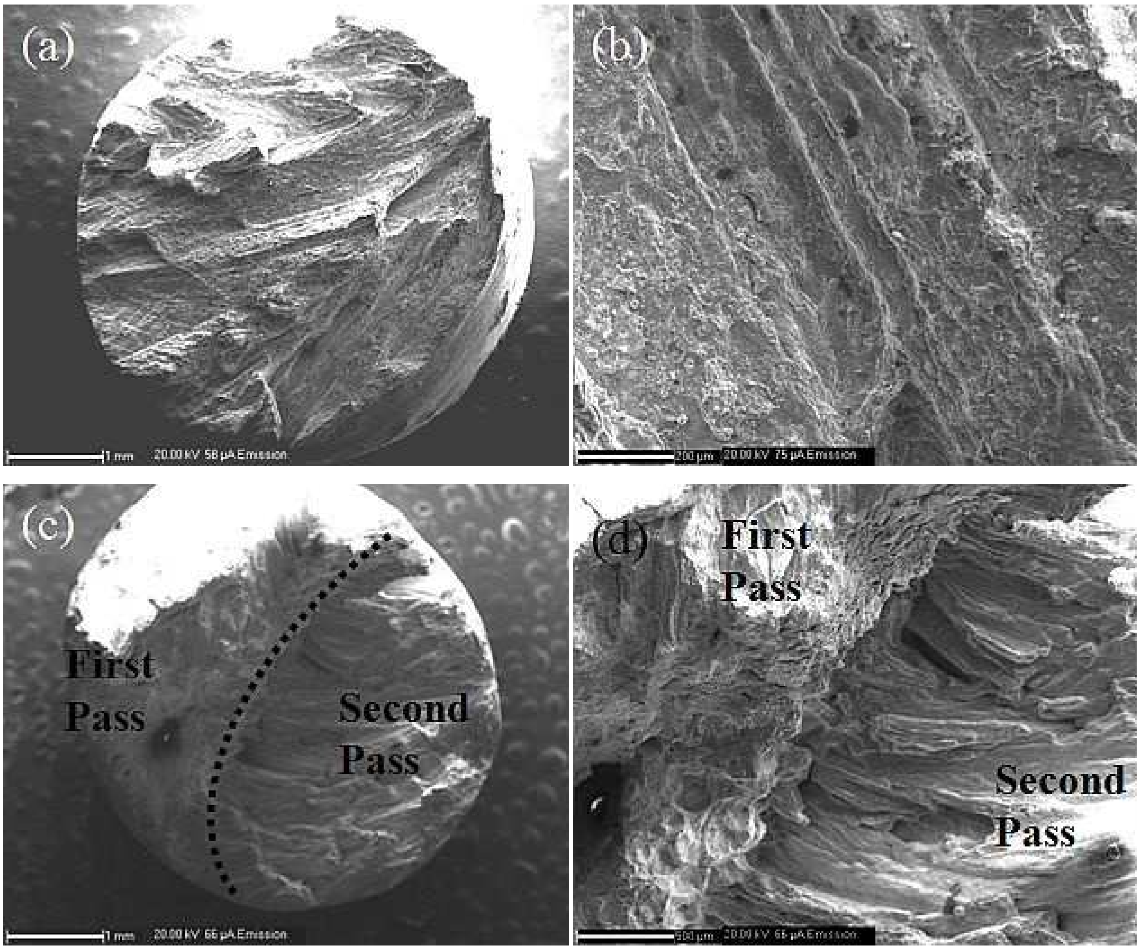

Figure 5.15 Fractographs of (a) single-pass weld joint (c) dual-pass weld joint tested at 140 MPa; figures (b) and (d) show the respective magnified images.

As discussed earlier in case of the single-pass weld joint, the cavitation which occurs in the grain boundaries enables easy propagation of the cracks resulting in lower creep rupture ductility when compared to the dual-pass weld joint (Figure 5.14 (a and b)). In case of the dual-pass weld joint tested at 140 MPa a dual mode of failure was clearly evident. The fractured surface of the first pass showed dimples suggesting a ductile mode of failure. The fractured surface of the second pass of the dual-pass weld joint consisted of intergranular failure similar to that of the single-pass weld joint. This distinct dual mode of failure consisting of dimples and intergranular fracture regions is substantiated by the marginal increase in ductility values of the dual-pass weld joint over that of the single-pass weld joints.

5.8 Conclusions

In the previous chapter it was shown that the subsequent weld pass deposition results in both morphological and sub-structural changes caused by a thermo-mechanical effect in the previous pass. It was concluded that both these changes influenced the creep cavitation behavior significantly thereby dictating the creep rupture strength of the joints. In this chapter, in order to understand the influence of the 'thermo-mechanical effect' alone, the creep rupture properties of single and dual-pass A-TIG weld joints were studied. Since the delta ferrite content in the fusion zone is very low in these joints, the associated morphological changes are considerably negligible.

The presence of the thermo-mechanically treated region could be characterized explicitly by impression creep testing of individual regions of the weld joint. It was seen that the minimum creep rate in the fusion zone of the first pass was lower than that of the second pass in case of the dual-pass weld joint. This suggested that the first pass exhibited considerably higher creep strength. During creep exposure, the presence of this thermo-mechanically treated first pass offered resistance to creep crack propagation, enhancing the rupture life of the dual-pass weld joint over the single-pass joint. The single-pass weld joint which was devoid of the 'thermo-mechanically treated' region did not offer resistance to creep crack propagation, thus resulted in comparatively lower rupture life.

Hence, it could be concluded that by incorporating an additional pass, the creep rupture life of the joints can be enhanced. It would be of interest to study in more detail, the influence of weld passes on the creep rupture behavior of the weld joints. The next chapter discusses this issue, by evaluating the creep rupture properties of weld joints of similar thickness fabricated with varying number of weld passes employing weld electrodes of two different diameters.

CHAPTER 6

INFLUENCE OF SIMULTANEOUS VARIATION OF THE MICROSTRUCTURAL FEATURES

Chapter 6

Influence of Simultaneous Variation of the Microstructural Features

6.1 Introduction

In the previous chapter, it was demonstrated how the additional pass in an autogenous 316 LN SS A-TIG weld joint improved its creep rupture strength. The influence of the ‘thermo-mechanically affected’ region generated by the additional pass, on the creep cavitation was exhaustively discussed. As the delta ferrite content in these joints were low, its influence on rupture behaviour of the A-TIG was considered insignificant. It was shown that the rupture life of the joints made with the additional pass enhanced, due to the presence of the 'thermo-mechanically treated' region. Since the laying of additional passes seems to be beneficial in the perspective of creep rupture life enhancement, it would be a logical consequence to study the influence of the number of weld passes on the creep deformation and rupture behaviour of weld joint. In this chapter, the influence of the number of weld passes on creep rupture properties of 316LN SS weld joints has been evaluated by fabricating joints with two different electrode sizes having almost the same chemical composition using SMAW process. The influence of the number of weld passes on the extent of both the microstructural features viz., morphological and dislocation sub-structural change has been elucidated. Detailed conventional creep, ABI testing, ICT, hardness testing, optical, SEM, TEM, EBSD investigation and finite element analysis (FEA) have been carried out to illustrate features of creep deformation and damage of the weld joints.

6.2 Microstructure in as-welded condition

Two weld pads were prepared each employing 2.5 and 4 mm electrode diameter using similar restraint conditions to prevent distortion. The variation in chemical composition between the electrodes was within the range (Table 3.1) specified for design of welded components for FBRs [91]. The welding parameters used for the fabrication of the joints are shown in Table 6.1. It can be seen from the table that the variation in heat input was not significant between the two weld joints. The macrostructure of the weld joints fabricated with 2.5 and 4 mm electrode diameters are shown in Figures 6.1 (a) and (b) respectively and the region from which the creep specimens were extracted is also indicated. Since the bead size of the fusion zone deposited by 4 mm electrode was larger, the weld pad could be fabricated with less number of passes than that of the joint fabricated by 2.5 mm electrode.

It could also be clearly seen from the figure that the number of weld pass interfaces in the fusion zone of the weld joint made with 2.5 mm electrode was considerably higher than that in the weld joint fabricated by 4 mm electrode. Figures 6.2(a) and (b) taken at the vicinity of the weld pass interface of the joints, show the presence of both vermicular (Figure 6.2(c)) and globular morphology (Figure 6.2(d)) delta ferrite. The variations in delta ferrite morphology were evident in both the weld joints. As discussed in Chapter 4, due to the laying of the subsequent pass, the continuous vermicular delta ferrite gets transformed in to globular delta ferrite in regions adjoining the weld pass interface. Since the volume of fusion zone deposited is slightly higher in case of the weld joint fabricated with 4 mm electrode, the extent of the globular region was marginally higher than what was observed for the weld joint made with 2.5 mm electrode diameter.

Table 6.1 Welding Parameters.

Electrode Size(mm)	2.5	4
Current (A)	80	128
Voltage (V)	24	24
Travel speed (mm/min)	80	97
Heat input (kJ/mm)	1.44 (each pass)	1.89 (each pass)

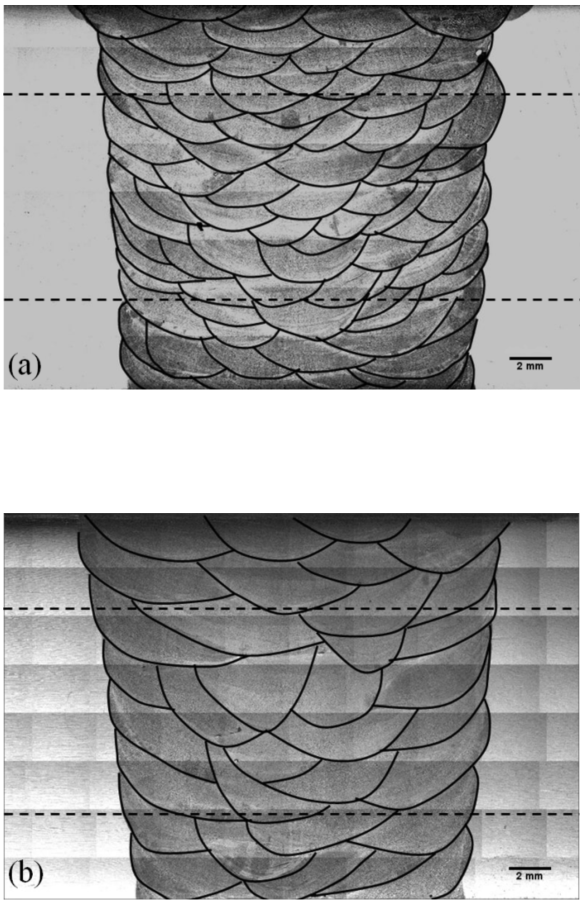

Figure 6.1 Macrostructure of the weld joints fabricated with (a) 2.5 mm and (b) 4 mm electrode diameter showing the weld passes. Lines are inscribed to demarcate weld pass interface. The dashed line shows the region from where the creep specimens were extracted.

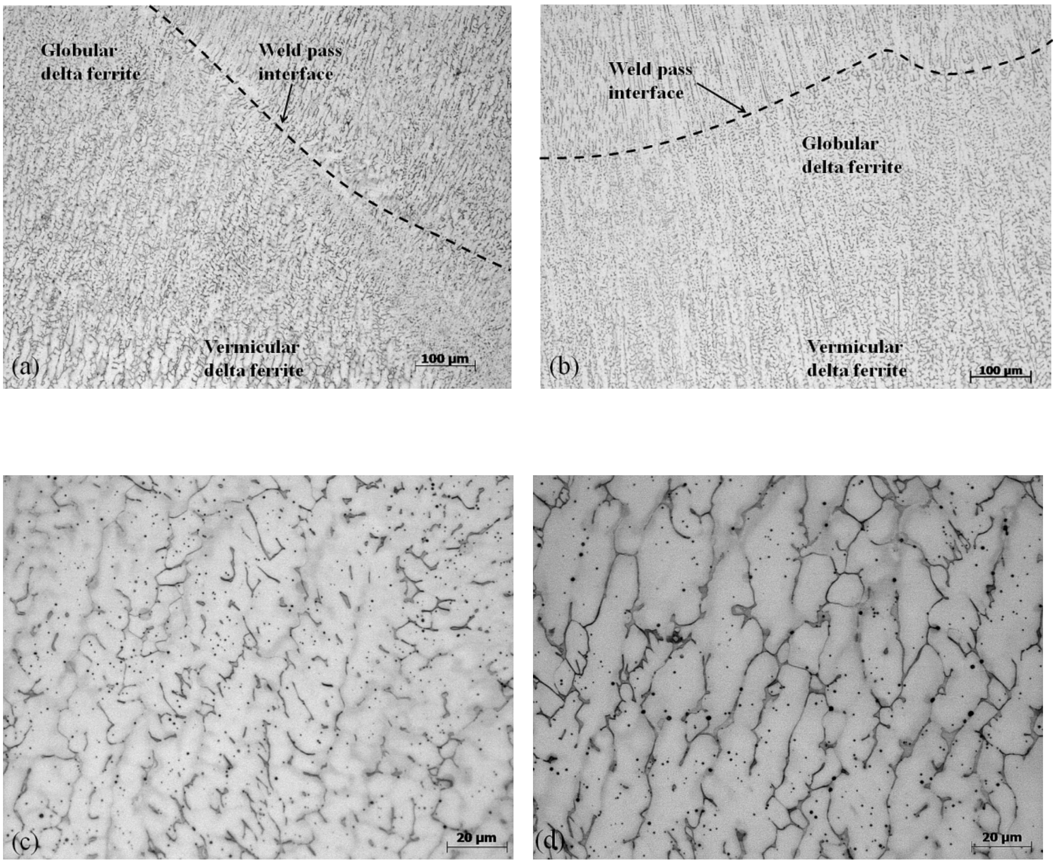

Figure 6.2 Microstructure near the weld pass interface of weld joints fabricated with (a) 2.5 mm and (b) 4mm electrode diameter, and delta ferrite having (c) globular morphology and (d) vermicular morphology (micrographs from weld joint made with 2.5 mm electrode size).

The hardness variations taken across the transverse direction of the weld joints are shown in Figure 6.3. The hardness in the fusion metal region of both the weld joints is substantially higher than that of the base material. The presence of strong as-cast structure in the fusion metal is the cause of higher hardness [103]. The hardness in the HAZ was also higher due to multiple thermal cycling which this zone is subjected to during multi-pass welding [104]. The HAZ in both the weld joints were not defined as the region containing coarse grain, but that having higher hardness than the base metal due to the influence of multiple thermal cycling.

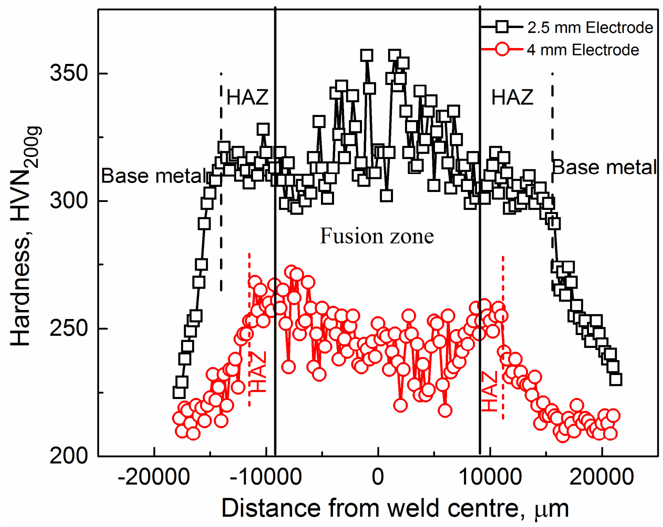

Figure 6.3 Hardness variations across the transverse direction of the weld joints.

The hardness values in the fusion region and the HAZ of the weld joint fabricated with 2.5 mm electrode size was higher than in the respective regions of the weld joint fabricated with 4 mm electrode due to comparatively higher number of thermal cycles which the joint is subjected to during welding. The width of the HAZ in the joint fabricated with smaller electrode diameter was substantially higher than that of the joint made with larger electrode size. The hardness values in HAZ was higher than the base metal in case of SMA welded joints, which was in contrast to the hardness values obtained from the HAZ of the A-TIG joint. The reason for such variations in hardness in the HAZ region with welding process has already been discussed in the previous chapter. The TEM micrographs taken from the vermicular delta ferrite region of both the weld joints are presented in Figures 6.4(a) and (b). It can be clearly seen that the dislocation substructure in case of the joint fabricated with 2.5 mm electrode diameter consisted of comparatively denser tangles when compared to a more uniform distribution of dislocation tangles in the fusion region of the joint fabricated with 4 mm diameter.

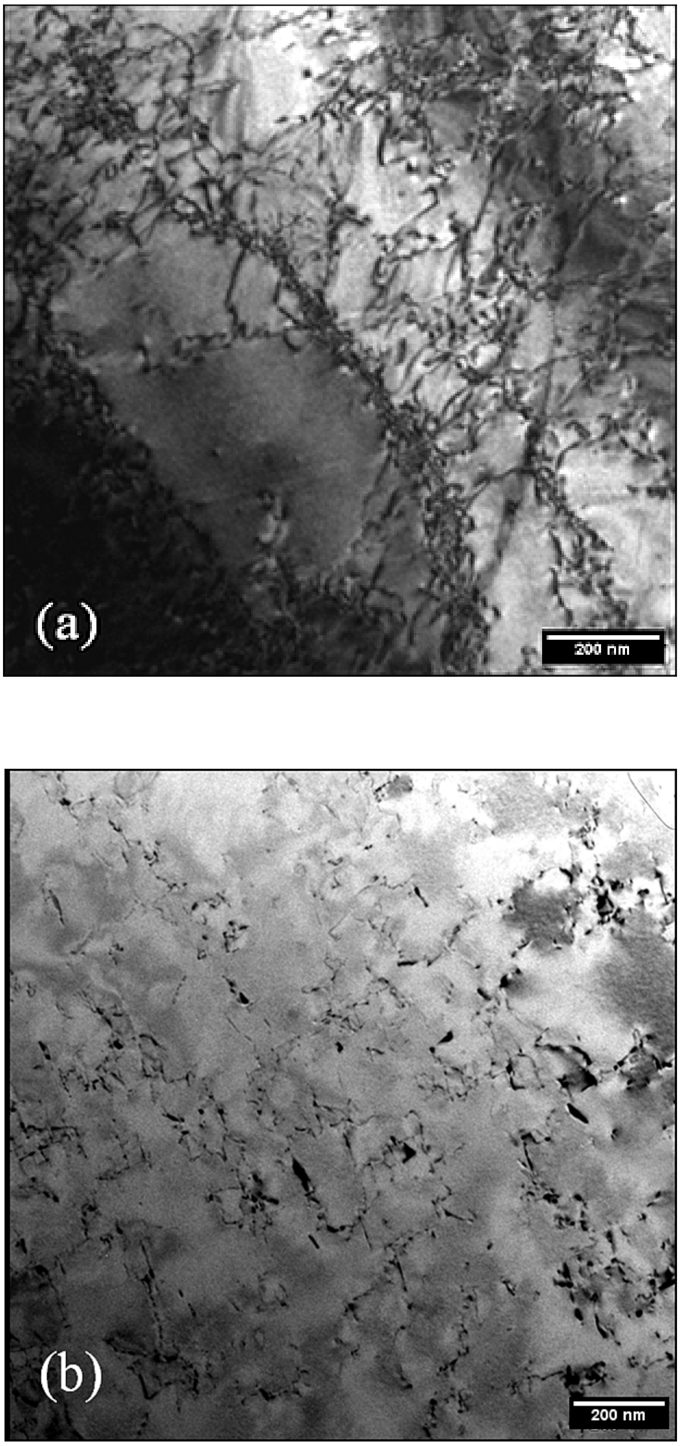

Figure 6.4 TEM microstructures taken from vermicular delta ferrite region of fusion zone for weld joints fabricated with (a) 2.5 mm and (b) 4 mm diameter in as-welded condition.

6.2.1 Hardness and KAM variation across weld pass interface

Figures 6.5(a) and (b) show the hardness variation across the short transverse direction along the weld centre line of both the weld joints. The lines shown in the micrographs demarcate the weld pass interface. It can be clearly seen that due to the laying of subsequent pass, hardness values in the region just adjoining the weld pass interface of the previous pass increased significantly. As shown in case of the dual pass A-TIG weld joint, (Figure 5.4(b)) the hardening which this narrow zone undergoes is a consequence of the 'thermo-mechanical treatment' which was induced by the subsequent weld pass. Both the weld joints had similar variations across the weld pass interface. However, for the joint fabricated with 2.5 mm electrode, there was a progressive hardening in each of the weld pass towards the root side. This could be attributed to the comparatively higher number of thermal cycles which the regions in the root pass are subjected to when compared to the root region of the weld joint made with 4 mm diameter.

Though the hardness of the joint made with larger electrode was lower, the constraint on the previously deposited weld pass in these joint created significant variations in hardness within the weld pass (Figure 6.5(b)). This is because the extent of the constraint invariably depends on the volume of fusion zone being deposited in a single pass. Larger electrode diameter results in excess deposition of weld metal, resulting in more constraint on the previously deposited pass. This constraint is the basis for generating the 'thermo-mechanical effect' on the previous pass, which causes strengthening in the globular ferrite region. It should be noted that hardness values are only indicative to the strength. The variation in constraint in the two weld joints can be better understood by using the kernel average misorientation (KAM) maps generated by the EBSD. A brief description of KAM is presented below.

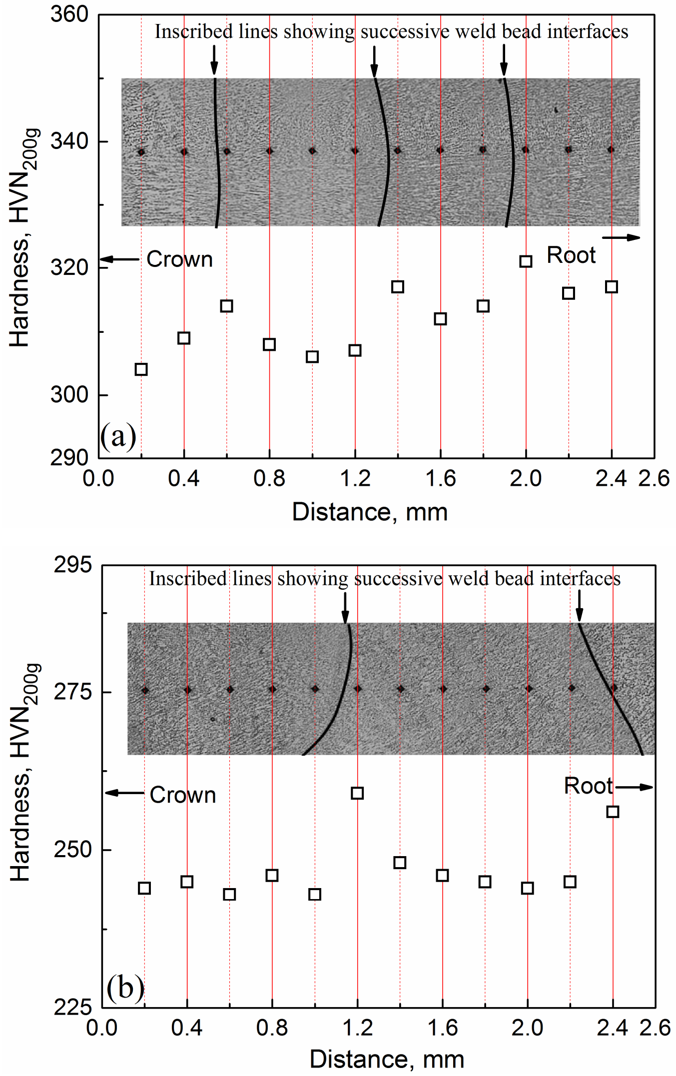

Figure 6.5 Hardness variations across the weld pass interface in weld joint fabricated with (a) 2.5 mm and (b) 4 mm electrode diameter.

As strain induced in a material increases, the orientation difference between neighboring pixels within a grain also increases. Strain gradient in the material can be quantified by many EBSD based misorientation maps. Detailed discussion regarding estimation of strain by EBSD is presented in Chapter 7. Amongst these maps the KAM map is most suited for quantifying the localized strain concentration [121]. These maps are constructed by taking the average misorientation value of a pixel with its neighbors.

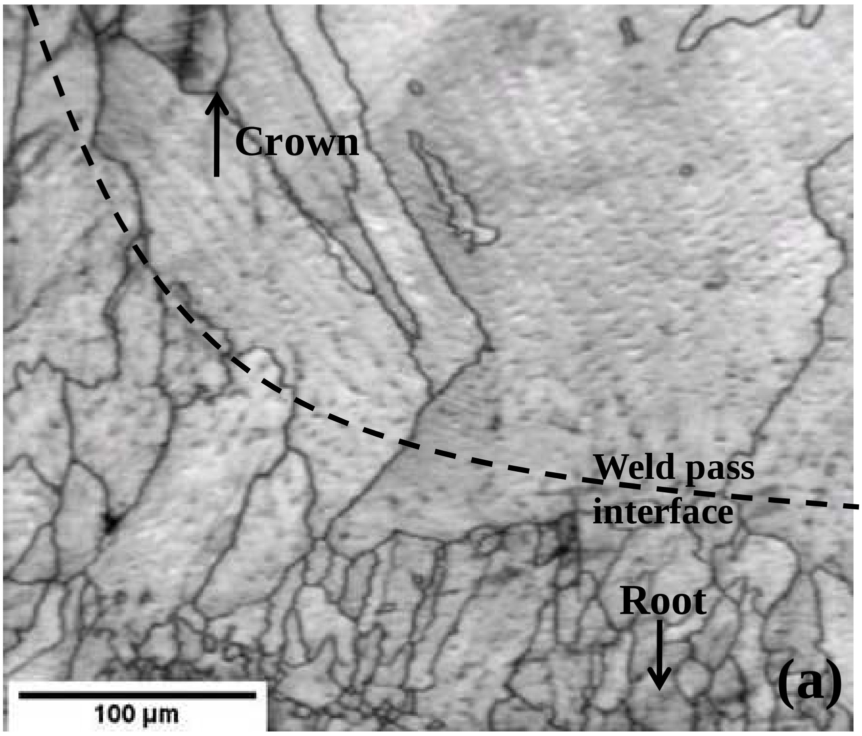
Crown
Weld pass
interface
Root
(a)
100 µm

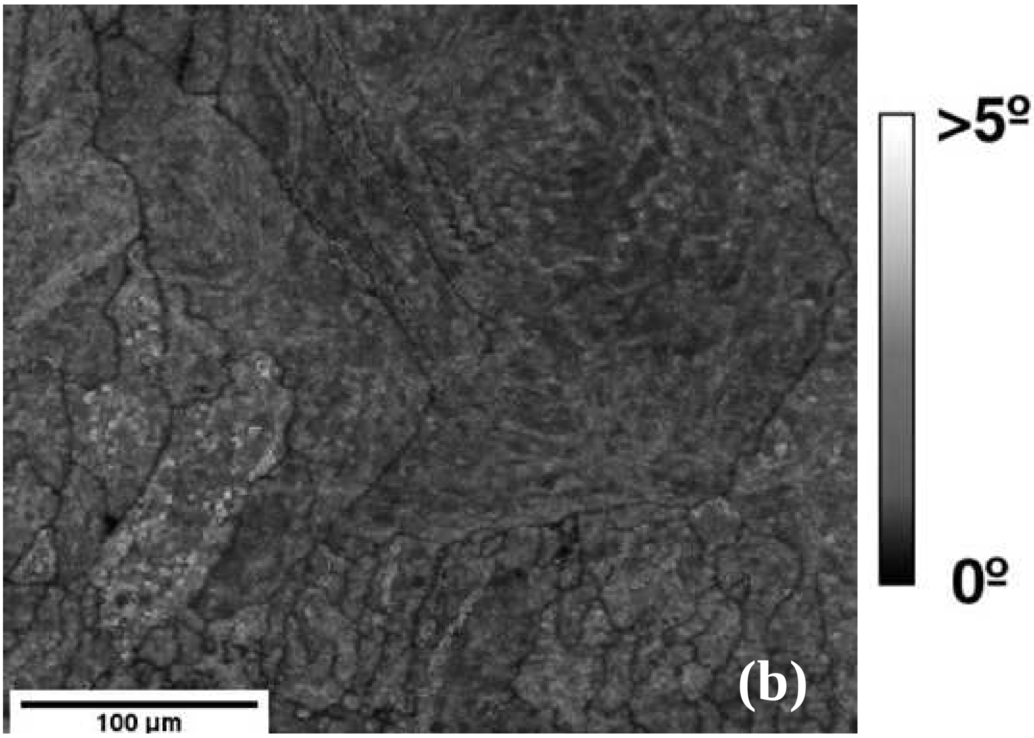
>5º
0º
(b)
100 µm

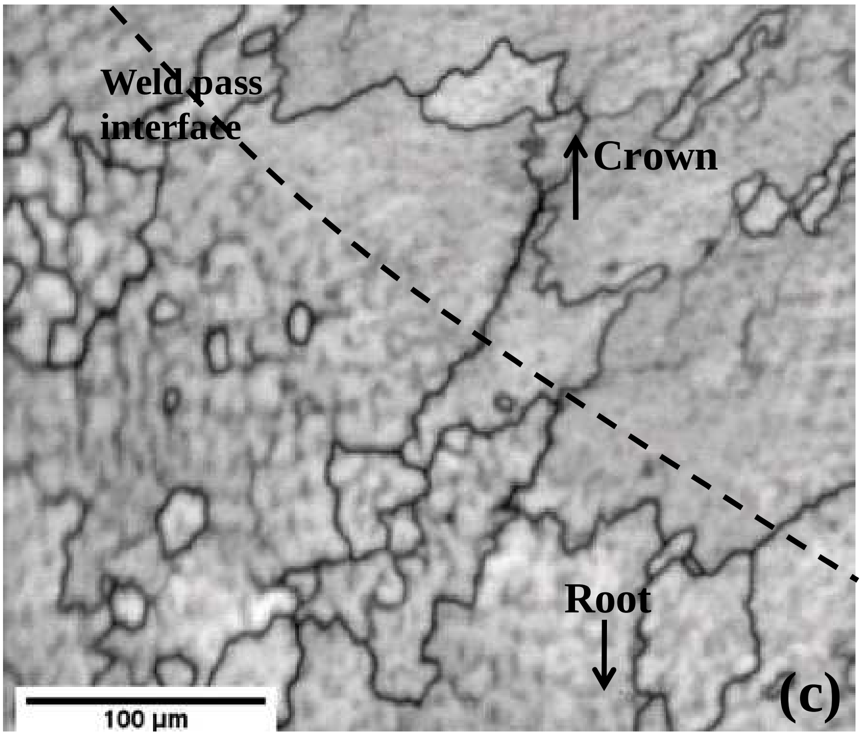

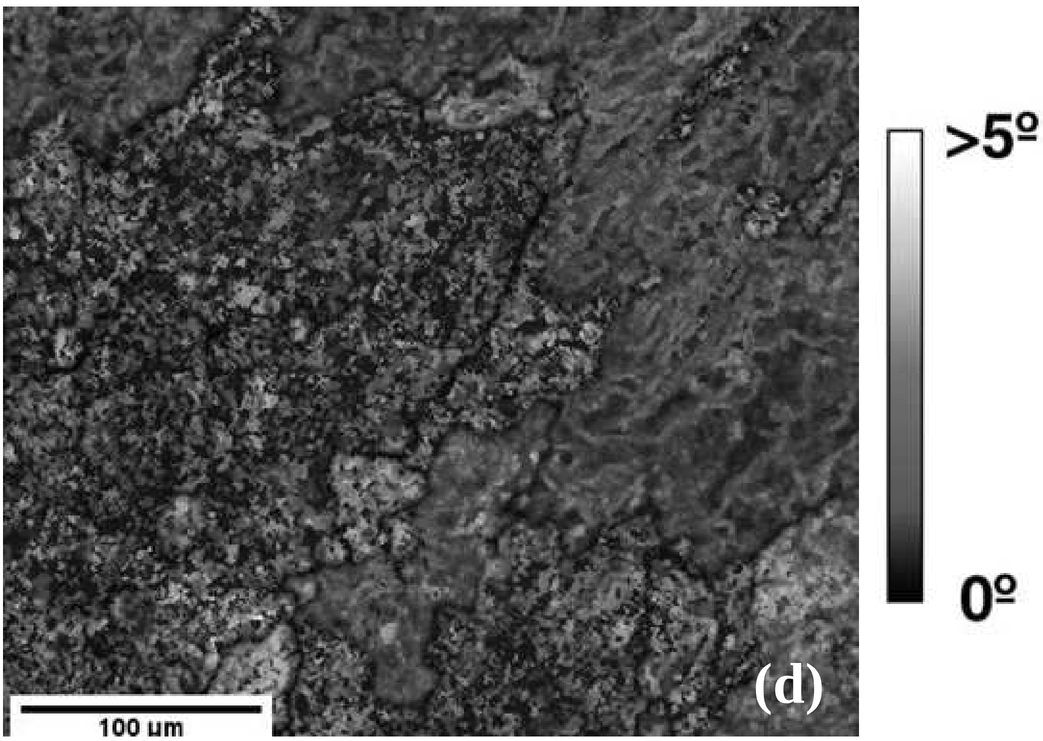

Figure 6.6 IQ maps of weld joints fabricated with (a) 2.5 mm, (c) 4 mm electrode diameter and the corresponding KAM maps((b) and (d)).

Figure 6.6(a-d) shows the image quality (IQ) and the corresponding KAM maps taken at the weld pass interface of the weld joints in the as-welded condition. For the weld joint made with larger diameter, there was a greater spread in the KAM values especially in the previous pass. In case of the weld joint fabricated with smaller electrode, the variation in KAM was less prevalent. The KAM variations substantiated the presence of a more pronounced 'thermo-mechanically processed' region in the joint fabricated with 4 mm electrode diameter.

6.3 Rupture life and elongation

The variation in rupture life of the two weld joints and the base metal with applied stress are shown in Figure 6.7. At higher applied stresses, the rupture life of both the weld joints was higher than that of the base metal. However, at lower applied stresses the life of the joints was shorter than the base metal. This transition in rupture life as mentioned in the previous two chapters can be attributed to the microstructural instability of the delta ferrite present in the fusion zone of the weld joints, as well as variations in stress redistribution across the weld joint which arises due to the microstructural inhomogeneity. Though this transition in rupture life trend occurred in both the weld joints, there was a change in the time duration at which this transition occurred. The substantial delay in the transition of the rupture life trend of the weld joint fabricated with 4 mm electrode can be attributed to the kinetics of creep damage evolution associated with the microstructural degradation in the fusion zone.

The rupture life of the weld joint made with 3.15 mm electrode size which was investigated in Chapter 4 was almost similar to that of the joint made with 2.5 mm electrode. The lack of distinct trend in rupture life with electrode diameter can be attributed to the variations in chemical composition of the electrodes (Table 3.1). Both the electrodes examined in this chapter (2.5 and 4 mm diameter) were procured from the same supplier hence the variation in chemical composition between these two electrodes was negligible. Apart from this the welding praetors in these two investigations also varied significantly (Tables 4.1 and 6.1)

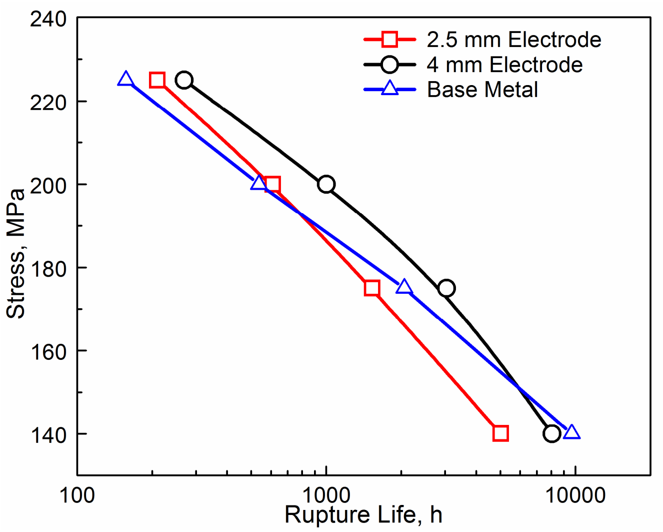

Figure 6.7 Rupture life variations of the weld joints as compared to the base material.

The plot of variations in rupture elongation and reduction in area with rupture life are shown in Figures 6.8(a) and (b) respectively. The variation of ductility of the joints showed a similar trend with respect to rupture life. The rupture elongation values in the weld joints are lower than the base metal at all the testing conditions and the trend in the variation of the values reversed when compared to the base metal with increase in rupture life. The presence of the hard as-cast fusion zone as well as creep cavitation prevalence due to the presence of delta ferrite are the causes for reduction in rupture elongation and area reduction in the weld joints when compared to the base metal.

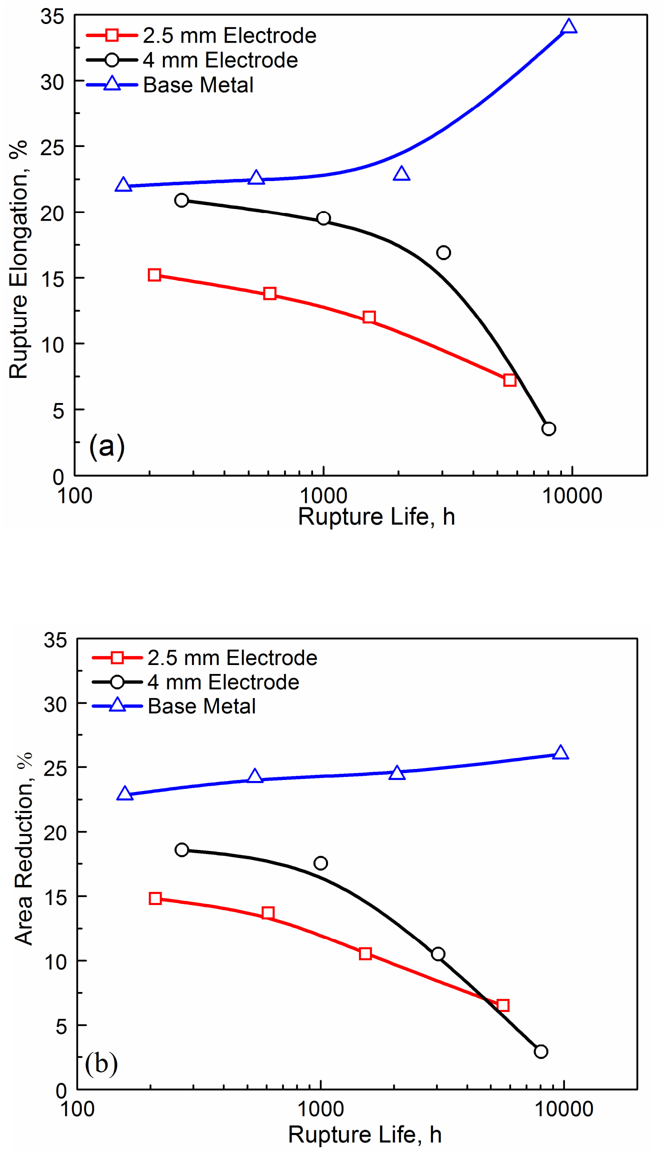

Figure 6.8 Comparison of (a) rupture ductility and (b) reduction in area with life for the weld joints and the base metal.

The continuous reduction in rupture elongation with rupture life is due to the time dependent precipitation of brittle intermetallic phases like sigma and chi which precipitate from the delta ferrite. These phases are more brittle than the matrix, which results in deformation mismatch across the matrix and precipitate, as a consequence cavities nucleate along the interface resulting failure without significant elongation during creep deformation [73]. The elongation values for the weld joint fabricated with 4 mm electrode diameter was higher than that of the weld joint made with 2.5

mm diameter. As shown from the hardness values taken across both the weld joints (Figure 6.3), substantial increase in the number of weld passes in case of the weld joint made with a smaller diameter, hardens the fusion zone and the HAZ. As a consequence, ductility of the weld joint made with smaller electrode diameter is lower than that of the joint made with 4 mm diameter.

The cause for reduction in rupture ductility and rupture life for both the joints after longer test durations can be explained based on the evolution of damage attributed to the creep cavitation and its propagation.

6.3.1 Variation in creep cavitation behavior with electrode diameter

Macrostructure of the failed weld joints tested at the different stress levels are shown in Figures 6.9(a-f). The failure of the weld joints tested at 225 MPa occurred in the base metal region in both the joints. The failure of the weld joint made with smaller electrode size (2.5 mm) occurred in the fusion zone at all the other stress levels. In case of the joint made with larger electrode diameter (4 mm), the failure at 200 and 175 MPa occurred at the fusion zone/HAZ interface (Figure 6.9(b) and (d)). Though the failure occurred at the interface, at both these stress levels significant cavitation was observed in the fusion zone of the weld joint made with larger electrode diameter. As discussed in the previous two chapters, the microstructural inhomogeneity caused by the deposition of subsequent passes and the associated cavitation damage play a dominant role in dictating the rupture life of the joints. The findings and the conclusions drawn from the previous chapters are discussed again for giving a better insight to the variations in failure mechanisms of the weld joints under current investigation.

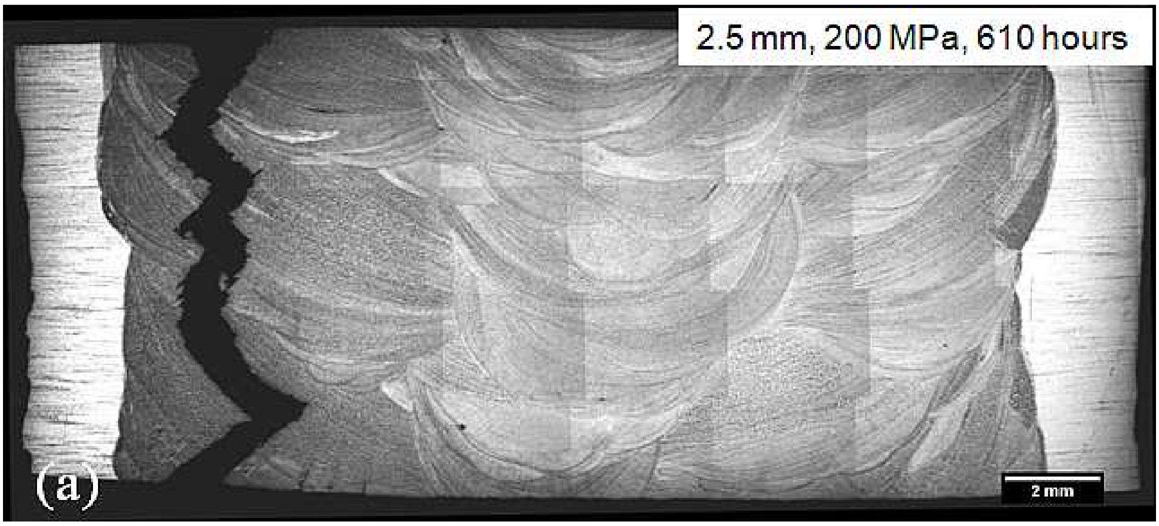
2.5 mm, 200 MPa, 610 hours
(a)
2 mm

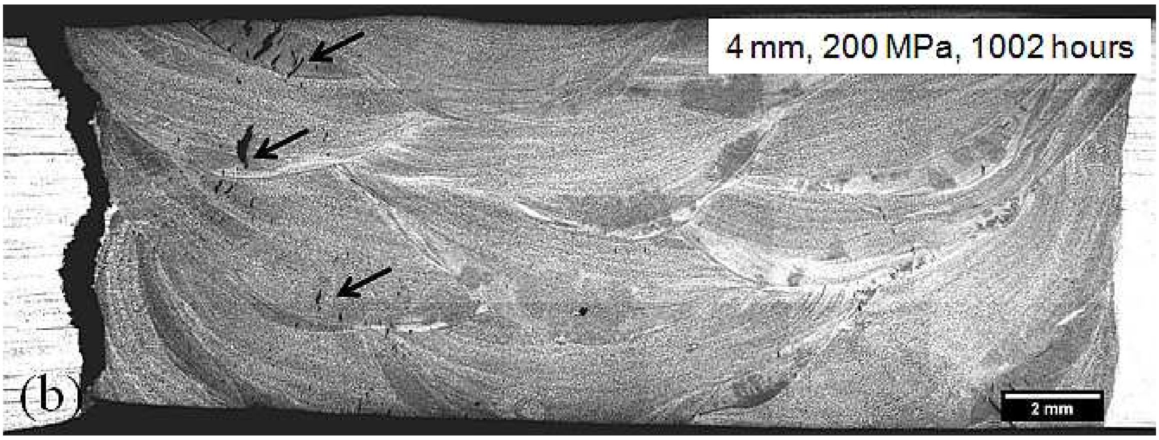
4 mm, 200 MPa, 1002 hours
(b)
2 mm

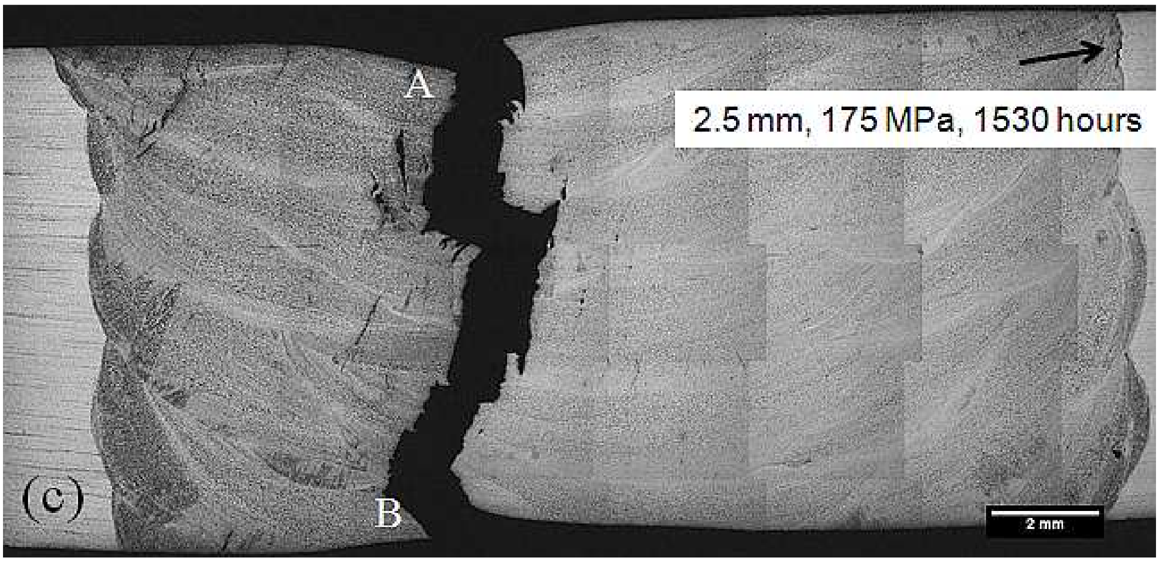
A
2.5 mm, 175 MPa, 1530 hours
(c)
B
2 mm

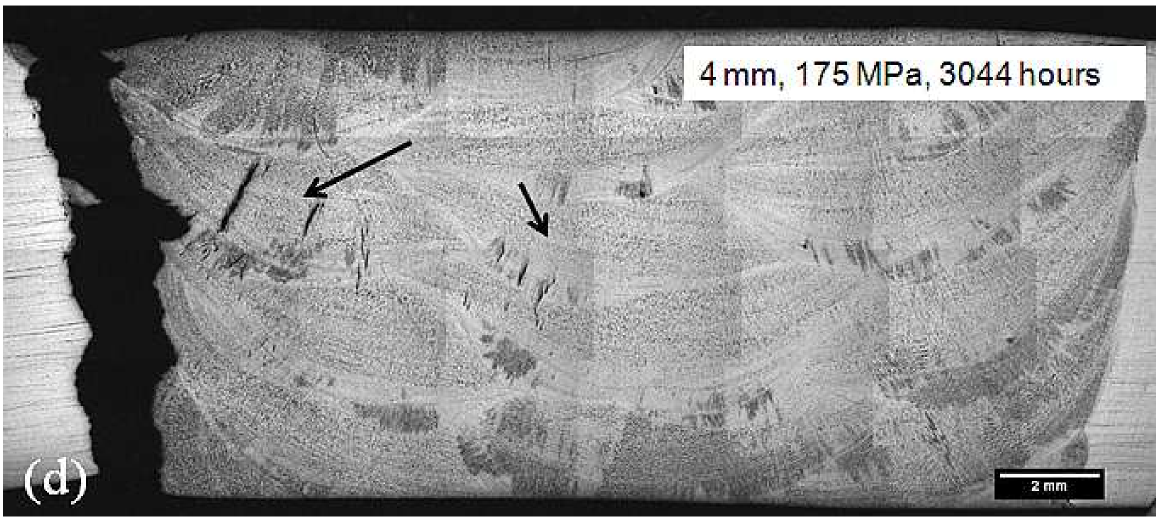
4 mm, 175 MPa, 3044 hours
(d)
2 mm

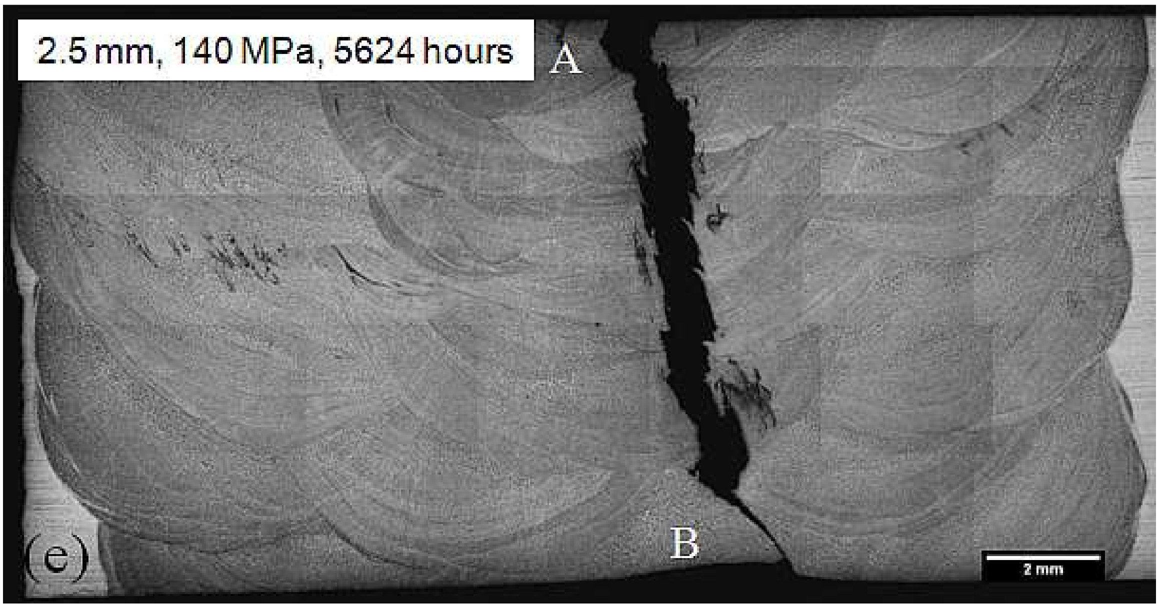

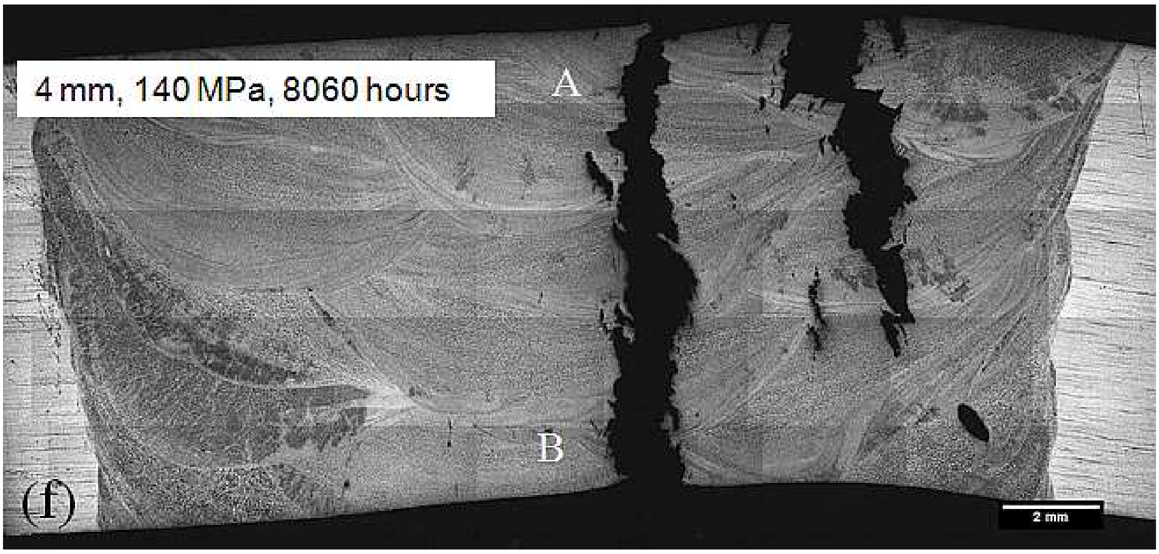

Figure 6.9 Macrostructure of weld joints tested at (a) 200 MPa (2.5 mm electrode diameter), (b) 200 MPa (4 mm electrode diameter), (c) 175 MPa (2.5 mm), (d) 175 MPa (4 mm), (e) 140 MPa (2.5 mm) and (f) 140 MPa (4 mm).

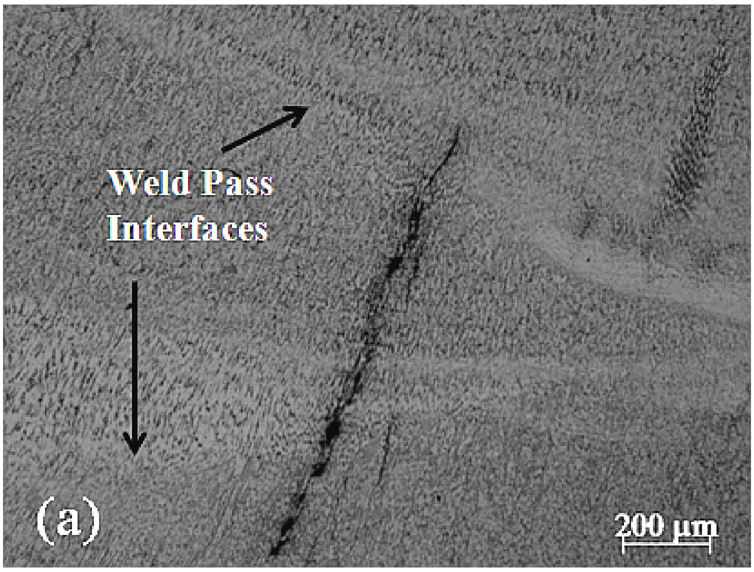

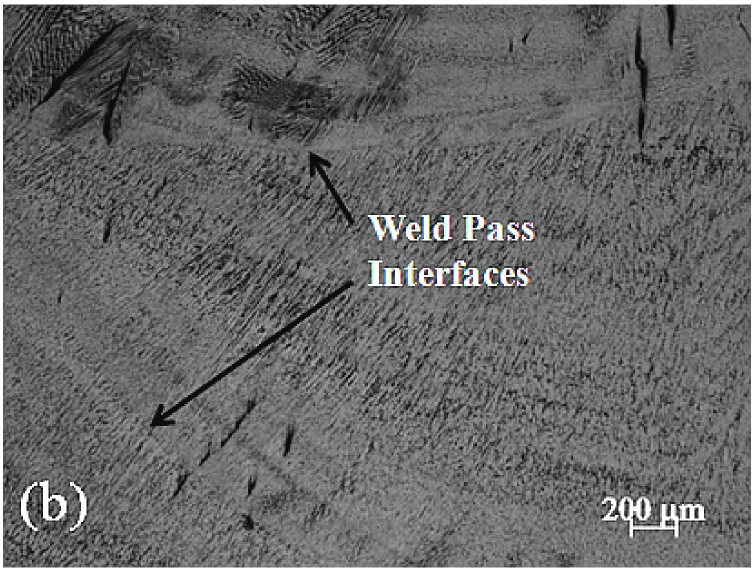

Figure 6.10 Micrograph showing the cavity nucleation sites in weld joints fabricated with (a) 2.5 mm and (b) 4 mm electrode diameter creep tested at 175 MPa.

As reported in Chapter 4, two types of inhomogeneities have been reported in multi-pass weld joints, one is caused by the change in delta ferrite morphology and the other the formation of a locally strengthened region. Both these changes occur in the regions of the previous pass which are subjected to a thermal cycle due to the deposition of the subsequent weld pass. While the change in morphology is a resultant of shape instability of delta ferrite, the hardening in this region is caused by local constraint evolved during solidification. These two inhomogeneities were evident in both the investigated weld joints. As in Chapter 4, the region containing both these modifications is designated as globular region and the unaffected region is termed as the vermicular region. The influence of these modifications on the creep damage has been summarised below.

Elevated temperature exposure of austenitic steel weld joints containing delta ferrite in the fusion zone results in the precipitation of intermetallic phases like sigma, chi and Laves. The formation of these phases is extensively controlled by diffusion of Cr and Mo from the austenite matrix to the delta ferrite/matrix interface. A more continuous vermicular morphology could result in enhanced diffusivity of Cr and Mo, when compared to the isolated globular delta ferrite with lower interface area. Hence the precipitation of the intermetallics can occur readily in the delta ferrite having a vermicular morphology.

The variations in dislocation substructure across the weld pass interface would result in a strength gradient. This gradient causes redistribution of stress preferentially at the softer region. As a consequence, the deformation in the vermicular region adjoining the weld pass interface is more significant than the globular region. Since the intermetallic phases are hard and brittle, their deformation characteristics vary significantly from the adjoining ductile austenite matrix. Deformation incompatibility generates stress concentration at the interface between the intermetallics and the matrix. As a result, cavitation occurs at the matrix/precipitate interface during prolonged elevated temperature exposure [71].

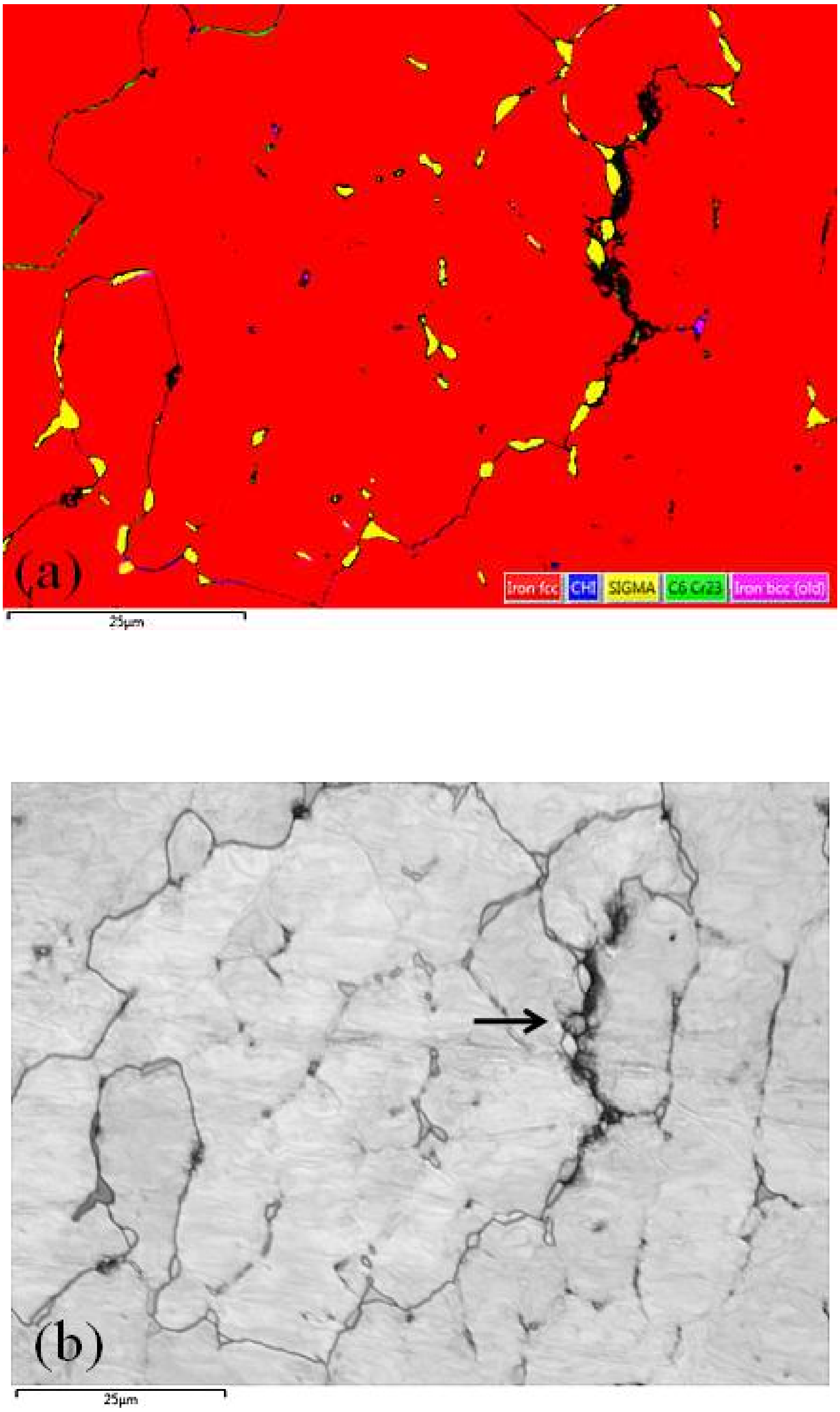

Figure 6.11 Phase map and the corresponding band contrast map showing creep cavitation across the intermetallic/matrix interface in fusion zone of weld joint tested at 140 MPa.

The growth of these cavities is also influenced by the prior morphology of delta ferrite, a more continuous morphology causes a rapid propagation of the cavities. The propagated cavities are then arrested at the weld pass interface as they cannot propagate into the more hardened globular region. Further propagation of cavities depends on the applied stress level. The formation of creep cavities in the fusion zone of the weld joint specimen fabricated with 4 mm electrode diameter, ruptured after testing at an applied stress of 140 MPa is shown in Figure 6.11. The phase map and the corresponding band contrast image is presented in the figure. The nucleation of cavities occurs at the interface of the transformed intermetallics and the austenite matrix.

It can be clearly seen from Figures 6.10 (a) and (b) that the nucleation sites for such cavities usually pertain to the region near the weld pass interface. These micrographs show how the cavities nucleated in the vermicular region are arrested at the weld pass interface, and did not propagate into the globular ferrite region. For the weld joint fabricated with smaller electrode the cavities propagated through many weld pass interfaces (Figure 6.10 (a)). This suggests that crack propagation proceeded without much hindrance resulting in shorter rupture lives for these joints. Although the sequence by which the damage proceeded in both the weld joints are similar, there were variations in the kinetics influencing nucleation and propagation of cavities.

In the present context, there are two attributes caused by the microstructural variations in the fusion metal of the weld joints, which influence both the kinetics of cavity nucleation and propagation in weld joint - a) extent of variation in strength gradients across the weld pass interface and b) distance between two successive vermicular regions which are more prone to creep cavitation. Localized strain variation is more significant for the joint made with larger electrode when compared to the joint made with smaller diameter as observed from the hardness distribution (Figure 6.5(b)) and the KAM map (Figure 6.6(d)). Thus the ‘thermo-mechanical treatment’ induced by thermal cycling during solidification of the weld pool is more pronounced in the weld joint made with 4 mm electrode diameter. This results in arresting of creep cavities at the weld pass interface. In case of the weld joint made with 2.5 mm electrode, the localized variation in strain across the weld pass interface was not so significant, which enabled easier propagation of the creep cavities.

The propensity for propagation of cracks also depends on the distance between the cavity nucleating regions. In case of the joints fabricated with 2.5 mm electrode, the distance between the cavitated regions were shorter (Figure 6.11(a)) when compared to the creep cavities in the fusion zone of the joints fabricated with 4 mm electrode (Figure 6.11(b)). This is because a comparatively smaller fusion zone volume is deposited using a 2.5 mm electrode diameter. In case of joints fabricated with 4 mm electrode, the susceptible delta ferrite regions with vermicular morphology are placed farther apart. With the application of stress, the propagation of the creep cavities did not progress due to the lack of interconnectivity with other cavitated regions and was blocked at the weld pass interface having globular morphology with thermo-mechanical heat treated hard structure. Considerable propagation of creep cavities in case of the weld joint made with smaller electrode diameter result in lowering of the load bearing cross sectional area causing failure of the weld joints. The summary showing the variation of creep cavity nucleation and its propagation with respect to change in electrode diameter has been illustrated in Figure 6.12.

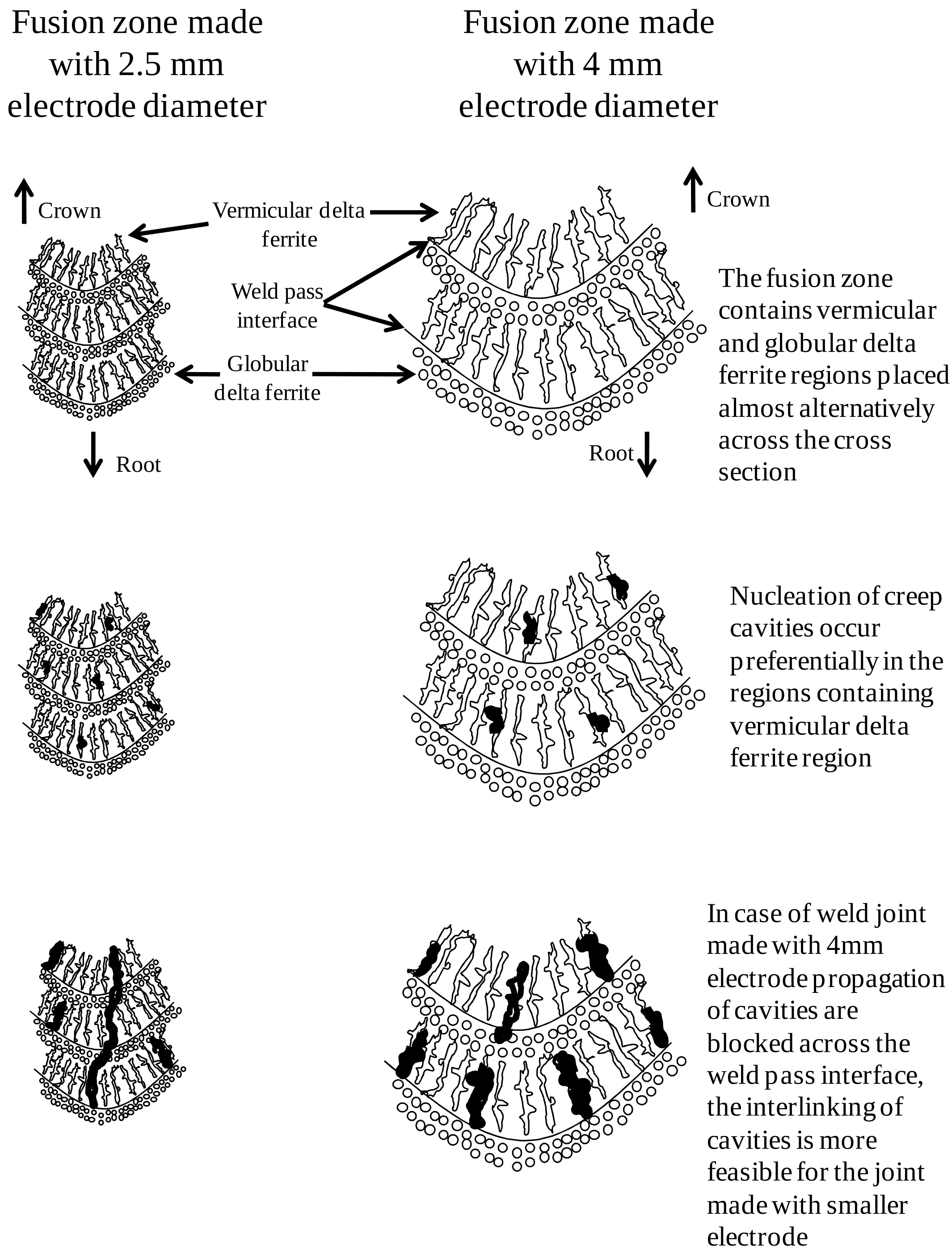

Figure 6.12 Schematic depicting the nucleation and propagation of creep cavities in both the weld joints.

6.4 Factors influencing the failure location

The fusion zone is the weakest link in the weld joint; it is in this region where failure occurred for the weld joints fabricated with smaller electrode, except in the case of the weld joints tested at 225 MPa. But in case of the joints fabricated with 4 mm electrode diameter, the failure occurred in the base metal/ HAZ interface at stress levels of 200 and 175 MPa. Investigation of the localized deformation behaviour is therefore essential to comment on the variation in failure location with respect to change in electrode size.

The weld joint specimen is broadly composed of three regions viz., fusion zone, HAZ and base metal which are microscopically distinct with appreciably different hardness (Figure 6.3) and so the deformation characteristics. Under creep loading, stress redistribution is likely to occur resulting in inhomogeneous deformation across the composite weld joint specimen [122].

In order to clearly assess the deformation behavior of the composite weld joint specimen, it is first essential to understand the mechanical behaviour of the individual region of the composite weld joint. Miniature specimen techniques offer a valuable insight in this regard. As shown in the previous chapter, mechanical properties of microstructurally narrow zones in weld joints can be evaluated using such techniques. In this study, the Automated Ball Indention Technique (ABI) has been used to evaluate the tensile properties and Impression Creep Testing (ICT) was utilized to obtain the steady state creep rate of the different regions of the weld joints. The mechanical properties obtained from these two techniques have been used in FEA simulation. Through this simulation, the underlying causes for change in failure location of the weld joint under creep loading condition, with respect to change and electrode diameter has been discussed.

6.4.1 Evaluation of tensile properties of various weld joint constituents

It has been shown that the tensile properties obtained from ABI technique can be well correlated to the uniaxial properties [99]. The variation of yield stress (YS) and the ultimate tensile strength (UTS) of the fusion zone, HAZ and base metal region of the weld joints fabricated with 2.5 and 4 mm electrode size obtained from ABI technique at 923 K is shown in Figure 6.13.

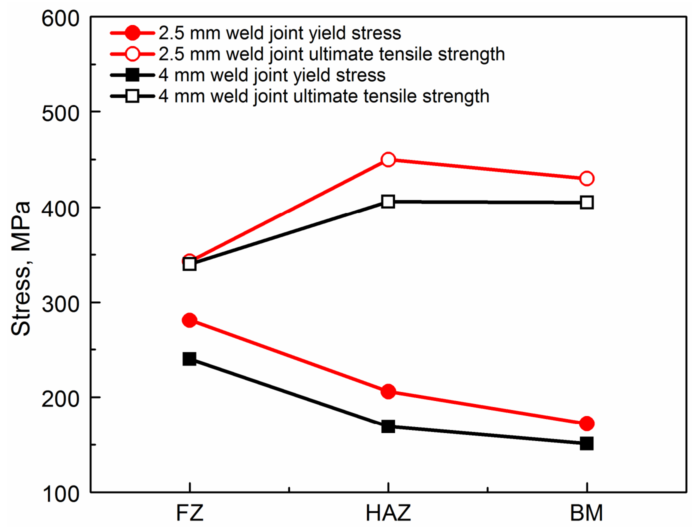

Figure 6.13 Tensile properties estimated by ABI technique across various zones of the weld joints.

The fusion zone (FZ) possessed the highest yield stress (YS) but its ultimate tensile strength (UTS) was the least among the three zones. The microstructure of the as-cast structure fusion zone is composed of higher dislocation density generated during solidification when compared to the HAZ and the base metal; this increases the YS in this region. The lower UTS in this fusion zone can be attributed to the presence of delta ferrite phase having less work hardening capability especially at higher temperatures. The YS and the UTS of the HAZ was marginally higher than that of the base metal in both the weld joints as a result of work hardening induced due to repeated thermal cycling produced during multi-pass weld. The YS of the fusion zone and HAZ regions of the weld joint fabricated with 2.5 mm was higher than that was observed in the corresponding regions of the weld joint fabricated with 4 mm electrode. This is because the regions in the 2.5 mm joint were subjected to more number of thermal cycles when compared to the joints fabricated with 4 mm joint.

6.4.2 Creep deformation properties of the weld joint constituents

The impression creep curves showing the relative depths of penetration with time, taken from the three regions of both the weld joints tested with a punching stress of 681 MPa (uniaxial equivalent of 225 MPa) at 923 K are shown in Figures 6.14(a) and (b). The trend in variation of penetration rate in the various regions of both the weld joints was similar. The fusion zone in both the joints showed the lowest penetration rate. As indicated earlier, the presence of the hard as-cast dendritic structure renders the microstructure more resistant to creep deformation. The HAZ in both the joints exhibited lower penetration rate than the base metal, this could be possibly due to higher yield stress which results in sluggish recovery. The base metal in both the weld joints exhibited highest penetration rate, as the influence of multi-pass deposition was minimal in this region. It can be distinctly seen that the cumulative depth of penetration in the HAZ and base metal regions of the weld joint fabricated with 4 mm electrode was substantially higher than the weld joint fabricated with 2.5 mm electrode for the same test duration. Though the penetration rate in the fusion zone of both the weld joints was comparable, there was marked difference in the cumulative depth in other two regions.

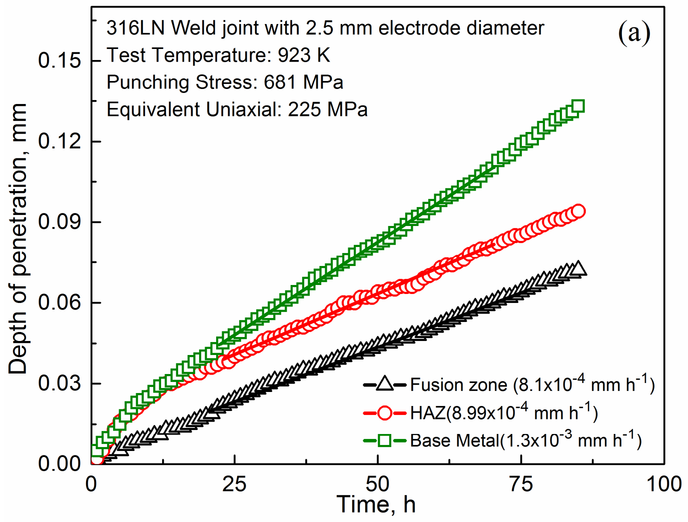

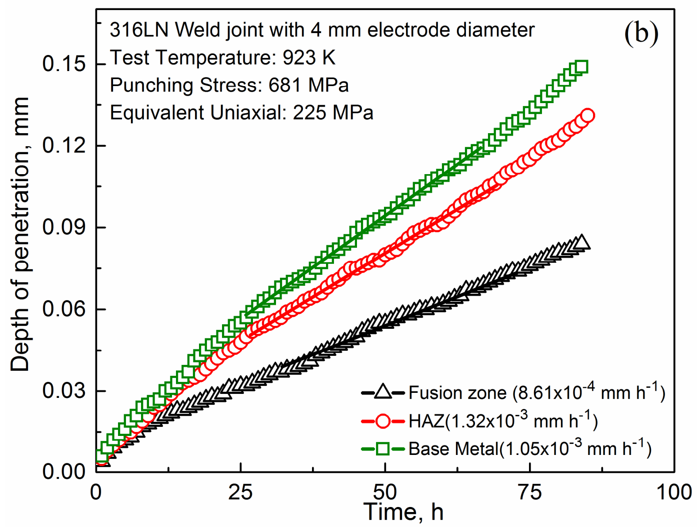

Figure 6.14 Impression creep curves showing the penetration with time for various regions in the weld joints made with (a) 2.5 mm and (b) 4 mm electrode diameter.

For the fusion zone made with 4 mm electrode, there was a distinct primary region in the impression creep curve, which was not explicit in the impression creep curve of the fusion zone made with 2.5 mm electrode diameter. This is a consequence of excessive hardening induced in the fusion zone of the weld joint made with 2.5 mm electrode size as a result of higher number of thermal cycles.

The variations of steady state creep rate of the different constituents of the joints with the applied equivalent stress obtained from impression creep tests (ICT) are shown in

Figure 6.15. In this study a conversion factor of 0.33 for converting the punching stress into uniaxial stress has been adopted [98].

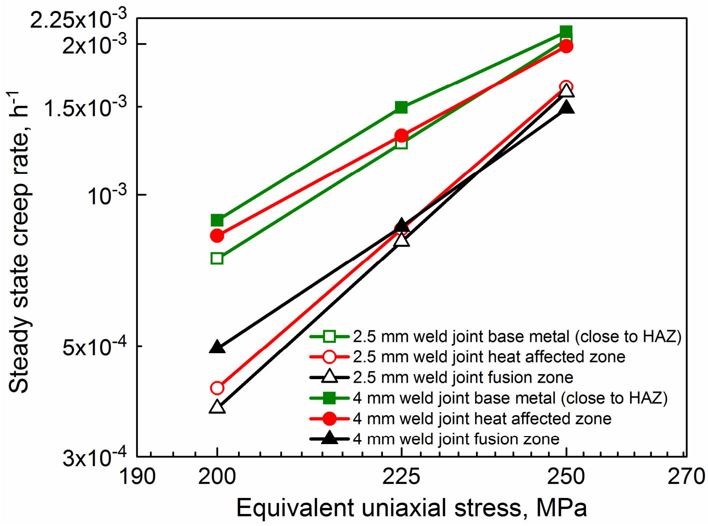

Figure 6.15 Stress dependence of steady state strain rate of the base metal, heat affected zone and fusion zone of both the weld joints.

There was a distinct variation in the creep deformation rate of the HAZ with respect to size of the electrode used. Since HAZ of the weld joint made with smaller electrode diameter endured comparatively higher number of thermal cycles, the microstructure was hardened, which offered more resistance to creep deformation. Though the ICT tests were short and could not characterize the precipitation phenomenon, the results did give a fair idea on the time dependent deformation behaviour of the different constituents.

The steady state creep rate and applied stress obeyed Norton's power law equation of the form $\dot{\varepsilon}_s = A\sigma^n$, where $\dot{\varepsilon}_s$ is the steady state creep rate, σ is the applied stress, A is a material constant and n is the stress exponent. Table 6.2 gives the values of Norton's law constants. It can be clearly seen that the values of n which is the stress exponent, varied within the range of 3-7 suggesting that the dislocation creep was the dominating mechanism in all the three regions. Increase in values of n suggests the presence of higher back stress. Since the fusion zone has comparatively higher dislocation density its microstructure generated higher back stress thereby causing significant increase in values of the constant n [123].

Table 6.2 Values of the Norton's power law constants A and n used in the ABAQUS simulation.

	Weld joint fabricated with 2.5 mm electrode diameter			Weld joint fabricated with 4 mm electrode diameter		
	Fusion Zone	HAZ	Base Metal	Fusion Zone	HAZ	Base Metal
A($MPa^{-n}h^{-1}$)	1.77×10^{-19}	2.23×10^{-18}	1.86×10^{-14}	2.24×10^{-15}	6.46×10^{-13}	1.05×10^{-12}
n	6.5	6.17	4.5	4.5	3.9	3.88

The possible cause for changes in failure locations can be attributed to the difference in tensile and creep flow behaviour of the different constituents in the weld joint. Finite element analysis (FEA) simulation using the properties deduced from miniature testing techniques has been used for further understanding the evolution stress gradients across various regions in the weld joints.

6.4.3 Finite element (FE) simulation of stress state across the weld joints

FE simulation has been carried out on the weld joint geometry using tensile properties obtained from ABI testing and the creep properties obtained from ICT. The data from these techniques were used for populating the properties of the regions in the weld joint for simulating the stress distribution. One-fourth of the specimen's gauge length was used in the analysis. The partitioning of various regions was based on the microstructure and hardness values obtained across the weld joint. The width of the HAZ in the weld joint made with smaller electrode was significantly higher than the joint made with larger electrode diameter due to the pronounced hardening resulting from higher number of weld passes (Figure 6.3).

Figure 6.16 shows the geometry of both the weld joints meshed using two dimensional four nodded quadrilateral element. Since the groove angle was small (10°) and the welded plate thickness (22 mm) was larger than the specimen gauge diameter (10 mm), the weld angle was not considered in the simulated geometry. The refinement of the mesh was carried out until convergent values for von-Mises stress was obtained. The contours of the stress distribution obtained with an applied stress of 175 MPa after duration of 750 hours of creep exposure for both the weld joint geometries are shown in Figure 6.17. Figures 6.18(a) and (b) show the variation in stress gradients with different hours of creep exposure.

Figure 6.19 (a-c) shows the tri-axiality factor, von-Mises stress and principal stress normalised with the applied stress. For the weld joint made with 2.5 mm electrode diameter, the gradients in von-Mises stress and principal stress were more prominent in the base metal/HAZ interface. Since the boundary between the base metal and HAZ is not distinct, failure is not likely to get initiated at this interface. On the contrary, stress gradients across the fusion zone and the HAZ are likely to initiate failure across the interface. Since the gradients between the fusion zone and the HAZ are sharper for the joint fabricated with 4 mm electrode diameter, failure occurred at fusion metal/HAZ interface (Figures 6.9(b) and (d)).

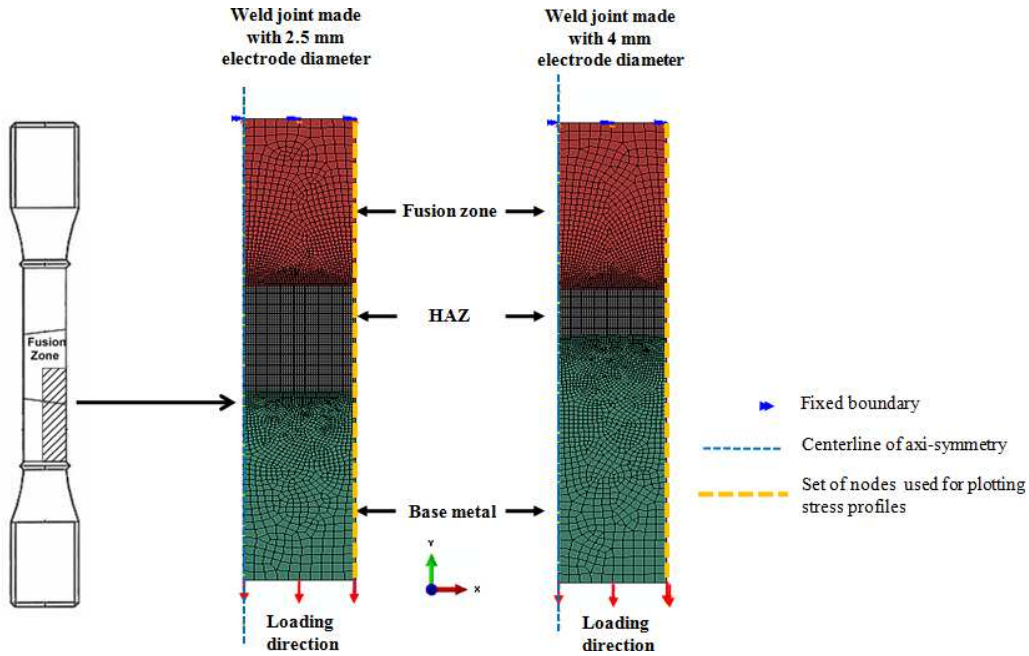

Figure 6.16 One-fourth of the weld joint geometry meshed using quadrilateral elements showing the boundary conditions and the surface where load was applied.

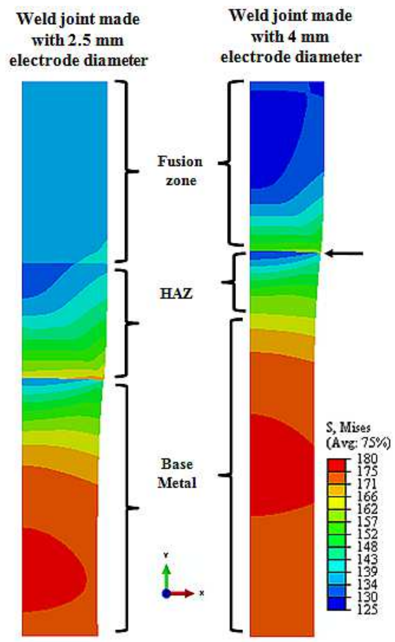

Figure 6.17 Stress contours on the deformed geometries modelled with an applied stress of 175 MPa for 750 hours. The region where significant deformation occurred in 4 mm electrode diameter weld joint is indicated.

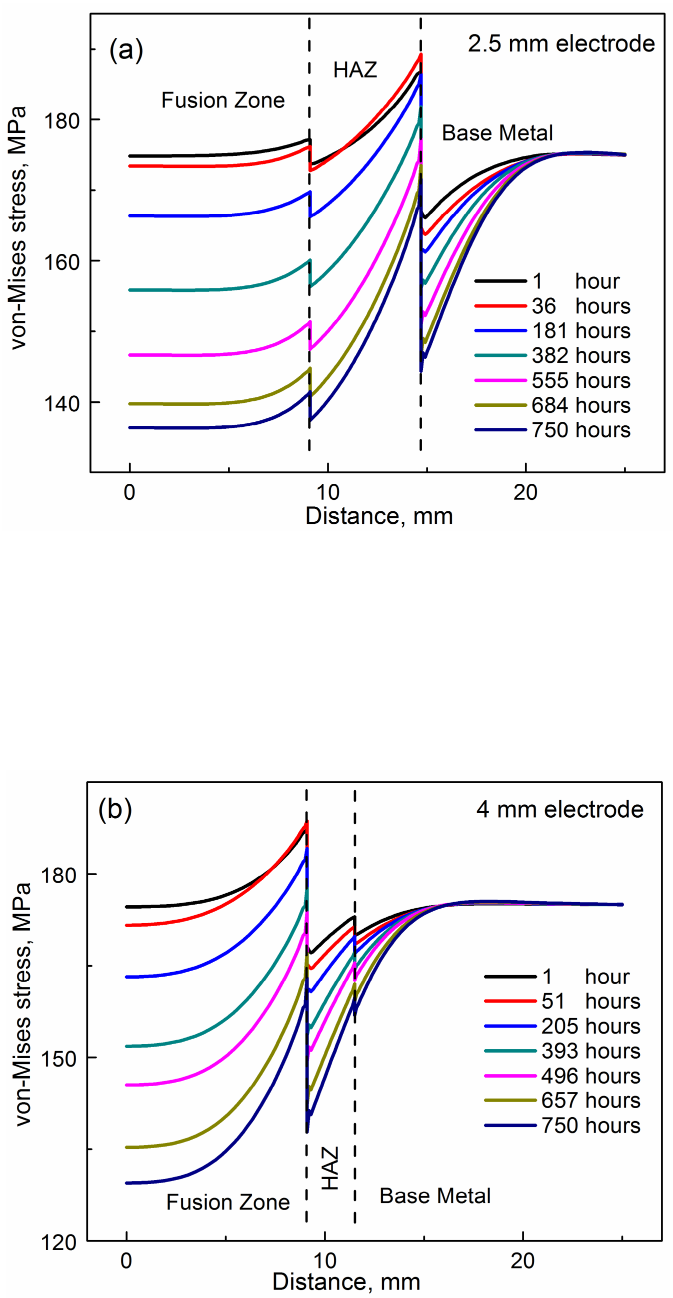

Figure 6.18 Variation of von-Mises stress for weld joint made with (a) 2.5 mm electrode diameter and (b) 4 mm electrode diameter along the set of nodes indicated in Figure 6.16 with different durations of creep exposure.

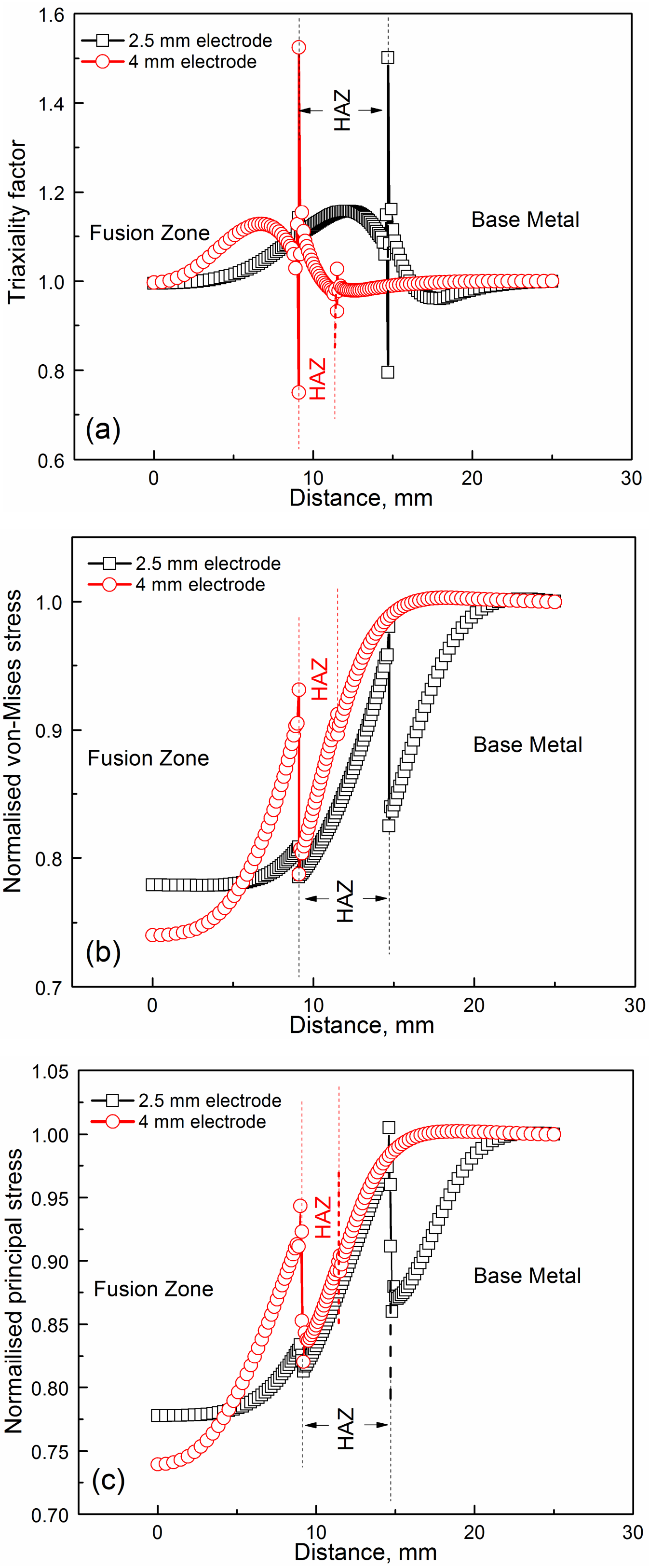

Figure 6.19 Variation of (a) tri-axiality factor (b) normalised von-Mises stress and (c) normalised principal stress across the set of nodes indicated in Figure 6.16.

FE simulations also give greater understanding about the creep cavitation in the two weld joints. The von-Mises stress not only causes plastic deformation, but also aids in nucleation of cavities [124]. The principal stress on the other hand promotes cavity growth by diffusion process [124]. The tri-axiality factor $((\sigma_1 + \sigma_2 + \sigma_3)/\ \sigma_{von\text{-}Mises})$ gives the measure of constraint caused by the 'metallurgical notch' [125]. Though the von-Mises stress and principal stress are higher in the base metal and HAZ region, fusion zone is the most susceptible region to creep cavitation due to the presence of transformed intermetallics in this region. Within the fusion zone, the normalised von-Mises stress, principal stress and tri-aixiality factor are higher near the fusion metal/HAZ interface for both the joints. Amongst the two weld joints, this factor was marginally higher for the weld joint made with 4 mm, thus the propensity of cavity nucleation and growth is more significant in this joint. In addition to this gradient, the increase in the tri-aixiality factor in this region restricts plastic deformation and aids cavity growth by diffusion. Thus, the influence of the 'metallurgical notch' is more pronounced in case of weld joint fabricated with larger electrode diameter. Thus, creep cavitation is more pronounced in fusion zone of the weld joint made with larger electrode diameter, especially at regions adjacent to the fusion metal/HAZ interface at stress levels of 175 and 200 MPa (Figure 6.9 (b) and (d)).

As mentioned in the previous section, though cavitation was prevalent in this region its propagation was restricted in the vermicular ferrite region, and could not propagate due to the presence of the thermo-mechanically treated globular ferrite region. The failure in these joints occurred at fusion metal/HAZ interface where stress gradients were more significant. For the weld joint made with smaller electrode, though the tri-axiality factor near the fusion metal/HAZ interface was lower than that of the joint made with larger electrode, the distance between the cavity nucleating vermicular delta ferrite region was smaller (Figure 6.12), this caused the failure location to be within the fusion zone.

6.5 Fractographic characteristics of failed weld joints

Though the failure of the weld joints made with 2.5 mm electrode was within the fusion zone at both the applied stress levels of 175 and 140 MPa, the nature of nucleation of cavities and crack propagation was quite different. Figure 6.20 (a) and (b) shows the fractography of the corresponding weld joints. The leading (A) and the trailing edges (B) of the fractograph and those in the corresponding optical micrographs (Figure 6.9(c) and (e)) are indicated. It can be clearly seen from the corresponding cross-sectional optical images that the dendritic facets were fairly coplanar for the joint tested at 140 MPa whereas, there were more corrugations in the fractograph of the specimen tested at 175 MPa. Variations in failure mechanism in both these testing conditions can be explained by either the domination of nucleation or the propagation during creep exposure.

At elevated temperature exposure under the influence of an applied stress, nucleation of cavities occurs in the vermicular delta ferrite region near the weld pass interface. Since the weld pass interfaces are higher in number for the joints made with 2.5 mm electrode diameter, there are comparatively several nucleating sites for creep cavities. But at higher applied stress, the propagation of these cavities is more dominant and therefore fewer nucleating sites are sufficient for interlinking of these propagated cracks. Another attribute assisting the formation of cavities is the tri-axiality factor. The increase in the tri-axiality factor denotes more constraint to plastic deformation. It can be seen that for both the weld joints, the tri-axiality factor was quite high at the fusion metal/HAZ interface (Figure 6.19(c)). However, cavities originate at boundaries which are at an angle of 45° to the stress axis, where the critically resolved shear stress is highest to cause extensive grain boundary sliding. This is the reason why cavitation was more prevalent in the fusion metal region adjacent to the interface rather than at the interface itself (Figure 6.9 (b)). The propagation of creep cracks at an angle of 45° creates significant corrugations at the fracture surface of the weld joint made with the smaller diameter. The presence of such corrugations is a signature of significant propagation of creep cavities. The number of cavity nucleation sites needed for reducing in the load bearing cross sectional area is comparatively less in number at 175 MPa when compared to the joint tested at 140 MPa. This trend was more explicit for the joint tested at 200 MPa, where even more corrugations could be observed (Figure 6.9(a)).

For the weld joints fabricated using 4 mm electrode diameter at an applied stress of 200 and 175 MPa, there were similar cracks which had propagated at an angle of 45° to the stress axis (Figures 6.9(b) and (d)) as observed in the weld joint fabricated with smaller electrode diameter, but the lack of interconnectivity between the cracks enhanced the rupture life. The contributing factor for failure of this joint was the significant strength mismatch between the HAZ and the fusion zone, which resulted in interface failure. The fractograph of this weld joint showed dimples endorsing the contribution of the more ductile HAZ (Figure 6.21 (a)). At the applied stress level of 140 MPa, the fractograph of the weld joint fabricated with 4 mm diameter had fewer corrugations (Figure 6.21(b)) as observed in case of the joint fabricated with 2.5 mm diameter. Prolonged elevated temperature exposure resulted in complete transformation of delta ferrite even in the globular ferrite region. As the cavity nucleating sites are abundant at this stress level, failure occurred by interlinking of these cavities without significant crack propagation.

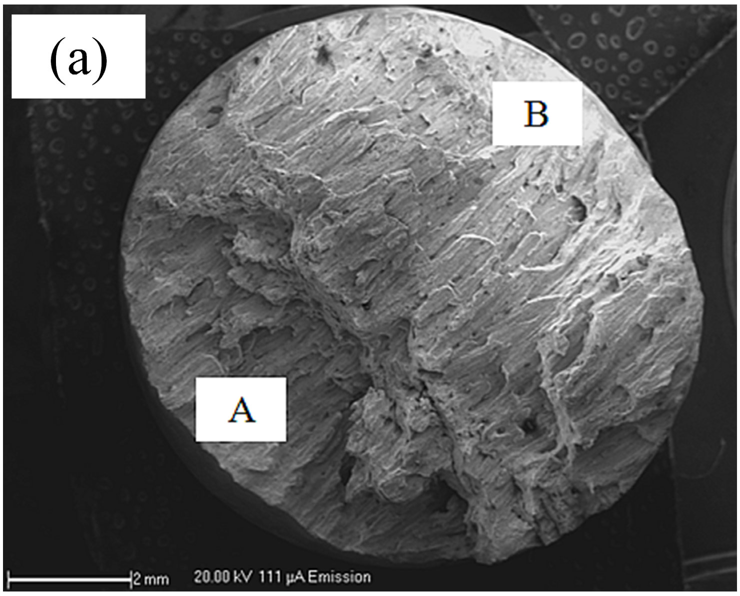

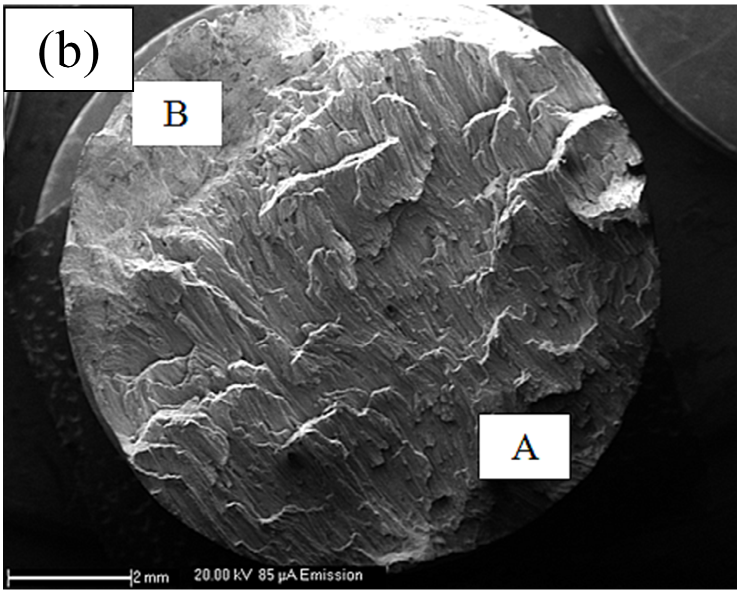

Figure 6. 20 Fractograph of the weld joint specimen fabricated with 2.5 mm electrode diameter creep tested at (a) 175 MPa and (b) 140 MPa. A and B refer to the leading and trailing ends respectively.

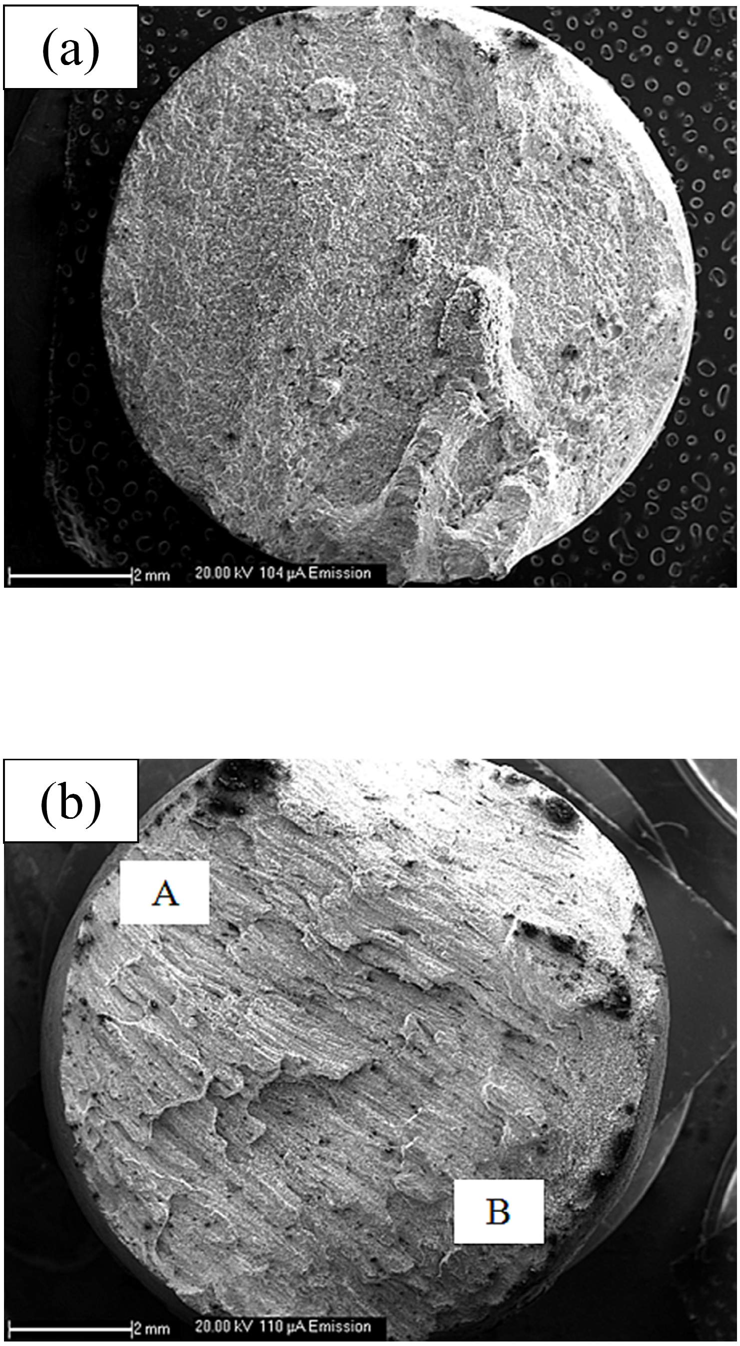

Figure 6. 21 Fractograph of the weld joint specimen fabricated with 4 mm electrode diameter creep tested at (a) 175 MPa and (b) 140 MPa. A and B refer to the leading and trailing ends respectively.

6.6 Conclusions

Based on the detailed investigation of creep deformation and fracture behaviour of 316LN SS joints, fabricated employing two different electrode diameters, the following conclusions have been drawn:

1. The two microstructural modifications (viz., change in delta ferrite morphology and formation of a localized thermo-mechanically treated region) as a resultant of subsequent weld pass deposition were evident in both the weld joints.
2. The change in electrode diameter resulted in significant variations in the formation of thermo-mechanically treated regions adjacent to the weld pass interface. The influence of electrode diameter on morphological change was not pronounced.
3. The increase in size of electrode diameter led to the increase in creep rupture strength.
4. Though the sequence by which failure occurred was similar in both the weld joints, the kinetics of damage caused by creep cavitation varied significantly which influenced the creep rupture life.
5. The constraint created in the previous pass was more significant in case of the joints fabricated with larger electrode, which prevented the propagation of creep cavities leading to increase in creep rupture life.
6. The propensity of crack propagation was enhanced in the weld joint made with smaller electrode as the cavity nucleating sites were closer, resulting in shorter rupture life.

CHAPTER 7

CREEP STRAIN ESTIMATION USING EBSD

Chapter 7

Creep Strain Estimation using EBSD

7.1 Introduction

The inhomogeneity in microstructure of the fusion zone and its influence on creep rupture properties has been exhaustively discussed in the previous three chapters. It is however essential to note that strain inhomogeneities can occur even in the adjoining base material region of the weld joint during creep deformation. The fusion zone generates stress gradients across the weld joint which is the cause for generating such inhomogeneities. The stress gradients in turn can produce variations in strain across the various regions of the base material on creep exposure of the joint. In this chapter, a novel method has been described to estimate the strain in various regions of the base metal using an EBSD based parameter. The values obtained by this parameter were correlated with the results obtained from FEA simulation. In this investigation the weld joint fabricated with 3.15 mm electrode diameter, whose creep deformation properties were discussed in Chapter 4 is analyzed.

7.2 Strain measurement by EBSD- an overview

In recent years, measurement of strain using EBSD analysis has gained significant momentum [126]. The general understanding in such analysis is that the presence of dislocations can cause lattice distortions which can alter the EBSD patterns. The presence of geometrically necessary dislocations (GNDs) which cause such lattice distortions can result in a net non-zero Burgers vector in the region; as a result the local orientations in the lattice are altered. Measuring the orientation gradient can therefore give a measure of the plastic strain accumulated in the material [127]. This method can be used to correlate the effect of crystal orientation changes in submicron level and the accumulated bulk plastic strain. In cases where the area under investigation for the determination of strain is very small, this method can be well suited for measuring localized plastic strains. Many parameters have been developed based on EBSD, which can be correlated with the gross plastic strain in the material. Quantifying plastic strain based on change in EBSD patterns which is reflected in the image quality is one of the earliest method which has been attempted by some researchers [128, 129]. It has also been found out that the average orientation spread could be an effective parameter characterizing the degree of plastic deformation. Plastic strain induces an orientation gradient in the lattice and using the orientation gradient the GNDs can also be directly estimated [130, 131]. Alternatively, it has been shown that the plastic strain in a material can be related to a scalar parameter which characterizes the orientation within a grain. The calculation of mean misorientation can be carried out either by spatially correlated or uncorrelated misorientations. The various parameters used to evaluate the plastic strain have been reviewed by Brewer [132] and Wright [127]. A brief description of three popular methodologies is given below.

a) *Grain Orientation Spread (GOS):* In this method the misorientation is calculated between each scan point in the grain and the average orientation in the grain. The average orientation of the grain is calculated by a method described by Kunze [133]. The GOS of the grain is then calculated from the mean of these calculated misorientations.

b) *Grain Average Misorientation (GAM):* This is a measure of average misorientation between a neighboring pair of scan points in a grain. This method is more sensitive to step size. Smaller step sizes yield lower values of GAM.

c) *Kernel Average Misorientation (KAM):* Kernel is described as a set of points surrounding a central scan point. The KAM is similar to GOS except that it is estimated for a kernel. The misorientations are calculated for each point with respect to the nearest neighbors. The calculated average of the kernel is then assigned to the central scan point. KAM is very useful for estimating localized strain.

Apart from these methods, commercial EBSD software have other customized tools for estimating strain.

7.2.1 Quantification of orientation spread within the grain

In this study, the crystal deformation (C_d) parameter which quantifies the average intra-grain misorientation (AMIS) [134, 135] has been used to measure the localized strain variation across the base metal of the creep tested 316LN austenitic stainless steel weld joint. It was reported that this parameter is less sensitive to scan step size when compared to the strain measurements using other parameters based on local misorientation [126, 135]. However, it should be noted that the step size should be judiciously chosen to get a gross representation of the orientation spread within the grain. A comparatively larger step size can average out the minor gradients across smaller scan distances. The grain size also holds a definitive role in determining the appropriate step size needed for the analysis. In most of the analysis, the step size was fixed in such a way that at least 10 scan points could be obtained from each grain. In this study, the threshold misorientation angle between neighboring points for demarcating two different grains was 10°. Since the orientation spread of only austenite grains was evaluated, all other indexed phases like delta ferrite and $M_{23}C_6$ were not considered during estimation of the orientation spread. The scaling up of orientation spread within a grain to the bulk strain was carried out based on the assumption that the contribution of strain is only due to GNDs and not by statistically stored dislocations. Since the estimation of the parameter is based on comparison between the strained and unstrained material, it requires the construction of a calibration curve using materials deformed to predetermined plastic strain levels. Using the calibration curve, the strain can be back-calculated from the measured C_d which characterizes the orientation spread. The calculation of C_d in this study was based on the Euler angles obtained by orientation imaging microscopy (OIM) using a fully automated EBSD system. A brief description of the methodology adopted in correlating bulk strain and with parameter C_d is provided in the following section.

7.2.2 Calculation of the parameter C_d

Plastic strain induces orientation gradient within a grain. The misorientation of each point with reference to a central orientation increases with plastic strain. In this analysis, the central orientation value of the grain is assigned to the location which has the least sum of misorientations with all the other orientations in that particular grain. The misorientation between two points i and j can be computed from their respective orientation matrixes g_i and g_j. The 24 symmetry operators applicable for fcc crystals were applied to get the least value for both the orientation matrices. The misorientation M (i,j) between two points is then given by

$$M(i,j) = min\left[\cos^{-1}\left(\frac{trace\left[g_i(g_j)^{-1}\right]-1}{2}\right)\right] \tag{7.1}$$

Here *min* refers to the minimum of value obtained after applying the 24 symmetrical operators to both the points i and j, *trace* refers to the sum of the main diagonal elements in the computed matrix.

The scan point having the least sum of misorientations (S_c) with respect to all the other pixels (n) is defined as

$$S_c = \min \sum_{i=0}^{n} \sum_{j=0}^{n-1} M\,(i,j) \qquad (7.2)$$

This point is considered as the one having central orientation for that particular grain.

The crystal deformation C_d is given by

$$C_d = \sum_{i=0}^{n} M(c,i)\,/\,n \qquad (7.3)$$

where c refers to the point with the central orientation. The arithmetic mean of this parameter derived for several grains in the region of interest was used to obtain the value of C_d. In this study an algorithm written using C program was used for the calculation of parameter C_d.

Figure 7.1 shows the Inverse Pole Figure (IPF) map and the corresponding orientation spread for the solution annealed specimen and for the specimen deformed plastically to a strain of 0.15 at ambient temperature by tensile pulling using a universal testing machine. It is clear from these figures that the orientation spread within a grain increases with plastic strain. In fact it has been shown that the parameter C_d is linearly dependent on the plastic strain [126,135].

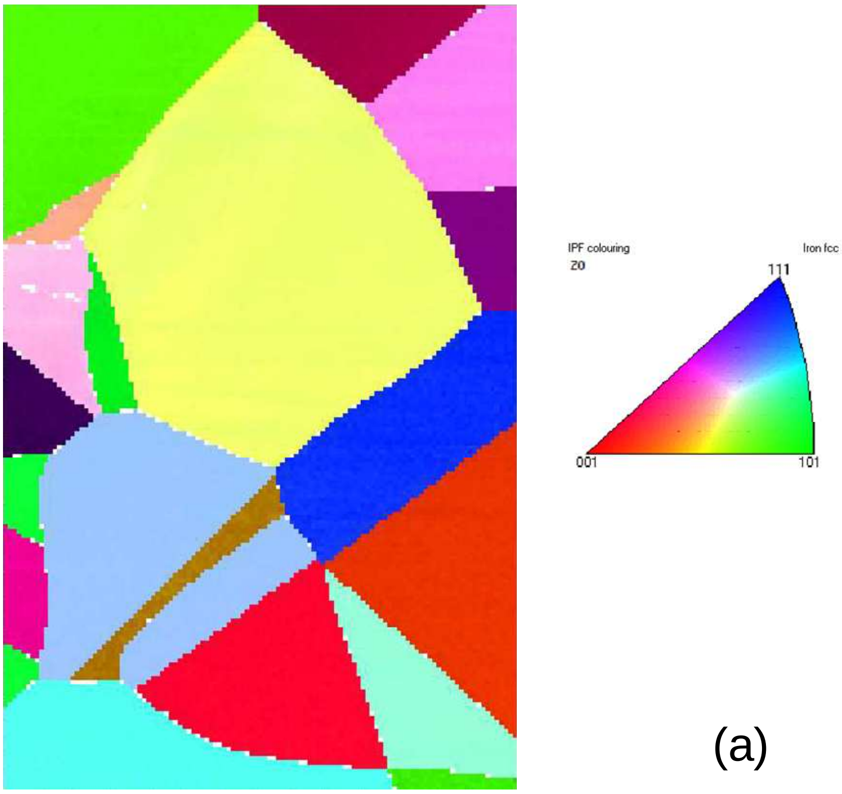

(a)

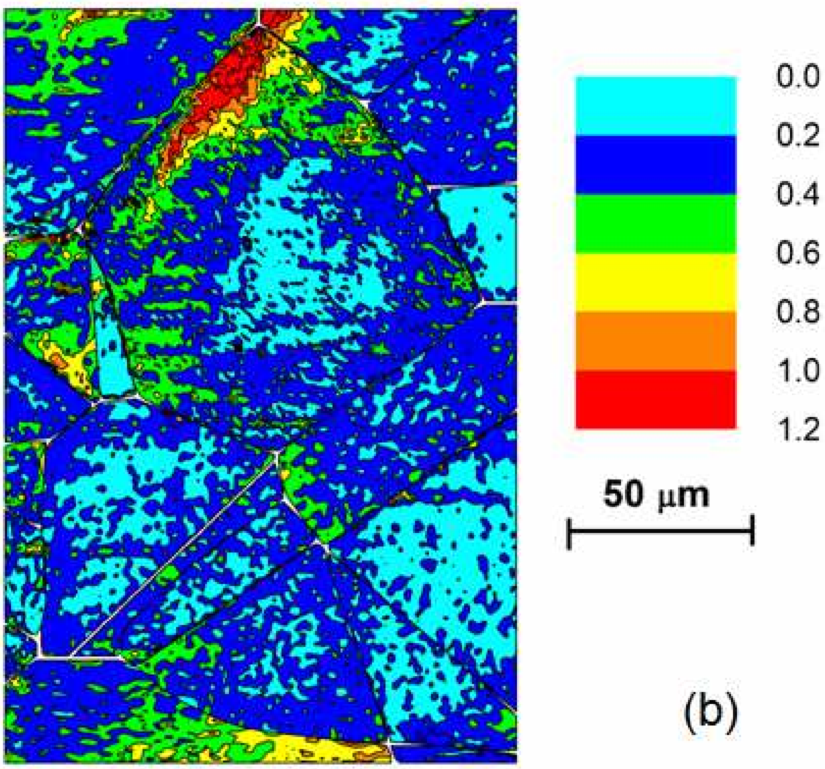

(b)

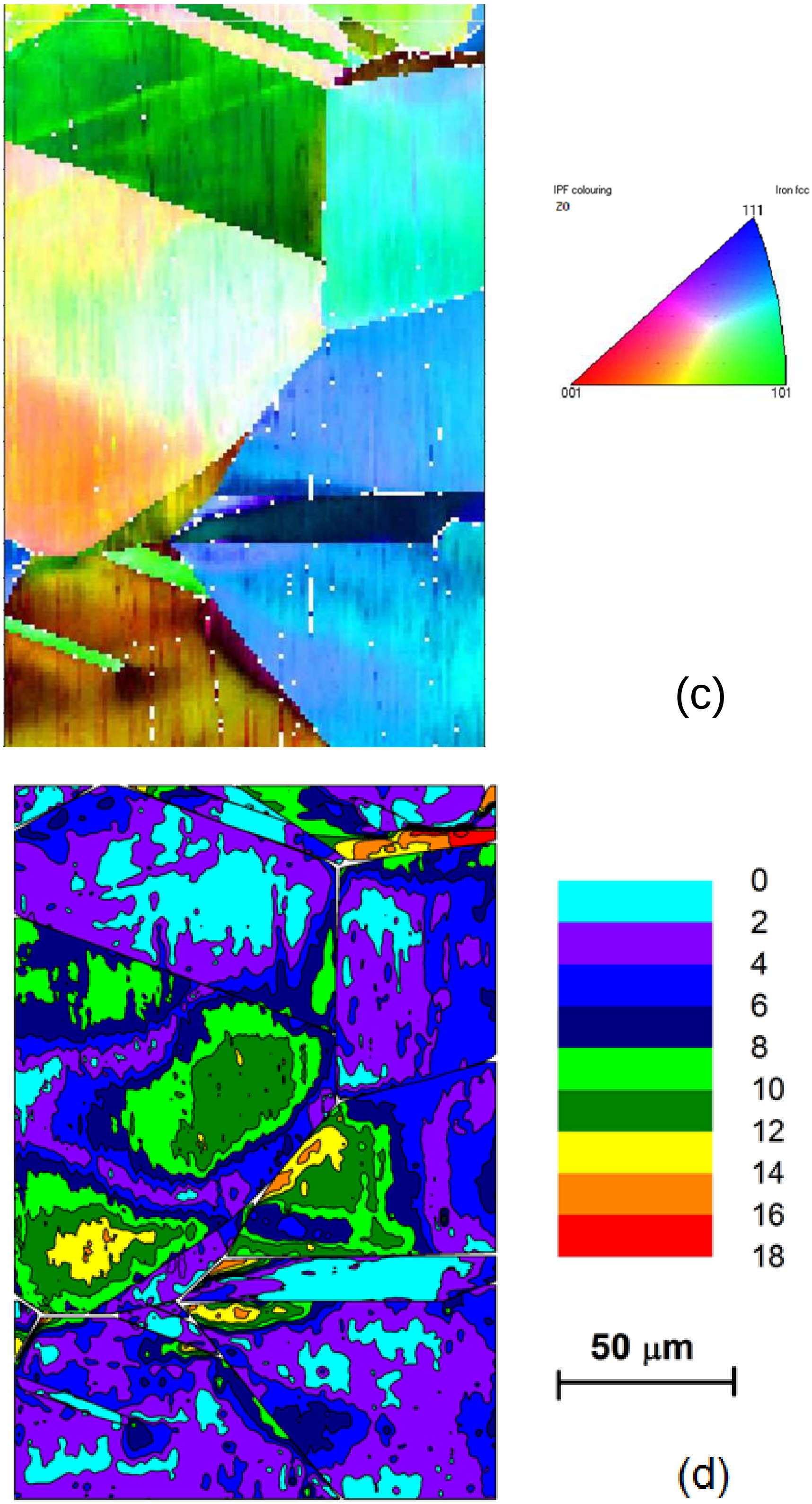

Figure 7.1 IPF map of (a) solution annealed and (c) with a cold work of 0.15 and their corresponding misorientation profiles (b) and (d).

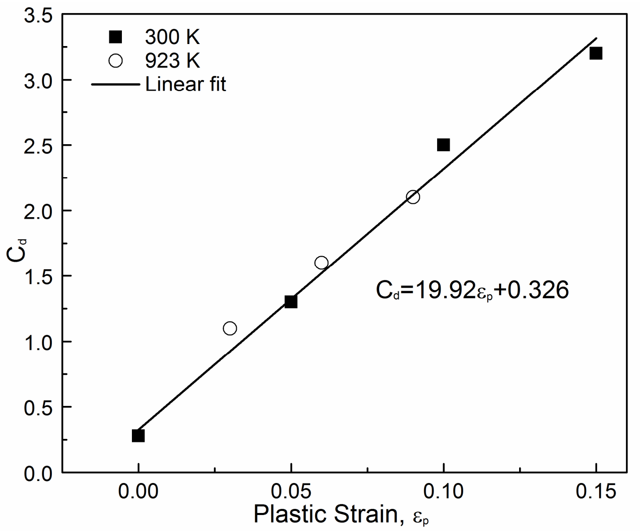

Figure 7.2 Calibration graph relating crystal deformation parameter C_d and plastic strain ε_p at 300 and 923 K.

In this study, a calibration curve was constructed by plotting values of C_d for various known strain levels imposed on the base metal by uniaxial tensile load. An empirical equation deduced from this relationship was then used to estimate the plastic strain directly from the parameter C_d. A calibration graph correlating C_d and various strain levels obtained after deforming the base metal to different strain levels at 300 and 923 K is shown in Figure 7.2. It could clearly be seen that at both the room and high temperatures, the values of C_d could be satisfactorily correlated to the plastic strain by a linear equation. It has been reported that the C_d values are independent of temperature [136] but can depend on the strain rate [135]. Though the strain rates during creep were relatively lower (of the order of 10^{-6} s^{-1}) than that of the tensile tested specimens (10^{-4} s^{-1}), the correlation of this parameter is still considered quite valid for lower values of accumulated strain (< 0.13). The non-zero value of C_d for the specimen with no plastic strain could be due to minor strains introduced by processes like solution annealing followed by cooling and mechanical polishing [134].

The measurement of strain by EBSD parameter C_d has been restricted to base metal due to complications in estimating the orientation spread and obtaining reference pre-strained specimens for the fusion zone and HAZ. Estimation of the parameter in the fusion zone was even more complicated due to the presence of delta ferrite. As mentioned earlier, for correlating the bulk strain to the metric C_d, a calibration curve was required which could be generated from base material deformed to various levels of plastic strain. Generating this calibration curve is much more complicated for the fusion zone, which requires extraction of all-weld specimens from the weld joints, which during the process can induce additional strain. Further, deriving the parameter C_d for fusion zone and HAZ is more intricate because of its larger grain size.

In this study, the EBSD data was acquired from three equidistant regions in the base metal which are indicated in Figure 7.3. These locations were designated as near HAZ (region1), midway (region 2) and near ridge (region 3). The step size used in the analysis was 1.25 µm. The average orientation spread for at least 20 grains were used to get the average value of the EBSD parameter in that particular location. The number of data points in each grain varied from 1200-2500.

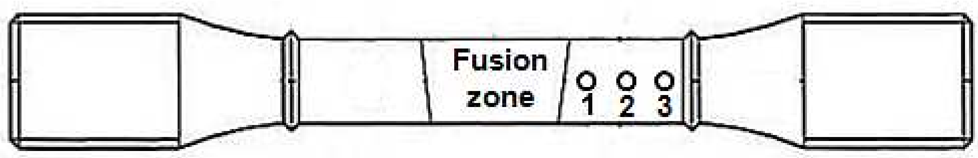

Figure 7.3 Schematic showing the locations from where the EBSD analysis was performed in the weld joint specimen.

7.3 Evolution of strain gradients in weld joints

The deformation characteristics of the fusion zone and HAZ are markedly different from that of the base material. As a consequence plastic flow occurs non-uniformly across the fusion zone, heat affected zone and base metal to redistribute the stress generated due to the imposed constraint. Conventional elongation measurement techniques estimate only the overall elongation of the composite weld joint specimen. Since there is a gradient in strain across the weld joint, its estimation becomes cumbersome. Therefore, estimation of the strain by calculating the orientation spread in the narrow regions is a more viable technique for such complicated cases.

7.3.1 Estimation of local mechanical properties

Though estimation of strain gradients in 316LN weld joints by conventional techniques is improbable, the finite element analysis can provide an overall trend in the strain gradients. The strain values obtained from FEA can be useful to validate the results obtained from the EBSD parameter. ABAQUS version 6.11 was used for simulating the stress and strain gradients in the constructed weld joint geometries. The creep specimen used in the testing had geometrical symmetry and hence only one half of it was modeled. The region beyond the gauge length was also used in the model to give a clearer trend of the stress and strain distribution in the specimen. The properties of the fusion zone, HAZ and the base metal were assigned to each region after partioning the specimen based on the hardness values. Three dimensional 4-noded linear tetrahedron (C3D4) was used to model the entire geometry of the specimen (Figure 7.4). A 3-D simulation could be attempted in this case as the strain incompatibly between the three regions was not as significant as observed in the weld joint made with 4 mm electrode diameter which was examined in the previous chapter. The mesh size was refined until convergent values for von-Mises stress was obtained.

Y-axis symmetry boundary condition was applied to face 1 thus constraining the displacement along this axis. The load was applied on face 2 of the specimen.

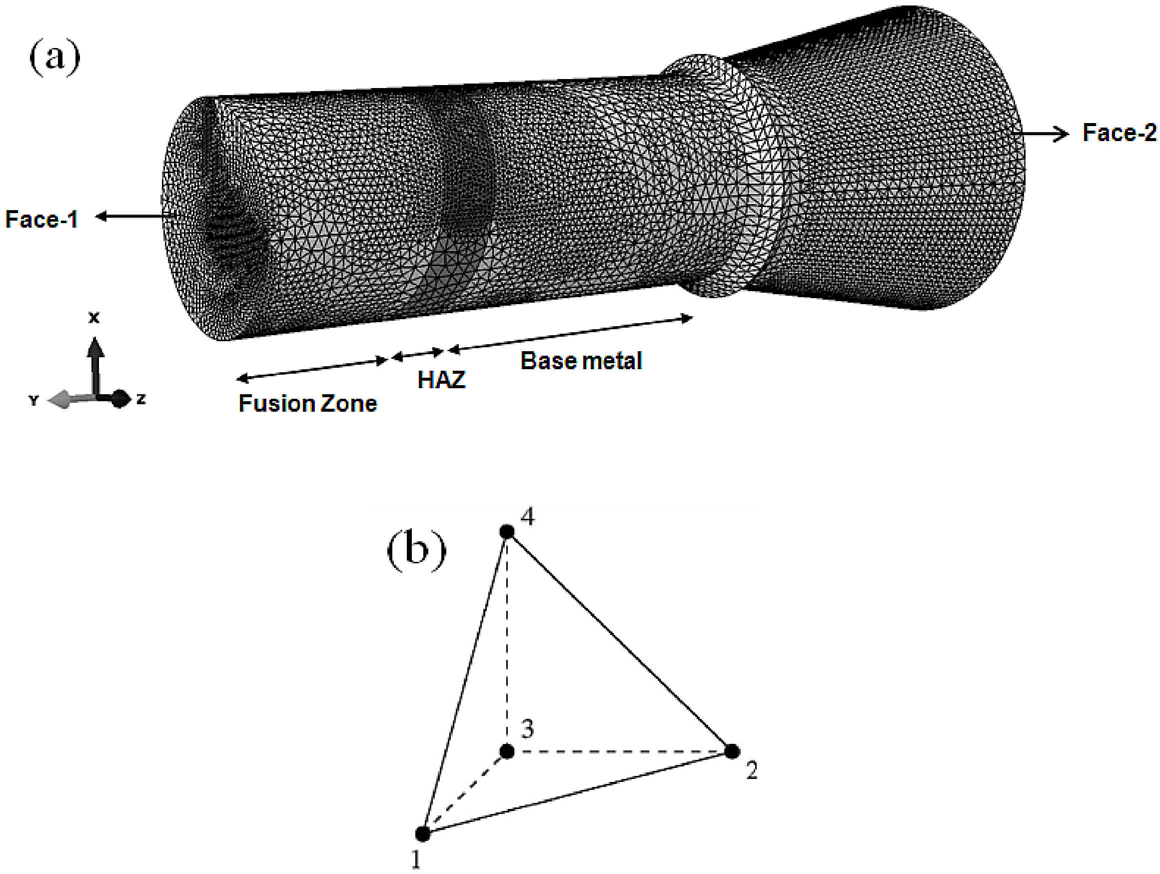

Figure 7.4 (a) One-half of the meshed weld joint specimen partitioned into different regions based on the variation of microstructure and geometry, (b) Schematic of the 4-node linear tetrahedron element (C3D4) used for meshing the specimen geometry.

Strain continuously accumulated to various degrees in the composite weld joint specimen during the creep test. The time duration for simulation should be fixed in such a way that the estimated value for strain gradients must be indicative values to the actual strain values in the specimen. Figure 7.5 shows the plot of time to onset of tertiary of the base metal, the rupture life of the weld joint and the duration of simulation used in the FEA analysis. The duration of the secondary regime of the weld joint was much shorter than the onset of tertiary in the base metal; hence the steady state creep behavior of the base metal could be used for the entire duration of simulation. The simulation also reached a saturation solution after this time duration.

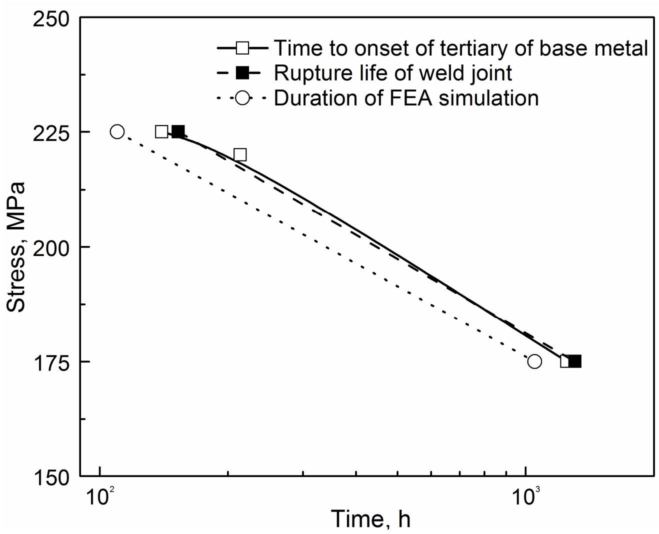

Figure 7.5 Plot of time to onset of tertiary in base metal, the rupture life of weld joint and the duration of simulation. The duration of simulation for both the stress levels was shorter than the time to onset of tertiary in the base metal and was equivalent to the duration of the secondary state regime of the weld joint specimen.

The estimation of mechanical properties of the three individual regions is essential for carrying out FEA simulation on the corresponding geometry. The tensile properties were obtained from the ABI technique and the creep properties from ICT. The tensile properties were incorporated by the dependence of true plastic stress on true plastic strain obtained from ABI testing. As mentioned in Chapter 6, there are sources in literature citing excellent correlation between the data obtained from the miniature specimen testing techniques and the conventional uniaxial testing [98,99]. Figure 7.6 shows the variation of the tensile properties as estimated by the ABI technique. The base metal region of the weld joint had the lowest yield stress followed by the HAZ. The ultimate tensile strength was highest for the HAZ when compared to the other two regions. The trend in variation of tensile properties in the three regions was similar to what was observed in the previous chapter.

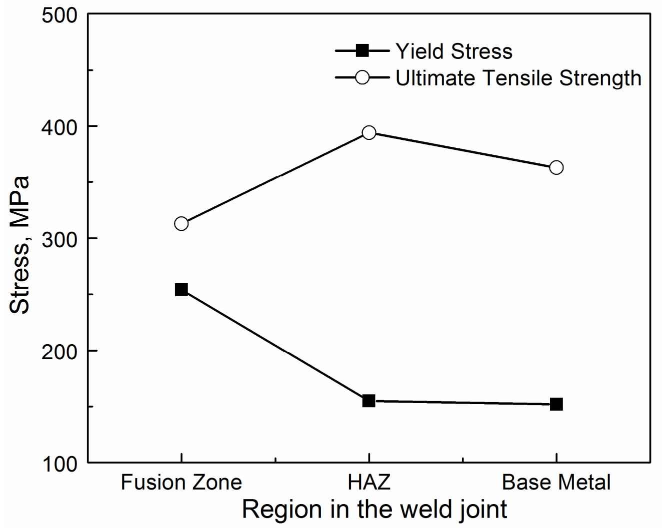

Figure 7.6. Variation of yield stress and ultimate tensile strength of the fusion zone, HAZ and base metal at 923 K.

The Norton's law $\dot{\varepsilon}_s = A\sigma^n$, relating the secondary creep rate and the applied stress obtained by ICT was used as the constitutive equation for creep deformation analysis using FEA. Since the Norton's law characterizes only the second stage of the creep deformation behaviour, FEA analysis was carried out only up to the duration of the secondary stage. The values of the constants A and n of the Norton equation ($\dot{\varepsilon}_s = A\sigma^n$) were obtained from the impression creep tests conducted at 923 K and at equivalent uniaxial stress levels of 150-225 MPa are given in Table 7.1. The stress values of n are greater than 3 suggesting that the governing mechanism for creep deformation in all the three regions was dislocation creep. The values of n were higher in case of fusion zone and HAZ than the base metal suggesting that there was significant back stress present in these two regions as a result of higher dislocation density. The modulus of elasticity (150 GPa) and the Poisson's ratio (0.29) were assumed to be similar for the fusion zone, HAZ and base metal of the joint [137]. Since the FEA were carried out for the weld joints creep tested at high temperature, the effect of initial welding residual stress was not incorporated in the simulations and the joint was assumed to be fully relaxed before loading.

Table 7.1 Values of the Norton's power law constants A and n used in the ABAQUS simulation.

	Fusion Zone	HAZ	Base Metal
A($MPa^{-n}h^{-1}$)	2.51×10^{-24}	1.74×10^{-26}	2.13×10^{-20}
n	8.6	9.3	6.9

From the results of the ABI and ICT it is clear that the deformation behavior of the three regions in the weld joint is quite different. This is the reason why the presence of fusion zone and HAZ in the composite weld joint specimen is equivalent to the presence of a circumferential notch. As in case of such a mechanical notch, this 'metallurgical notch' creates stress gradients across the length of the weld joint.

7.3.2 FE analysis of stress distribution across the weld joint

The von-Mises stress gradient across the weld joint specimens at applied stresses of 175 and 225 MPa are shown in Figures 7.7(a) and (b). The contours shown in the figures were plotted after running the simulation for the duration corresponding to the secondary creep regime of the weld joint. The steady state condition was reached in the base metal region in all the three weld joints. The gradients in stress distribution were more pronounced in the central region of creep specimen than those at the surface for the specimens tested at 175 and 225 MPa. Figures 7.8 (a) and (b) shows the variation of normalized von-Mises stress (with respect to applied stress) along the axis of the specimen and Figures 7.9 (a) and (b) show the variation of equivalent creep strain along the same axis. It could be clearly seen that due to the presence of fusion zone and the HAZ, the von-Mises stress was higher than the applied stress of 175 and 225 MPa in significant portion of the base metal.

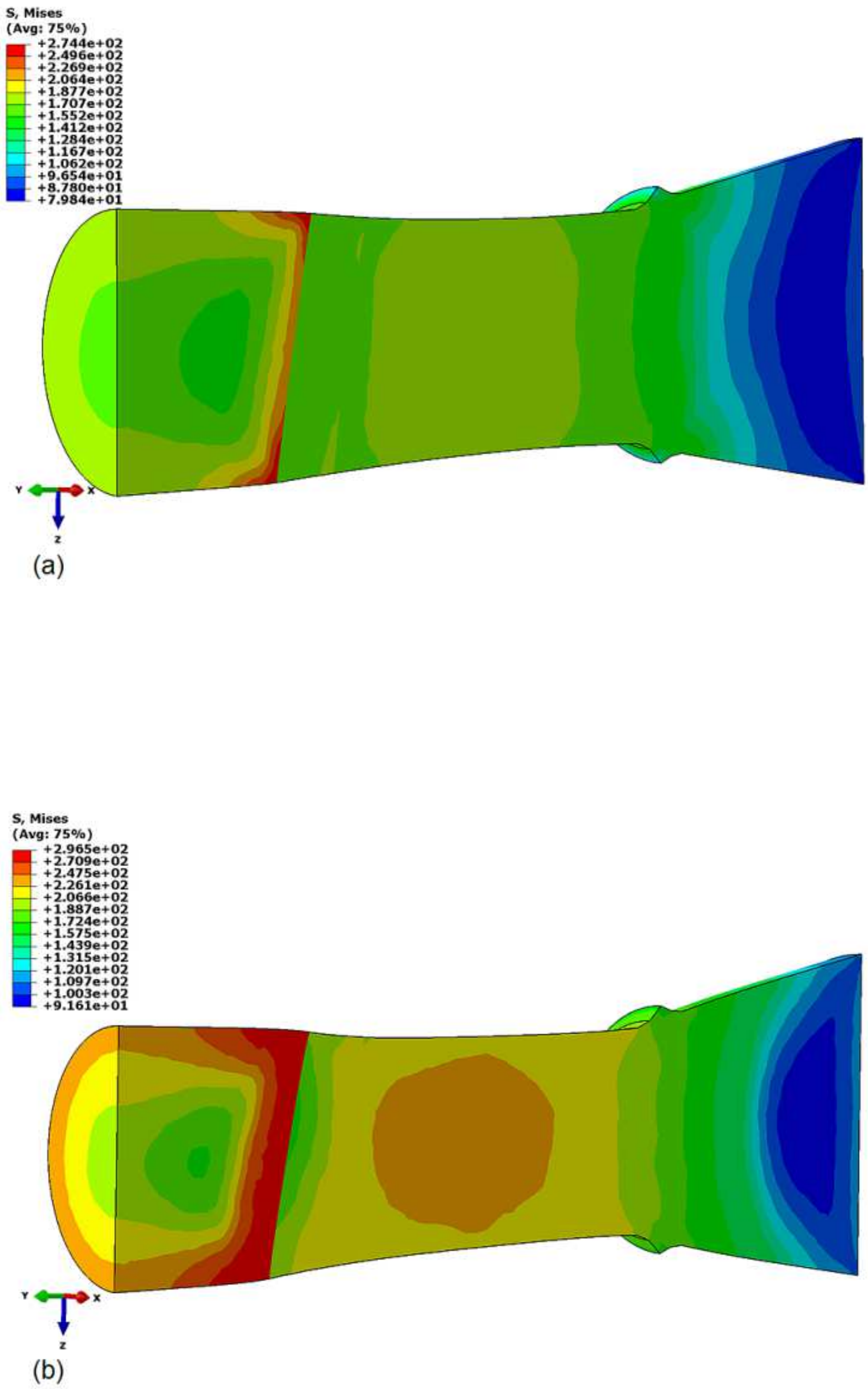

Figure 7.7 Contours of von-Mises stress for weld joints creep tested at (a) 175 MPa and (b) 225 MPa after running the simulation up to the duration of the secondary creep regime in the weld joint specimen.

The effects of stress distributions arising due to microstructural inhomogeneity in 2.25Cr-1Mo/2.25Cr-1Mo similar and modified 9Cr-1Mo / Inconel 182 / Alloy 800 dissimilar weld joints on creep rupture behaviour of the joints have been reported earlier [138, 139]. Since, plastic deformation is mainly facilitated by von-Mises stress; the variation in von-Mises stress across base metal of the joint in the present investigation would result in corresponding variation in the plastic deformation.

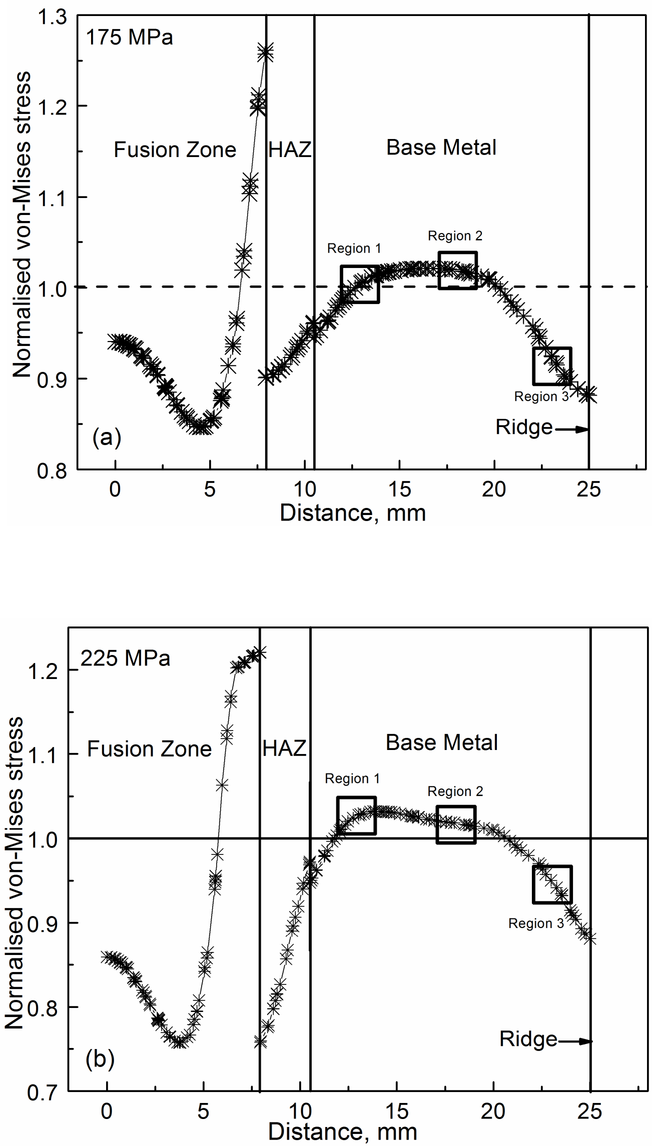

Figure 7.8 von-Mises stress distribution along the axis of the creep specimen tested at (a) 175 MPa and (b) 225 MPa.

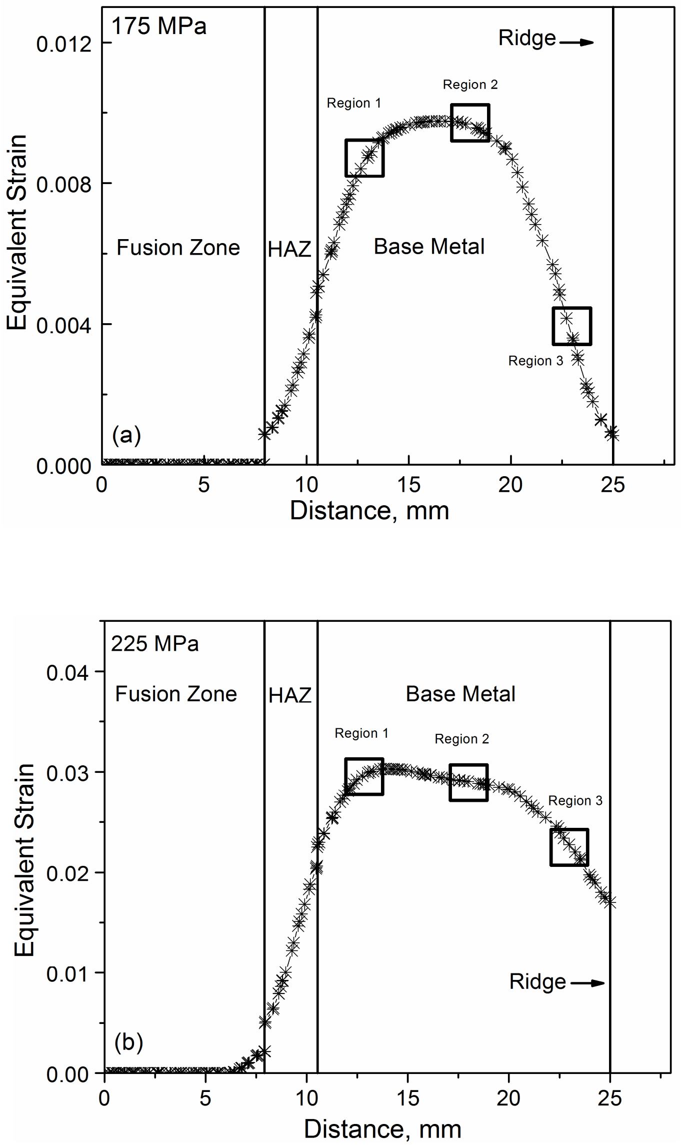

Figure 7.9 Equivalent strain distribution along the axis of the creep specimen tested (a) 175 MPa and (b) 200 MPa.

For the weld joint tested at 225 MPa there was a steady decrease in von-Mises stress and equivalent strain from the near HAZ region to the ridge portion. As discussed in previous chapter, the stress gradients are higher at interfaces, which result in significant creep deformation in the region near the HAZ. Since the gauge thickness was higher near the region 3 (near ridge portion), creep deformation was least in this region of the base metal at both 175 and 225 MPa. At 175 MPa, the fusion zone offered more resistance to creep deformation which resulted in more constraint in region 1 (near HAZ). This resulted in higher values of von-Mises stress and equivalent strain in region 2 of the weld joint.

7.4 Strain mapping using the EBSD parameter C_d

The distribution of orientation spread within the grains varied significantly on creep exposure under different applied stresses. Figure 7.10 shows the orientation spread within a typical grain in each of the three regions mentioned in Figure 7.3. Figure 7.10 also shows the variation of the accumulated bulk creep strain calculated using the EBSD parameter. The orientation spread within grain of base metal near the HAZ had a non-zero value even before creep test and this could be due to plastic strain developed by the thermal cycle of multi-pass welding process [104]. The orientation spread particularly at regions adjoining the grain boundary increased with applied stress. These values were especially higher around the boundary containing precipitate particles and at grain boundary triple points as indicated in Figure 7.10. The phase map showing the carbides pinned against grain boundaries is shown in Figure 7.11. The restriction in grain boundary sliding by grain boundary particles and grain boundary triple points results in stress concentration which increases the misorientation values in these regions with reference to the central orientation of the grain and this consequently develops strain localization.

Creep cavitation is often associated with the grain boundary precipitates and triple points. Stress concentrations are produced when precipitates resist grain boundary sliding. If these stress concentrations are not relaxed, then cavities nucleate at the precipitate/matrix interface by athermal decohesion of atomic bonds between the precipitate and matrix. The detailed sequence of caviation during creep has been discussed in Chapter 2.

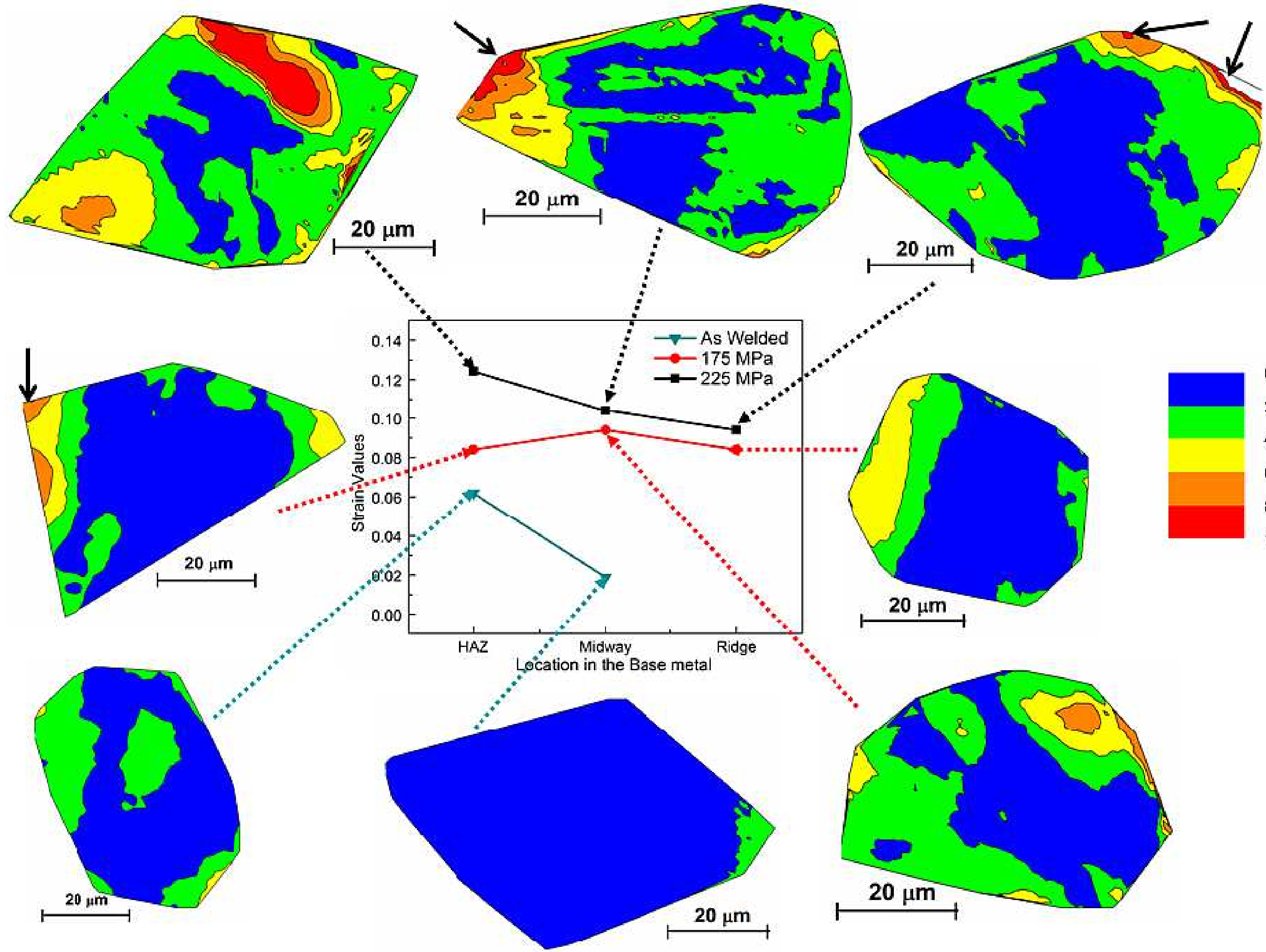

Figure 7.10 Variation of orientation spread within typical grains located in each of the three regions indicated in Figure 7.3. Variation of strain values at various regions in the base metal of the weld joint calculated using the EBSD parameter C_d is also given in the figure.

The higher misorientation around the grain boundary precipitates and triple points, leads to nucleation of creep cavity by rupturing the bond between the adjacent grains. Thus the information of misorientation around the grain boundary precipitates and triple points by EBSD technique has the potential of early detection of creep cavitation in service exposed components.

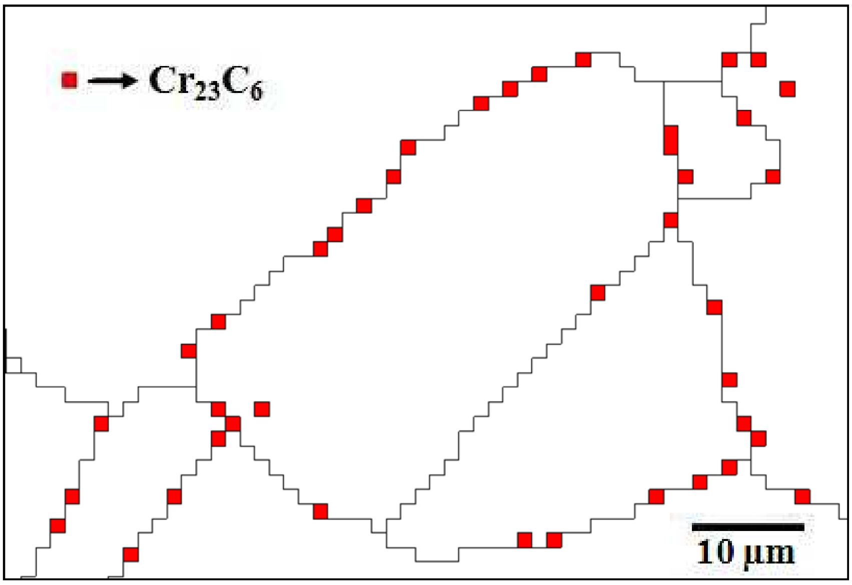

Figure 7.11 Phase map showing $Cr_{23}C_6$ carbides precipitated along austenitic grain boundaries in the near HAZ region of the specimen tested at 225 MPa.

The estimated strain values showed that the creep strain accumulation across base metal of the joint varied considerably with respect to applied stress. The base metal near to the HAZ region experienced higher creep strain which decreased progressively towards the ridge of the creep specimen tested at 225 MPa. The overall strain values increased with increase in applied stress level. As discussed earlier, for the creep specimen in the as-welded condition, the strain accumulation in base metal near to the HAZ might be due to residual stress generated by multiple thermal cycles during welding.

The strain values obtained from C_d parameter across base metal of the weld joint are in good agreement with the von-Mises stress variation (Figures 7.8 (a) and (b)). At 225 MPa applied stress, higher von-Mises stress in base metal near to the HAZ is reflected into high strain accumulation. At stress level of 175 MPa, the higher von-Mises stress in region 2 (the mid-region of base metal) when compared to region 1 is reflected into marginally higher creep strain accumulation in this region. It should be noted here that the values of strain obtained were considerably higher than the values estimated by simulation (Figures 7.9(a) and (b)). This is because the FEA simulation takes into account only the secondary stage. The trend however was comparable in both the cases.

The variations in stress gradients across the weld joint occur due the presence of the "metallurgical notch" [89]. The presence of this metallurgical notch increases the von-Mises stress to values higher than the applied stress resulting in a higher strain in region 1 and 2 of the base metal. The effect of this metallurgical notch was more severe at higher stress level of 225 MPa. At an intermediate stress level of 175 MPa, the contribution of the geometrical notch was less severe resulting in a comparatively uniform distribution of plastic strain throughout the base metal region of the specimen.

7.5 TEM analysis

The dislocation substructure in the creep tested joints can be correlated with the values of C_d estimated by EBSD. In this section, the microstructural evolution has been studied by TEM, by extracting specimens from the near HAZ region. In the as-welded condition, relatively fewer dislocations in the matrix (Figure 7.12 (a)) were observed. After creep exposure at 175 MPa, the dislocation substructure had started to evolve (Figure 7.12 (b)), signifying creep strain accumulation. For the weld joint tested at 225 MPa, there was a considerably higher density of dislocations. The presence of higher amount of these tangled dislocations resulted in an increased value of C_d (Figure 7.12(c)) than that was observed for stress level of 175 MPa. It can hence be stated that the parameter C_d can also indicate the type of dislocation substructure evolved during creep.

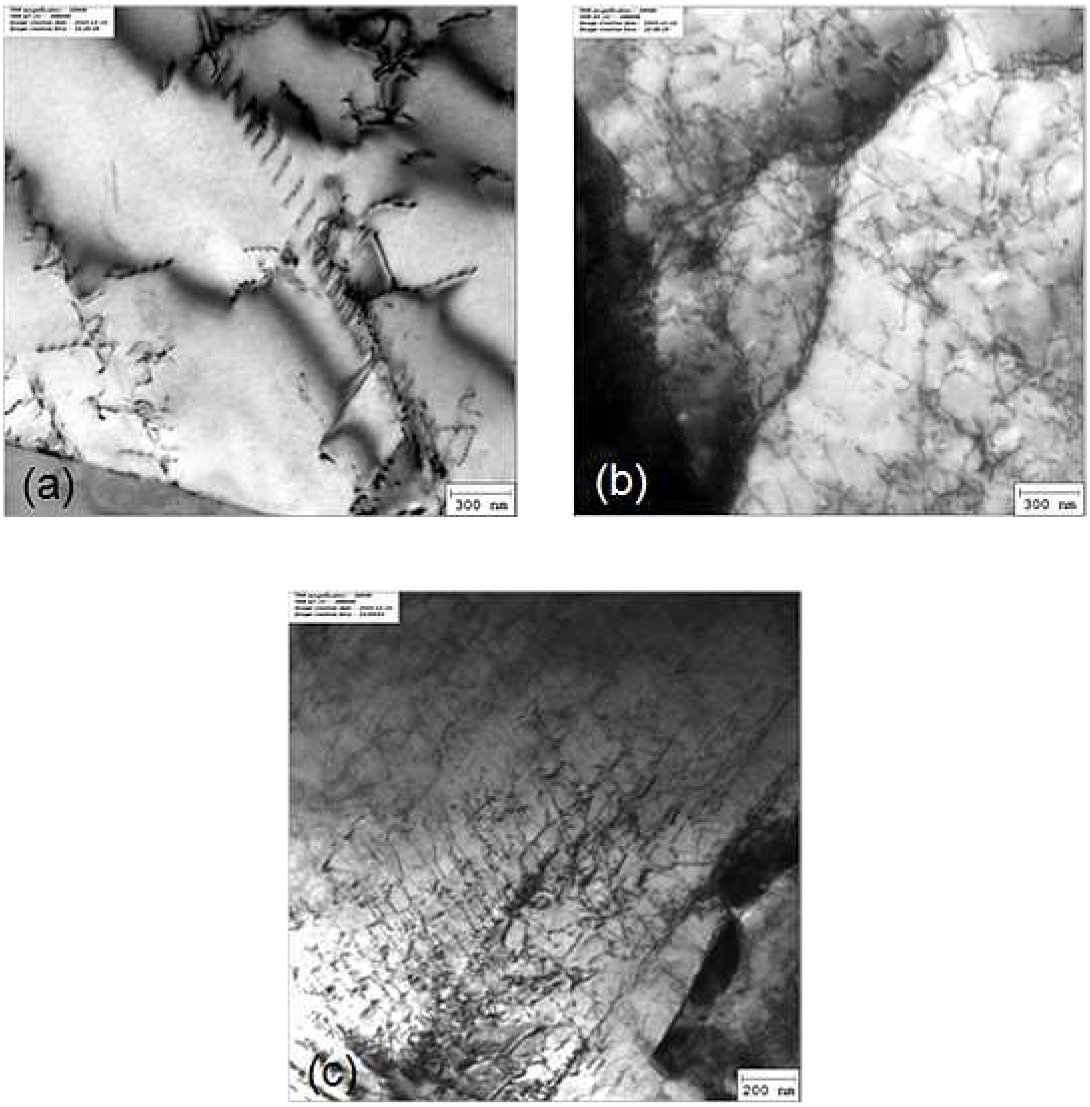

Figure 7.12 TEM micrographs of the near HAZ region (region 1) (a) in as-welded condition, (b) creep tested at 175 MPa and (c) 225 MPa.

7.6 Conclusions

The EBSD technique of estimating localized accumulation of creep strain along with FE analysis of state of stress distribution has the potential to predict the remnant life of component, which can be complemented with standard metallographic techniques. Minor variations of strain within the component can be estimated using this technique.

In this investigation, based on the studies on crystal orientation parameter C_d obtained by EBSD analysis coupled with FE analysis of von-Mises stress distribution across the base metal and TEM investigation of dislocation substructure of creep tested 316 LN steel weld joint, following conclusions have been drawn:

1. Creep strain accumulation which manifested as orientation spread across the grain varied considerably and was dependent on the applied stress. Higher strain concentration was observed near to the grain boundary region and particularly around the grain boundary pinned with particles.
2. Base metal near to the HAZ, which was subjected to higher von-Mises stress due to stress distribution resulting from the microstructural inhomogeneity across the joint, experienced higher orientation spread and strain.
3. Near one to one correspondence between the EBSD estimated orientation parameter C_d, FE estimated von-Mises stress and dislocation substructure evolution was observed.

CHAPTER 8

SUMMARY AND RECOMMENDATIONS FOR FUTURE WORK

Chapter 8

Summary and Recommendations for Future Work

8.1 Summary

The fusion zone of the austenitic steel weld joints exhibits a complex microstructure. Therefore, unlike the base metal, creep deformation and damage behaviour in weld joints are much more complicated. One of the attribute responsible for the complex and composite microstructure is the deposition of multiple passes especially while fabricating thicker sections which generate repeated thermal cycles which can significantly modify the microstructure. This study details the evolution of two types of microstructural modifications caused by the deposition of subsequent weld passes. The modifications in microstructure of the fusion zone pertained to a narrow region which was subjected to thermal cycling. Two types of modifications occurred in this regions –a) morphological changes in delta ferrite and b) dislocation sub-structural change. In the as-welded condition, the morphology of delta ferrite is usually continuous and interconnected. The higher surface area-to-volume ratio of this ‘vermicular’ morphology delta ferrite makes it unstable, which upon elevated temperature exposure fragmented into isolated ‘globular’ morphology. The thermal cycling also induced localized expansion and contraction which strengthened the region containing globular delta ferrite. In other words, it can be stated that this region is subjected to a 'thermo-mechanical treatment'. Both these microstructural modifications had significant influence on the damage caused by creep cavitation.

At elevated temperatures as during creep exposure, the delta ferrite transforms into intermetallics and carbides. The kinetics of this transformation is dependent on the morphology of delta ferrite. Since the vermicular morphology comprised of a continuous interface within the austenitic matrix, diffusion of Cr and Mo occurred readily in this region compared to the regions containing globular morphology. The precipitation of intermetallics in the globular region containing isolated packets of delta ferrite was delayed, as its morphology was comparatively less continuous.

The formation of a hardened microstructure in the globular region as a consequence of the 'thermo-mechanical effect' produced a strength gradient across the weld pass interface. Upon creep loading the gradient affected the stress redistribution which induced significant creep deformation and grain boundary sliding in the vermicular regions. Creep cavitation occurred preferentially in the vermicular delta ferrite regions due to the arrest of grain boundary sliding by prior transformed delta ferrite and lack of relaxation of stress. Therefore, both the microstructural changes played a synergistic role for nucleating cavities. The propensity for propagation of the cavities was significant in the vermicular region when compared to the globular region. This again can be attributed to the preferential stress redistribution in the softer vermicular region during creep loading. After significant propagation in the vermicular regions these cracks are arrested at the weld pass interface and do not propagate into the region having globular ferrite. The hardened globular region offered resistance to crack propagation to a greater extent.

Since both these microstructural modifications complement each other in dictating the damage kinetics in the weld metal, it is difficult to isolate their individual influences in a SMA weld joint. Hence, studies were carried out on weld joints fabricated with the autogenous A-TIG process. The fusion zone in these joints contain very low amount of delta ferrite and as a consequence the morphological changes of delta ferrite induced by subsequent weld pass is also insignificant. In this case the creep rupture properties of single and dual-pass weld joints were studied. It was observed that the rupture life of the dual-pass weld joint was higher than the single pass weld joint, depicting the beneficial effect of thermo-mechanically treated region on the creep deformation and rupture behaviour of the stainless steel weld joints.

Since the volume of the constituents within the weld passes were significantly higher when compared to those observed in the SMA joint, impression creep studies were more feasible on A-TIG joints. The results obtained from impression creep testing of the individual constituents of the weld joint showed that in the dual-pass weld joint, there was significant strength disparity between the first and second pass. The creep strength of the first pass was considerably higher than that of the second pass. As a result of which the creep cavities which nucleated in the second pass could not propagate into the first pass. Thus, with introduction of an additional pass in A-TIG weld joints, the rupture life was enhanced up to around two times than what was observed for the single-pass weld joint over the stress levels investigated.

It was clearly established that the microstructural modifications which evolved during multi-pass welding is beneficial as it enhanced the rupture life of the austenitic steel weld joints. A natural consequence of this understanding was to compare the rupture life of the weld joints, which differed due to changes in number of weld passes. Towards this perspective, creep tests were carried out on weld joints which were fabricated using two different electrode diameters viz., 2.5 and 4 mm. The number of weld passes could be varied significantly, keeping the heat input almost similar for both the sizes. The two types of microstructural modifications were evident in both the weld joints. Since the number of passes in the weld joint made with smaller electrode size was higher, it contained relatively more interface regions comprising of these two types of inhomogeneities.

The creep rupture life of the joints which had less number of weld passes i.e., weld joint made with larger electrode diameter was higher than the joint made with smaller electrode diameter. The extent of the constraint created in the previous pass due to the variation in volume of weld metal deposited had a significant role in dictating the nucleation and propagation of creep cavities. It was shown through local orientation gradients obtained from EBSD that the deposition of a larger volume of weld metal resulted in more constraint in the previous weld. Though the strength gradients across the weld joints made with larger electrode diameter was significant, the 'thermo-mechanically treated' region, which was more prominent in this weld joint resisted the propagation of creep cavities to a greater extent. Another attribute which resulted in inferior rupture life of the weld joints made with smaller electrode diameter is the proximity of the cavity nucleating regions. Since the number of weld passes was significantly higher in this weld joint, the cavity nucleating vermicular regions which were separated by globular regions were closer to each other. During creep exposure the interlinking of the cavitated regions was more feasible which reduced the rupture life of these joints.

Incorporation of additional pass in weld joints results in microstructural modifications in the fusion zone. These transformed regions offer resistance to creep cavitation. Therefore, weld joints fabricated using an additional pass for the same section thickness exhibits better rupture life. But it should also be considered that increasing the number of weld passes does not enhance the rupture life as the cavity nucleating regions are in closer proximity. This results in accelerated interlinking of creep cavities thereby reducing the joints rupture life. Thus depending on the welding process the number of weld passes can be altered suitably, for the joints to exhibit better creep rupture life.

The multi-pass welding not only generates regions of microstructural disparity in the fusion zone, but also results in significant strain gradients across the base metal. These strain gradients result in a non-homogenous elongation of the weld joint during creep loading. Conventional methods cannot be used for estimating the evolution of strain gradient. Therefore, estimation of strain using orientation gradients obtained from EBSD prove to be a viable solution. It has been well understood that orientation spread within a grain can be related to the inherent strain in the material. A calibration graph was constructed relating the orientation spread and pre-strain levels for the base material under the current investigation. The calibration graph was used to estimate the strain in different regions of the base metal by measuring the orientation spread in these locations. This technique can be used to estimate creep strain of service exposed components and hence has a potentiality for remnant life assessment.

8.2 Suggestions for future work

The current investigation which demonstrated the influence of microstructural changes on the creep rupture properties of 316LN weld joints has opened many new avenues for further research. Some of the possible directions for future work are suggested below:

1. The influence of number of weld passes on creep rupture properties of thermally aged weld joints can be investigated. The current studies were carried out on as-welded specimens, where precipitation of intermetallics occurred only during creep testing. Thermal aging for sufficiently longer durations would result in complete

transformation of the delta ferrite regardless of its morphology. The propensity of creep damage in such joints can further deepen the understanding in this subject.

2. The influence of number of weld passes and fusion metal volume on the creep rupture properties of weld joints made with submerged arc welding (SAW) can be studied. Using the SAW technique the number of weld passes and fusion zone volume can be varied over a wider window and its effect on the mechanical properties can be evaluated.
3. Interrupted creep tests can be carried out to investigate the different stages of cavity nucleation in multi-pass weld joints, to further validate the mechanisms proposed in this study.
4. The creep rupture properties of multi-pass weld joints can be evaluated at lower temperatures where the precipitation of intermetallics is sluggish.
5. The influence of nitrogen content on the creep rupture properties of single and dual pass 316LN SS A-TIG weld joints can be evaluated.
6. In light of findings from the current investigation, the creep properties of all-weld specimens extracted from weld joints made with different processes can be studied.
7. Long term (more than 10,000 hours) creep rupture properties can be carried out the check the validity of the findings from this thesis
8. Creep strain measurements can be attempted in the fusion zone using the crystal orientation parameter.
9. The influence of microstructural inhomogeneities in the fusion zone of other materials having different deformation characteristics can be attempted.
10. Studies can be carried out on careful considerations of welding techniques to reduce the scatter in creep properties. This can help enhance the design life of welded components.

REFERENCES

1. Dieter G E, Mechanical Metallurgy, McGraw-Hill, London, 1988.
2. Orowan E, *J. West Scotland Iron Steel Inst.*, 54(1946)45-96.
3. Evans R Wand Wilshire R, Creep of metals and alloys, Institute of Metals, London, 1985.
4. Frost H J and Ashby M F, *Fundamental aspects of structural alloy design*, Jaffee R I and Wilacox B A (Eds), Plenum Press, New York (USA), 27-65, 1977.
5. Mukherjee A K, Bird J E, and Dorn J E, *Trans. ASM*, 62(1969)155-179.
6. Nabarro F R N, Report on a Conference on The Strength of Metals, (Phys. Soc. London), 1948.
7. Herring C, *J. Appl. Phys.*, 21(1950)437-445.
8. Coble R L, *J. Appl. Phys.*, 34(1963)1679-1682.
9. Harper J G, and Dorn J E, *Acta Metall.*, 5(1957)654-665.
10. Mohammad F A, Murty K L, and Morris J W(Jr.), in John E Dorn Memorial Symposium, Cleveland, Ohio, USA, (ASM), 1973.
11. Mullendore A W and Grant N J, *Trans. Metall. Soc. AIME*, 227(1963)319-330.
12. Stevans R N, *Metall. Rev.*, 11(1966)129-142.
13. Ashby M F, Gandhi C and Taplin D M R, *Acta Metall.*, 27(1979)699-729.
14. Ganesan V, 2006, *unpublished work*.
15. Williams J A, *Acta Metall.*, 15(1967)1119-1124.
16. Oliver P R and Girifalco L A, *Acta Metall.*, 10(1962)765-771.
17. Raj R, *Acta Metall.*, 26(1978)995-1006.
18. Raj R and Ashby M F, *Acta Metall.*, 23(1975)653-666.

19. Argon A S, Chen I W and Lao C W, Creep-Fatigue Environment Interactions, Pelloux R M and Stoloff N S(Eds.), AIME, New York, USA, 1980.
20. Chang H C and Grant N J, *Trans. Metall. Soc. AIME*, 194(1952)619-625.
21. Swindeman R W, Farrell K and Yoo M H, *Res. Mech. Lett.*, 1(1981)67-71.
22. Nieh T G and Nix W D, *Scripta Metall.*, 14(1980)365-368.
23. Shiozawa K and Weeertman J R, *Acta Metall.*, 31(1983)993-1004.
24. Hull D and Rimmer D E, *Phil. Mag.*, 4(1959)673-687.
25. Dyson B F, *Metal Sci.*, 10(1976)349-353.
26. Miller D A, Pilkington R, *Metall. Trans. A*, 11(1980)177-180.
27. Needleman A and Rice J R, *Acta Metall.*, 28(1980)1315-1332.
28. Chen C W and Machlin E S, *Acta Metall.*, 4(1956)655-656.
29. Intrater J and Machlin E S, *Acta Metall.*, 7(1959)140-143.
30. Gifkins R C, Gittins A, Bell R L, and Langdon T G, *J. Mater. Sci.*, 3(1968)306-313.
31. Gittins A and Williams H D, *Phil. Mag.*, 16(1967)849-851.
32. Monkman F C and Grant N J, *Proc. Amer. Soc. Testing Mater.*, 56(1956)593-620.
33. Dobes F and Milicka K, *Metal Sci.*, 10(1976)382-384.
34. Asby M F and Dyson B F, Advances in Fracture Research, vol. 1, Pergamon Press (Oxford), 1984.
35. Larson F R and Miller J, *Trans ASME*, 74(1952)765-775.
36. Maruyama K, Armaki H G, Yoshimi K, *Int. J. Press. Ves. Pip.*, 84(2007)171-176.
37. Robinson E L, *Trans. Am. Inst. Min. Engrs.*, 74(1952)777-781.

38. Goodall W, Techniques for multiaxial creep testing. Gooch D J and How I M (Eds.), Elsevier Applied Science, Amsterdam, 1986, 3-27.

39. Metals Handbook vol.1, 10th Ed., American Society of Metals, Ohio (USA) 1991.

40. Novak C J, Handbook of Stainless Steels, Peckner D and Bernstein I M (Eds.), McGraw Hill, New York, 1978.

41. Fontana M G, Corrosion Engineering, (Tata McGraw-Hill, New Delhi), 2008.

42. Paul C S Wu, Report ORNL TM 6311, ORNL, Tennessee (USA), 1978.

43. Laha K, Kyono J, Sasaki T, Kishimoto S and Shinya N, *Mater. Metal. Trans. A*, 36(2005)399-409.

44. Eckenrod J J and Kovach C W, Properties of austenitic stainless steels and their weld metals, Brinkman C R and Garwin H W (Eds.), ASTM STP 679: 17-41, 1979.

45. Irvine K J, Gladman T and Pickering F B, *J. Iron Steel Inst.*, 199(1969)1017-1028.

46. Marshall P, Austenitic Stainless Steels: Microstructure and Mechanical Properties, Elsevier Apllied Science Publishers, London and New York, 1984.

47. Gavriljuk V G and Hans Berns, High Nitrogen Steels, Springer, New York, 1999.

48. Their H, Baumel A and Schmidtmann E, *Arch. Eisenhuttenwes*, 40(1969)333-339.

49. Kujanpaa V P, *Weld. J.*, 63(1984)369-375.

50. Ritter A M and Savage W F, *Metall. Trans.*, 17(1986)727-737.

51. Hull F C, *Weld. J.*, 46(1967)399-409.

52. Hammar O and Svensson U, Solidification and casting of metals, The Metals Society, London, 401-410, 1979.

53. Koseki T, Matsumiya T, Yamada W and Ogawa T, *Metall. Trans.*, 25(1994)1309-1321.

54. Lippold J C and Kotecki D J, Welding metallurgy and weldability of stainless steel, John-Wiley and sons, New Jersey (USA), 2005.

55. Suutala N, *Metall. Trans. A,* 14(1983)191-197.

56. Brooks J A and Thompson A W, *Int. Mater. Rev.*, 36(1991)16-44.

57. Kotecki D J and Siwert T A, *Weld. J.,* 71(1992)171-178.

58. Schaeffler A L, *Weld. J.,* 26(1947)603-620.

59. Delong W T, *Weld. J.,* 53(1974)273-286.

60. Lundin C D, Ruprecht W and Zhou G, Ferrite Measurement in Austenitic and duplex steel castings, University of Tennessee, Knoxville (USA), 1999.

61. Berggren R G, Cole N C, Goodwin G M, Stiegler J O, Slaughter G M, Gray R J and King R T, *Weld. J.*, 57(1978)167-174.

62. Matsuda F, Nakagawa H, Katayama S and Arata Y, *Trans. Jpn. Weld. Res. Inst.*, 12(1983)89-95.

63. Sourmail T, *Mater. Sci. Technol.,* 17(2001)1-14.

64. Lo K H, Shek C H and Lai J K, *Mater. Sci and Engg. R,* 65(2009)39-104.

65. Sundararaman D, Shankar P and Raghunathan V S, *Metall. Trans. A,* 27(1996)1175-1186.

66. Weiss B and Stickler R, *Metall. Trans.*, 7(1972)851-866.

67. Horton C A P, Marshall P and Thomas R G, Mechanical behavior and nuclear applications of stainless steel at elevated temperatures, The Metals Society, London, 66-72, 1982.

68. Keown S R and Thomas R G, *Metal Sci.,* 16(1981)386-392.

69. Thomas R G, Proc. specialists meeting on mechanical properties of structural materials including environment, Chester (UK), 297-313, 1983.

70. Mathew M D, Sasikala G, Mannan S L and Rodriguez P, *Mater. Sci. Technol.,* 7(1991)533-535.

71. Senior B A, *J. Mater. Sc.,* 25(1990)45-53.

72. David S A, *Weld. J.,* 60(1981)63-71.

73. Smith J J and Farrar R A, *Int. Mater. Rev.,* 38(1993)25-51

74. Wood D S, Report EUR 10124 EN, Commission of the European Communities, Nuclear Science and Technology, Luxemburg, 1985.

75. Van der Schaaf, Proc. conf. Life of welds at high temperature, Institution of mechnical engineers, London, 1990.

76. Sakthivel T, Vasudevan M, Laha K, Paraeswaran P, Chandravathi K S, Mathew M D and Bhaduri A K, *Mater. Sci. and Engg. A,* 528(2011)6971-6980.

77. Gowrisankar I, Bhaduri A K, Seetharaman V, Verma D D N and Achar D R G, *Weld. J.,* 66(1987)147-154.

78. Polygary S, ESAB Technical report No. SDA 83001, 1982.

79. Ogawa T, Suzuki K and Zaiken T, *Weld. J.,* 63(1984)213-223.

80. Cole N C, Berggren R G, Goodwin G M, King R T and Slaughter G M, 55th Annual Meeting of the American Welding Society, Texas (USA), 1974.

81. Kleuh R L and Edmonds D P, *Weld. J.,* 65(1986)156-161.

82. Vitek J M and David S A, *Weld. J.,* 63(1984)246-253.

83. Mansfield J F, *J. Met.*, 22(1987)1275-1285.

84. Froes F H, Wells M G H and Banerjee B R, *Met. Sci.*, 2(1968)232-234.

85. Foulds J R and Moteff J, *Weld. J.*, 61(1982)189-196.

86. Horton C A P and Lai J K, *Met. Sci.,* 10(1980)502-505.

87. Hongo H, amazaki M Y, Watanbe T, Tabuchi M and Albert S K, Pressure Vessels and Piping: Manufacturing and Performance, Baldev Raj, Choudhary B K and Albert S K (Eds.), Narosa publishing House, New Delhi, 2009, 307-316.

88. King R T, Stieger J O and Goodwin G M, *Weld. J.*, 53(1974)307-313.

89. Manjoine M J, *Weld. J.,* 61(1982)50-57.

90. Thomas R G, *Weld. J.,* 57(1978)81-86.

91. Baldev Raj, Chellapandi P and Vasudeva Rao P R, Sodium Fast reactors with Closed Fuel Cycle, CRC Press, Florida (USA), 2015.

92. RCC-MR Design Code, Section 1, Sub Section Z, French Society for Design and Construction Rules for Nuclear Island Components, 2002.

93. ASME Boiler and Pressure Vessel Code, Section III, Division 1, Subsection NH, The American Society of Mechanical Engineers, New York, USA, 2004.

94. Heiple C R and Roper J R, *Weld. J.*, 61(1982)97-102.

95. Huang H Y, Shyu S W, Tseng K H and Chou C P, *Sci. Technol. Weld. Joining,* 10(2005)566-573.

96. ASTM E139-11, Standard Test Methods for Conducting Creep, Creep-rupture and Stress rupture Tests on Metallic Materials, ASTM International, West Conshohocken, PA (USA), 2011.

97. Vander Voort G F 1999: Metallography Principles and Practices, American Society of Metals, Ohio, 1999.

98. Naveena, Vijayanand V D, Ganesan V, Laha K and Mathew M D, *Mater. Sci. Eng. A*, 552(2012)112-18.

99. Murty K L and Mathew M D, *Nucl. Engg. Des.*, 228(2004)81-96.

100. ASTM E384-16, Standard Test Methods for Microindentation Hardness of Materials, ASTM International, West Conshohocken, PA (USA), 2016.

101. ABAQUS finite element software, version 6.11, Dassault Systemes, 2011.

102. Shankar V, Gill T P S, Mannan S L and Sundaresan S, *Sadhana*, 28(2003)359-382.

103. Valsan M, Sundararaman D, Rao K B S and Mannan S L, *Metall. Mater. Trans. A*, 26(1995)1207-20.

104. Etienne C F, Rossum D V and Roode F, *Proceedings of the International Conference on Engineering Aspects of Creep*, University of Sheffield, U.K. 2: 113-21, 1980.

105. Abe H, Watanabe Y, *Metall. Mater. Trans. A*, 39 (2008)1392-1398.

106. Thomas R G and Keown S R, *Mechanical behavior and nuclear applications of stainless steel at elevated temperatures*, The Metals Society, London, 30-38, 1982.

107. Calcagnotto M, Ponge D, Demir E and Raabe D, *Mater. Sci. Eng. A*, 527(2010)2738-2748.

108. Sasikala G, Ray S K and Mannan S L, *Mater. Sci. Engg. A*, 359(2003)86-90.

109. Goods S H and Brown L M, *Acta Metall.*, 27(1979)1-15.

110. Mathew M D, Sundararaman M and Mannan S L, *Mater. Trans.*, 38(1997)37-42.

111. Vasudevan M, Computational and Experimental studies on Arc Welded Austenitic Stainless Steels, PhD Thesis, Indian Institute of Technology, Madras, India, 2007.

112. Villafuerte J C, Pardo E and Kerr H W, *Metall. Trans. A*, 21(1990)2009-2019.

113. Elmer J W, Allen S M and Eagar T W, *Metall. Trans. A*, 20(1989)2117-2131.

114. Vasantharaja P, Maduraimuthu V, Vasudevan M, and Palanichamy P, *Mater. Manuf. Processes*, 27(2012)1376-1381.

115. Folkhard E, *Welding Metallurgy of Stainless Steel*, Springer Verlag, Wein, New York, 1986. Kou S and Le Y, *Weld. J.*, 65(1986)305-313.

116. Kou S and Le Y, *Weld. J.*, 65(1986)305-313.

117. Petersen W A, *Weld. J.*, 52(1973)74-79.

118. Feaugas X, *Acta Metall.*, 13(1999)3617-3632.

119. Naveena, Vijayanand V D, Ganesan V, Laha K and Mathew M D, *Mater. Sci. Technol.*, 30(2014)1223-1228.

120. Sasikala G, Mathew M D, Rao K B S and Mannan S L, *Mater. Metall. Trans. A*, 31(2000)1175-1185.

121. Jorge- Badiola D, Iza-Mendia A and Gutierrez I, *J. Microsc.*, 228(2007)373-383.

122. Goyal S, Laha K, Chandravathi K S, Parameswaran P and Mathew M D, *Phil. Mag. A*, 91(2011)3128-3154.

123. Bayley C J, Brekelmans W A M and Geers M G D, *Inter. J. Solids and Struct.*, 43(2006)7268-7286.

124. Nix W D, Earthman J C, Eggeler G and Ilschner B, *Acta Metall.,* 37(1989)1067-1077.

125. Wu D, Christian E M and Ellison E G, *J. Strain Analysis,* 19(1984)209-220.

126. Kamaya M 2011, *Ultramicroscopy,* 111(2011)1189-1199.

127. Wright S I, Nowell M M and Field D P, *Microsc. Microanal.,* 17(2011)316-329.

128. Wilkinson A J and Dingley D J, *Acta Metall. Mater.,* 39(1991)3047-3055.

129. Wright S I and Nowell M M, *Microsc. Microanal.,* 12(2006)72-84.

130. El-Dasher B S, Adams B L and Rollett A D, *Scripta Mater.,* 48(2003)141-145.

131. Sun S, Adams B L and King W E, *Phil. Mag. A,* 80(2000)9-25.

132. Brewer L N, Field D P and Merriman C C, in Schwarz A J, Kumar M, Adams B L and Field D P (Eds.), Electron Backscatter Diffraction in Material Science, Kluwer Academic/Plenum Publishers, New York, 251-262, 2000.

133. Kunze K, Wright S I, Adams B L and Dingley D J, *Text Microstruct.,* 20(1993)41-54.

134. Kamaya M, Wilkinson A J and Titchmarsh J M, *Nucl. Eng. Des.,* 235(2005)713-725.

135. Githinji D N, Northover S M, Bouchard P J and Rist M A, *Mater. Metall. Trans. A,* 44(2013)4150-4167.

136. Mino K, Fukuoka C and Yoshizawa H, *J. Japan Inst. of Met.,* 64(2000)50-55.

137. Muransky O, Smith M C, Bendeich P J, Holden T M, Luzin V, Martins R V and Edwards L, *Int. J. of Solids Struct.,* 49(2012)1045-1062.

138. Laha K, Chandravathi K S, Rao K B S, Mannan S L and Sastry D H, *Mater. Metal. Trans. A,* 32(2001)115-124.

139. Laha K, Chandravathi K S, Parameswaran P, Goyal S and Mathew M D, *Mater. Metal. Trans. A*, 43(2012)1174-1186.